

1. Begutachter	<u>Doz. Dr. H. ROTT</u>
2. Begutachter	<u>Doz. Dr. A. DENOTH</u>
Promotionsdatum	<u>23. Nov. 1996</u>

Methods and Analysis of Synthetic Aperture Radar Data from ERS-1 and X-SAR for Snow and Glacier Applications

Dissertation
zur Erlangung des akademischen Grades
eines Doktors der Naturwissenschaften
an der
Leopold-Franzens-Universität
Innsbruck

eingereicht von
Mag. Thomas Nagler

Innsbruck, im September 1996

Abstract

The capabilities and methods of spaceborne Synthetic Aperture Radar (SAR) for snow and glacier monitoring are investigated. 21 SAR scenes of the European Remote Sensing Satellite ERS-1 from 1992/93 and 10 X-SAR scenes of the Shuttle Imaging Radar-C / X-SAR from April and October 1994, acquired over the high alpine region Ötztal and the region near Innsbruck, are analyzed. The ERS calibration strategy is discussed. The calibration constant of the European Space Agency is compared with values based on trihedral corner reflectors deployed on the Ötztal glaciers. The SAR scenes were terrain corrected; the geocoding accuracy was determined using corner reflectors as geodetic reference. Comparative field measurements of the physical target properties are the basis for the interpretation of the seasonal and short term variations of backscattering, including its incidence angle dependence, for various targets (snow, firn, glacier ice, vegetation, rocks, meadows, fields, forests). Models are used to explain the influence of different snow conditions on backscattering. SAR image statistics are discussed as relevant for parameter estimation and target discrimination. Different speckle filters and their effects on the classification are studied. A new algorithm for wet snow mapping is developed using repeat pass SAR images of crossing orbits. After several pre-processing steps wet snow maps are generated by thresholding the ratio of the actual SAR image to a reference SAR image and combining the snow maps of crossing orbits. The ERS snow maps are compared with snow classifications based on Landsat Thematic Mapper. Possibilities and limitations of single channel SAR for glacier studies have been investigated. The wet snow algorithm was found useful for mapping accumulation and ablation areas on glaciers; examples are shown for ERS-1 and X-SAR in comparison to field observations.

Contents

Acknowledgements	v
1 Introduction	1
1.1 Cryospheric remote sensing	1
1.2 Outline	2
2 Imaging principles and sensor characteristics	5
2.1 Basic imaging principles	5
2.2 Range and azimuth resolution	5
2.3 ERS-1 AMI SAR	7
2.4 SRL SIR-C/X-SAR missions	9
3 Test sites and available remote sensing data	11
3.1 Description of the test sites	11
3.1.1 Test site Ötztal	11
3.1.2 Test site Leutasch/Seefeld and Inn valley	11
3.2 The DEM of the test site Ötztal	12
3.3 ERS-1 SAR and Landsat TM acquisitions in 1992/93	13
3.4 SRL SIR-C/X-SAR experiments at the Ötztal test site	14
4 Radiometric calibration of SAR images	17
4.1 End-to-end SAR system model	17
4.1.1 Imaging point scatterers	17
4.1.2 Imaging homogeneous distributed targets	18
4.1.3 Noise	18
4.2 Calibration of ERS-1 SAR PRI products	18
4.2.1 Calibration constant published by ESA	19
4.2.2 Derivation of the calibration constant from SAR images	19
4.2.2.1 The integral method applied to pixel values	20
4.2.2.2 Theoretical radar cross-section of trihedral corner reflectors	21
4.2.2.3 Derivation of the calibration constant	21
4.2.3 Calibration constant based on corner reflectors of Ötztal test site . .	21
4.3 Backscattering cross section from ERS-1 PRI data	22
4.3.1 Range Spreading Loss Compensation	25
4.3.2 Elevation Antenna pattern correction	25
4.3.3 Replica power and chirp energy density correction	26
4.3.4 Power loss due to ADC saturation	27
4.4 Backscattering coefficient from X-SAR data	27

5	Geocoding of SAR images	29
5.1	Overview	29
5.2	Analytic formulation of spaceborne SAR image geocoding	30
5.2.1	DEM-to-image transformation	30
5.2.2	SAR image simulation of the test site Ötztal	31
5.2.3	Auxiliary products	32
5.2.3.1	Layover mask	36
5.2.3.2	Radar shadow mask	37
5.2.3.3	Local incidence angle map	37
5.3	Quality control of geocoded Ötztal ERS-1 PRI scenes	38
5.3.1	Definition of quality parameters	38
5.3.1.1	Actual residuals	38
5.3.1.2	Artificial residuals	39
5.3.1.3	Quality parameter \mathcal{Q}	39
5.3.2	Absolute accuracy of geocoded ERS-1 PRI images of the test site Ötztal	39
5.3.3	Relative accuracy of geocoded ascending and descending images of the test site Ötztal	41
6	Microwave interaction with snow	43
6.1	Dielectric properties of snow	43
6.1.1	Dry snow	43
6.1.2	Wet snow	44
6.1.2.1	Penetration depth and attenuation	44
6.2	Snow as a scattering medium	45
6.2.1	Surface scattering	47
6.2.1.1	Definition of surface parameters	47
6.2.1.2	Single scattering model for surfaces	48
6.2.2	Volume scattering	49
6.2.3	Effect of layering and frozen crusts	52
6.3	Backscattering contributions from snow covered terrain	52
7	Signature study based on SAR data	57
7.1	ERS-1 surveys in Ötztal 1992/93	58
7.1.1	Field measurements	58
7.1.1.1	Characterization of the snow medium during ERS-1 passes	58
7.1.1.2	Surface roughness measurements	64
7.1.2	Incidence angle dependence of backscattering from alpine targets	66
7.1.3	Temporal variation of backscattering	69
7.1.4	Snow surface roughness experiment	71
7.2	SRL SIR-C/X-SAR missions in Ötztal	75
7.2.1	Field measurements during SRL-1 and SRL-2	77
7.2.2	Incidence angle dependence of backscattering in the X-band	78
7.2.3	Short term backscatter variations	80
7.3	Investigations at Leutasch/Innsbruck	83
7.3.1	Field measurements	83
7.3.2	Temporal variations of backscattering	85

- 8 SAR image statistics and filtering 91**
 - 8.1 Rayleigh clutter model 91
 - 8.1.1 Statistical properties of the scattered radiation 91
 - 8.1.2 Distribution of the detected intensity 92
 - 8.2 Parameter estimation 93
 - 8.2.1 Averaging of samples 93
 - 8.2.2 Effect of multi-looking and averaging on distributions 95
 - 8.2.3 Statistical sampling effects 95
 - 8.3 Change detection technique 98
 - 8.3.1 Difference versus ratio images 98
 - 8.3.2 Statistics of the ratio image 99
 - 8.3.3 Discrimination of changes based on the ratio method 99
 - 8.4 Speckle reduction in SAR images 101
 - 8.4.1 Digital filtering 104
 - 8.4.1.1 Median Filter 104
 - 8.4.1.2 Frost Filter 104
 - 8.4.1.3 Modified Frost Filter 105
 - 8.4.1.4 Gamma MAP filter 105
 - 8.4.2 Filtering experiments 106

- 9 Classification of snow and glaciers based on Landsat TM 113**
 - 9.1 Processing of Landsat TM images 113
 - 9.1.1 Rectification and auxiliary products 113
 - 9.1.2 Calibration of Landsat-5 TM 113
 - 9.1.3 Planetary albedo, surface albedo and atmospheric radiative transfer 115
 - 9.2 Classification rules 117
 - 9.3 Analysis of Landsat TM images of Ötztal 118

- 10 Wet snow mapping by means of SAR 121**
 - 10.1 Review of snow mapping procedures 121
 - 10.1.1 Snow mapping procedures using single SAR images 122
 - 10.1.1.1 Snow mapping procedure of Rott *et al.* (1985) 122
 - 10.1.1.2 Snow mapping procedures of Haefner *et al.* (1993) and Shi and Dozier (1993) 123
 - 10.1.2 Snow classification using polarimetric parameters 125
 - 10.2 Snow mapping based on repeat-pass SAR images 125
 - 10.2.1 Discussion of the wet snow mapping procedure 126
 - 10.2.1.1 Required input data 126
 - 10.2.1.2 Co-registration, calibration, and lowpass filtering of repeat-pass images 127
 - 10.2.1.3 Classification rule for snow covered areas 129
 - 10.2.1.4 Combination of snow maps of ascending and descending orbits 130
 - 10.2.2 Temporal dynamics of snow extent by means of SAR 131
 - 10.2.2.1 Estimation of the threshold TVAL 131
 - 10.2.2.2 Late winter conditions 131
 - 10.2.2.3 Spring conditions 133
 - 10.2.2.4 Summer conditions 133
 - 10.2.3 Comparison of SAR based and TM based snow maps 135

10.2.3.1	ERS-1 SAR images of 1 June and 6 July versus TM image of 29 June	135
10.2.3.2	ERS-1 SAR of 10 August versus Landsat TM 16 August 1992	139
10.2.4	Temporal consistency of SAR based snow maps	139
10.2.5	Snow extent of the basin Venter Ache based on SAR	142
11	SAR as a tool for glacier investigations	145
11.1	Introduction	145
11.1.1	Definitions	145
11.1.2	Mass balance studies on Ötztal glaciers	146
11.2	Procedure for mass balance estimation based on SAR	148
11.3	Examples for SAR based glacier investigations	150
11.3.1	Glacier mass balance estimation using C-band SAR	150
11.3.2	Glacier mass balance studies by means of X-SAR	152
11.3.3	Regional trend of glacier behaviour derived from SAR images	157
12	Summary and conclusions	161
A	ERS-1 PRI image quality assessment based on corner reflectors	167
	Bibliography	177

Acknowledgements

The research described in this thesis could not have been carried out without the help and guidance of a number of people all of whom I am grateful to. Most of all I wish to thank my supervisor Dr. Helmut Rott, who fascinated me for passive and active microwave remote sensing and its applications. He gave me the opportunity to carry out some research in different regions of the world, from the Ötztal glaciers to the Patagonian Icefield and the Antarctic Peninsula. Discussing problems and working in projects with him has inspired me for a fuller understanding of many topics.

I also like to thank Dr. Armin Denoth, the second supervisor of the thesis, for his helpful comments of this work.

I want to thank Dr. Shaun Quegan and Dr. J.C. Shi for the fruitful discussions about analyzing SAR images and understanding of backscattering from snow during my visits at the University of Sheffield and at the University of California, Santa Barbara and during their visits in Innsbruck. Thanks also to Dipl. Ing. Birgit Schättler and Dr. Richard Bamler at the Deutschen Fernerkundungs-Datenzentrum DFD at Oberpfaffenhofen, for providing updated information about ERS SAR and X-SAR processing and calibration, and Dr. Heidi Escher-Vetter, Kommission für Glaziologie, Bayerische Akademie der Wissenschaften, München, for providing the field based mass balance analysis of Vernagtferner. Special thanks to Dr. Robert Davis, CRREL, for providing his knowledge about measuring snow structure and his help during a field campaign at the Ötztal glaciers.

Furthermore, I want to thank all my friends and colleagues of the remote sensing group at the Institut für Meteorologie und Geophysik, Universität Innsbruck for helpful discussions and for joining me during several field campaigns at the Ötztal glaciers and measurements at the Leutasch site; Mag. Klaus Sturm, Mag. Dana-Marie Floricioiu, Susi Lentner, Mag. Wolfgang Rack, and Mag. Martin Stuefer. Furthermore, I owe a great deal to Dana, Shaun, Friedl Obleitner, and Martin for giving their time for proof-reading and their valuable comments on this work.

Last but not least, I am grateful to my parents, Eva and Heinrich Nagler, for all what they have done for me over the last years. Finally, I wish to thank Dana for her general encouragement, particularly when the light at the end of the tunnel was still far off.

The ERS-1 data for this work were provided by the European Space Agency (ESA), experiments *AO.A1* and *A02.A101*, the SIR-C/X-SAR data by NASA/DARA/ASI, *High Alpine SAR Experiment*. This work was supported within the project *ERS/SIR-C/X-SAR* of National Space Research Program of the Austrian Academy of Sciences.

Chapter 1

Introduction

Snow and ice have an important impact on men's life in many direct and indirect ways. The optical, thermodynamic, and mechanical properties of snow are so special that many processes on the earth surface (including ice covered oceans) are strongly affected by the presence of snow [57]. The seasonal snow cover is widespread, continuously changing in structure, irregular in thickness, and rapid in formation and disappearance. Monitoring the amount and the distribution of the seasonal snow cover helps to predict floodings, water supply for irrigation and hydropower stations, to estimate frost damage, and may contribute to the improvement of weather forecasts and the understanding of the climate system. Alpine glaciers are valuable natural water reservoirs which store water during winter and release it due to melting during summer, when water is needed for irrigation and hydropower generation. The gain or loss of mass of glaciers is also an indicator for climatic changes. Because of the spatial and temporal variability of snow the use of remote sensing techniques is highly appropriate to monitoring seasonal snow cover and glaciers.

1.1 Cryospheric remote sensing

Table 1.1 gives an overview of sensors available for snow mapping and glacier observation on an operational basis. Because of the dynamic behaviour of the cryospheric elements change detection is a key issue for remote sensing techniques.

Imaging in the microwave region has the advantage over passive optical imaging of being independent of clouds and of solar irradiance. Passive microwave sensors with a resolution of several kilometers to tens of kilometers are excellent tools for mapping the snow extent at large scales, but they are not useful for mountainous terrain [51]. Synthetic Aperture Radar (SAR) is an active microwave imaging device with high spatial resolution. This, along with the sensitivity of radar wavelengths to surface roughness and moisture content of snow, means that SAR is a potentially ideal remote sensing tool for detecting rapidly changing situations on the earth's surface occurring at any weather situation or time of the day. As an example, ERS-1 offered the unique possibility to study the collapse of an ice shelf at the time scale of a few days [72]. Another application example is the detection of changes in the ice margin and nearby lakes and the mapping of snow facies boundaries on the Greenland ice sheet [18].

Prior to 1991 SAR data were only available from short experimental missions, like Seasat in 1978, Space Shuttle missions in 1981 and 1984, and several airborne missions with mainly regional coverage. Nevertheless, the potential of SAR for applications in hydrology and glaciology in combination with ground based scatterometer signature measurements was investigated [61]. [48]. Since the launch of the European Remote Sensing Satellite

Satellite	Sensor	Spectral range	channels	Ground resolution	Repeat (*) Observation
Optical spectrum					
Landsat-5	TM	0.45 - 2.4 μm	6	28.5 m	16 d
		10.50 - 12.5 μm	1	120 m	16 d
Spot	HRV	0.50 - 1.1 μm	3	20 / 10 m	3 d
NOAA	AVHRR	0.58 - 12.5 μm	5	1 km	12 h
IRS-1C	PAN	0.50 - 0.75 μm	1	5.8 m	5 d
	LISS-III	0.52 - 1.70 μm	3 / 1	23 / 70 m	5 d
	WiFS	0.62 - 0.86 μm	2	188 m	5 d
Passive microwaves					
DMSP	SSM/I	19-85 GHz	7	12 - 60 km	12 h
Active microwaves					
ERS	AMI SAR	5.3 GHz, VV	1	25 m	16 d ⁽¹⁾
JERS-1	SAR	1.28 GHz, HH	1	18 m	44 d ⁽²⁾
Radarsat	SAR-SB ⁽³⁾	5.3 GHz, HH	1	26 - 100 m	3 d
	SAR-FRB ⁽³⁾	5.3 GHz, HH	1	9 m	6.5d

Table 1.1: Sensors for snow mapping and glacier monitoring: (d...days, h...hours). (*)...repeat observations are given for mid-latitudes under considerations of overlapping swaths and side view capabilities. (1) for 35 d repeat cycle. (2) 44 d repeat cycle; overlapping of swath is not taken into account. (3) for 24-day cycle, Standard Beam (SB) and Fine Resolution Beam (FRB) .

1 (ERS-1) by the European Space Agency (ESA) in July 1991, followed by JERS-1 in 1992 (National Space Development Agency, Japan, NASDA), ERS-2 (ESA) and Radarsat (Canadian Space Agency, CSA) in 1995. images have become available on a regular basis and all around the globe. Furthermore, during the next decade new SAR systems will be launched, e.g. Advanced SAR (ASAR) on ENVISAT (ESA, planned for launch in 1998). The amount of data requires the development of automatic and semi automatic procedures for analyzing SAR images in order to generate operational products.

1.2 Outline

To discuss these topics a basic knowledge of the SAR principles and of the interaction of microwaves with snow is required. Chapter 2 describes the imaging principles of side looking spaceborne SAR sensors and specifies the characteristic parameters for ERS-1 and X-SAR. A description of the test sites Ötztal and Leutasch/Innsbruck and a list of available remote sensing images is given in Chapter 3. Chapter 4 addresses the absolute calibration of the SAR images, the derivation of the calibration constant from trihedral corner reflectors deployed at the glacier plateaus of the Ötztal site, and the derivation of backscattering cross-sections from SAR images. Geocoding of SAR images using a digital elevation model is described in Chapter 5 including the estimation of the absolute geocoding accuracy and relative accuracy of ascending and descending ERS-1 PRI scenes.

Chapter 6 gives an introduction on the interaction of microwaves with snow covered terrain using simple theoretical models. Although natural snow is more complex than assumed in these models, this chapter provides basic knowledge on the questions of how

the presence of snow influences the radar backscattering, which backscattering processes primarily contribute to the backscattered signals, and how scattering is related to the snow properties. This knowledge is needed for the interpretation of signatures of various alpine targets (winter snow, firn, glacier ice, high alpine vegetation, rocks and moraines, cultivated meadows, agricultural fields and forest) derived from ERS-1 and X-SAR images in relation to field measurements of characteristic target parameters (Chapter 7).

Because SAR is a coherent system the images are corrupted by speckle, which is the reason why the images cannot be interpreted pixel by pixel. Speckle also effects the detection of changes in radar backscatter between repeat pass images. Methods for optimal estimation of parameters from SAR images including the change detection technique and speckle reduction methods are discussed in Chapter 8.

Remote sensing methods and applications for monitoring the cryosphere are presented in Chapter 9, Chapter 10, and Chapter 11. In Chapter 9 snow cover and glaciers were analyzed with optical satellite data (Landsat-5 Thematic Mapper) to produce comparative data sets and to verify the SAR classifications presented in Chapter 10 and Chapter 11. The use of SAR images for mapping snow is discussed in detail in Chapter 10. It includes the state of the art in snow mapping by means of SAR and the presentation of a new snow mapping procedure using repeat pass SAR images of crossing orbits. Based on this new algorithm the snow retreat during the melting season April to September 1992 was determined on a 35 day cycle using ERS-1 images. For the use in runoff models the change of snow extent was derived for the Alpine basin Venterache, which was separated into several altitude zones and in glaciers and ice free terrain. Chapter 11 is dedicated to specific applications of SAR data in glaciology. It is shown that the snow mapping procedure can be applied to estimate the accumulation area and to map the ablation pattern. Several glaciers in the Ötztal were analyzed using ERS-1 data from 1992 and X-SAR SRL-1/2 data from April 1994 and October 1994, which were compared with field observations and Landsat TM classifications.

Chapter 2

Imaging principles and sensor characteristics

2.1 Basic imaging principles

Principles of imaging radars, with real aperture (RAR) and synthetic aperture (SAR), are based on the properties of antenna arrays and pulsed waves and on the ability of coherent recording of emitted pulses. An extensive description of the theory of imaging radar can be found in [8], [13], [92]. Using data from the European Remote Sensing Satellite ERS-1 as examples the full SAR image formation process from data acquisition and the SAR processing steps to the final image product is described in detail in [2].

Figure 2.1 sketches the scanning geometry of spaceborne radar systems. For the generation of an image of the earth's surface two scanning mechanisms, in the across swath (range) direction and in the along track (azimuth) direction, are employed. Scanning in azimuth (along track) direction is done by moving the side looking antenna along its orbital path. At the same time electromagnetic pulses at the rate of the pulse repetition frequency (PRF) are transmitted and their echoes are received by the same antenna; this enables scanning in the range direction. The pulses propagate across the swath with the velocity of light c , while the sensor is moving with the velocity v_s . Because the time scales of the two scanning mechanisms for spaceborne SAR systems differ by several orders of magnitude they can be treated as mutually independent and are often called slow time (azimuth direction) and fast time (range direction). According to the antenna properties each single pulse covers a spot on the surface called the antenna footprint. The elevation beam of the antenna illuminates the total swath width and is given by $\theta_v \sim \frac{\lambda}{D}$; the azimuth beamwidth is given by $\theta_a \sim \frac{\lambda}{L}$, where L and D are the length and the width of the antenna.

2.2 Range and azimuth resolution

The minimum range distance between two points on the surface which can be separated by a pulsed radar system is given by the range resolution r_s

$$r_s \simeq \frac{c\tau}{2} = \frac{c}{2B} \quad (2.1)$$

where τ is the duration of the compressed pulse with bandwidth B . The corresponding ground range resolution r_g at a specific incidence angle θ_i is

$$r_g \simeq \frac{c}{2B \sin \theta_i} \quad (2.2)$$

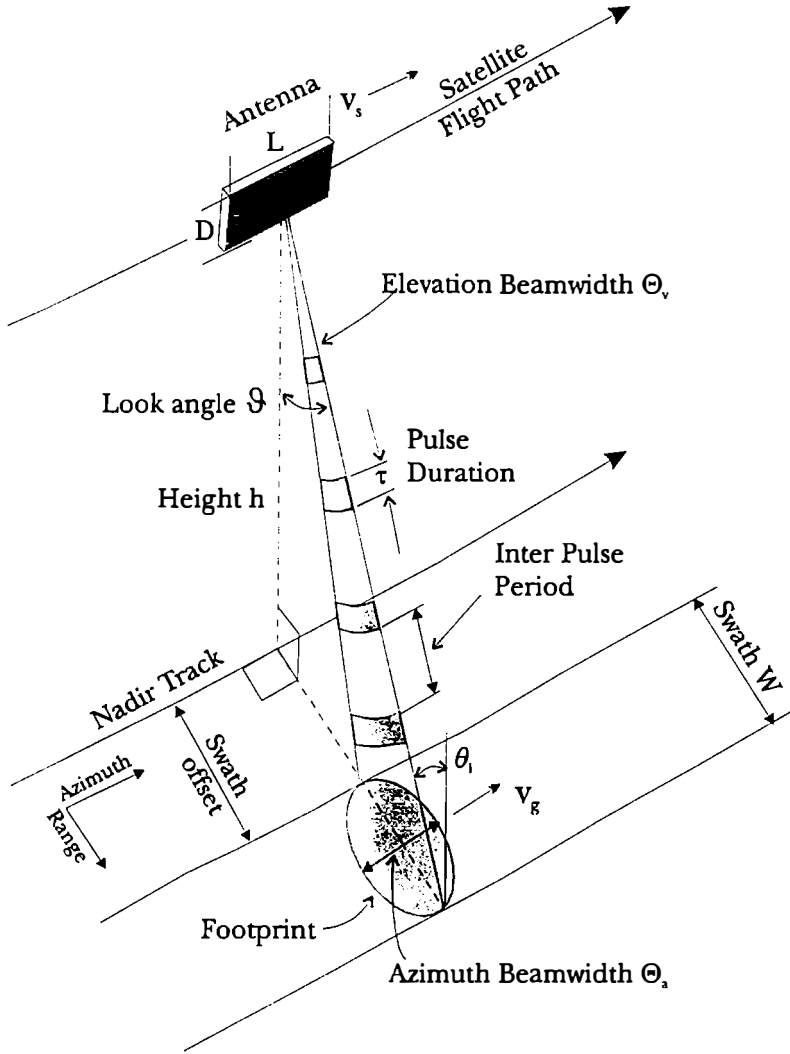


Figure 2.1: Simplified geometry of a right looking radar system (after Curlander *et al.* '81).

To achieve a reasonable range resolution and a high detection capability the pulses are modulated as chirps, which enables the transmission of pulses with high total power and large B whereas the real peak transmit power is low.

In general it can be assumed that the antenna pattern of a spaceborne radar system is separable into range and azimuth direction. For a rectangular antenna with length L the one way antenna pattern for small angles is a sinc^2 -function¹, with first zeros at an angle of $\theta_{a,0} = \lambda/L$. To define the size of the footprint the half power beam width is applied, which is given by [2]

$$\theta_{a,3dB} = 0.638\lambda/L \quad (2.3)$$

To improve the resolution in the azimuth direction the synthetic aperture technique can be applied, which requires coherent recording of the backscattered pulses. As long as a stationary target on the earth surface is within the antenna footprint, the range distance changes while the sensor passes by. But even a small change in the range distance will result in a change in the measured phase of the pulse; e.g. for C-band a change of r_s of only 2.8 cm will cause a change in the phase by about 180° . The change in phase due

¹ $\text{sinc}(x) = \sin(\pi x)/(\pi x)$

to along track motion is approximately parabolic and causes the instantaneous frequency (frequency at a certain range distance to a target, often also called *Doppler*-frequency) to vary along the flight path in an approximately linear manner. The change of the instantaneous frequency is called azimuth chirp. The finest possible azimuth resolution r_a of a SAR system is given by

$$r_a \simeq \frac{L}{2} \quad (2.4)$$

It depends only on the antenna length L and is independent of the height of the sensor and of the wavelength. In practice there are technical limitations in increasing the azimuth resolution by decreasing L [8].

Due to earth rotation an additional phase shift (equal to the change in range distance) is introduced. For this reason the Doppler centroid (instantaneous frequency at antenna beam center) is not observed when the range line to the target is perpendicular to the line of motion. The additional phase shift has a maximum at the equator and becomes zero near the poles. For most spaceborne SAR sensors the influence of earth rotation is compensated to a large part by continuously adjusting the antenna's yaw angle in the opposite direction (yaw steering), which keeps the Doppler centroid at low frequency values.

To avoid azimuth ambiguities the PRF of the system should be high enough to enable sufficiently high sampling of the Doppler spectrum ($PRF > 2v_s/L$). On the other hand the PRF must be low enough that not more than one pulse touches the swath W at the same time, to avoid range ambiguities (at least across the predefined swath width) [13].

2.3 ERS-1 AMI SAR

ERS-1 was launched on 17 July 1991 and operates in a sun synchronous orbit, with an inclination of 98.516° . On board ERS-1 several sensors are installed, the Active Microwave Instrument (AMI), the Radar Altimeter (RA), the Along-Track Scanning Radiometer and Microwave Sounder (ATSR-M) [15]. The AMI incorporates two separate radar systems, a SAR working in the *Image* or *Wave Mode*, and a scatterometer for *Wind Mode* operation. In this study products from the ERS-1 AMI SAR in Image Mode are used.

Table 2.1 summarizes the main parameters of the ERS-1 AMI SAR. The antenna points to the right of the flight direction. The size of the antenna footprint is about 100 km in range and 4.3 km in azimuth. Between two pulses the footprint, which has a velocity on the earth surface of $v_{gr} = 6650 \text{ m/s}$, moves about 4 m. A target is covered by more than 1000 pulses, each of them giving backscatter with a typical instantaneous frequency depending on its location within the footprint (Doppler frequency shift). The approximate distance between sensor and scatterer at mid swath is about 850 km, which results in a two way echo time delay of $5.67 \times 10^{-3} \text{ s}$. With a pulse repetition frequency (PRF) of 1640 to 1720 Hz more than 9 pulses are transmitted before the echo of the first pulse is received.

Nominally ERS-1 operates in yaw steering mode, which keeps the Doppler centroid frequency within about $\pm 900 \text{ Hz}$ ($\pm 8000 \text{ Hz}$ in Roll Tilt Mode). At the equator the yaw angle reaches its maximum value of $\pm 3.9^\circ$, whereas it becomes zero near the poles.

The two-way power antenna azimuth pattern is proportional to the sinc^4 -function. According to eq. 2.3 the half power width is $\theta_{a,3dB} = 0.207^\circ$. In the range direction the antenna main beam is modified so that the elevation beamwidth becomes wider and the transmitted power is distributed more uniformly across the swath. The two way power antenna pattern in the range direction is shown in figure 4.5 and must be taken into account for the absolute calibration of the SAR data.

ERS-1 AMI Image mode characteristics	
Orbital altitude (nominal)	785 km
Frequency	5.3 GHz (C-Band)
Polarisation	Linear – Vertical
Antenna size	10 m × 1 m
Swath width	100 km
Swath stand off	250 km (side of orbital track)
Incidence angle	23° (at mid swath)
Nominal ground resolution	30 m × 30 m
Nominal radiometric resol.	2.5 dB at $\sigma^0 = -18$ dB
Pulse Bandwidth	15.55 ± 0.1 MHz
PRF range	1640 to 1720 Hz
Transmit pulse length	37.12 ± 0.06 μ s
Chirp frequency rate	~ 0.41889 MHz/ μ s
Compressed pulse	64 ns
Bandwidth in azimuth	1410 Hz
Peak power	4.8 kW
Analog to Digital complex	
Sampling	18.96 10 ⁶ samples/s
Sampling window	296 μ s
Quantisation	5I/5Q or 6I/6Q

Table 2.1: ERS-1 sensor characteristic (The Data Book of ERS-1, 1992, ERS-1 System, 1992).

Due to different requirements for various scientific fields the ERS-1 mission was divided into several phases with different orbit characteristics. Table 2.2 gives an overview of the ERS-1 mission phases. Depending on the phase, the repetition rate of the orbits varies between 3 days and 168 days, and the number of orbits per cycle between 43 and 2411. Due to the orbit planning of ESA the imaging geometry of repeat passes is reproduced very accurately, so that the incidence angle to the same target is within tenths of a degree. The accurate repeat orbits enable the use of ERS-1 images for radar interferometry [24], and the detection of changes on the earth surface by decorrelation of speckle or by a change of the backscattered intensity (without influence of the incidence angle) [60], [93].

ERS-1 Precision Images (PRI) are used in this study. PRI products are in ground range projection and each scene covers an area of about 100 km × 100 km. The image

Code	Mission Phase	Date	RC	OC
A	Commissioning Phase	25.07.91 - 10.12.91	3	43
B	1 st Ice Phase	28.12.91 - 30.03.92	3	43
—	Roll Tilt Mode Campaign	04.04.92 - 13.04.92	35	—
C	1 st Multidisciplinary Phase	14.04.92 - 21.12.93	35	501
D	2 nd Ice Phase	23.12.93 - 10.04.94	3	43
E	Geodetic Phase	10.04.94 - 28.09.94	168	2411
F	Geodetic Phase	28.09.94 - 21.03.95	168	2411
G	—	21.03.95 - onward	35	501

Table 2.2: ERS-1 mission phases. Repeat cycle in days (RC), orbits per cycle (OC) (from: ESRIN usERServices: <http://gds.esrin.esa.it/>).

X-SAR Characteristics	
Orbital Altitude	225km
Frequency	9.6 GHz (<i>X – Band</i>)
Polarisation	<i>Linear – Vertical</i>
Antenna size	12 m × 0.4 m
Antenna Gain	43.5 dB
Swath width	15 to 45 km
Look angle range	15° to 55°
Azimuth antenna pattern model	$\text{sinc}^2(\phi/0.151^\circ)$
Range resolution (10/20 MHz)	15 / 7.5 m
Azimuth resolution	6.3 m
Nominal radiometric resol.	2.5 dB at $\sigma^\circ = -18$ dB
Pulse bandwidth	10 or 20 MHz
PRF range	1240 to 1736 Hz
Transmit pulse length	40 μ s
Azimuth bandwidth	650 to 1180 Hz
Peak transmit power	3.35 kW

Table 2.3: SRL-1/2 X-SAR sensor characteristic (Zink and Bamler. 1995, Jordan *et al.*, 1995).

Data can be absolutely calibrated in terms of radar cross-section. The calibration and derivation of the backscattering coefficient σ° from PRI products is discussed in detail in chapter 4. Further specifications of the PRI product are:

- pixel spacing: 12.5 m in azimuth and 12.5 m in ground range
- 3 independent looks in azimuth, each with a non-overlapping look bandwidth of 320 Hz (total processed bandwidth: 960 Hz); looks are oversampled, power detected and summed without weighting; the square root of the summed result is provided by the PRI product
- image quality parameters [2]:
 - integrated side lobe ratio (ISLR): -15.4 dB (azimuth), -16.5 dB (range),
 - peak side lobe ratio (PSLR): -16.8 dB (azimuth), -19.8 dB (range)
 - spatial resolution: azimuth: 20.8 m (nominal: < 30 m), ground range: 28.0 (nominal: < 33 m)

For information on the image quality parameters see appendix A. Dependent on the SAR processor and the processor version different correction factors (range spreading loss, antenna pattern, etc.) are implemented in the processing scheme (see Chapter 4).

2.4 SRL SIR-C/X-SAR missions

During the Space Radar Laboratory (SRL) missions 1 and 2 the Shuttle Imaging Radar C (SIR-C) and X-SAR were mounted on the space shuttle *Endeavour* for two 10 day missions in April and September / October 1994. SIR-C/ X-SAR is a co-operative experiment between NASA, the German Space Agency (DARA) and the Italian Space Agency ASI. SIR-C, which was developed by NASA JPL, provides full polarimetric data at C-band (5.8

cm wavelength) and L-Band (23.5 cm wavelength). X-SAR, developed by Dornier, Germany, and Alenia Spazio, Italy, operates at 9.6 GHz (3.1 cm wavelength), VV-polarization. In this work only X-SAR data will be investigated.

The orbit inclination for SRL flights was about 57° . The shuttle orbit had a slight westward drift in the equatorial crossing longitude, which enabled the repeat coverage of the test sites at different incidence angles. Between the flights SRL-1 and SRL-2 no degradation of the system parameters (azimuth pattern, pulse shape) of X-SAR was found [99]. The sensor characteristics of X-SAR are summarized in table 2.3. Using eq. 2.3 the azimuth half power beamwidth is estimated as $\theta_{\alpha,3dB} = 0.0952^\circ$, leading to an approximate footprint of ~ 4.9 km at a look angle of 40° .

For this study Multi-look Ground range Detected (MGD) products (which are equivalent to the ERS-1 PRI product) and Geocoded Terrain Corrected (GTC) products processed at D-PAF (German Processing and Archiving Facility) are available. For MGD products of different data takes the pixel spacing and the ground resolution are kept constant at 12.5 m \times 12.5 m and approximately 25 m \times 25 m, respectively, as long as the look angle to a test site and the pulse band width allow it. Hence, the effective number of looks varies depending on the PRF, the processed azimuth bandwidth, and the chirp bandwidth [1]. The image quality parameters of MGD products were analyzed by Zink and Bamler [99], who report a spatial resolution of 22.4 m and 23.4 m and an ISLR of -14.8 and -19 dB in range and azimuth, respectively.

GTC products are generated by the geocoding software package GEOS at D-PAF, which is based on the range-Doppler approach [77]. For geocoding the Ötztal data, a DEM of 25 m \times 25 m resolution was provided by the Institute of Meteorology and Geophysics, University of Innsbruck, and was implemented into the GEOS software database.

Chapter 3

Test sites and available remote sensing data

3.1 Description of the test sites

3.1.1 Test site Ötztal

The Ötztal in the Central Alps has been a test site for several SAR campaigns during the last 15 years. In this area, research on glacier mass balance, glacier dynamics, snow melt runoff and hydrology has been carried out for several decades. Two runoff gauges, a climate station, and a research station of the Institute of Meteorology and Geophysics, University Innsbruck, are located in the test site (figure 3.1). It includes elevations between 1900 m a.s.l. at the village Vent, located in a narrow valley, and 3770 m a.s.l. at the highest peak Wildspitze (WS) and 3739 m a.s.l. at Weißkugel (WK). The area is partly covered by glaciers. The narrow valleys were formed by glacial erosion during the last ice age. The firn areas of the glaciers Gepatschferner / Langtauferer Ferner (21 km²) and Kesselwandferner (4.5 km²) form a large plateau with gentle topography, which is a useful target for studies of snow and ice signatures by means of SAR. The partly crevassed termini of the glaciers extend into narrow valleys. Glacier research and field measurements during the ERS-1 and SRL-1/2 missions were focussed on the glaciers Kesselwandferner / Gepatschferner and Hintereisferner (9 km² in size), and on the icefree areas of the Rofental. Above 2100 m the vegetation of the area is mainly made up by sedges, grasses and dwarf-shrubs. Below 2100 m coniferous forests and cultivated meadows dominate.

During the SAR surveys of ERS-1 in 1992 and during the SRL-1/2 missions in 1994, the field activities included the deployment of corner reflectors for calibration and geocoding purposes, measurements of snow and meteorological parameters and the mapping of the snow line and the ablation pattern.

3.1.2 Test site Leutasch/Seefeld and Inn valley

This test area includes the Inn valley between Innsbruck and Telfs at about 600 m a.s.l. and the plateau of Leutasch Seefeld at 1100 m to 1300 m a.s.l.. The area is covered mainly by cultivated meadows, agricultural fields and forests. Urban areas like Innsbruck and some villages are located in the test site. The Inn valley is aligned in a west-east direction enclosed by steep slopes in the north and south of the valley, rising up to mountain ridges of more than 2000 m altitude. The highest peaks are about 2700 m. Due to the steep incidence angle of ERS-1 these slopes are in foreshortening and layover regions or at pronounced backslopes depending on the direction of SAR illumination. The region

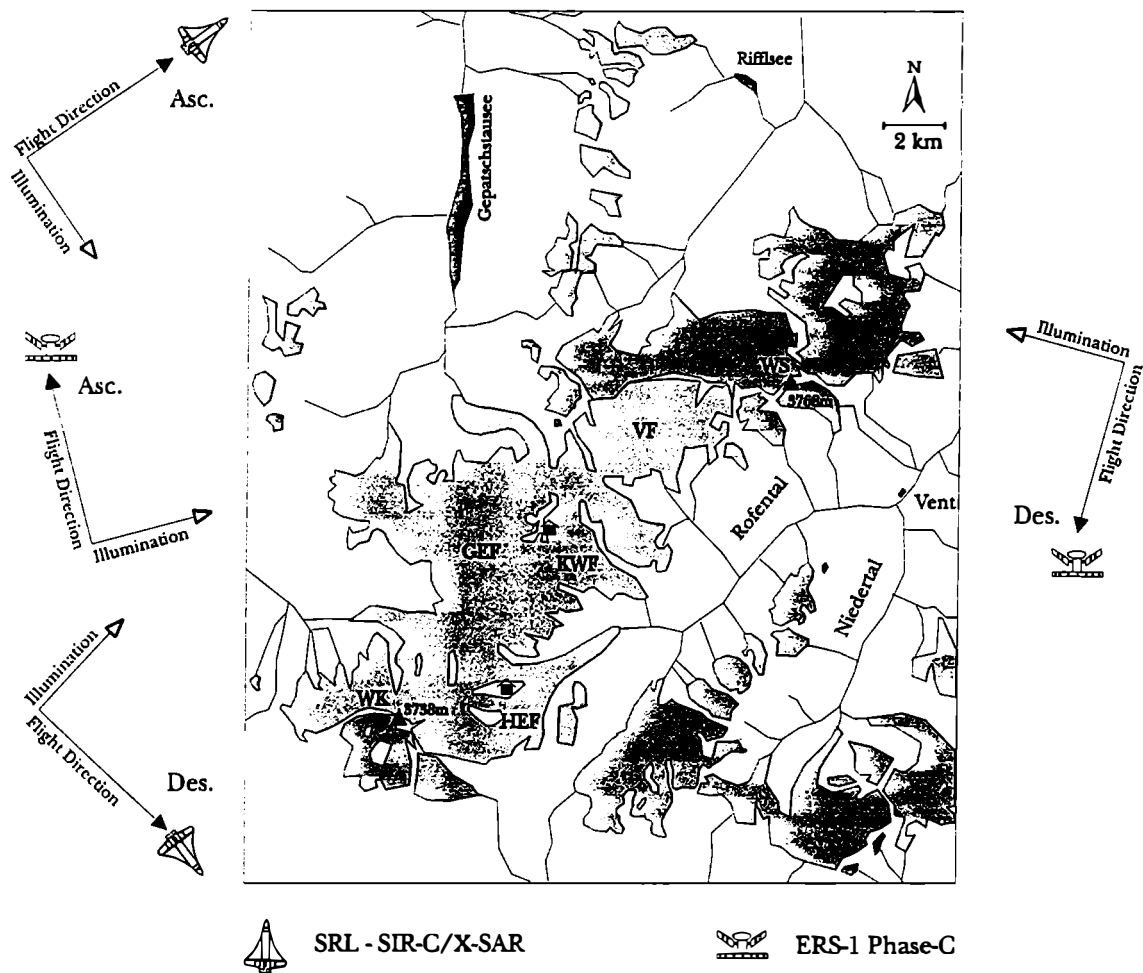


Figure 3.1: Sketch map of the test site Ötztal. The main glaciers and peaks in the test site are labelled: Hintereisferner (HEF), Kesselwandferner (KWF), Gepatschferner (GEF), Vernagtferner (VF), Wildspitze (WS), Weißkugel (WK). Two huts, which are used during the field campaigns, are shown. The mean flight direction and the direction of illumination for ascending and descending passes are shown to the left and right of the sketch map for ERS-1 during Phase C and for SIR-C / X-SAR.

of Leutasch/Seefeld in the north of the Inn valley consists mainly of cultivated meadows and coniferous forest. Because of its location close to the northern boundary of the Alps and the elevation the duration, thickness and snow morphology of the snow cover are significantly different from those observed in the Inn valley.

3.2 The DEM of the test site Ötztal

For the Ötztal test site a digital elevation model (DEM) is available, which covers an area of 26 km in East-West by 16 km in South-North direction (figure 3.2). It was generated at the Institute for Image Processing and Computer Graphics, Joanneum Research, Graz. The 20 m and 10 m contour lines of the official Austrian Topographic Map 1:25000, ÖK sheet 172-Weißkugel and 173-Sölden were digitized and interpolated to a grid with $25 \times 25 \text{ m}^2$ pixel spacing. A part of the DEM including the glacier areas Hintereisferner, Kesselwandferner and Gepatschferner was resampled and interpolated to a grid with 12.5

A-Date	UTC	Orbit	Frame	Track	Pass	PAF	P-Date
27 Apr 92	10:07	4089	2655	437	des	E	920925
	21:27	4096	927	444	asc	E	920926
1 Jun 92	10:08	4590	2655	437	des	E	920625
	21:28	4597	927	444	asc	E	920701
6 Jul 92	10:08	5091	2655	437	des	E	920923
	21:28	5098	927	444	asc	E	920817
10 Aug 92	21:28	5599	927	444	asc	E	920918
14 Sep 92	10:08	6093	2655	437	des	D	921013
	21:28	6100	927	444	asc	E	921012
19 Oct 92	10:08	6594	2655	437	des	E	930406
	21:28	6601	927	444	asc	E	921124
28 Dec 92	10:08	7596	2655	437	des	U	930831
8 Mar 93	10:08	8598	2655	437	des	D	930408
	21:28	8605	927	444	asc	E	930501

Table 3.1: Available ERS-1 AMI SAR scenes in PRI format of Ötztal for the period April 1992 to March 1993. Each scene is specified by acquisition date (A-Date) and time (UTC), by orbit, frame, track and pass (ascending or descending). The required corrections for retrieving the backscattering coefficient depend on the date of processing (P-Date) and on the Processing and Archiving Facility (PAF: E...EECF, D...D-PAF, U...UK-PAF).

Date	UTC	Path	Row	Quarter
29 Jun 92	9:27	193	27	4
16 Aug 92	9:27	193	27	4
17 Sep 92	9:26	193	27	4

Table 3.2: Landsat-5 Thematic Mapper images available for investigations in Ötztal.

m x 12.5 m spacing. The original DEM was generated in Transverse Mercator TM (Gauss-Krüger) projection, using a Bessel ellipsoid and local datum of Austria. For SAR image simulation and geocoding purposes the DEM was transformed to Universal Transverse Mercator UTM projection, zone 32, Bessel ellipsoid, with 12.5 m E x 12.5 m N and 25 m E x 25 m N grid spacing, respectively.

3.3 ERS-1 SAR and Landsat TM acquisitions in 1992/93

During the period 27 April 1992 to 12 April 1993 a multitemporal data set has been acquired by ERS-1 over the Ötztal. Central Alps and the Inn valley including the plateau Leutasch /Seefeld, Austria. ERS-1 was in phase C, the first multi-disciplinary phase with a repeat cycle of 35 days (table 2.2). Table 3.1 gives an overview of the available ERS-1 SAR PRI scenes covering the test site Ötztal. For several dates images of crossing orbits, ascending (asc) and descending (des) passes, are available. The ERS-1 heading at scene center for repeat pass images (same frame and track) was 47° for descending passes and 345° for ascending passes. During the same period three almost cloud free Landsat-5 TM images were acquired (table 3.2). The location of ERS-1 frames and of the Landsat TM images is shown in figure 3.2. The flight path and the direction of SAR illumination are plotted in figure 3.1.

The available ERS-1 PRI SAR images of the test site Inn valley and Leutasch/Seefeld are presented in table 3.3, the location of the frames is shown in figure 3.3. Scenes shared

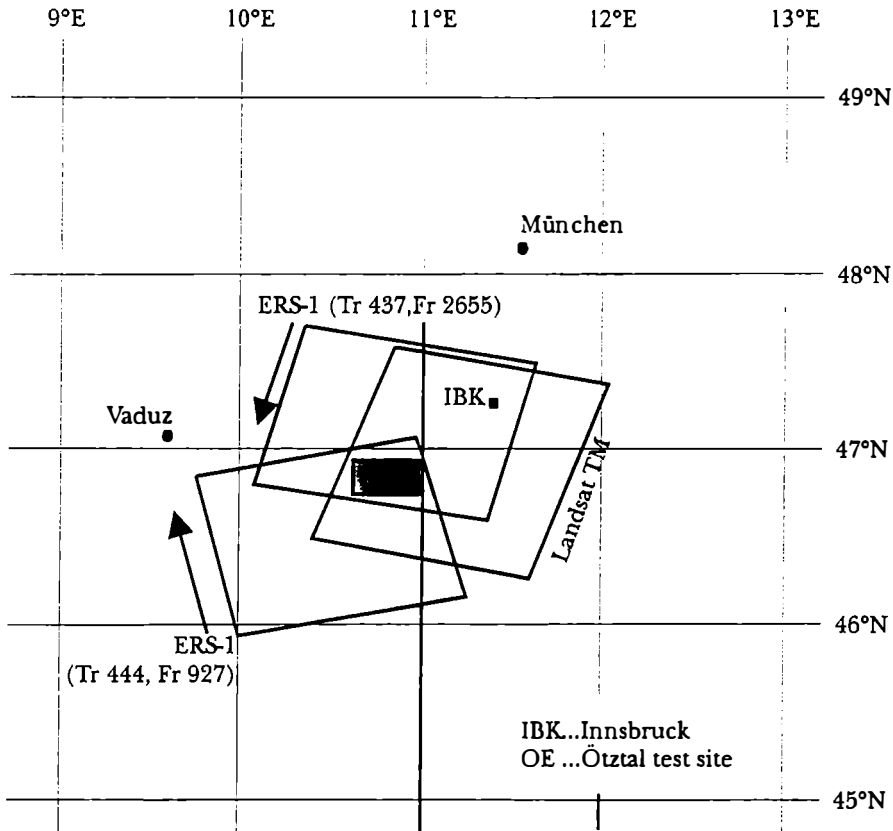


Figure 3.2: Location of ERS-1 scenes and Landsat TM scenes. The area covered by the digital elevation model of 25 m pixel spacing is shown in grey and is marked by the initials OE.

with investigations in the Ötztal test site are included for reasons of completeness and are labelled with *. Because a DEM was not available for this site the analysis of the backscattering cross section of different targets is limited to flat areas, where the local incidence angle is known from the imaging geometry.

3.4 SRL SIR-C/X-SAR experiments at the Ötztal test site

The SIR-C/X-SAR was operating on the space shuttle *Endeavour* during two 11-day missions in April (SRL-1) and October 1994 (SRL-2). The glacier area of Ötztal was selected as super test site for snow hydrology. In this thesis only data of X-SAR are analyzed, which are available as multi-look ground range detected images (MGD) and as geocoded terrain corrected (GTC) products, including local incidence angle maps, layover and shadow masks (GIM), processed and generated by D-PAF. Table 3.4 summarizes parameters for each data take acquired over the test site Ötztal. These data are useful to study short term and seasonal variations of backscattering on glaciers and the possibilities for estimating mass budgets of glaciers. Figure 3.1 shows the mean flight direction and radar illumination for ascending and descending passes.

A-Date	UTC	Orbit	Frame	Track	Pass	PAF	P-Date
*14 Sep 92	10:07	6093	2655	437	Des	D	921013
*19 Oct 92	10:07	6594	2655	437	Des	E	930406
*28 Dec 92	10:07	7596	2655	437	Des	U	930831
13 Jan 93	10:04	7825	2655	165	Des	D	930831
1 Feb 93	10:07	8097	2655	437	Des	U	930308
17 Feb 93	10:07	8326	2655	165	Des	D	930311
5 Mar 93	21:22	8562	945	401	Asc	D	930408
*8 Mar 93	10:07	8598	2655	437	Des	D	930408
9 Apr 93	21:22	9063	945	401	Asc	U	930423
12 Apr 93	10:08	9099	2655	437	Des	U	930427

Table 3.3: ERS-1 AMI SAR scenes in PRI format available for investigations at the Inn valley and in Leutasch/Seefeld; ascending (Asc) and descending (Des) pass, time (UTC) and date of image acquisition (A-Date), date of scene processing (P-Date), Processing and Archiving Facility (PAF: E...EECF, D...D-PAF, U...UK-PAF). Scenes covering also Ötztal are labelled by *.

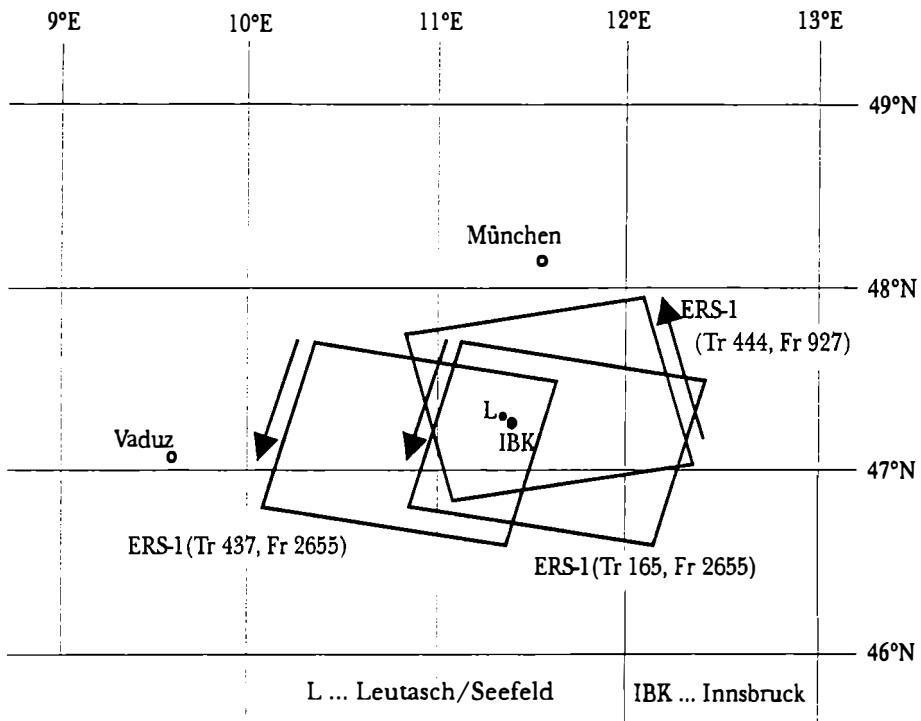


Figure 3.3: Location of ERS-1 frames available for investigations in the Inn valley and at Leutasch/Seefeld.

DT	Pass	LDir	A-Date	UTC	α [°]	θ_i [°]
SRL-1						
14.20	Asc	S	10 Apr	06:32	53.5	36.0
18.21	Des	N	10 Apr	12:42	132.2	44.8
34.31	Des	N	11 Apr	12:24	133.1	52.8
46.10	Asc	S	12 Apr	05:55	55.3	50.4
78.00	Asc	S	14 Apr	05:16	57.5	58.1
SRL-2						
14.20	Asc	S	1 Oct	06:41	53.5	36.3
18.21	Des	N	1 Oct	12:50	132.3	45.1
34.31	Des	N	2 Oct	12:32	133.2	52.0
46.00	Asc	S	3 Oct	06:02	55.2	50.3
78.10	Asc	S	5 Oct	05:23	57.0	58.0

Table 3.4: Acquisition of SRL/X-SAR data at test site Ötztal: data take (DT), ascending (Asc) and descending (Des) pass, look direction of radar (LDir) to north (N) or south (S), heading (α), incidence angle at scene center (θ_i).

Chapter 4

Radiometric calibration of SAR images

For determination of backscattering coefficients the SAR data have to be absolutely calibrated. In section 4.1 the end-to-end SAR system model and the calibration philosophy for point scatterers and homogeneous distributed targets is presented. In section 4.2 the calibration procedures published by ESA for images processed at different Processing and Archiving Facilities (PAF) are summarized. The ESA calibration constant is compared with calibration constants derived from trihedral corner reflectors, which were deployed on glaciers in the test site Ötztal during ERS-1 overflights in 1992. Section 4.3 and section 4.4 show the derivation of σ^0 from ERS-1 PRI and X-SAR MGD data including all necessary corrections.

4.1 End-to-end SAR system model

The transformation from an object, given by the complex function $\gamma^\circ(r_s, t)$, to the image, given by the complex function $u(r_s, t)$, can be modeled as [2]

$$u(r_s, t) = \gamma^\circ(r_s, t) *_{r_s} *_{t} s(r_s, t) \quad (4.1)$$

where $s(r_s, t)$ is the end-to-end complex impulse response function, and r_s and t are the slant range coordinate and the azimuth time coordinate, respectively. The operator $*_{r_s} *_{t}$ denotes the convolution in range and azimuth. The real intensity value $i(r_s, t)$ is given by $|u(r_s, t)|^2$.

4.1.1 Imaging point scatterers

In the end-to-end SAR imaging system model of the ERS-1 SAR processors (D-PAF, EECF) the calibration gain K_σ for point scatterers is modelled as constant over range and is defined by [2]

$$K_\sigma = \iint_{-\infty}^{+\infty} |s(r_s, t)|^2 dr_s dt = constant \quad (4.2)$$

where $|s(r_s, t)|^2$ is the point spread function of the SAR system. It describes the spatial distribution of the energy of a point object in the image. The total energy of the image

of an object with a radar cross section σ is [2]

$$\sigma K_{\sigma} = \iint_{-\infty}^{+\infty} i(r_s, t) dr_s dt \quad (4.3)$$

Based on this equation the radar cross section of a point target can be derived from the image data if K_{σ} is known.

4.1.2 Imaging homogeneous distributed targets

The Rayleigh imaging model assumes that distributed homogeneous targets are composed of many single point scatterers with similar radar cross section, which are randomly distributed over an area. The Rayleigh model is discussed in detail in section 8.1. Although the end-to-end SAR system model is normalized by the constant calibration gain for point scatterers K_{σ} (which is given in zero Doppler coordinates r_s [m] and t [s]), the image of a distributed target (which is given in ground coordinates r_g [m] and a [m], where a corresponds to the along track direction) exhibits a $1/\sin \theta_i$ dependence. This is simple due to imaging geometry, which means that the point spread function, which is constant in slant range, depends on θ_i when projected on the ground. The area on the ground contributing to one image pixel becomes larger for low values of θ_i . Therefore the calibration gain for distributed targets K_{σ^o} is a function of the incidence angle. In the ERS-1 PRI image generation the $1/\sin \theta_i$ -dependence is not taken into account; a constant incidence angle of 23° is assumed. This has the advantage that the true local incidence angle need not to be known for SAR processing. Some SAR processors (such as the X-SAR processors at D-PAF) correct for $1/\sin \theta_i$ assuming an ellipsoidal earth without real terrain for deriving the local incidence angle.

4.1.3 Noise

The dominant noise sources in a SAR system are quantization noise and thermal receiver noise [12]. If noise is uncorrelated with the signal it will show up as an additive noise floor in the final image. For considering noise the image intensity may be splitted [2]:

$$\langle i \rangle = \langle i_n \rangle + \langle i_s \rangle \quad (4.4)$$

where the subscripts n and s stand for noise and signal, respectively. $\langle \cdot \rangle$ denotes the expected value. The noise level in an image can be expressed as noise equivalent σ^o , the knowledge of which is required for noise corrections. For ERS-1 the noise equivalent σ^o is about -26 dB at 23° incidence angle [99]. Natural surfaces, which are investigated later in this study (snow, glacier ice, rocks and low vegetation) usually show σ^o -values above -20 dB. Because the noise floor is at least several dB (usually more than 10 dB) lower than the expected signals the system noise has not been corrected in this study.

4.2 Calibration of ERS-1 SAR PRI products

The ERS-1 SAR Precision Images are composed of 16 bit numbers, which are proportional to the amplitude of the backscattered signal [41]. For PRI products K_{σ^o} is specified at the reference incidence angle $\theta_{ref} = 23^\circ$, which is the incidence angle at mid range. Therefore

$$K_{\sigma^o}(\theta_i) = K_{\sigma^o}(\theta_{ref}) \frac{\sin \theta_{ref}}{\sin \theta_i} \quad (4.5)$$

Processed	D-PAF	EECF	UK-PAF
before 1 Sept 1992	K=58.32 dB	K=58.32 dB	K=59.49 dB
after 1 Sept 1992	K=58.24 dB	K=58.24 dB	K=60.30 dB

Table 4.1: Table of the calibration constants for different PAFs and processor versions (from Laur [39]).

$K_{\sigma\sigma}(\theta_{ref})$ is different for each Processing and Archiving Facility (PAF), where the images are processed.

4.2.1 Calibration constant published by ESA

For this work PRI images processed by the German Processing and Archiving Facility (D-PAF), the United Kingdom Processing and Archiving Facility (UK-PAF), and by the ESRIN ERS-1 Central Facility (EECF) have been used. Depending on the SAR processor version different calibration constants are required [39]:

- PRI products processed before 1st September 1992: for these images no correction for the antenna pattern was applied and products processed at D-PAF and EECF were not compensated for range spreading loss.
- PRI products processed after 1st September 1992: products processed at all PAFs are corrected for standard antenna pattern and compensated for range spreading loss.

In table 4.1 the calibration constant $K_{\sigma\sigma}$ for different PAFs and various versions of processors are summarized [39]. The differences of $K_{\sigma\sigma}$ are due to different gains and corrections used for processing the images at different PAFs [40].

Updated values of the calibration constants $K_{\sigma\sigma}$ from table 4.1 were derived in [42] by taking into account non-linearities in the analog to digital convertor (ADC) onboard ERS-1 and variations of the replica power pulses. An updated calibration constant is obtained by applying the correction

$$K_{\sigma\sigma,updated}(\theta_{ref}) = K_{\sigma\sigma}(\theta_{ref}) + 0.39dB \quad (4.6)$$

The error bounds (maximum variation of $K_{\sigma\sigma}$ derived from ESA reference targets) of $K_{\sigma\sigma,updated}$ are $\pm 0.42dB$ [42] (table 4.2).

The radiometric stability, the radiometric accuracy and the maximum variation of the measured radar cross section are used to specify the calibration accuracy of a system. The radiometric stability is defined as the standard deviation of the time series measurements of σ of a calibration target, using always the same value of the calibration constant. The radiometric accuracy is given by the time series average of the absolute difference between the nominal radar cross section and the measured radar cross section of a calibration target, using always the same value of $K_{\sigma\sigma}$. These parameters were derived for the active transponder 2 of the Flevoland test site over 2 years (38 measurements) [42] and are summarized in table 4.2.

4.2.2 Derivation of the calibration constant from SAR images

During the ERS-1 SAR surveys in 1992 several corner reflectors were deployed at the glacier plateaus of the test site Ötztal. This enables the comparison and verification of the calibration constant published by ESA (section 4.2.1).

	No Replica and ADC Correction	Replica correction	Replica and ADC correction
radiometric stability	0.43 dB	0.38 dB	0.18 dB
radiometric accuracy	0.38 dB	0.32 dB	0.16 dB
max. variation of σ	± 0.92 dB	± 0.75 dB	± 0.42 dB

Table 4.2: Radiometric calibration measurements without correction, with correction of replica pulse power variations and with correction of replica pulse power variations and ADC non-linearity (Laur *et al.* [42]).

There are several methods for deriving the calibration constant K_{σ} from point targets, including [98]

- the peak method
- the integral method applied to pixel values
- the integral method applied to interpolated values.

In this work we followed an integral method which was first proposed by Gray *et al.* [25].

4.2.2.1 The integral method applied to pixel values

This method estimates the total intensity backscattered from a point target by integrating over an area around the point target. The power reflected by the point target as well as by the background clutter are included in the total power of the area. Therefore the contribution of the background has to be taken into account. Figure 4.1 shows a subarea of a PRI image containing a corner reflector. The position of the reflector is evident from the contour lines. Each dot represents the center of a SAR image pixel. The area used for deriving the backscatter intensity of the background, and the area containing the point target are marked. The total backscattered intensity of the background area is

$$I_B = \sum_{k=1}^m \sum_{l=1}^n i_B(k, l) \quad (4.7)$$

where i_B is the intensity of the pixel (k, l) in the background area, which contains N_B pixels ($m \times n$ pixels in range and azimuth direction, respectively). The intensity I_{TB} from the area containing the point target including the contribution from the background is calculated by

$$I_{TB} = \sum_{k=1}^p \sum_{l=1}^q i_{TB}(k, l) \quad (4.8)$$

where i_{TB} is the intensity of the pixel (k, l) in the target area, which contains N_{TB} pixels ($p \times q$ pixels in range and azimuth direction, respectively). Using eq. 4.7 and eq. 4.8 the total backscattered intensity of the point target itself can be estimated by

$$I_T = I_{TB} - \frac{N_{TB}}{N_B} I_B \quad (4.9)$$

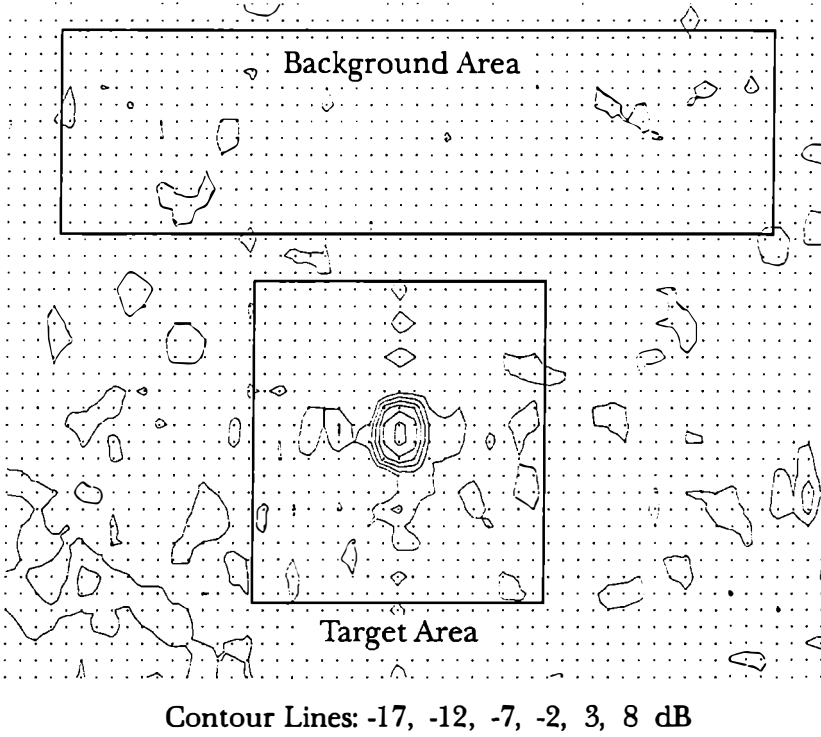


Figure 4.1: The target area centered at the trihedral corner reflector and the background area for the reflector K2, 6 July 1992, ascending pass. Pixel centers are indicated by dots, pixel spacing is 12.5 m x 12.5 m.

4.2.2.2 Theoretical radar cross-section of trihedral corner reflectors

The theoretical radar cross-section of a trihedral corner reflector was derived in [76]. The radar cross-section σ is a function of the incidence angle α , the azimuth angle ϕ , the wavelength λ , and the side length l , and can be calculated using

$$\sigma = \frac{4\pi}{\lambda^2} l^4 \left\{ \cos \alpha + \sin \alpha (\sin \phi + \cos \phi) - 2 [\cos \alpha + \sin \alpha (\sin \phi + \cos \phi)]^{-1} \right\}^2 \quad (4.10)$$

The parameters α , ϕ , and l are defined in figure 4.2.

4.2.2.3 Derivation of the calibration constant

Using eq. 4.9 and eq. 4.10 the calibration constant $K_{\sigma\sigma}$ at the local incidence angle θ_i can be derived from

$$K_{\sigma\sigma}(\theta_i) = \frac{I_T}{\sigma} \delta_a \delta_{r_g} \quad (4.11)$$

where δ_a and δ_{r_g} are the pixel spacings in the azimuth and ground range directions. For PRI images δ_a and δ_{r_g} are both 12.5 m. According to eq. 4.5 $K_{\sigma\sigma}(\theta_i)$ is converted to the reference incidence angle θ_{ref} of 23°. This enables the comparison of $K_{\sigma\sigma}$ -values derived from calibration devices at different locations.

4.2.3 Calibration constant based on corner reflectors of Ötztal test site

Using the method described in the last section $K_{\sigma\sigma}$ has been derived from trihedral corner reflectors, which were deployed on the firm areas of Hintereisferner and Kesselwandferner

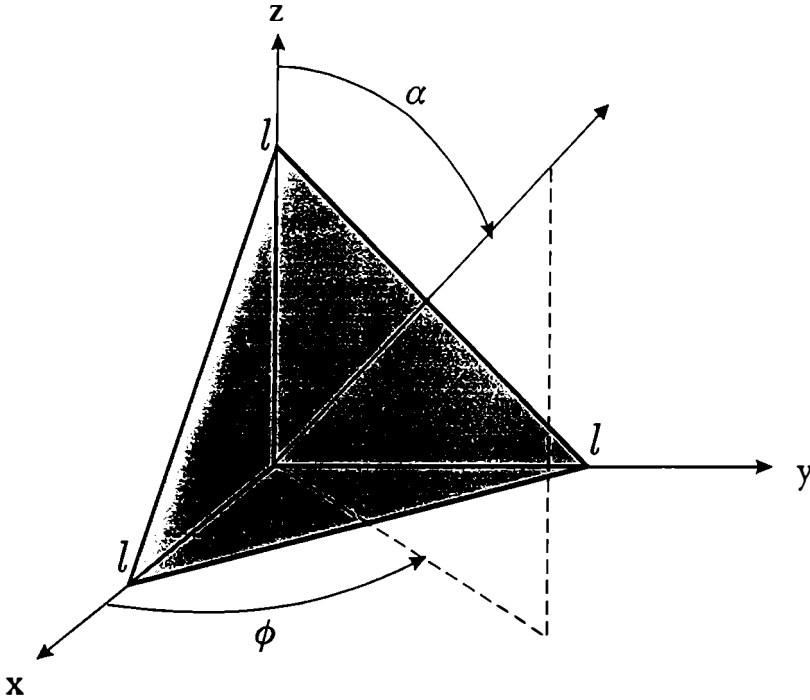


Figure 4.2: Definition of angles for trihedral corner reflectors.

/ Gepatschferner during several field campaigns between 27 April 1992 and 19 October 1992 (figure 4.3). Table 4.3 summarizes the values $K_{\sigma^o}(\theta_{ref})$, derived from the corner reflectors labelled as K1, K2, K3, K4, H1, and H2, respectively. The processing date of the images is required to know the processor version at the corresponding PAF. In this table values of K_{σ^o} are shown only for those reflectors where the response was not affected by precipitation. For each individual image the mean calibration constant $\langle K_{\sigma^o}(\theta_{ref}) \rangle$ with the corresponding standard deviation $sdev$ and the mean calibration constant after replica power correction $\langle K_{\sigma^o,p}(\theta_{ref}) \rangle$ are presented. For the images of 1 June 1992 and 14 September 1992 the standard deviation is not shown because too few values are available. Figure 4.4 shows the comparison between the calibration constants derived from corner reflectors with the corresponding ESA specifications (table 4.1). In general $\langle K_{\sigma^o}(\theta_{ref}) \rangle$ is within the ESA specifications with error bounds of ± 0.95 dB (table 4.2) [42]. Only for the descending orbit in September, where large variations between K_{σ^o} of single corner reflectors are observed, $\langle K_{\sigma^o}(\theta_{ref}) \rangle$ is slightly too low. When compared with $K_{\sigma^o,updated}$ and the corresponding error bounds ± 0.42 dB, $\langle K_{\sigma^o,p}(\theta_{ref}) \rangle$ is at most dates slightly too low. The reasons for the differences could be small distortions of the reflectors due to transportation in the field, so that the true σ is less than the theoretical cross section from eq. 4.10 (the σ of corner reflectors was not measured), and the neglect of the ADC power loss correction. Snow in the corner reflectors has similar effects.

4.3 Backscattering cross section from ERS-1 PRI data

The backscattering coefficient σ^o of a distributed target can be determined from PRI images, using the relation

$$\sigma^o = \frac{\langle DN^2 \rangle \sin \theta_i}{K_{\sigma^o}(\theta_{ref}) \sin \theta_{i,ref}} Q \quad (4.12)$$

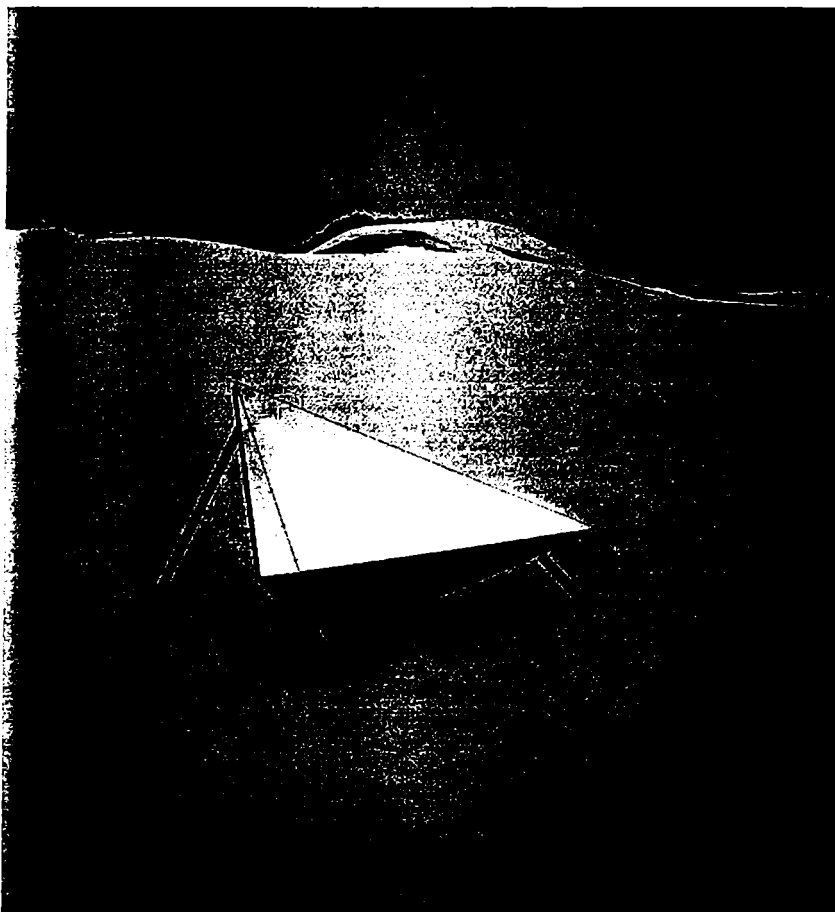


Figure 4.3: Trihedral corner reflector K1, 1.5 m sidelength, on Kesselwandferner during ERS-1 ascending pass on 14 September 1992.

where DN denotes the digital pixel values. The calibration constant $K_{\sigma^0}(\theta_{ref})$ is discussed in detail in section 4.2. The factor $\sin \theta_i / \sin \theta_{i,ref}$ represents the correction for the local incidence angle θ_i . In the case of ERS-1 $\theta_{i,ref}$ is 23° . The factor Q depends on the update of the corrections applied during the image processing, which is given by the processing date and the PAF (D-PAF, pers. communic.):

Processing-Date		Q	
from	to	D-PAF & EECF	UK-PAF
launch	31/8/92	$\frac{r_s^3(\vartheta)}{r_{s,ref}^3(\vartheta)} \frac{1}{G_{im}^2(\vartheta)} \frac{Pr,img}{Pr,ref} A$	$\frac{1}{G_{im}^2(\vartheta)} \frac{Pr,img}{Pr,ref} A$
5/9/92	8/4/93	$\frac{G_{st}^2(\vartheta)}{G_{im}^2(\vartheta)} \frac{Pr,img}{Pr,ref} A$	$\frac{G_{st}^2(\vartheta)}{G_{im}^2(\vartheta)} \frac{Pr,img}{Pr,ref} E(\varphi, \vartheta) A$
9/4/93	15/7/95	$\frac{G_{st}^2(\vartheta)}{G_{im}^2(\vartheta)} \frac{Pr,img}{Pr,ref} A$	$\frac{G_{st}^2(\vartheta)}{G_{im}^2(\vartheta)} \frac{Pr,img}{Pr,ref} A$

(4.13)

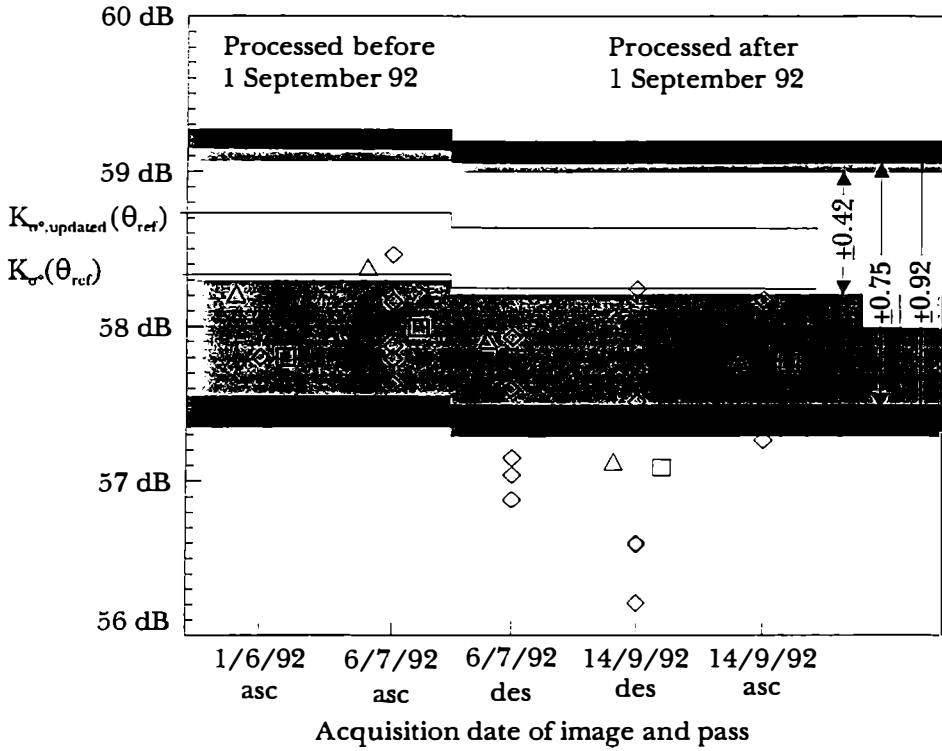


Figure 4.4: Calibration constant derived from Ötztal corner reflectors 1992 (see table 4.3): \diamond ...calibration constant of single corner reflector, \square ...average calibration constant of all corner reflectors in the scene, \triangle ...average calibration constant after correction of the replica power variation. K_{σ^0} , $K_{\sigma^0, updated}$...ESA calibration constants from table 4.1 and eq. 4.6; maximum variation of ESA calibration constant from table 4.2: without correction (dark grey), with replica power correction (medium grey), with replica power and ADC-power loss correction (white).

A-Date	1/6/92	6/7/92	6/7/92	14/9/92	14/9/92
Pass	asc	des	asc	des	asc
PAF	EECF	EECF	EECF	D-PAF	EECF
P-Date	25/6/92	23/9/92	17/8/92	13/10/92	12/10/92
K1	—	57.60	57.63	58.24	—
K2	—	57.03	57.87	57.51	57.26
K3	—	57.14	58.16	56.59	—
K4	—	—	—	56.21	—
H1	57.80	57.92	58.46	56.60	58.17
H2	—	56.87	57.79	—	—
$\langle K_{\sigma^0}(\theta_{ref}) \rangle$	57.80	57.33	57.99	57.10	57.74
sdev	—	± 0.41	± 0.33	± 0.83	—
$\langle K_{\sigma^0, p}(\theta_{ref}) \rangle$	58.21	57.90	58.38	57.13	57.77

Table 4.3: Calibration constant $K_{\sigma^0}(\theta_{ref})$ in dB derived from trihedral corner reflectors deployed on glacier areas at the test site Ötztal. Acquisition date (A-Date), ascending (asc) and descending (des) pass, K1 to H2 are the labels of the corner reflectors, standard deviation of $K_{\sigma^0}(\theta_{ref})$ (sdev). $\langle K_{\sigma^0, p}(\theta_{ref}) \rangle$ is corrected in respect to replica power variations (see figure 4.4).

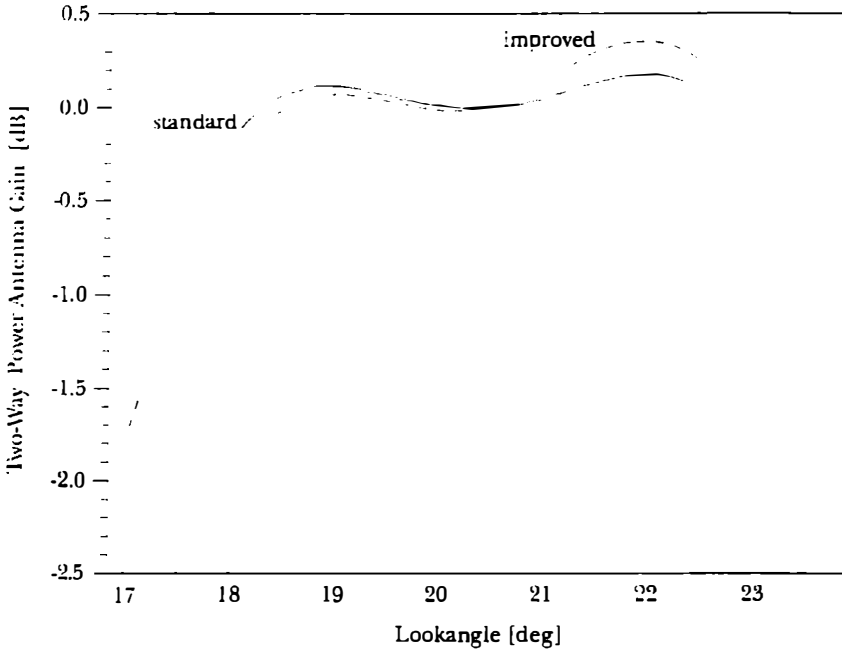


Figure 4.5: ERS-1 standard (solid line) and improved (dashed line) power antenna pattern (source: ESRIIN usERServices WWW: <http://services.esrin.esa.it>).

G^2 is the elevation antenna pattern applied in power values, p_r the pulse replica power, and A the power loss due to saturation of the analog to digital converter. The correction factors will be briefly discussed below.

4.3.1 Range Spreading Loss Compensation

This correction is required, because of the range dependence of the radar equation for SAR. The range spreading loss can be corrected by the factor $r_i^3/r_{s,ref}^3$, where $r_{s,ref} = 847$ km is a reference slant range distance [39]. After 1 September 1992 this correction is applied on all images during SAR processing.

4.3.2 Elevation Antenna pattern correction

The in-flight elevation antenna pattern is measured over large tropical rain forests, which show a backscattering coefficient independent of the incidence angle. In general the elevation antenna pattern is corrected by the factor $1/G^2(\vartheta)$. For ERS-1 data the improved antenna pattern G_{im}^2 has to be applied to the data. Because the standard elevation antenna pattern G_{st}^2 was applied to images processed before 16 July 1995, G_{st}^2 has to be removed and G_{im}^2 has to be applied. This requires the correction

$$\frac{G_{st}^2(\vartheta)}{G_{im}^2(\vartheta)} \quad (4.14)$$

Figure 4.5 compares the standard and improved power antenna pattern. For UK-PAF images with processing dates between 1 September 1992 and 8 April 1993 the elevation antenna pattern was not applied correctly. This requires the correction factor $E(\varphi, \vartheta)$, which depends on the geographic latitude φ and on the look angle ϑ . At 47.5°N $E(\varphi, \vartheta)$ varies from near to far range between 1.76 dB to -1.78 dB [41].

A-Date	27/4/92	27/4/92	1/6/92	1/6/92	6/7/92
Orbit	4089	4096	4590	4597	5091
Frame	2655	0927	2655	0927	2655
$p_{r,img}$	-0.21*	-0.39*	-0.77*	n.a.	-0.79*
$p_{r,ref}$					
$p_{c,img}$	-0.25	-0.38	-0.63	-0.41	-0.57
$p_{c,ref}$					

6/7/92	10/8/92	14/9/92	14/9/92	19/10/92	19/10/92
5098	5599	6093	6100	6594	6594
0927	0927	2655	0927	2655	0927
-0.40*	n.a.	-0.07	n.a.	-0.11*	n.a.
0.39	-0.13	-0.03	-0.08	0.003	-0.08

28/12/92	13/1/93	1/2/93	17/2/93	5/3/93	8/3/93
7596	7825	8097	8326	8562	8598
2655	2655	2655	2655	0945	2655
-0.04	-0.04	-0.05	-0.09	-0.06	-0.09
n.a.	n.a.	n.a.	n.a.	-0.08	-0.07

8/3/93	9/4/93	12/4/93
8605	9063	9099
0927	0945	2655
n.a.	-0.05	-0.1
-0.07	n.a.	n.a.

Table 4.4: Comparison of replica power correction and mean average chirp energy density per sample correction in dB. Acquisition date (A-Date) in day/month/year. values labelled with * were provided by D-PAF (pers. communications); for images processed at UKPAF values of $p_{c,img}$ were not available.

4.3.3 Replica power and chirp energy density correction

Within the ESA SAR processors, a single replica pulse associated with the processed image product is extracted and used for gain normalization and range compression [42]. In the processor the replica pulse power p_r is assumed to be directly proportional to the transmitted power. The replica pulse power was examined since the beginning of the ERS-1 mission in July 1991. Generally p_r was stable within $\pm 0.1dB$, but for short periods it varied within $\pm 1.0dB$. After [42] two periods were observed with high replica power variations:

- the early commissioning phase (July to early October 1991),
- the early multi disciplinary phase (May to July 1992).

To obtain correctly calibrated images the temporal variation of replica power p_r has to be included. This is done by comparison of $p_{r,img}$, used for generation of the image to be calibrated, with $p_{r,ref}$ of the reference image of Flevoland, 13 October 1991. In general $p_{r,img}$ is specified in the CEOS header of each image. But for images processed in 1992 at EECF $p_{r,img}$ is not annotated. For these images the mean average of the chirp energy density per sample $p_{c,img}$ can be used instead. This parameter can be extracted from the ESA reserved Facility Data Record PCS Type (starting byte: 3449, binary VAX format:

Integer*4, in units 10^{-3}). Further the relation

$$\frac{p_{r,una}}{p_{r,ref}} \simeq \frac{p_{c,una}}{p_{c,ref}} \quad (4.15)$$

is valid. The values for the reference replica power and chirp energy density per sample are specified by ESA with $p_{r,ref} = 205220$ [42] and $p_{c,ref} = 267.2$ (ESA Helpdesk Information, HD 5789). The values of this correction for the ERS-1 images used in this study are given in table 4.4. The difference between the correction based on replica power values or based on chirp energy density values is less than 0.2 dB in the 1992 images, in the 1993 images it was less than -0.1 dB. During the period April to August 1992 the correction reached almost -0.8 dB.

4.3.4 Power loss due to ADC saturation

Non-linearities of the analog to digital converter (ADC) occur over large distributed targets with high backscatter [42]. If the input signal level to the ADC is high, a large number of data values will occupy the lowest and highest quantization levels. The analysis of the standard deviation of the in-phase channel over Europe showed that the ADC loss A was less than about 0.25 dB and ADC saturation was observed mainly over rough sea surfaces. For areas in France and central Europe the ADC loss was less than 0.04 dB [42]. In this study the ADC saturation was not taken into account.

4.4 Backscattering coefficient from X-SAR data

The derivation of σ^0 from X-SAR MGD (multi look, ground range, detected) is similar to the procedure presented above. The X-SAR MGD product corresponds to the ERS-1 PRI product. From MGD products all geocoded products like GTC (geocoded terrain corrected) and GEC (geocoded ellipsoid corrected) are derived.

For MGD products the image pixel intensity i is related to σ^0 by [99]

$$\langle i \rangle = K_{\sigma^0} \frac{\sin \theta_{i,ellips}}{\sin(\theta_{i,ellips} - \alpha)} \sigma^0 - K_N(r_s) \cdot N_{raw} \quad (4.16)$$

where K_{σ^0} is the calibration constant, $\theta_{i,ellips}$ is the local incidence angle on the ellipsoid (GEM-6, corrected by mean scene terrain altitude), α is the local terrain slope (which is given by the DEM). The second term of eq. 4.16 represents the correction for noise power equivalent σ^0 , where N_{raw} is the raw data noise power, and $K_N(r_s)$ is the processor noise gain. N_{raw} and $K_N(r_s)$ are annotated in the CEOS header. The noise equivalent σ^0 varies across the swath and is about -40 dB in near range ($\theta_{i,ellips} = 20^\circ$) and about -27 dB in far range ($\theta_{i,ellips} = 60^\circ$). This means that the noise effects can be neglected for the derivation of σ^0 of most natural targets. The absolute calibration factor determined at the calibration site Oberpfaffenhofen [99] is

$$K_{\sigma^0} = 1 \cdot 10^6 \simeq 60 \text{ dB} \quad \text{for} \quad \text{MGD} - \text{products} \quad (4.17)$$

For flat terrain the local slope α is 0° and the backscatter cross section can be easily derived by eq. 4.16. For inclined surfaces where $\alpha \neq 0^\circ$, eq. 4.16 requires the calculation of $\theta_{i,ellips}$ as a function of range position. This can be done e.g. by fitting a spline to $\theta_{i,ellips}(r_g)$ at near, mid and far range (values are annotated in the CEOS header). If only small regions are analyzed the variation $\theta_{i,ellips}(r_g)$ can be neglected and the average value $\theta_{i,ellips}(r_0)$ can be used for the derivation of σ^0 in this area.

Chapter 5

Geocoding of SAR images

For many applications in remote sensing such as multi-temporal investigations or combinations of data from different sensors and also for comparison with groundbased observations it is necessary to transform all the information to the same coordinate system or map projection. On the other hand images taken by Synthetic Aperture Radar are generally distributed in slant range or ground range geometry. In rugged terrain a SAR image in this projection shows topographic induced distortions, shadow and layover areas. The transformation of the SAR image from the sensor specific image projection into a reference map projection is called geocoding [8].

5.1 Overview

Different methods for geocoding SAR images were developed during recent years. After Raggam *et al.* [56] parametric and non-parametric approaches to geocoding can be separated. Generally only full parametric procedures enable exact SAR image geocoding [56]. Parametric procedures use sensor, orbit and SAR processor specific information as well as high precision digital elevation models (DEM).

At first standard geocoding schemes based on rubber stretch wrapping by using ground control points (GCP) were applied to SAR images. More sophisticated methods were developed by the photogrammetric community, which simulated the SAR imaging geometry by applying modified formulas of geometric optics. Modern SAR geocoding systems are based on a range-Doppler approach, where the relationship between the SAR image generation and the dynamic location of points on the earth's surface is reconstructed [8], [50]. Software packages including precision terrain geocoding and estimation of the quality of the geocoded product were developed at different institutes. Some of them are still under development and are used for demonstration purposes, but some are working operationally (the geocoding system GEOS at D-PAF, DRA Geocoder designed by GEC Marconi, Earth Observation Sciences EOS, and University College London UCL, the geocoding system GEO at I-PAF developed by Telespazio).

For this study a simple approach to geocoding was applied, which follows an analytic formulation of spaceborne SAR image geocoding. This procedure, which is briefly presented in the next section, is used in the wet snow classification procedure (chapter 10) and for glacier investigations (chapter 11).

5.2 Analytic formulation of spaceborne SAR image geocoding

The analytic formulation of spaceborne SAR image geocoding was developed by B. Guindon and M. Adair [26]. The objective was to design a simple geocoding methodology, which can also be adapted to inexpensive computer systems. The software is available in the radar module of the image processing system EASI/PACE of PCI Inc.

The geocoding process uses a two step transformation to relate the three-dimensional coordinates of the DEM to the two-dimensional SAR coordinates. First the DEM is re-sampled to the nominal SAR projection using a simple sensor, orbit, and earth model. Applying a universal backscatter model, the radiometric influence of the topography is taken into account; the backscatter variations due to different surface types are not considered. The result is a geometrically and radiometrically simulated SAR image, which is visually rather similar to the real SAR image. In the second step tie points are selected in both the simulated and the real SAR image. The tie points are used for a low order polynomial transformation between the images. Both transformation steps (DEM to simulated image, simulated to real image) define the requisite mapping for transforming the real SAR image to the original DEM. The DEM is the source of height information as well as absolute geodetic control. This procedure optimizes the co-registration between the real SAR image and the DEM.

5.2.1 DEM-to-image transformation

The transformation from three-dimensional DEM coordinates (E, N, h) to two-dimensional SAR ground-range / azimuth coordinates (r_g, a) is done by a simple imaging model. E and N are the Easting and Northing in Universal Transverse Mercator (UTM) projection, h is the height in meter above the reference ellipsoid. The following assumptions are made in the imaging model, which are valid for relatively small areas (less than 100 km x 100 km):

- spherical earth approximation (with radius R_E)
- constant heading angle Ω
- constant velocity of the sensor
- constant satellite altitude H

From the constant velocity and heading assumption the image azimuth coordinate can be derived from

$$\alpha = E \sin \Omega - N \cos \Omega \quad (5.1)$$

where the image azimuth origin is selected at the corner of the DEM nearest to the satellite. The range coordinate can be calculated as shown in figure 5.1. For two points at the same azimuth coordinate, a reference point A and point B , the ground range coordinate of B relative to A , which is seen at a look angle ϑ , is calculated by

$$r_g = (R_E + h_A) (\zeta - \beta) \quad (5.2)$$

where

$$\zeta = \cos^{-1} \left\{ \frac{- \left[r_s^2 - (R_E + H)^2 - (R_E + h_A)^2 \right]}{2 (R_E + h_A) (R_E + H)} \right\}$$

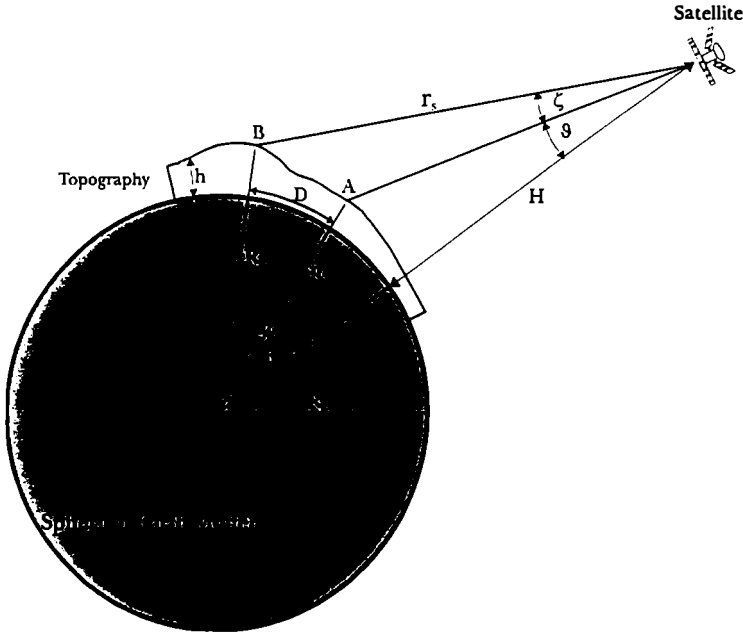


Figure 5.1: Simple model for SAR image simulation using a DEM (after Guindon and Maruyama, [27]).

$$\beta = \frac{\pi}{2} - \vartheta - \cos^{-1} \left(\frac{R_E + H}{R_E + h_A} \sin \vartheta \right) \quad (5.3)$$

$$r_s = \sqrt{(R_E + h_B)^2 + (R_E + H)^2 - 2(R_E + h_B)(R_E + H) \cos(\alpha + \beta)}$$

$$\alpha = \frac{D}{R_E}$$

where h_A and h_B are the heights of the point A and B above the reference ellipsoid, r_s is the slant range distance between point B and the sensor, and D is the true ground distance between A and B on the surface of the spherical earth model. If the coordinates of the reference point A and the point B do not have the same image azimuth coordinate, the true ground range distance D is equal to the distance of B to the straight line passing through A with the heading Ω .

5.2.2 SAR image simulation of the test site Ötztal

Based on the imaging model of section 5.2.1 simulated ERS-1 SAR images were derived from the UTM-32 DEM (section 3.2) by specifying the following parameters for descending and ascending swaths:

- sensor altitude H
- look angle to the reference point $A(\vartheta)$
- heading angle Ω (with: $\Omega = 0^\circ$ to North, increasing in clockwise direction)

	Ascending Swath	Descending Swath
Reference Point	NW corner of DEM	NW corner of DEM
Look angle ϑ	21.5°	20.9°
Heading angle Ω	346.5°	191.2°
Sensor Altitude H	790567 m	790567 m

Table 5.1: Input parameters for SAR image simulation of the test site Ötztal .

- grid spacing of the simulated image (which is the same as the grid spacing of the real SAR image)

As a first approach these parameters were extracted from the CEOS SAR-leader-file. With this set of parameters a first simulated image was generated and compared with the original SAR image. Due to the characteristic shape of foreshortening and layover regions it was possible to use cross correlation of manually selected image chips of different window sizes for fine matching of the images. Artificial targets like corner reflectors were not used, because their positions are not known in the simulated image. The comparison of the simulated and real SAR image indicates necessary modifications of the input parameters, which can be tuned to get a sufficiently accurate match of the simulated and the real image. Once the input parameters including tie points were found a PRI image of the Ötztal test site could be geocoded within a few minutes on a SUN SPARC 20 computer.

In table 5.1 the input parameters for the simulation of a ERS-1 PRI image of ascending and descending swaths are listed. In figure 5.2 and 5.3 the results of the SAR image simulation are shown in comparison to the corresponding parts of PRI images of July 6, 1992 for both swaths.

For this study 14 ERS-1 PRI scenes of the test site Ötztal, ascending and descending repeat passes, were available (table 3.1). Due to the stable orbit of ERS-1 the look angle to a target is conserved within tenths of a degree, which requires only a linear azimuth shift to match the images. Therefore the same input parameters were used for all images. Small differences in the repeat passes were taken into account by individually selected tiepoints for each image. All available PRI images were geocoded based on the UTM-32 DEM with 12.5 m and 25 m grid spacing, respectively. For the total area 25 E x 25 N UTM-32 DEM of Ötztal the original 12.5 m PRI images were averaged over 2 by 2 pixels due to limitations in the computer memory. Geocoding based on the smaller 12.5 E x 12.5 N UTM-32 DEM of Ötztal was performed with the original PRI pixel spacing of 12.5 m. As a first step the images of repeat passes were matched in SAR imaging geometry. The results are stacks of matched repeat pass images in PRI geometry and the corresponding geocoded products of ascending and descending swaths. Repeat pass images have the advantage that multitemporal classification can be done in SAR geometry with well known image statistics (section 8) and the classification result can be transformed to a map projection. Examples of the geocoded PRI SAR images from figures 5.2 and 5.3 are shown in figure 5.4 for ascending and descending passes. About 30% and 35 %, respectively, of the geocoded images are covered by layover.

5.2.3 Auxiliary products

For the interpretation and classification in SAR images additional information is necessary or at least useful. These auxiliary products are based on image simulation and require an accurate DEM for rugged terrain. The most important products are

- layover mask

Descending

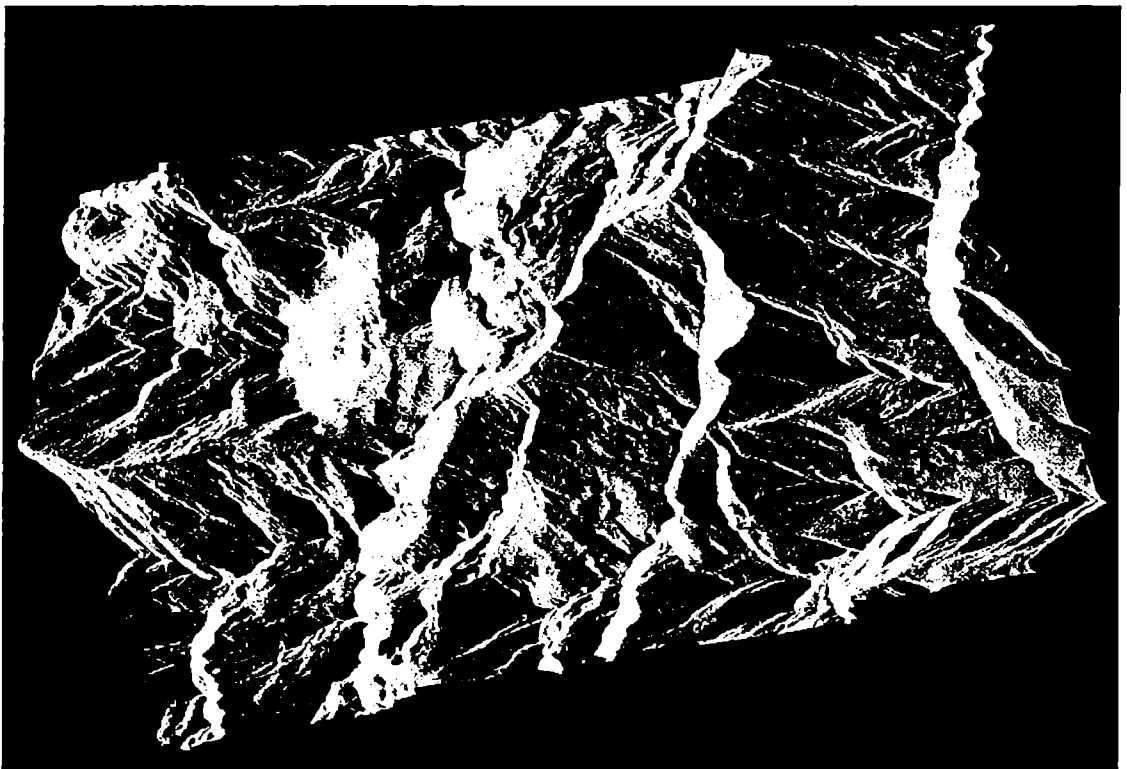
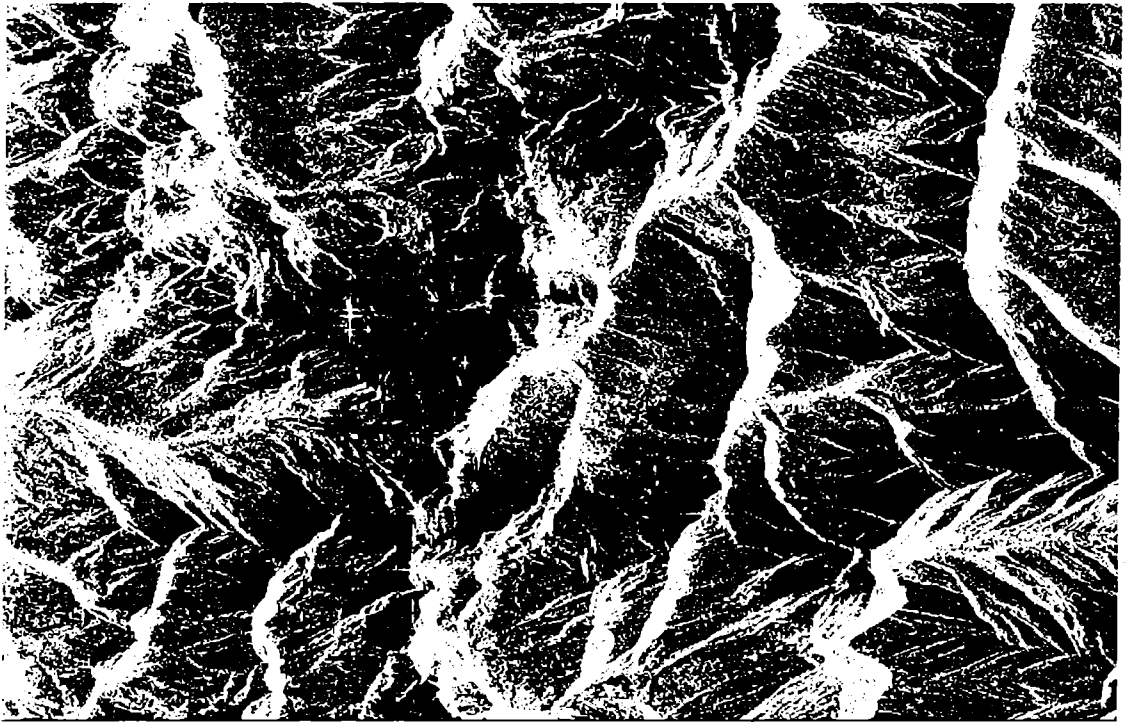
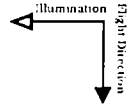


Figure 5.2: ERS-1 SAR PRI image of 6 July 92. (top) and simulated SAR image (bottom) of descending pass.

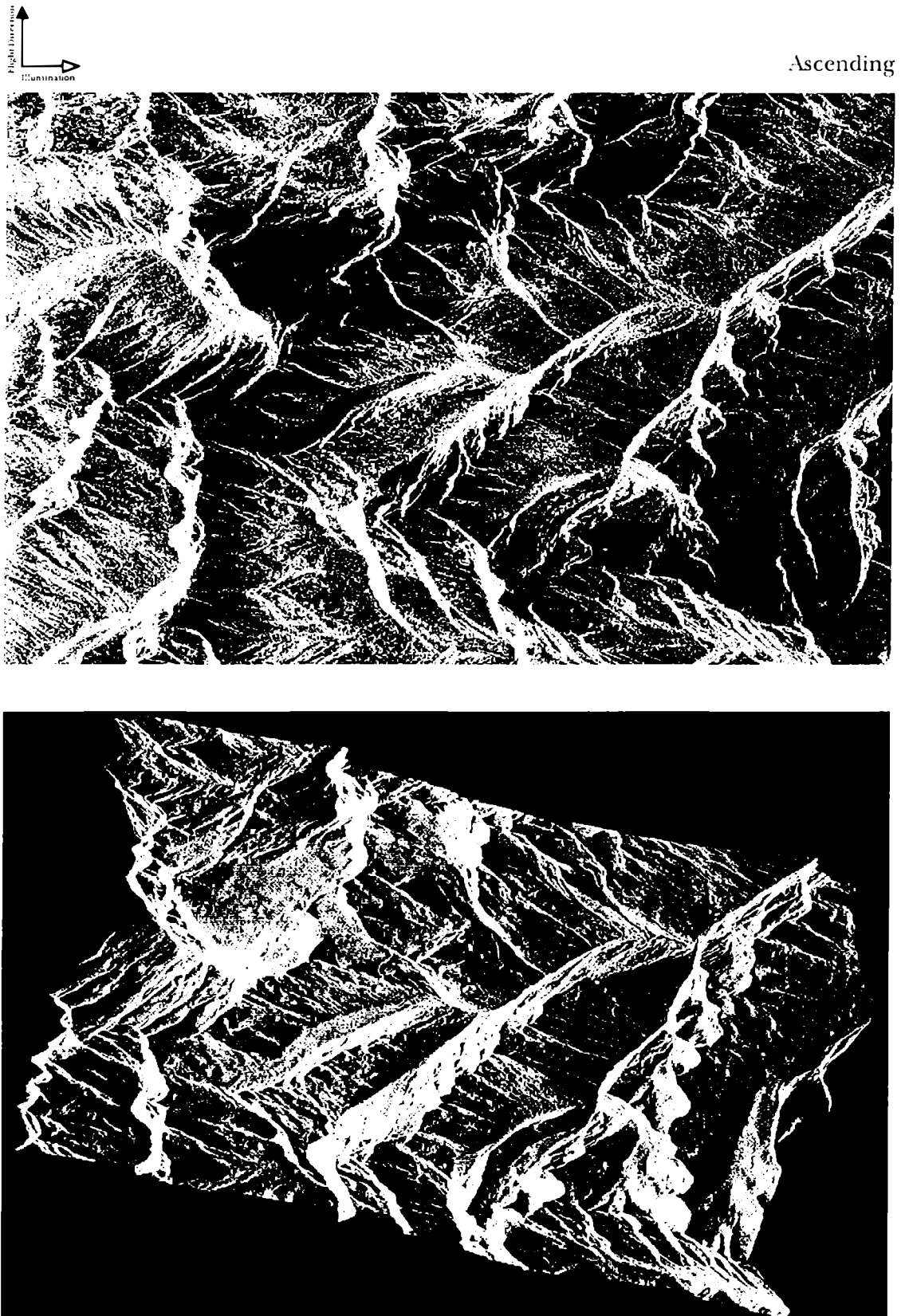


Figure 5.3: ERS-1 SAR PRI image of 6 July 92. (top) and simulated SAR image (bottom) of ascending pass.

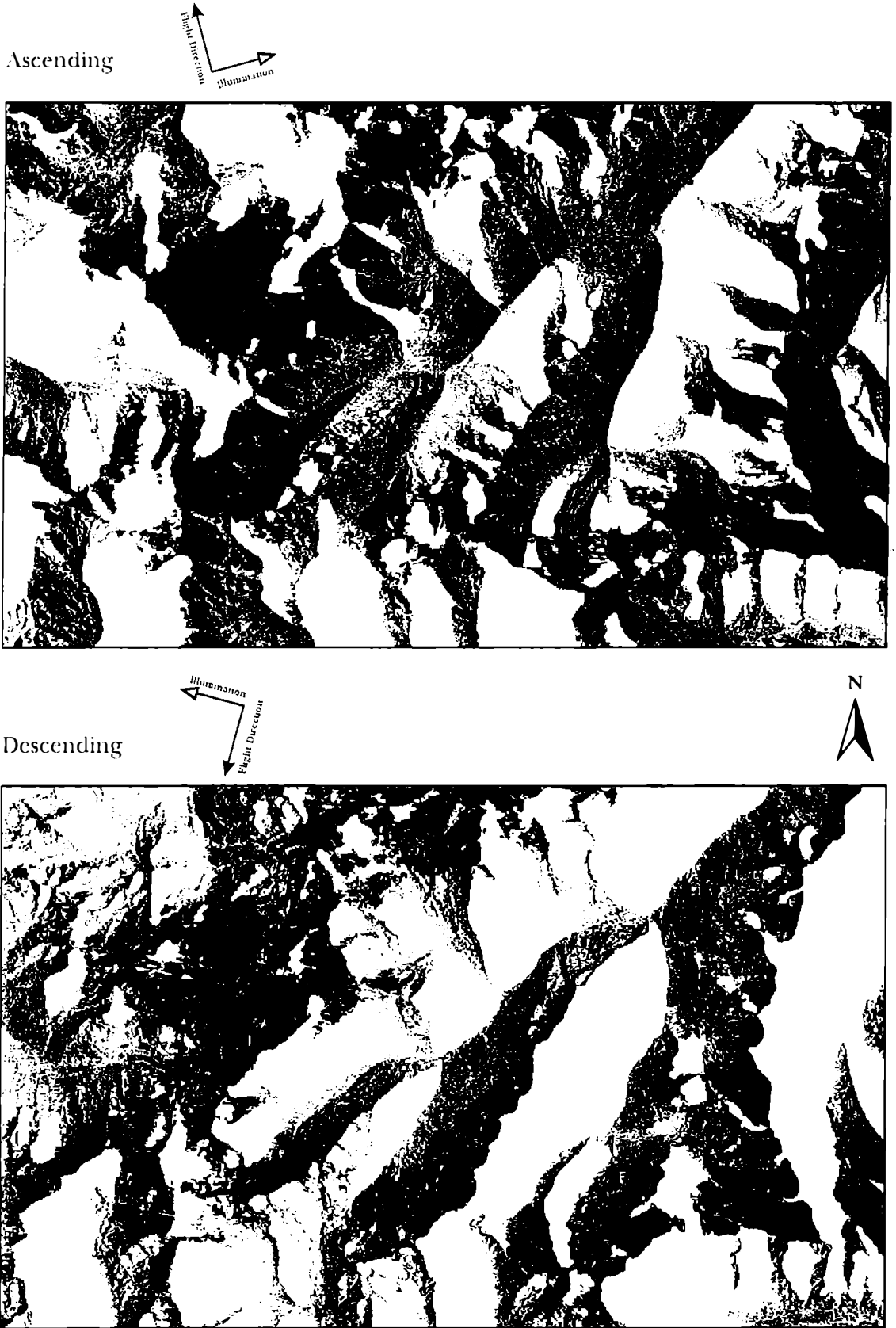


Figure 5.4: Geocoded images of the ascending (top) and descending (bottom) passes of ERS-1 on July 6, 1992. Based on the 25E x 25N UTM-28 DEM of Ötztal test site. Layover areas are shown in white.

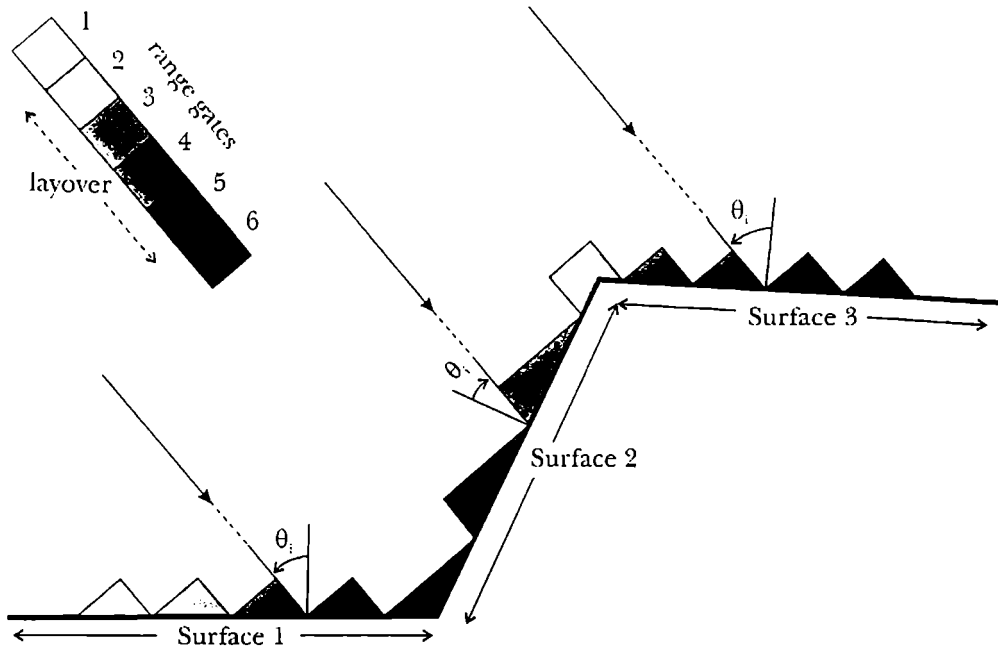


Figure 5.5: Example of imaging geometry resulting in layover. The regions on the surface contributing to each range gate are indicated by different shading (from [7]).

- shadow mask
- map of local incidence angle

All three products are in the same projection as the geocoded images and are secondary results of the geocoding procedure. The layover and shadow information represent binary masks. The local incidence angle of the radar beam for each pixel is quantized in 1° intervals and stored in 8 bits. These products are important for the classification procedures in chapter 10 and will be discussed in the following sections.

5.2.3.1 Layover mask

Layover areas occur when the distance r_s (figure 5.1) between the sensor and the target decreases with increasing horizontal distance between the subsatellite track and the target. Figure 5.5 sketches a situation leading to layover in the final SAR image. In general layover areas may be detected by monitoring the change of r_s in across track direction. Referring to figure 5.5 the total backscattered energy within the range gates 2 to 5 result from scattering from the slope causing the layover (surface 2) and from surfaces in front and above (surface 1 and 3). Therefore the spatial assignment of the reflected power is ambiguous, which does not allow the estimation of the backscattering coefficient in layover regions. So they can in general not be used for classification. The increase of the area from which the backscattered power of the pulse is integrated in one range gate and the low local incidence angles θ_i on surface 2 have the effect that layover regions appear bright. Figure 5.6 shows typical layover regions in the ground range PRI image geometry, the corresponding geocoded terrain corrected image with typical blurring in the geocoded layover zones, and the derived layover mask. In general the quality of the layover mask is dependent on the accuracy of the DEM and of the simulation of the imaging process.

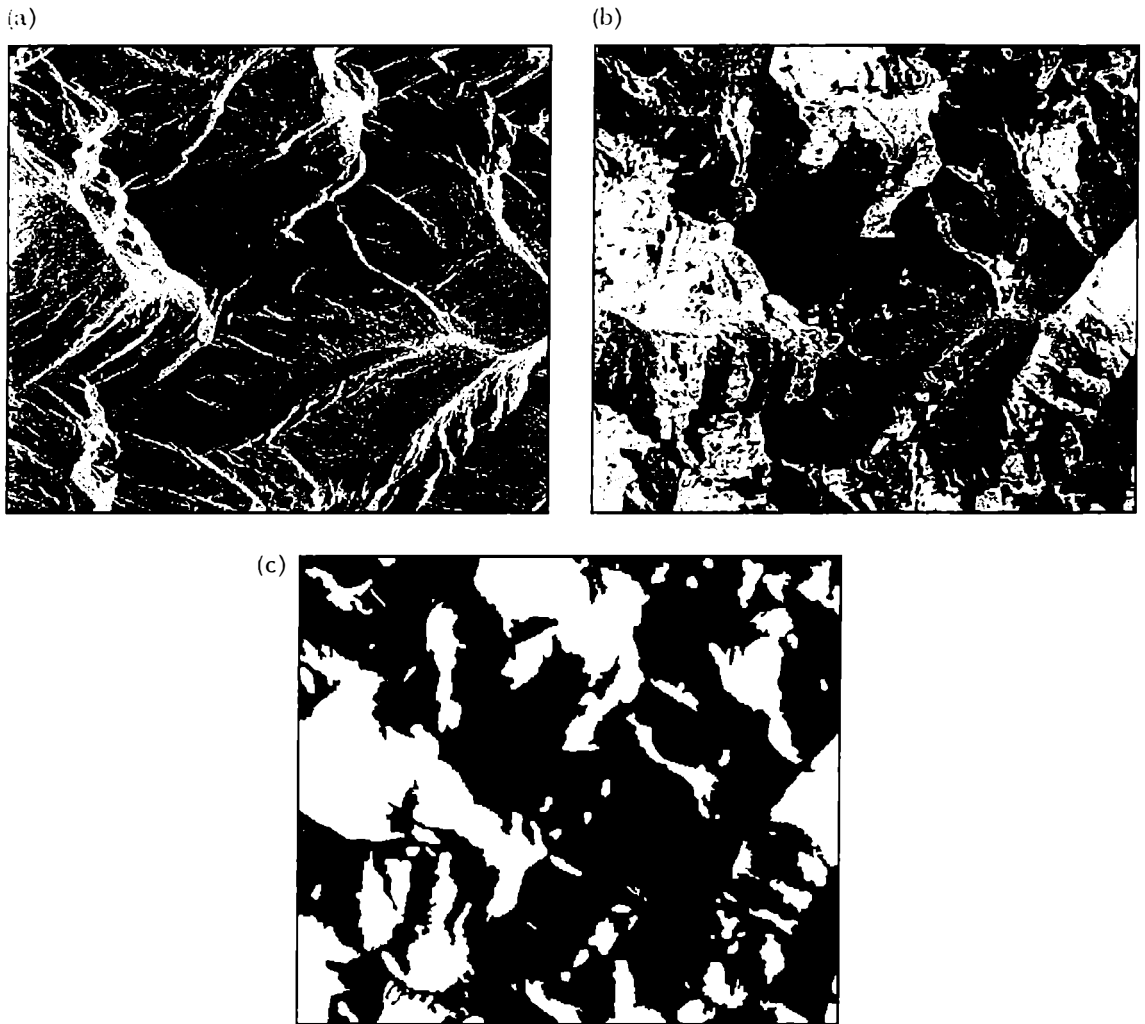


Figure 5.6: ERS-1 image of test site Ötztal, 1 June 1992, ascending pass: (a) original PRI image in ground range projection, (b) the corresponding geocoded terrain corrected image (layover zones are blurred bright regions), (c) mask of layover areas in white.

5.2.3.2 Radar shadow mask

Where the local incidence angle is greater than $\pi/2$ the radar beam does not intersect the earth surface [8]. If this extends over several range gates a region of radar shadow is observed where all the recorded power is due to system noise. The term *shadow* denotes that no energy is received from a target *due to masking of the beam* and not *due to very low backscattering*. Shadow enables a quick estimation of the system noise level, also specified as noise equivalent- σ^0 . Due to the steep look angle radar shadow is rarely observed in ERS-1 images, but it appears more often in SRL X-SAR images, with look angles up to 57° .

5.2.3.3 Local incidence angle map

The local incidence angle is important for deriving σ^0 . It is defined as the angle between the normal to the backscatter element and the incoming radar beam. The slope as well as the relative azimuth orientation of the backscatter element and the sensor position have to be taken into account. For a detailed discussion of the derivation of the local incidence

angle in mountainous terrain see e.g. [100]. The local incidence angle determines the ground scattering area per pixel. Large ground scattering areas are observed on slopes facing towards the SAR showing small local incidence angles, while backslopes with higher local incidence angles show smaller scattering areas per pixel.

5.3 Quality control of geocoded Ötztal ERS-1 PRI scenes

In this section the quality of the geocoded ERS-1 PRI images, based on the parameters for the simulation given in table 5.1 and using the 12.5 E x 12.5 N UTM-32 DEM of the test site Ötztal, is assessed. At the beginning the quality parameters are defined. Then the absolute and relative residuals of the geocoded PRI images are presented.

5.3.1 Definition of quality parameters

5.3.1.1 Actual residuals

After Raggam *et al.* [56] actual residual vectors represent the difference vectors between the location of the GCP in the geocoded SAR image and the location in the reference map. For the k^{th} GCP the residual vector \mathbf{r}_k is given by

$$\mathbf{r}_k = \mathbf{p}_{i,k} - \mathbf{p}_{r,k} \quad (5.4)$$

where p is the location vector with components East and North in the geocoded image (index i) and the reference map (index r).

A good estimation of the overall geometric accuracy in a geocoded image is possible by using statistical parameters such as the average and the root mean square (rms) of the residual vectors ($\mathbf{r}_{ave}, \mathbf{r}_{rms}$), the maximum and minimum residual vector ($\mathbf{r}_{max}, \mathbf{r}_{min}$), as well as the average, the root mean square and standard deviation of the magnitude of the residual vector ($r_{ave}, r_{rms}, r_{std}$). For n GCPs those parameters are defined by [56]

$$\mathbf{r}_{ave} = \frac{1}{n} \sum_{k=1}^n \mathbf{r}_k \quad (5.5)$$

$$\mathbf{r}_{rms} = \sqrt{\frac{1}{n} \sum_{k=1}^n (\mathbf{r}_k)^2} \quad (5.6)$$

$$\mathbf{r}_{max} = \begin{pmatrix} \max |E_k| \\ \max |N_k| \end{pmatrix} \quad (5.7)$$

$$\mathbf{r}_{min} = \begin{pmatrix} \min |E_k| \\ \min |N_k| \end{pmatrix} \quad (5.8)$$

$$r_{ave} = \frac{1}{n} \sum_{k=1}^n |\mathbf{r}_k| \quad (5.9)$$

$$r_{rms} = \sqrt{\frac{1}{n} \sum_{k=1}^n |\mathbf{r}_k|^2} \quad (5.10)$$

$$r_{std} = \sqrt{\frac{1}{n-1} \sum_{k=1}^n (|r_k| - r_{m,ave})^2} \quad (5.11)$$

For visualization of the geometric accuracy a residuals vector plot is produced where the location of the GCP in the reference map and the corresponding residual vector is displayed.

5.3.1.2 Artificial residuals

Artificial residuals result from the mislocation of control information in the geocoded image and in the reference map and from errors in the DEM. They are characterized by the factors f_i , f_m and f_{ed} . According to error propagation artificial residuals are defined by

$$r_{art} = \sqrt{f_i^2 + f_m^2 + f_{ed}^2} \quad (5.12)$$

where

$$f_i = \text{pixel_size} \times \text{identification_accuracy_image}$$

$$f_m = \text{map_scale} \times \text{identification_accuracy_map}$$

$$f_{ed} = \cot(\theta_i) \times \text{Height_error}$$

The parameter $\text{identification_accuracy_image}$ is assumed to be one pixel for manually identified GCPs [56]. The factor f_m describes the error for digitizing GCPs from a map, the parameter $\text{identification_accuracy_map}$ has to be expressed in units of meters. When the position of the GCP is known very accurately e.g. measured by geodetic surveys, $\text{identification_accuracy_map}$ is about 0 m and f_m can be neglected. The factor f_{ed} is the expected displacement caused by height errors in the DEM, where the parameter Height_error is the difference between the true (measured) height of the GCP and the height in the DEM at the corresponding location. For ERS-1 the incidence angle θ_i on a horizontal surface is between 19° and 26° (at mid swath 23°), resulting in $f_{ed} \approx 2.36 \times \text{Height_error}$. For estimations of the geocoding quality parameter \mathcal{Q} a characteristic artificial residual is used. It is determined by the root mean square of all available artificial residuals r_{art} derived from the GCPs in the image.

5.3.1.3 Quality parameter \mathcal{Q}

The quality parameter \mathcal{Q} is used to describe the geometric accuracy in one single number [56]. \mathcal{Q} can assume values between 0 (best quality) and 9 (worst quality) and is defined as

$$\mathcal{Q} = \text{NINT} \left[9 \left(1 - e^{-b \frac{r_{rms}}{r_{art}}} \right) \right] \quad (5.13)$$

A value of $b = \frac{1}{3}$ was empirically determined for ERS-1 data acquired during phase-C [56].

5.3.2 Absolute accuracy of geocoded ERS-1 PRI images of the test site Ötztal

The geometric accuracy has been determined for those geocoded SAR images, for which accurate GCPs are available. In this study only trihedral corner reflectors, which were deployed on the glaciers Hintereisferner and Kesselwandferner / Gepatschferner during

Asc. Pass	1-Jun-92	6-Jul-92	10-Aug-92	14-Sep-92
Nr of GCP	1	3	6	4
$r_{ave} [E, N]$	(26.15, 38.35)	(29.87, 20.49)	(22.28, 21.60)	(37.13, 22.72)
$r_{rms} [E, N]$	—	(34.83, 22.08)	(30.05, 24.42)	(41.69, 24.25)
$r_{std} [E, N]$	—	(21.94, 10.09)	(22.09, 12.46)	(21.89, 9.80)
$r_{max} [E, N]$	—	(43.67, 26.94)	(48.71, 39.11)	(67.64, 29.86)
$r_{min} [E, N]$	—	(4.56, 8.86)	(8.19, 9.08)	(20.62, 8.95)
r_{ave}	46.41 m	39.90 m	34.09 m	22.74 m
r_{rms}	—	12.76 m	20.12 m	22.62 m
r_{art}	—	19.18 m	19.88 m	24.40 m
Q	—	5	5	6

Table 5.2: Residual analysis of geocoded ERS-1 SAR images of ascending swath.(E and N are the Easting and Northing in meters of the residual vector, Q is the overall quality parameter.

Desc. Pass	6 Jul 92	14 Sep 92
No. of CR	3	4
$r_{ave} [E, N]$	(8.67, 0.01)	(6.16, -0.39)
$r_{rms} [E, N]$	(22.87, 12.17)	(15.67, 4.79)
$r_{std} [E, N]$	(25.91, 14.90)	(16.64, 5.51)
$r_{max} [E, N]$	(28.45, 15.92)	(23.26, 7.21)
$r_{min} [E, N]$	(18.24, 2.37)	(4.71, 1.93)
r_{ave}	25.24 m	15.37 m
r_{rms}	25.90 m	16.39 m
r_{std}	7.11 m	6.54 m
r_{art}	20.53 m	24.40 m
Q	3	2

Table 5.3: Residual analysis of geocoded ERS-1 images of descending swath (E and N are the Easting and Northing in meters, Q is the overall quality parameter.

the overflights of ERS-1 in 1992. are used as GCPs. Most of the corner reflectors were geodetically surveyed within several centimeters accuracy.

During the overflights on 27 April 1992, 28 December 1992 and 8 March 1993 no corner reflectors were deployed. In the day image of the overflight on 1 June 1992 the corner reflector is not visible in the SAR image due to layover. During the field campaign of 19 October 1992, two corner reflectors were deployed on the Hintereisferner, but their geodetic positions could not be determined accurately due to bad visibility. Accurate positions of corner reflectors are available for the SAR images acquired on 6 July and 14 September ascending and descending pass, and on 1 June and 10 August ascending pass only. For each corner reflector the actual residual vector was derived. The results of the residual analysis and the overall quality of the geocoded images are given in table 5.2 and 5.3.

The images of the ascending passes ($Q = 5$ and $Q = 6$) are geometrically less accurate than the images of the descending orbit ($Q = 2$ and $Q = 3$). The residual vectors for the images are plotted in figure 5.7. In the descending images the mean length of the residual vector is between 15.4 and 25.2 m. which corresponds to two pixels in the DEM with 12.5 m grid spacing. The maximum error in the East and North direction is 28.5 m, 13.6 m and 23.3 m. 7.21 m respectively. In the ascending images an average magnitude of the residual vectors between 22.7m to 39.9 m (3.1 pixel) is observed. The maximum residual

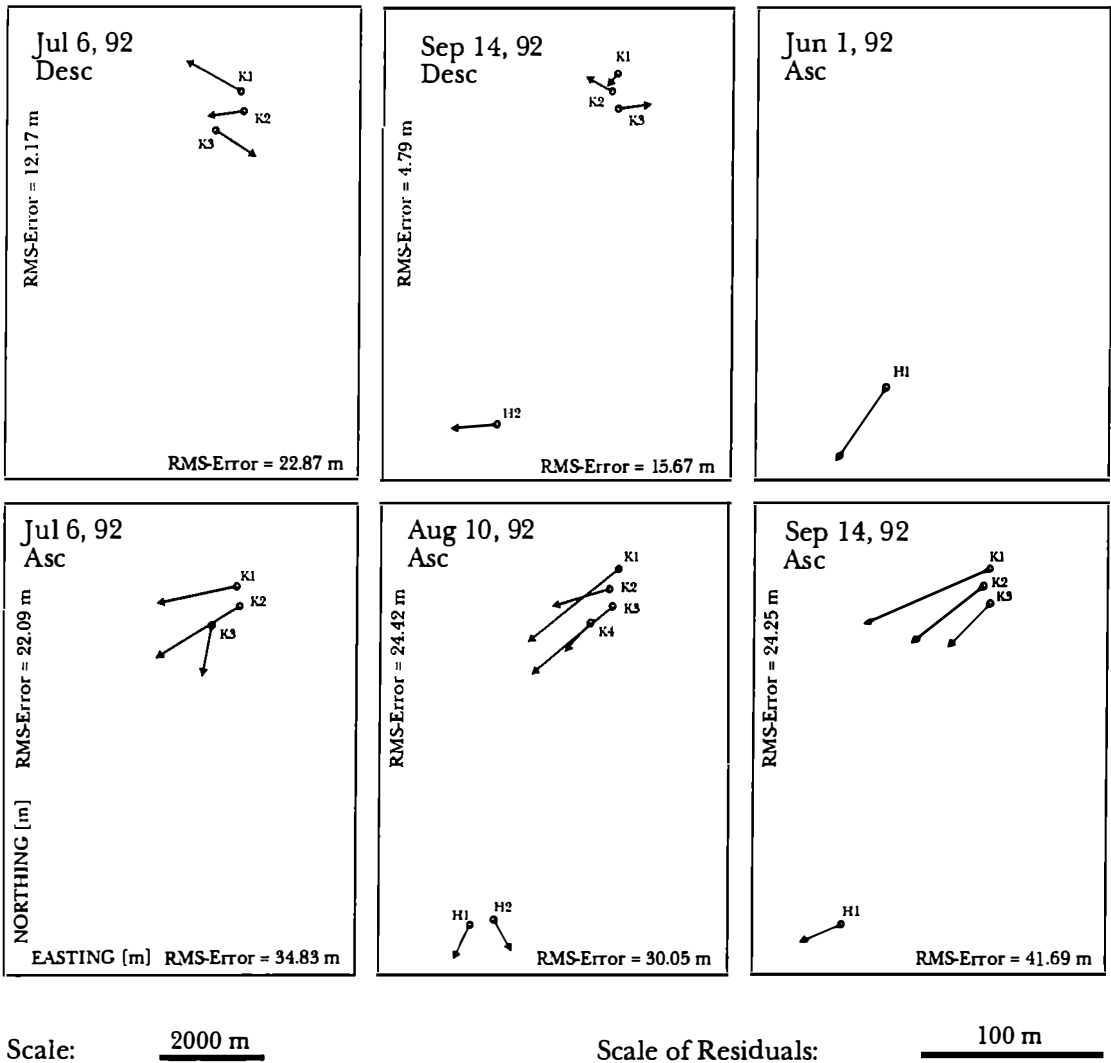


Figure 5.7: Absolute residual vectors of corner reflectors for ascending and descending passes of different cycles of ERS-1.

length is 67.6 m in the East direction observed at the corner reflector K1 in the image acquired on September 14, 1992. The residual vector plots in figure 5.7 show that the GCPs at Kesselwandferner (denoted by K1, K2, K3, K4) tend to be mapped too far in the south-west direction in the geocoded image. The GCPs at Hintereisferner show smaller residuals than at Kesselwandferner.

5.3.3 Relative accuracy of geocoded ascending and descending images of the test site Ötztal

The relative geometric accuracy is important for combining images of ascending and descending swaths. During Phase-C of ERS-1 the Ötztal test site was imaged by crossing repeat orbits, whereas the images of the ascending and descending swaths of the same cycle were acquired only 12 h apart. When combining geocoded images of crossing passes of the same cycle the corner reflectors should appear at the same location. Only the images acquired on July 6, 1992 and September 14, 1992 show corner reflectors in ascending and descending passes to analyze the relative accuracy of the geocoded images of crossing

Descending Swath	6-Jul-92	14-Sep-92
Nr of GCP	5	4
r_{ave} (E,N)	(7.7, 12.3)	(38.0, 30.6)
r_{rms} (E,N)	(18.8, 16.5)	(39.0, 31.3)
r_{std} (E,N)	(19.1, 12.2)	(17.5, 7.5)
r_{max} (E,N)	(25.4, 24.8)	(62.9, 37.1)
r_{min} (E,N)	(12.5,0)	(25.6, 24.37)
r_{ave}	23.26 m	50.6 m
r_{rms}	25.00 m	51.5 m
r_{std}	10.2 m	11.13 m

Table 5.4: Relative residual analysis of geocoded ERS-1 images of ascending and descending swath (E and N are the Easting and Northing in meters)

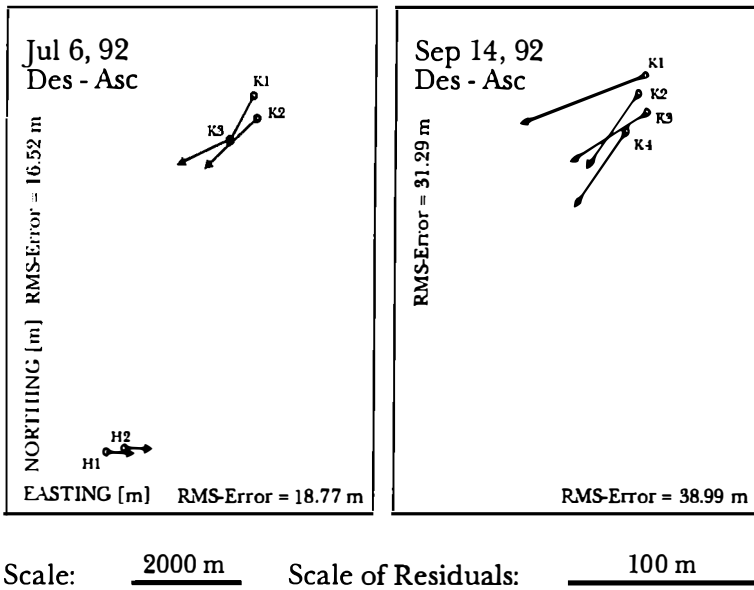


Figure 5.8: Relative residuals between ascending and descending passes of the same cycle.

orbits. To determine the relative location error the residual vectors of the corner reflectors in the ascending and descending geocoded image is calculated by

$$r_{da} = p_{des} - p_{asc} \quad (5.14)$$

where r_{da} is the relative residual vector with coordinates East and North in meters. p is the reflector position in the image of the descending (index des) and ascending (index asc) swath. In table 5.4 the statistical analysis of the residuals is presented.

The geocoded images on July 6, 1992 show a rms -difference of 25 m, which corresponds to 2 pixels in the DEM with 12.5 m \times 12.5 m spacing. In the images of September 14, 1992 the rms -error is 51.5 m corresponding to 4 pixels. This value is strongly influenced by the corner reflector K1, which shows the maximum difference of 62.9 m east and 23.9 m north. Without K1 the mean difference is 2.3 pixels in east and 2.7 pixels in north direction. In figure 5.8 the residuals of the single GCPs are plotted. Circles denote the true location of the GCPs in the geocoded descending image, and the arrow points to the position in the geocoded ascending image. The length corresponds to the magnitude of the residual vector.

Chapter 6

Microwave interaction with snow

The purpose of this chapter is to demonstrate the influence of the snow cover on the backscattering as the basis for the interpretation of backscattering signatures. In section 6.1 the bulk dielectric properties of dry and wet snow are discussed. The main scattering processes are explained and simple backscattering models are presented in section 6.2. In the last section a one layer model is used to demonstrate the backscattering effect of snow and ground properties. The major backscattering contributions for dry and wet snow conditions are compared.

6.1 Dielectric properties of snow

As long as snow is dry it is an inhomogeneous medium consisting of ice particles and air. When the snow becomes wet liquid water is present as a third component. The strong interaction of microwaves with liquid water drastically changes the dielectric properties of the snow pack. In the last years several empirical formulas have been derived to describe the permittivity (*dielectric constant*) $\varepsilon = \varepsilon' - i\varepsilon''$ of dry and wet snow.

6.1.1 Dry snow

As ε'_{ice} of fresh water ice, the real part of the permittivity of dry snow ε'_{ds} is independent of frequency and temperature in the microwave region. It only depends on the volume fraction of ice particles. Different relations between the snow density and the real part of the permittivity have been determined [37], [85]. Two widely applied relations are

$$\begin{aligned}\varepsilon'_{ds} &= 1 + 1.7\rho_s + 0.7\rho_s^2 && \text{Tiuri } et \text{ al. [87]} \\ \varepsilon'_{ds} &= 1 + 1.5995\rho_s + 1.861\rho_s^3 \quad \text{for } \rho_s < 0.45 \text{ gcm}^{-3} && \text{Mätzler [47]}\end{aligned}\tag{6.1}$$

where ρ_s is given in gcm^{-3} . Tiuri *et al.* [87] found the same dependence of ε'_{ds} on the density for snow at different metamorphic stages (old coarse snow, aged snow and new snow). On the other hand the imaginary part ε''_{ds} varies significantly in the microwave region and depends on the frequency, temperature, density and impurity of the snow pack. The imaginary part of the permittivity of dry snow can be estimated by [87]

$$\varepsilon''_{ds} = \varepsilon''_{ice} (0.52\rho_s + 0.62\rho_s^2)\tag{6.2}$$

where ε''_{ice} represents the dielectric loss of ice. With a value of $\varepsilon''_{ice} = 8 \times 10^{-4}$ (slightly impure ice at -20°C , at 2GHz) eq. 6.2 gives reasonable values for ε''_{ds} , which fit well to measurements of ε''_{ds} . Based on many measurements in the range of -70°C to 0°C the

temperature and frequency dependence of the dielectric loss of pure ice can be described by the empirical relation [46]

$$\varepsilon''_{ice} = \frac{\alpha}{f} + \beta f$$

$$\alpha[\text{GHz}] = (0.00504 + 0.0062T) \exp(-22.1T) \quad (6.3)$$

$$\beta[\text{GHz}^{-1}] = \frac{0.502 - 0.131T}{1 + T} 10^{-4} + 0.542 \times 10^{-6} \left(\frac{1 + T}{T + 0.0073} \right)$$

where the frequency f is given in GHz, and $T = 300K/(T - 1)$ with temperature T in Kelvin. In the range from 1 GHz to 10 GHz ε''_{ice} increases slowly with temperature; the increase is more pronounced at lower frequencies.

6.1.2 Wet snow

The real and imaginary part of the permittivity of wet snow, ε'_{ws} and ε''_{ws} , are frequency dependent and increase significantly with the liquid water content. The increase is less pronounced with the snow density. Two regimes of liquid water distribution are discriminated. In the pendular regime the air is continuous throughout the pore space and the liquid water exists as small inclusions: this regime is observed at low liquid water content. Above a saturation of liquid water (defined as the volumetric liquid content relative to the pore space between the grains) of 11% to 15%, the water is continuously distributed and the air occupies single bubbles: this is called the funicular regime. Between 10 MHz and ~ 1 GHz ε'_{ws} is nearly independent of the frequency. Between 50 MHz and 500 MHz ε''_{ws} passes a minimum and increases to a maximum in the X-band. By measuring the snow density and ε'_{ws} at frequencies between 15 MHz and 500 MHz the free liquid water content V_w in %^{vol} can be derived [9]. In the frequency range $1 \text{ GHz} < f < 30 \text{ GHz}$ ε_{ws} can be estimated as a first approximation by the relation [45]

$$\varepsilon'_{ws} = \varepsilon'_{ds} + \frac{23V_w f_o^2}{f_o^2 + f^2} \quad (6.4)$$

$$\varepsilon''_{ws} = \varepsilon''_{ds} + \frac{23V_w f_o}{f_o^2 + f^2} f$$

where $f_o = 10 \text{ GHz}$. Typical values for ε'_{ws} and ε''_{ws} are shown in figure 6.1 for C-band and X-band.

6.1.2.1 Penetration depth and attenuation

The penetration depth d_p for a uniform dielectric medium is the depth where the power of the incident wave is clamped to $1/e$ of its initial value. It is related to the volume extinction coefficient κ_e by

$$d_p[m] = \kappa_e^{-1} \quad (6.5)$$

where κ_e is the sum of the volume absorption and volume scattering coefficient κ_a and κ_s . The volume absorption coefficient for homogeneous snow can be estimated by [85]

$$\kappa_a[m^{-1}] = \frac{4\pi}{\lambda_o} \left[\frac{\varepsilon'_s}{2} \left\{ \left[1 + \left(\frac{\varepsilon''_s}{\varepsilon'_s} \right)^2 \right]^{\frac{1}{2}} - 1 \right\} \right]^{1/2} \quad (6.6)$$

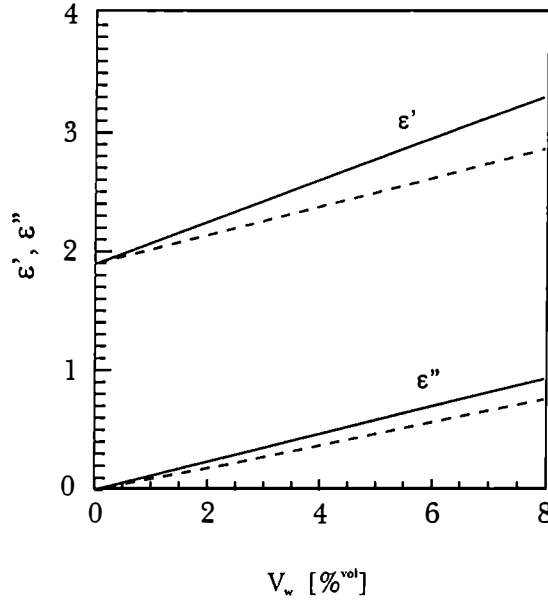


Figure 6.1: Dielectric constant of wet snow with varying liquid water content V_w , for snow density of 0.45 gcm^3 and temperature of 0°C for 5.3 GHz (C-band, solid line) and 9.6 GHz (X-band, dashed line).

where λ_o is the wavelength in vacuum, and ϵ'_s and ϵ''_s are the bulk dielectric constant of the dry or wet snow. Neglecting the influence of scattering ($\kappa_s \ll \kappa_a$) the penetration depth can be estimated for media with $\epsilon' \gg \epsilon''$ by

$$d_p \cong \frac{\lambda_o \sqrt{\epsilon'}}{2\pi\epsilon''} \quad (6.7)$$

The approximation $\kappa_s \ll \kappa_a$ is valid for wet snow in the GHz region. Taking into account only scattering processes at snow grains eq. 6.7 would also be valid for dry snow at frequencies below 10 GHz, where particles are significantly smaller than the wavelength. However, due to reflections at internal density boundaries, grain-cluster and ice lenses, which are usually present in natural snow packs, the scattering loss in dry snow may become significant also at low frequencies. In this case eq. 6.7 can be interpreted as the upper limit of the penetration depth. Measurements of κ_e in layered polar firn resulted in a penetration depth of 21.7 m at 5.2 GHz and 8 m at 10.3 GHz [75]. These values are close to d_p measured in dry alpine snow presented in figure 6.2 b.

6.2 Snow as a scattering medium

Any deviation of a dielectric medium from homogeneity gives rise to scattering. The scattering properties depend on the geometry and the magnitude of the inhomogeneities relative to the wavelength of the incident wave. In the case of snow covered terrain different processes contribute to the total backscattered power (figure 6.3):

- scattering at the air-snow interface
- scattering by ice particles and at density boundaries in the snow pack
- scattering at the snow-ground interface

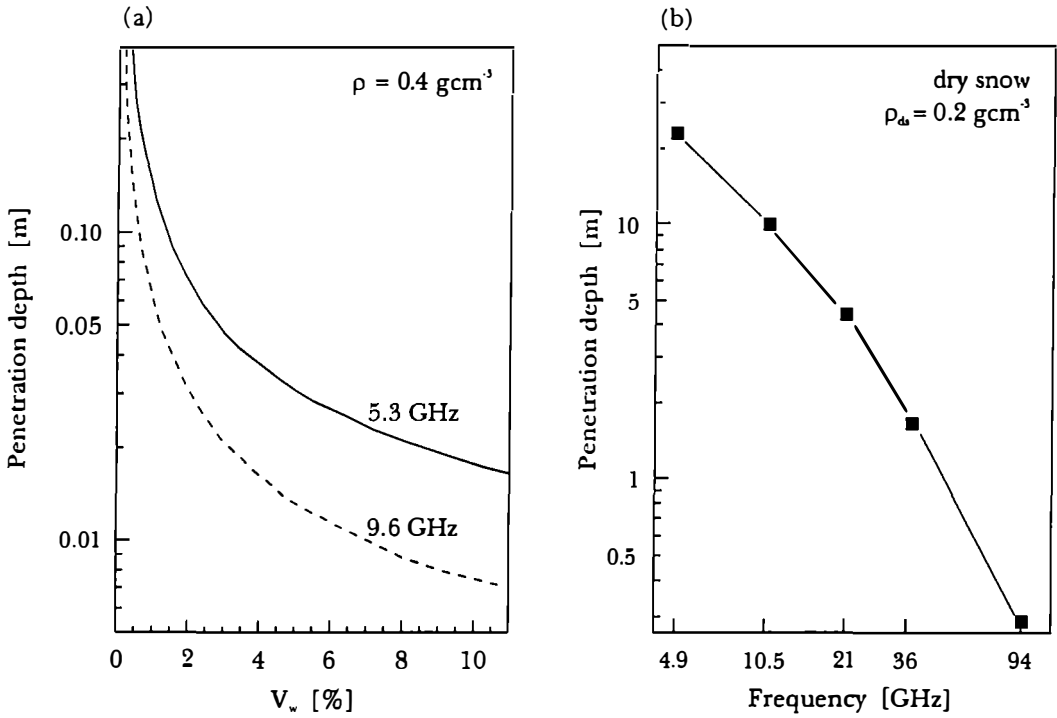


Figure 6.2: Penetration depth (a) in wet snow in dependence of liquid water content (V_w) and (b) in dry snow in dependence of frequency (from Hofer and Mätzler [31]).

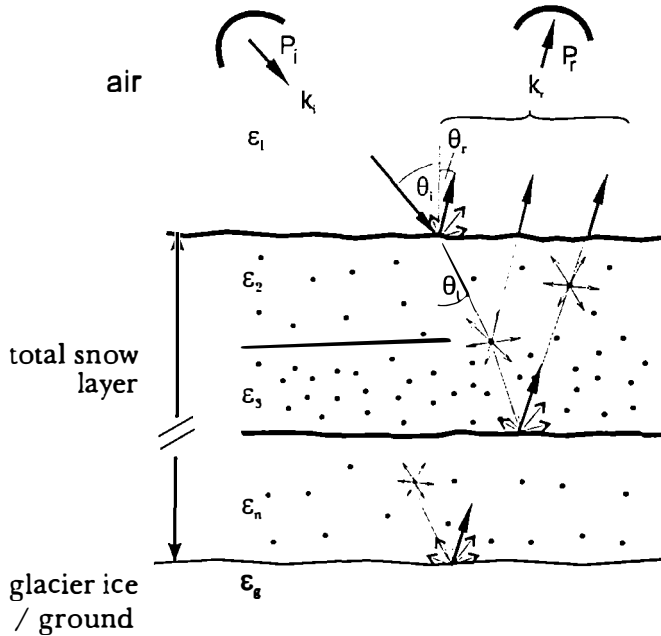


Figure 6.3: Backscattering processes of snow covered terrain.

The incident electromagnetic wave \mathbf{k}_i with power P_i hits the air-snow boundary at an angle θ_i . The incident wave is partly reflected and partly transmitted into the snow layer, each part consisting of a coherent and incoherent component. The coherent component is reflected and transmitted under the angles θ_r and θ_t , according to the law of Snellius [6]. In the snow pack the transmitted wave is attenuated by scattering and by absorption at individual grains, by scattering at boundaries of different layers and at crusts. Furthermore scattering at the rough boundary between the snow layer and the ground may contribute to the total backscattered power. Theoretical models cannot account for the full complexity of natural snow packs, which show a large variety of grain sizes, grain shapes and layered stratigraphy and sometimes also ice inclusions. But simple models can also be treated as a tool to understand the observed backscattering signatures.

6.2.1 Surface scattering

Surface scattering depends on the dielectric properties of the adjacent media, the roughness of the boundary and on the incidence angle. In this section the parameters for describing the surface roughness are defined, which are determined for real surface profiles of snow and ice in section 7.1.1.2. Then a model for backscattering from a rough surface and its sensitivity for varying surface roughness are discussed.

6.2.1.1 Definition of surface parameters

To characterize the surface roughness several parameters were defined, which describe different statistical components of the surface height:

- the standard deviation of the surface height variation
- the surface correlation length
- the shape of the correlation function

In general a two dimensional surface is specified by a value of the height z above a reference surface for every point (x, y) [92]. For random variations of z the reference surface may be a plane at the mean height of z .

If $z(x, y)$ is statistically independent of the azimuth angle in the x - y plane, the problem can be reduced to one dimension. For a discrete one-dimensional profile with \mathcal{N} samples of height z and spacing Δx its standard deviation σ_h is calculated by [92]

$$\sigma_h = \sqrt{\frac{1}{\mathcal{N} - 1} \sum_{i=1}^{\mathcal{N}} (z_i^2 - \mathcal{N}\bar{z}^2)} \quad (6.8)$$

where \bar{z} represents the average height of \mathcal{N} samples. For a discrete one-dimensional surface profile the normalized autocorrelation with spatial lags $x'(j) = (j - 1)\Delta x$, for $j \geq 1$, is given by [92]

$$\rho(x') = \frac{\sum_{i=1}^{\mathcal{N}-(j-1)} z_i z_{i+j-1}}{\sum_{i=1}^{\mathcal{N}-(j-1)} z_i^2} \quad (6.9)$$

The surface correlation length l is usually defined as the distance x' for which $\rho(x')$ is equal to $1/e$ [92]:

$$\rho(l) = \frac{1}{e} \simeq 0.368 \quad (6.10)$$

If two points are separated by a distance greater than l , they can be considered approximately statistically independent of each other. The variance of the surface slope is defined as [20]

$$m^2 = \sigma_h^2 \frac{d^2}{dx^2} \rho(x) \Big|_{x=0} \quad (6.11)$$

Figures 7.7 and 7.23 show examples for surface profiles and corresponding parameters derived by eq. 6.8, 6.9, 6.10 for different targets.

To estimate whether a surface is smooth or rough in respect to the wavelength, the Fraunhofer criterion may be used. For a smooth surface the condition [92]

$$\sigma_h < \frac{\lambda}{32 \cos \theta_i} \quad (6.12)$$

is valid, where λ is the wavelength and θ_i is the incidence angle.

6.2.1.2 Single scattering model for surfaces

Several models, which are valid for different ranges of roughness, have been developed to predict backscattering from rough surfaces. The Integral Equation Model (IEM) [20] is valid for a wider range of surface roughness than the standard surface models based on the Kirchhoff approximation (geometric optics model GM, physical optics model PM) and the small perturbation model (SPM). The IEM theory [23] explains the total backscattering coefficient as the sum of the single and multiple scattering terms. For surfaces of small to moderate roughness, $k\sigma_h < 3$ single scattering is dominant, where k represents the wavenumber. For $k\sigma_h > 3$, the multiple scattering term has to be taken into account unless the surface slope is small. In comparison with standard models, the single scattering term of IEM reduces to the SPM for slightly rough surfaces ($k\sigma_h \ll 1$), while it approaches the Kirchhoff GM for large values of the roughness parameters $k\sigma_h$ and kl . The single scattering term of the IEM model is given by [20]

$$\sigma_{pq,S}^o = \frac{k^2}{2} e^{-2\sigma_h^2 k^2 \cos^2 \theta_i} \sum_{n=1}^{\infty} \sigma_h^{2n} |I_{pq}^n|^2 \frac{W^{(n)}(-2k \sin \theta_i, 0)}{n!} \quad (6.13)$$

where

$$I_{pq}^n = (2k \cos \theta_i)^n f_{pq} e^{-\sigma_h^2 k^2 \cos^2 \theta_i} + \frac{(k \cos \theta_i)^n [F_{pq}(-k_s, 0) + F_{pq}(k_s, 0)]}{2} \quad (6.14)$$

with $k_s = k \sin \theta_i$. For VV-polarization (ERS-1, X-SAR) the parameters f_{pq} and $F_{pq}(-k_s, 0) + F_{pq}(k_s, 0)$ are given by [20]

$$f_{vv} = \frac{2R_{vv}}{\cos \theta_i} \quad (6.15)$$

$$F_{vv}(-k_s, 0) + F_{vv}(k_s, 0) = \frac{2 \sin^2 \theta_i (1 + R_{vv})^2}{\cos \theta_i} \times \left[\left(1 - \frac{1}{\varepsilon}\right) + \frac{\varepsilon - \sin^2 \theta_i - \varepsilon \cos^2 \theta_i}{\varepsilon^2 \cos^2 \theta_i} \right] \quad (6.16)$$

$W^{(n)}(\cdot)$ is the roughness spectrum related to the n^{th} -power of the correlation function. R_{vv} is the Fresnel power reflection coefficient for VV-polarization. As shown by [20] the

backscattering coefficient given by eq. 6.13 depends strongly on the assumed model of the surface correlation function. Standard models of the autocorrelation function are the exponential function, the Gaussian function and the modified exponential function [20]. But none of these functions approximates sufficiently the autocorrelation function derived from measured roughness profiles (figure 7.7, figure 7.23), because they do not match well the statistics of natural snow surfaces. It was found empirically for wet snow that the exponential function shows better agreement between calculated σ° -values and the ERS-1 based σ° values than the Gaussian and the modified exponential function. For the exponential correlation function $\rho(x)$ the variance of the slope m^2 and $W^{(n)}$ are given by

$$\rho(x) = e^{-\frac{|x|}{l}} \quad (6.17)$$

$$m^2 = \frac{\sigma_h^2}{l^2} \quad (6.18)$$

$$W^{(n)}(-2k \sin \theta_i, 0) = \left(\frac{l}{n}\right)^2 \left[1 + \left(\frac{-2kl \sin \theta_i}{n}\right)^2\right]^{-1.5} \quad (6.19)$$

The sensitivity of σ° to changes of the surface roughness parameters l and σ_h is shown in figure 6.4 and can be summarized as:

- for $kl = \text{constant}$ (figure 6.4 a): at small values of $k\sigma_h$, σ° increases with increasing roughness, while the shape of the angular dependence shows only a small change. When $k\sigma_h$ reaches a certain value (which depends on kl) σ° is almost constant at low θ_i values and the angular dependence of σ° is small. This effect is more pronounced when kl is small.
- for $k\sigma_h = \text{constant}$ (figure 6.4 b): increasing kl causes an increase of the θ_i -dependence of σ° . The dependence on kl is generally more pronounced when $k\sigma_h$ is large.

In spring and early summer the single scattering condition ($k\sigma_h < 3$) is in general valid for snow surfaces, as observed on the glacier areas of test site Ötztal during ERS-1 and SRL SIR-C/X-SAR passes in 1992 and 1994. During the main melt period the roughness of the snow and ice surfaces, especially on the glaciers (see section 7.1.1.2) increases strongly so that multiple scattering and shadowing should be included. For surfaces with large scale roughness the more simple GM Kirchhoff model can be used [20] [90].

6.2.2 Volume scattering

In the snow pack scattering and absorption processes determine the attenuation. The bulk volume absorption is discussed in section 6.1, while this section focuses on the scattering properties. The volume scattering coefficient κ_s , the total scattering cross-section per unit volume, is related to the particle size, the wavelength, the volume fraction and the dielectric properties of the scatterers [20], [34], [90].

Based on the radiative transfer theory and taking only the coherent transmission across the air to snow boundary into account, the volume scattering of a snow layer (with low permittivity) can be estimated by [20]

$$\sigma_{vol}^\circ = \frac{1}{2} \tilde{\omega} T_{as} T_{sa} \cos \theta_i \left[1 - e^{-2\kappa_e d / \cos \theta_t}\right] P_{pp}(\cos \theta_t, -\cos \theta_t, \pi) \quad (6.20)$$

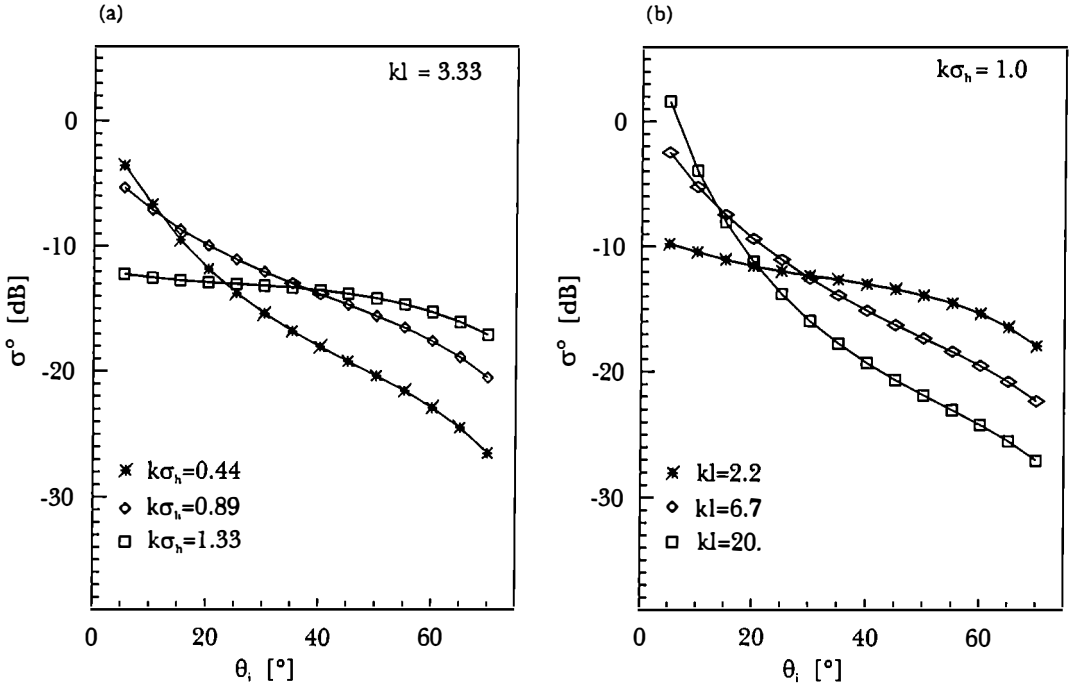


Figure 6.4: Backscattering coefficient for different values of $k\sigma_h$ and kl .

where T_{ij} is the Fresnel power transmission coefficient for the interface between medium i and medium j [6] and index a and s represent air and snow, respectively. $P_{pp}(\cdot)$ is the pp -element (p stands for polarization V or H) of the scattering phase function. The single scattering albedo $\tilde{\omega}$ represents the scattering properties of a snow volume and is given by

$$\tilde{\omega} = \frac{\kappa_s}{\kappa_e} \quad (6.21)$$

As long as the snow is dry the ice particles act as scatterers in a background medium which is air with $\varepsilon_b = 1$. In this case κ_a is determined by the absorption of the ice particles, which is very small. As long as the ice particles are small compared with the wavelength, the Rayleigh approximation for $P_{pp}(\cdot)$ may be used, which is defined e.g. in [20]. For independent spherical Rayleigh scatterers with ε_s , the volume scattering coefficient is given by

$$\kappa_s = \frac{3\pi}{3} N (k'_b)^4 a^6 \left| \frac{\varepsilon_s - \varepsilon_b}{\varepsilon_s + 2\varepsilon_b} \right|^2 \quad (6.22)$$

where $N = \frac{F}{4a^3\pi/3}$ is the number of scatterers with radius a per unit volume with fraction of scatterers F . When snow becomes wet the scattering ice particles reside in an effective background medium, which is a mixture of air and water. In this case absorption is effective in the background medium and in the ice particles and κ_a may be approximated by the bulk absorption of the snow medium given in eq. 6.6. Also when the Rayleigh conditions are not exactly valid, this model can still be used to estimate the magnitude of volume scattering. But this requires the assumption of values for the input parameters (grain radius, volume fraction), which do not correspond to the observed parameters.

Based on eq. 6.22, κ_s increases monotonically with increasing volume fraction of scatterers. But measurements show that after reaching a maximum, κ_s decreases at higher volume fractions of scatterers [20]. This is due to coherence (near field effects) between

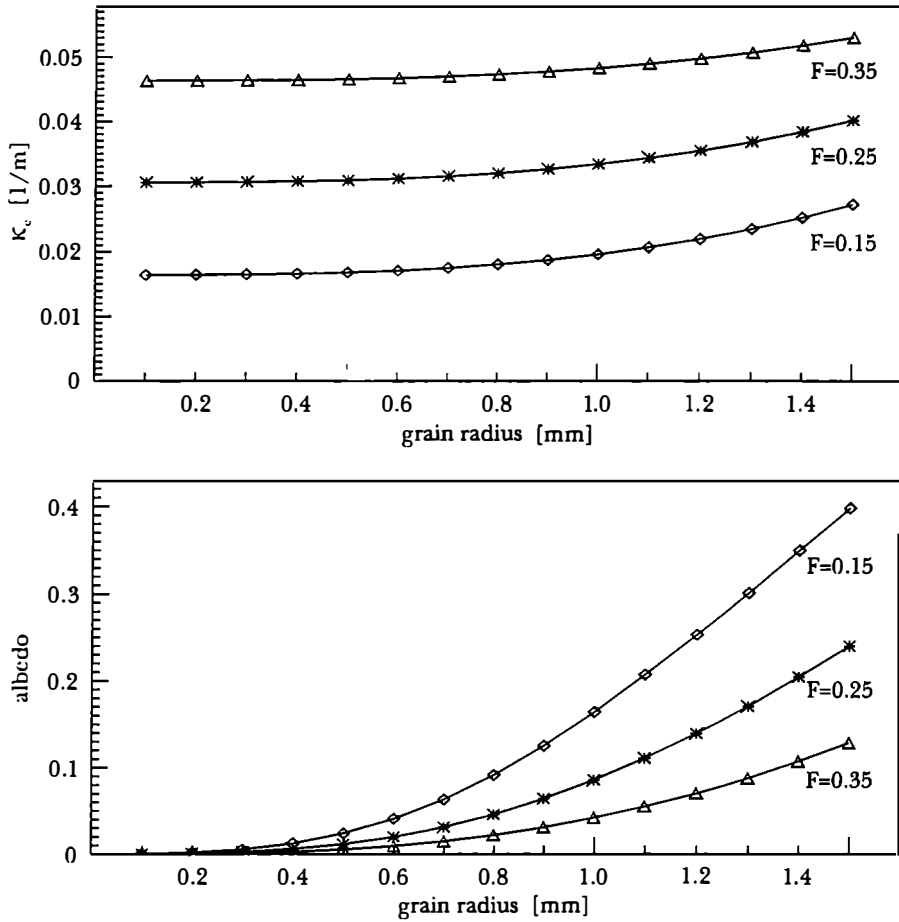


Figure 6.5: Extinction coefficient κ_e and albedo at 5.3 GHz of dry snow consisting of single sized spherical ice particles ($\epsilon_s = 3.13 - i0.023$, Percus-Yevick pair distribution function) for different values of volume fraction of ice $\mathcal{S}\{F\}$ S.

adjacent particles [34], [90]. For Rayleigh scatterers the interference is effectively destructive and results in less scattering than under the assumption of independent scatterers. The description of the dense medium effect depends also on the spatial correlation of the particles, which may be described by different functions (Percus-Yevick's pair distribution function [90], modified pair function [21]). The Dense Medium Radiative Transfer Model (DMRT) has the same form as the classical radiative transfer equation except that κ_e and $\tilde{\omega}$ are derived from the complex effective propagation constant $K = K' - iK''$, which includes absorption and scattering processes [89], [95]. Based on the Percus-Yevick's pair distribution function κ_e and $\tilde{\omega}$ for a dense medium with single size particles are given by [95]

$$\kappa_e = 2K'' \quad (6.23)$$

$$\tilde{\omega} = \frac{2 a^3 F}{9 \kappa_e} \left| \frac{k_s^2 - k^2}{1 + \frac{k_s^2 - k^2}{3K_0^2} (1 - F)} \right|^2 \frac{(1 - F)^4}{(1 + 2F)^2}$$

where k and k_s is the wavenumber in the background medium and in the scatterers, respectively. Figure 6.5 shows κ_e and $\tilde{\omega}$ after eq. 6.23 at C-band for dry snow assuming spherical

single sized scatterers. The albedo increases significantly with increasing grain size. Depending on the volume fraction of scatterers the dense medium radiative transfer model in the Rayleigh approximation predicts lower values of $\tilde{\omega}$ and κ_e than the independent scatterers model and shows lower backscattering values [90].

For modeling purposes the selection of the representative scatterer size of a snow layer is crucial. The grain size or its size distribution may be estimated e.g. from digitized thin section images by applying morphologic mapping [34]. Comparing the assumption of a particle size distribution in the form of a Rayleigh probability density function (with tail truncation) versus the assumption of single size particles (where the size is equal to the mode of the Rayleigh distribution) in the DMRT West *et al.* [96] found a difference of almost 10 dB between the predicted backscattering values. The reason is that grains larger than the mode of the particle size distribution show only a small concentration, but are much more effective Rayleigh scatterers. Thus their presence causes a significant increase in the cross section [96]. Additionally, depolarizing effects may be observed due to multiple scattering in the snow pack [95].

6.2.3 Effect of layering and frozen crusts

Quasi-horizontal layering effects the radar return from a dry snow pack. The layers with different density and/or wetness cause refraction and geometrical optic effects, and may produce significant interference and polarization effects [45]. This was quantitatively investigated by West *et al.* [97], who applied a multi-layer model with planar layer boundaries to predict the emission of dry polar firn. The calculations were in good agreement with in situ measurements of Rott *et al.* [75]. When the layering of the snow pack was not considered differences of 40 K to 50 K in the predicted and measured brightness temperatures were found. This type of layering is less important for backscattering of wet snow due to the low penetration depth, but frozen crusts at the surface may show a significant influence on backscattering [45].

Due to melting and refreezing crusts are formed in the surface layer. Due to accumulation of snow refrozen crusts may also be observed inside the snow pack. The effect of a frozen crust on backscattering was estimated by modelling the crust as a lossless layer of independent Rayleigh scatterers with a certain radius and with $\epsilon' = 3.15$ [45], or as a random medium using the Born approximation (1st order continuous random medium model) [58]. Both models showed good agreement between measured and predicted σ^o -values [45]. The large particles of the crust act as strong Rayleigh scatterers and contribute significantly to the backscatter of the snow pack, especially at frequencies above 10 GHz. At 35 GHz Mätzler [45] determined an increase of the normalized backscattering coefficient by $\Delta\gamma = 0.45$ (where $\sigma^o = \gamma \cos\theta_i$) due to the formation of a 3.7 cm thick crust.

If the thickness of the refrozen crust is of the order of the wavelength interference effects between the wave scattered back from the upper and lower boundary of the crust may be observed [45]. Measurements during the formation of a crust showed a change of the backscattering at X-band from about -23 dB to -15 dB [58].

6.3 Backscattering contributions from snow covered terrain

A simple single layer model is used to demonstrate the importance of the physical processes of backscattering of snow covered terrain. The total backscattering cross section σ_t^o is modeled as the incoherent sum of several components, each corresponding to a particular rough interface or volume scattering layer. Assuming one layer the total backscattering

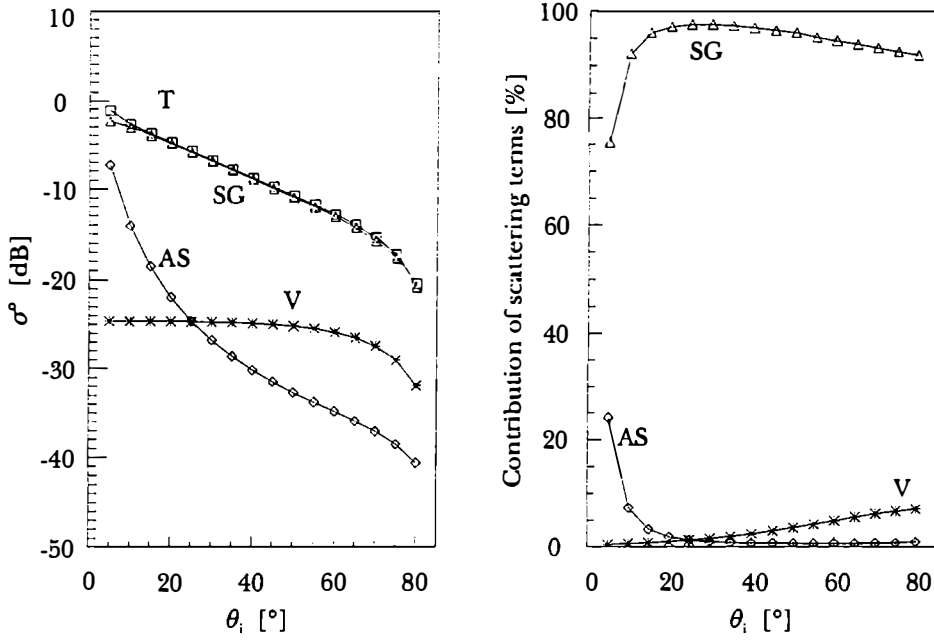


Figure 6.6: Scattering terms of soil covered by dry snow at 5.3 GHz (for parameters in table 6.1): AS ...scattering from the air to snow interface, V ...volume scattering of snow pack (independent Rayleigh scatterers), GS ... scattering from ground to snow boundary after attenuation by the snow layer.

coefficient σ_t^o is given by

$$\sigma_t^o = \sigma_{as}^o + \sigma_{vol}^o + \frac{\cos \theta_i}{\cos \theta_t} T_{as} T_{sa} e^{-2\kappa_e d / \cos \theta_t} \sigma_{gs}^o(\theta_t) \quad (6.24)$$

σ_{as}^o describes the backscattering from the air to snow boundary given by eq. 6.13, σ_{vol}^o represents the volume scattering given by eq. 6.20, assuming independent single sized Rayleigh scatterers. The third term on the right hand of eq. 6.24 describes the backscattering from the rough boundary between snow and ground, which is attenuated by the snow pack [20] (section 2.5.4).

This model is based on the following assumptions:

- only single scattering is important
- only coherent transmission across the air to snow boundary (Fresnel power transmission coefficients)
- only single particle size of scatterers
- all reflections and coherent interactions between ice layers are neglected

This model is only an approximation to the backscattering signatures of snow covered terrain. But due to its simplicity it enables useful insights into the backscattering processes.

Figure 6.6 and 6.7 show the contributions of the individual scattering processes for snow covered terrain with different snow properties. The snow pack and ground parameters for both simulations are summarized in table 6.1. The dielectric properties of the ground were estimated by the empirical relation of Hallikainen *et al.* [30], assuming 40% sand,

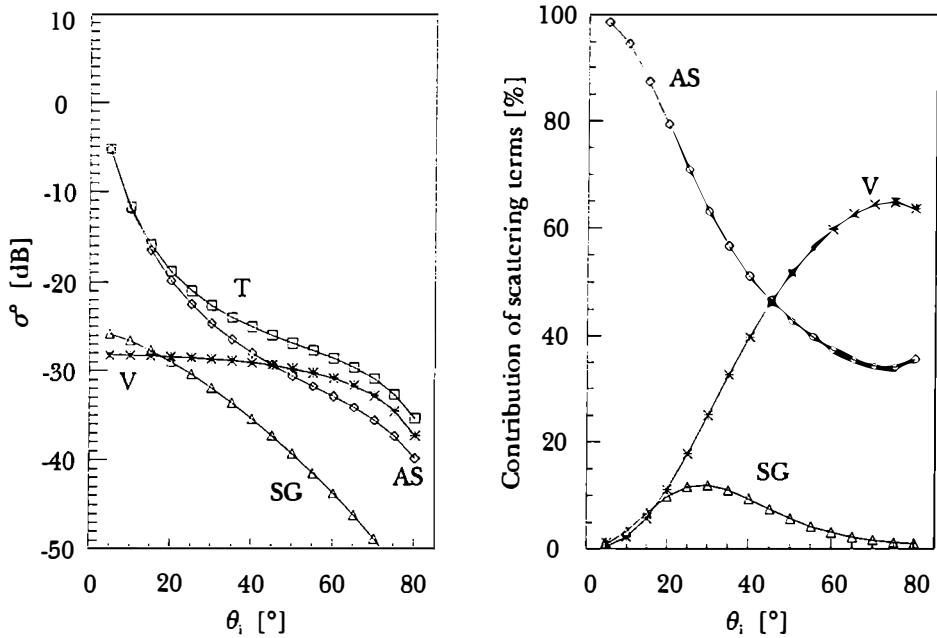


Figure 6.7: As figure 6.6, but for wet snow case (parameters in table 6.1).

15% clay and a volumetric moisture content of 20%; the surface roughness parameters σ_{sg} and l_{sg} correspond to the mean values of a smooth moraine/rock surface, measured in August 1992 in front of the terminus of Hintereisferner (table 7.3). The roughness parameters of the air-snow interface σ_{as} and l_{as} correspond to the mean values measured on Hintereisferner on 1 June 1992 (table 7.3), and are assumed for the dry and wet snow case. In the case of dry snow of 1 m depth the ground contribution is dominant. A large grain radius of 0.5 mm is assumed for dry snow. In general the effective scattering grains for fresh snow are smaller and the snow layer becomes more transparent. The surface scattering from the air to snow boundary contributes only at low incidence angles and can be neglected above 20° (depending on the surface roughness), while the volume scattering term becomes more important.

For snow of low wetness the backscattering contributions of the different processes are totally different. A thin snow pack of 0.3 m depth and $V_w = 1\%^{vol}$ is assumed, with a penetration depth at C-band of 0.11 m. The radius of 1 mm is realistic for grains of wet snow in spring. The snow to ground scattering has only a small contribution and can be neglected especially for deeper snow packs. At low incidence angles the total backscattering coefficient of the wet snow pack is dominated by the air to snow surface scattering process. With increasing incidence angle the volume scattering contribution increases and is for this example the dominating process at incidence angles above 45°. But when V_w increases surface scattering at the air-snow boundary becomes more important also at higher incidence angles. At X-band and C-band backscattering from wet snow can be approximated very well by taking only the surface scattering term into account.

Parameters	Units	Dry Snow	Wet Snow
Snow Depth	[m]	1	0.3
ρ_s, F	[gcm^{-3}]	0.3, 0.33	0.3, 0.32
a	[mm]	0.5	1
V_w	[%vol]	0	1
ϵ_{snow}		$1.53 - i0.0002$	$1.71 - i0.1$
$\sigma_{as}, k\sigma_{as}$	[mm]	4.4, 0.58	4.4, 0.58
l_{as}, kl_{as}	[mm]	116, 13.6	116, 13.614
d_p	[m]	53	0.11
$\tilde{\omega}$		0.144	0.002
κ_e		0.019	8.85

Ground properties			
ϵ_{ground}		$10 - i1.9$	$10 - i1.9$
$\sigma_{sg}, k\sigma_{sg}$	[mm]	15.8, 1.76	15.8, 1.76
l_{sg}, kl_{sg}	[mm]	117, 13.7	117, 13.7

Table 6.1: Parameters for dry and wet snow pack assuming independent scatterers and Rayleigh approximation.

Chapter 7

Signature study based on SAR data

Signature analyses were carried out for two test sites using ERS-1 and X-SAR data, which are described in section 3.1. At Leutasch/Innsbruck backscattering from agricultural fields, cultivated meadows and coniferous forest at incidence angles between 20° and 25° is investigated using a sequence of ERS-1 images (table 3.3). The Ötztal test site includes different types of surfaces, which are typical for high alpine regions. The investigated targets are:

- glaciated areas:
 - areas covered by snow accumulated during the winter
 - areas covered by snow of former years (névé)
 - glacier ice

- unglaciated areas
 - rocks and moraines
 - vegetated areas, mainly grass and dwarf shrubs.

Glacier ice can be divided into relatively smooth ice and heavily crevassed glacier ice areas. The last category was excluded from the analysis.

Previously, signature studies of snow covered and snow free alpine areas were made using ground based scatterometer systems [45], [65], [74], [86]. During SRL-1 and SRL-2 signature measurements with different ground based microwave radiometer / scatterometer systems (5.3 GHz, 10.3 GHz, 35 GHz) were carried out over snow covered areas [49] and over low alpine grass [53]. Investigations of signatures of alpine targets based on airborne or spaceborne sensors are described e.g. in [48], [65], [62] including research on the detection of wet snow.

This chapter is organized as follows. The first two sections deal with backscattering signatures in Ötztal based on ERS-1 C-band and on X-SAR X-band data. The last section describes the backscattering from targets of the test site Leutasch/Innsbruck. Each section starts with an overview of the field measurements, which helps to understand the backscattered signal. The incidence angle dependence of σ° is derived and temporal sequences of selected sites are investigated. For ERS-1 C-band data the seasonal variation and day and night changes of σ° are presented. X-SAR data enable the study of σ° changes

Depth [cm]	27Apr	1Jun	6Jul		10Aug		14Sep	19Oct
	D+A	D+A	D	A	D	A	D+A	D+A
0-10	.2- .5	2-3	.5-2.5	.2- .7	~2	0.5	1	0.2
10-20	.2- .5	1-3	1-1.5	1.5	1-2	.5-1.5	1.5	0.2

Table 7.1: Typical range of grain diameters in mm observed during field campaigns on Hintereisferner and Kesselwandferner/Gepatschferner.

within several hours and days. The importance of surface roughness will be demonstrated by a roughness experiment on Kesselwandferner for ERS-1 on 6 July 1992.

For the investigations in the Ötztal ERS-1 and X-SAR images were calibrated and geocoded to UTM-32 projection (see chapter 5). Layover and shadow zones (which were excluded from the analysis) and local incidence angle maps were derived from the DEM. In addition Landsat TM images, which provide the knowledge about the surface classes, are available in the same projection. For investigations at Leutasch/Innsbruck ERS-1 SAR images in PRI geometry are used.

7.1 ERS-1 surveys in Ötztal 1992/93

7.1.1 Field measurements

In 1992 five field surveys were carried out in the test site Ötztal at 35 day intervals related to ERS-1 overflights. The majority of the field measurements were carried out on the glacier plateau Kesselwandferner (KWF) / Gepatschferner (GEF) and on Hintereisferner (HEF) at altitudes between 2700 m and 3300 m. Between April and October 1992 the full annual cycle of snow conditions on glaciers and unglaciated high alpine areas (mainly moraines, rocks and low vegetation) was observed, which can be summarized as:

- 27 April 92: dry winter snow pack on glaciers. up to 3 m thickness in about 3000 m altitude
- 1 June 92: wet snow with fine grains and smooth surface
- 6 July 92: wet snow with medium grains, slightly rougher surface than in June
- 10 August 92: very rough wet snow with coarse grains, very rough glacier ice
- 14 September 92: slightly wet snow with coarse grains, snow and glacier ice surfaces less rough than in August
- 19 October 92: partly refrozen firn and 1 m of fresh dry snow

7.1.1.1 Characterization of the snow medium during ERS-1 passes

Information from several snow pits has been combined to give an overview of the snow conditions during the SAR passes. Table 7.1 and figure 7.1 summarize the typical grain sizes and the mean ranges of liquid water contents observed on KWF and HEF. Table 7.2 presents typical dielectric properties (at 5.3 GHz) of the snow pack during the ERS-1 SAR overflights.

On 27 April 1992 the snow pack was dry except for a thin surface layer on sunny slopes, which developed during the day due to strong solar illumination. In 2920 m altitude on HEF the snow temperature was -3.0°C at 0.3 m depth, -5.6°C at 1 m, and -5.2°C at

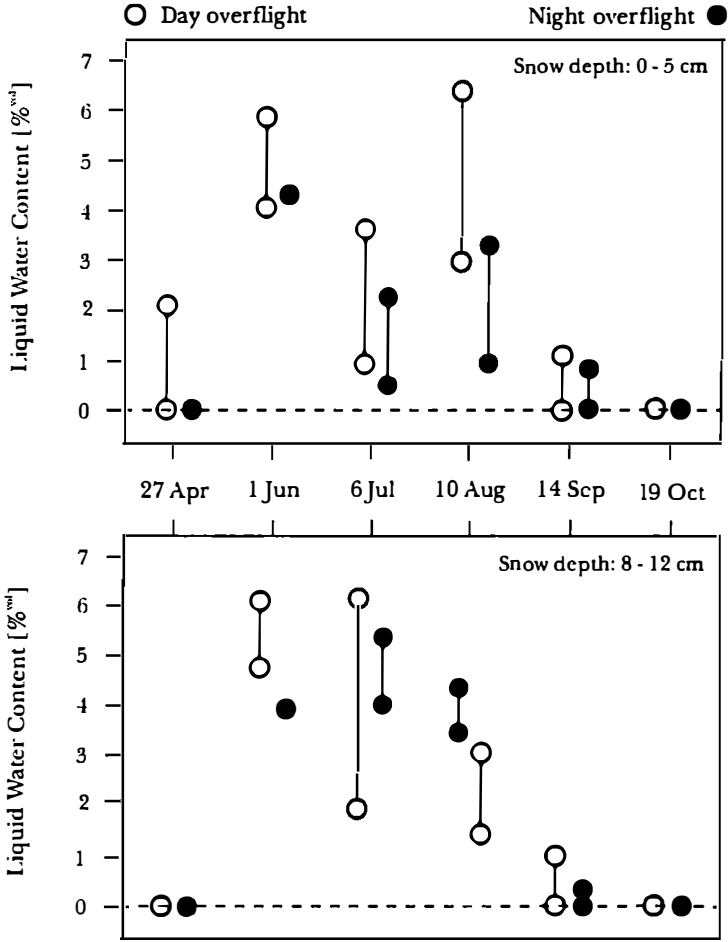


Figure 7.1: Liquid water content V_w in $\%^{vol}$ observed on HEF and KWF during ERS-1 SAR surveys in 1992.

	Units	27Apr	1Jun	6Jul	10Aug	14Sep	19Oct
ρ_s	$[kgm^{-3}]$	380	500	400	590	400	250
T_s	$[K]$	270	273	273	273	273	268
V_w	$[\%^{vol}]$	0	4	3	4	1	0
ε'		1.71	2.7	2.33	2.9	1.97	1.33
ε''		$<10^{-3}$	0.38	0.28	0.38	0.095	$<10^{-3}$
d_p	$[m]$	~ 10	0.039	0.048	0.04	0.13	~ 10

Table 7.2: Summary of dielectric properties of the snow pack at 5.3 GHz. The snow density (ρ_s), snow temperature (T_s), and liquid water content (V_w) were measured during ERS-1 passes on KWF and HEF. If wet snow is present ($V_w > 0$) the snow parameters were selected from the upper layer of the snow pack only.

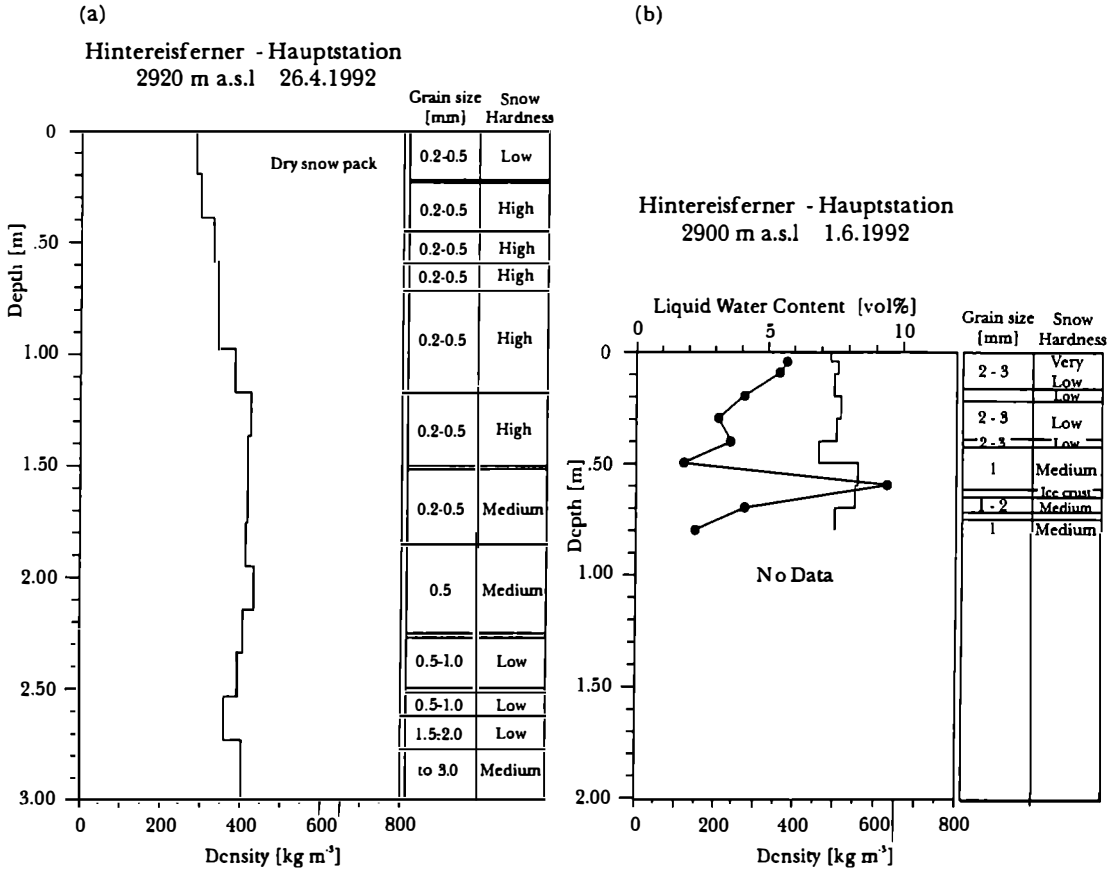


Figure 7.2: Snow pits on Hintereisferner, 27 April 1992 (a) and 1 June 1992 (b).

2 m depth. The grain diameter varied typically between 0.2 mm and 1 mm, but in crusts the grain size reached 3 mm. The snow density showed only small variations, from about 280 kgm^{-3} at the surface to 436 kgm^{-3} at about 2 m depth (figure 7.2 a). According to table 7.2 the real part of the dielectric constant was on the average $\epsilon'_{ds} = 1.71$ and d_p was of the order of several meters. During the day pass of ERS-1 the top centimeters of the snow pack on sunny slopes melted, especially at lower altitudes. On HEF about 1 %^{vol} liquid water content was measured in the top centimeters. During the night pass the air temperature was -2.1°C , and 3/8 cloud coverage was observed. These conditions caused the formation of a thin frozen crust at the top of the snow pack.

On 1 June 1992 rain up to 3000 m was observed. Even during the night the air temperature measured at HEF at 3000 m altitude remained above the freezing point (about 3°C during the SAR survey at 21:00 UTC). The whole snow pack was wet with up to 6 %^{vol} liquid water content. A typical snow profile on HEF at 2900 m on 1 June is shown in figure 7.2 (b). The snow temperature at 0.5 m depth was 0°C , at 0.7 m depth -0.3°C . According to table 7.2 the penetration depth was of the order of 5 cm, the wavelength of ERS-1 SAR.

In July, August and September field campaigns were carried out on HEF as well as on KWF/GEF. During the day of 6 July 1992 the snow pack was wet. On KWF up to 4 %^{vol} liquid water were observed. The round grains and clusters had typical diameters of 1-2.5 mm (figure 7.3). In the evening during the ascending overflight about 5 to 10 cm of fresh snow covered the surface. Moreover, a drop of air temperature between the day and night pass resulted in a decrease of wetness in the upper snow layer. A detailed description of

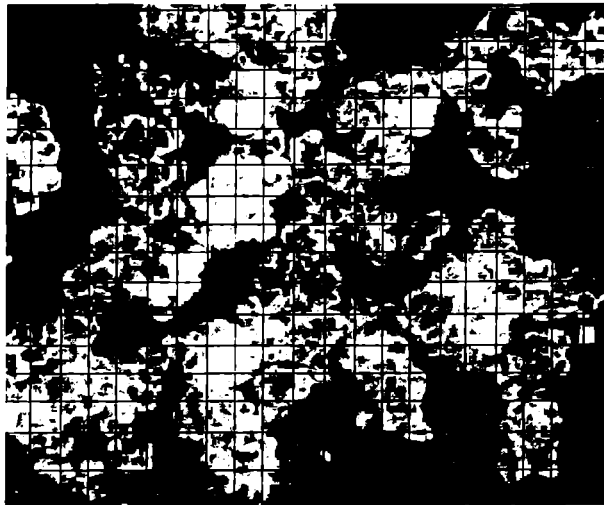


Figure 7.3: Photograph of grains from the top layer of the snow pack on KWF during ERS-1 descending pass on 6 July 1992. Spacing of reference grid is 1 mm. (Picture by Robert Davis).

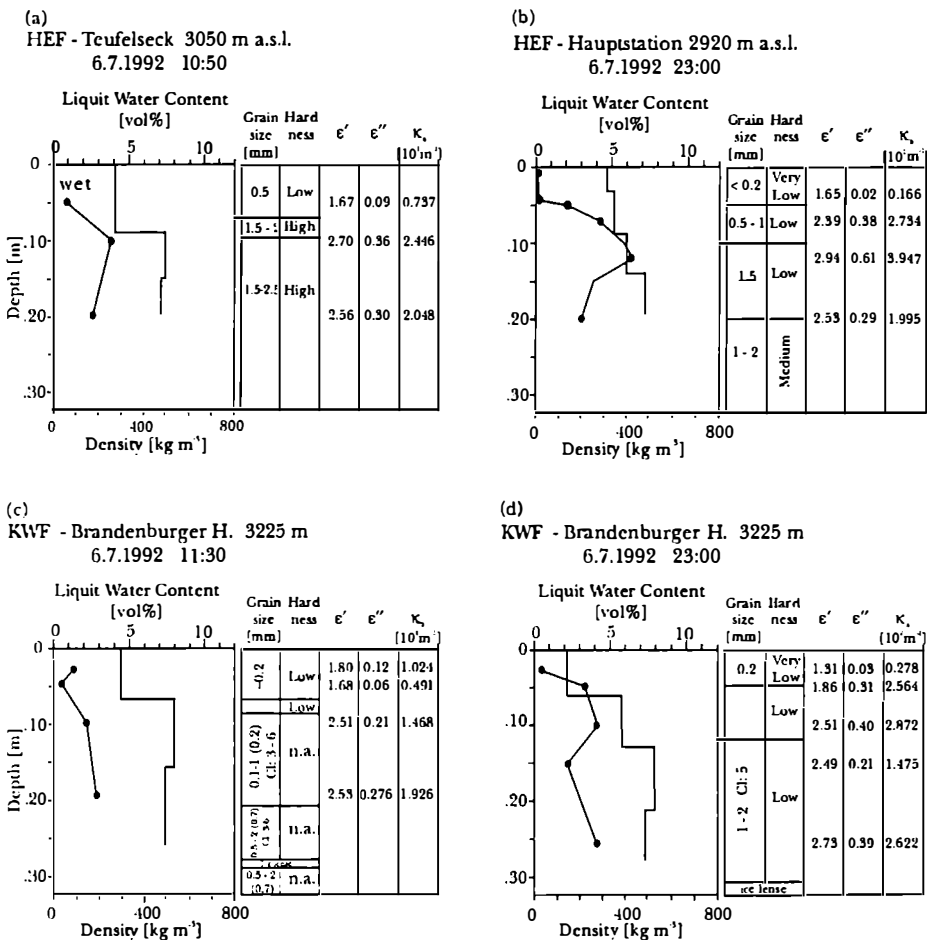


Figure 7.4: Properties of upper snow layer at HEF and KWF during ERS-1 SAR surveys on 6 July 1992.

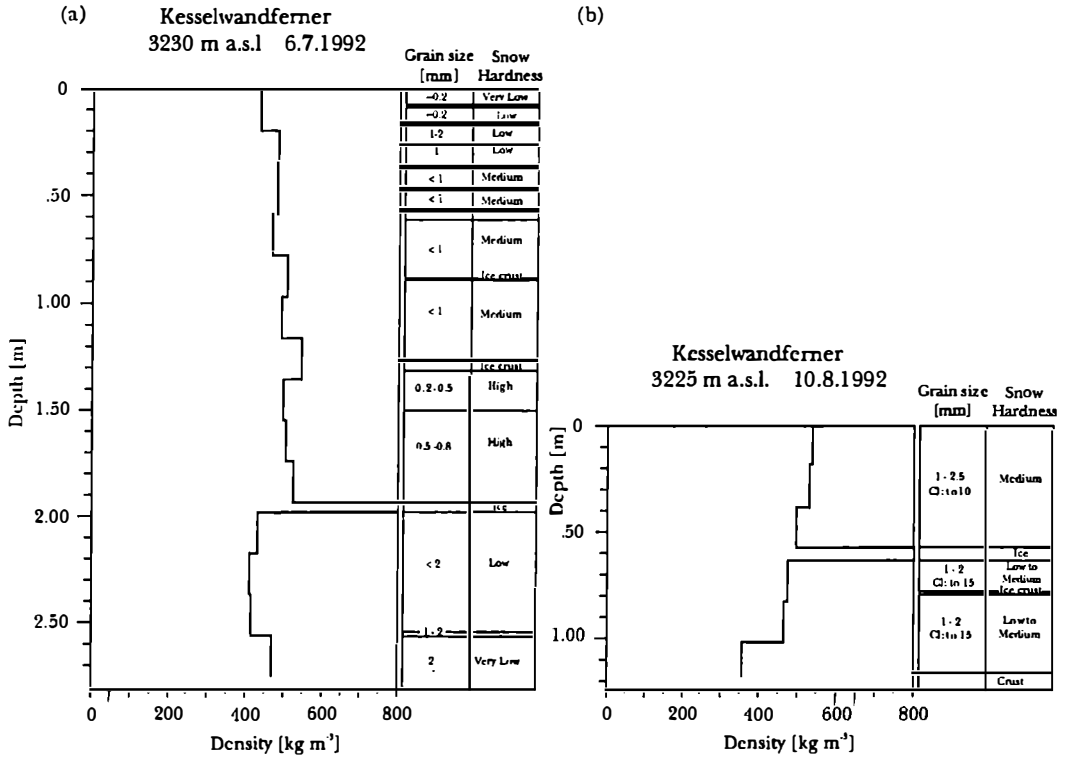


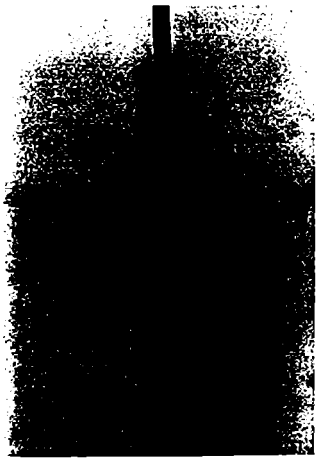
Figure 7.5: Snow pits on Kesselwandferner, 6 July 1992 (a) , 10 August 1992 (b), (Cl...Cluster size).

the conditions during the ERS-1 passes is given in figure 7.4. It shows vertical profiles of the top 0.30 m of the snow pack on KWF and HEF measured during day and night SAR surveys on 6 July, including the permittivity and the volume absorption coefficient κ_a for several layers.

From 6 July to 10 August the total height of the snow pack on Kesselwandferner decreased by about 1.6 m (figure 7.5). On the lower parts of the glaciers all the snow accumulated during the winter had been melted. Due to the warm period before the SAR survey in August the surface of the glacier ice and of the remaining snow was very rough. In August the snow and firn consisted of large, rounded grains up to 3 mm diameter and clusters up to 10 mm. The permittivity of the top layer was $\epsilon_{ws} = 3.0 - i0.38$ at 5 GHz and $d_p = 0.04$ m. The temperature decrease from 3°C during the day to -2°C during the night caused a decrease of the liquid water content in the top snow layer and an increase of d_p . Due to snowfall the plateau of KWF was covered by about 10 cm and HEF by about 3 cm of fresh snow during the night overflight.

Due to low temperatures in early September the old snow was frozen down to 0.4 m depth. Depending on the location the glaciers were covered with a maximum of 0.3 m of fresh snow. Most of it had been melted during the warm days before the ERS-1 SAR survey. On the day of the image acquisition only some patches of snow remained on the glacier ice. Outside the glaciers some snow patches were observed above 2800 m. On the glaciers this snow had typical grain sizes of about 1.5 to 2 mm, older snow from the previous winter had grain sizes up to 2.5 mm. Figure 7.6 shows three small snow pits on KWF at altitudes of 3300 m, 3230 m, 3160 m. An ice crust of 1 to 2 cm thickness from the last melting period is visible in all 3 pits, the upper one contained two ice lenses. The image of snow pit S3 shows also dirty glacier ice (formed close to the surface during several

KWF 3300 m



Depth [cm]	Density [kg m ⁻³]	V _v [% vol]
0	392	0
	396	1
15		
	492	0
23.5		
	508	
50.0		

KWF 3230 m



Depth [cm]	Density [kg m ⁻³]	V _v [% vol]
0	408	1.5
	372	1
	448	2
27.5		
	516	No Data
48.0		

KWF 3160 m



Depth [cm]	Density [kg m ⁻³]	V _v [% vol]
0	428	2.5
	492	2
21.0		
Firn, Glacier Ice		

Figure 7.6: Snow pits at KWF in 3300 m (a), 3230 m (b) and 3160 m (c) during ERS-1 descending pass on 14 September 1992..

Date	ST	N	$\sigma_{h,\min}$	$\bar{\sigma}_h$	$\sigma_{h,\max}$	$k\bar{\sigma}_h$	l_{\min}	l_{med}	l_{\max}	kl_{med}
1992			[cm]	[cm]	[cm]		[cm]	[cm]	[cm]	
1Jun	s	27	0.23	0.44	0.82	0.48	6.7	11.6	20.2	12.87
6Jul	s	16	0.15	1.09	1.59	1.20	4.7	15.1	21.3	16.76
10Aug	s	32	1.24	2.85	6.53	3.16	7.2	14.0	19.0	15.54
14Sep	s	10	1.95	3.37	5.95	3.74	5.9	10.5	26.3	11.66
14Sep	i	9	0.73	1.78	2.64	1.98	4.4	13.0	20.9	14.43
10Aug	m	5	0.95	1.58	1.98	1.71	4.2	11.7	21.4	12.99

Table 7.3: Number of measurements (N), mean, minimum and maximum values of standard deviation of surface roughness (σ_h) and median, minimum and maximum values of correlation length l , from laser and roughness plate measurements of different surface types ST (s...snow, i...smooth glacier ice, m...smooth moraine) at Hintereisferner and Kesselwandferner. k is the wavenumber at 5.3 GHz.

years of negative mass balance) with a smooth surface and large grains up to 4 mm in size.

On 19 October about 1 m of fresh snow had accumulated with a density between 200 kgm^{-3} and 300 kgm^{-3} . The snow temperature was $-9^\circ C$ in 0.1 m and $-1.2^\circ C$ in 0.9 m depth; the real part of the dielectric constant was determined as $\epsilon'_{ds} = 1.33$.

7.1.1.2 Surface roughness measurements

Surface profiles were measured parallel and perpendicular to the flight direction of ERS-1. For smooth snow no systematic differences were found for the roughness in these two directions. Therefore the snow profiles were analyzed independently of their azimuth orientation. Table 7.3 gives mean, maximum and minimum values of σ_h and l for 1 June, 6 July, 10 August and 14 September, measured over snow surfaces. On 10 August and 14 September laser profile meter measurements were also done over smooth glacier ice and moraines. For the same surface type large variations of the standard deviation of height σ_h and especially of the correlation length l were determined. Examples of measured roughness profiles and calculated autocorrelation functions are shown in figure 7.7. According to the Fraunhofer criterion [92] in the C-band (5.6 cm wavelength) and at the incidence angle of ERS-1 SAR ($\theta_i = 23^\circ$ at mid swath) a horizontal surface can be treated as smooth when the condition $\sigma_h < 0.19$ cm is valid. This requirement is not fulfilled by any surface measured in the test site Ötztal.

The surface roughness changed significantly from homogeneous rather smooth fresh snow surfaces in April to very rough snow surfaces in August and September. Based on measurements at the Leutasch test site typical values of σ_h for a fresh snow surface are between 0.20 cm and 0.30 cm. During June and July ERS-1 passes the snow surfaces were rougher due to rain and melting. After strong ablation the glacier ice was very rough on HEF in August. Two scales of roughness were observed, with small scale roughness in the range of millimeters and medium scale roughness in the range of several centimeters to tens of centimeters (figure 7.7 b). Over ice areas in the lower parts of the glaciers melting channels several centimeters up to several meters wide and small holes partly filled with slush or water appeared. This gives the impression of large scale periodic patterns with meter to several meters range in the horizontal direction (figure 7.8). Due to the limited range of the laser profile-meter we could not measure this type of surface.

Due to melting of most of the fresh snow over the ice areas, which had fallen during the first two weeks in September, the surface roughness was reduced and appeared smoother on 14 September than in August. Typical profiles for smooth glacier ice and for a rock /

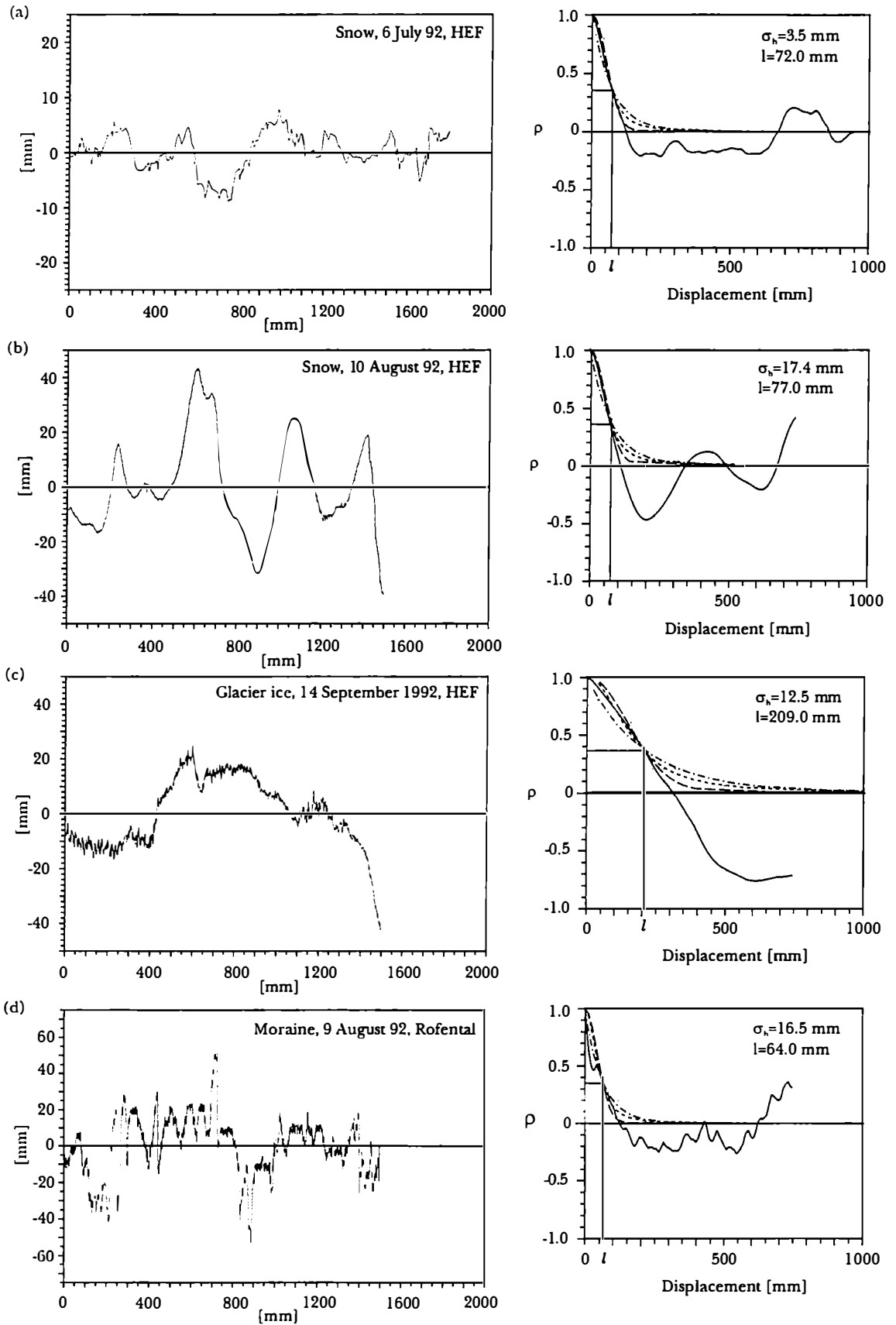


Figure 7.7: Examples of surface roughness measurements of different targets (left) and the corresponding autocorrelation (right) measured at Hintereisferner during ERS-1 SAR surveys in 1992. The correlation length l is marked by a line. Theoretical autocorrelation functions are plotted: exponential (— · —), modified exponential (— —), gaussian (— —).

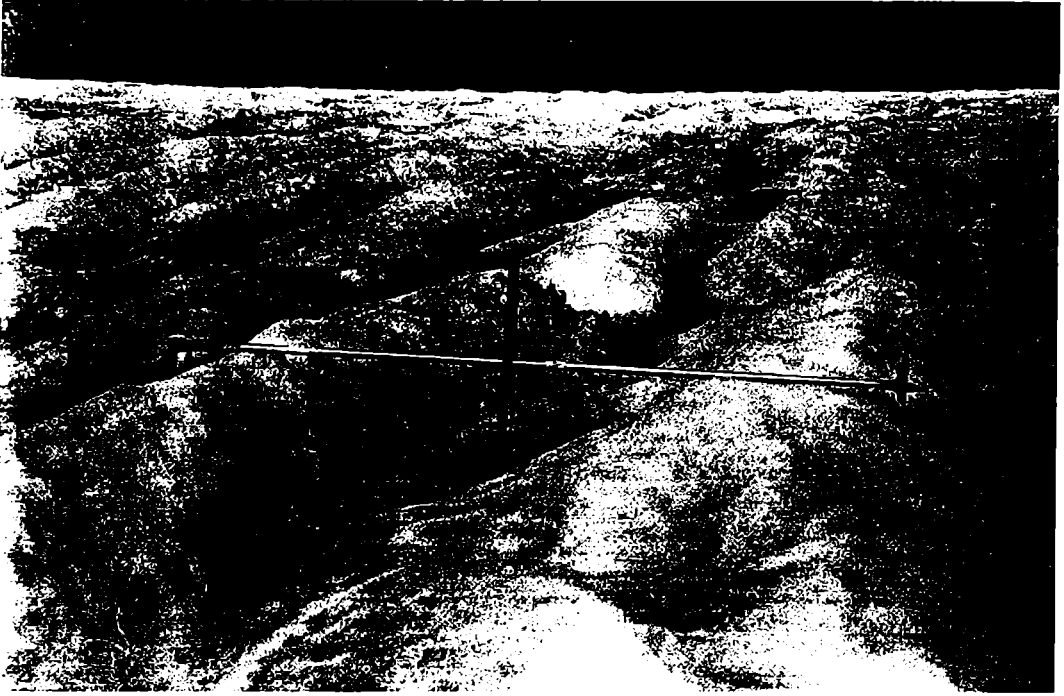


Figure 7.8: Rough glacier ice area at Hintereisferner with melt water channels, 10 August 1992. (Horizontal ski stick is about 1.4 m long).

moraine area are shown in figure 7.7 c and d.

For calculating the autocorrelation function a maximum displacement of half of the length of the measured profile was applied (see section 6.2.1.1). Additionally three models for the autocorrelation function, which are often used in surface backscatter models, are plotted, an exponential, a gaussian, and a modified exponential function [22], [20]. The measured autocorrelation functions differ significantly from these theoretical ones. One reason for this is that the observed profiles are not fully random (figure 7.7 b). Another problem results from the comparatively short profile length. A general recommendation on the theoretical function to be used for model calculations cannot be given.

7.1.2 Incidence angle dependence of backscattering from alpine targets

To determine the incidence angle dependence of σ^o fully calibrated and geocoded ERS-1 SAR images were used. The georeferenced Landsat TM image of 16 August 1992 was used to generate masks of the main surface types (chapter 9), which are applied to the SAR images. The main targets are vegetation, rocks/moraines, snow on glaciers, firn on glaciers (which is snow from previous years) and glacier ice. The masks were manually modified to eliminate heavily crevassed glacier zones, and those pixels which are influenced by corner reflectors, layover and shadow in the SAR image. The co-registration between TM and ERS-1 images and the quality of the generated surface masks are crucial for deriving representative signatures. The mask for each class includes areas with different orientation of the slope and altitudes, which (in particular in case of snow and ice) may be related to different target properties. Figure 7.9 shows the surface mask used for the derivation of the θ_i dependence of σ^o . The incidence angle dependence of σ^o for those targets is derived only for 27 April, when the site was covered by dry or slightly humid

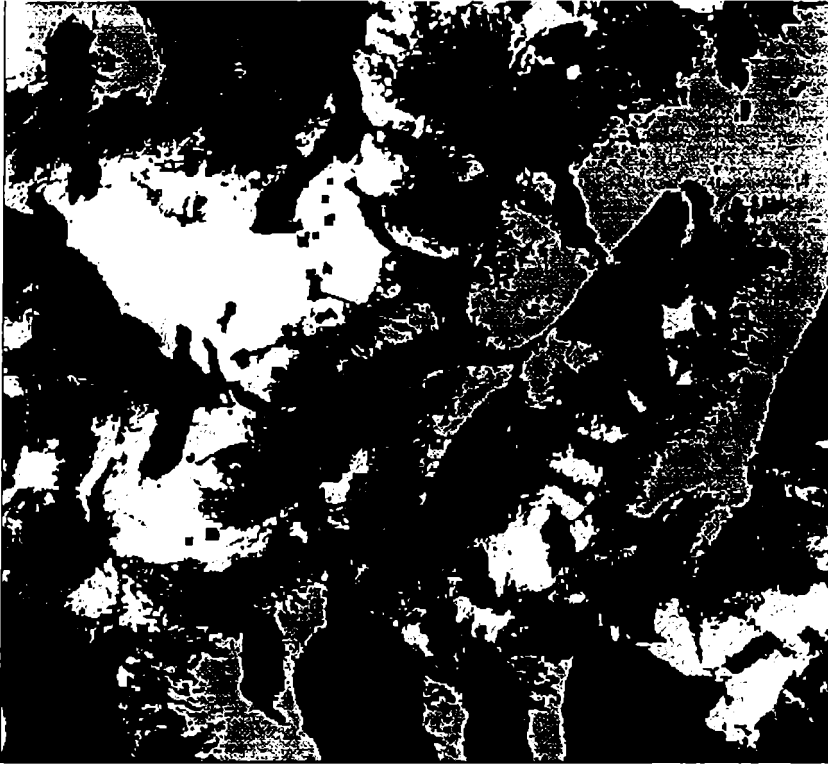


Figure 7.9: Surface mask for ERS-1 images of ascending pass based on Landsat TM image, 16 August 1992: black...eliminated areas (layover,shadow), grey levels (dark to light)...rocks, glacier ice, vegetation, firn, white...accumulation area (snow), black boxes on glaciers: corner reflectors.

snow, and for 10 August, when the surfaces are exposed.

Figure 7.10 a-e shows the mean incidence angle dependence of σ^o for vegetation, rocks, glacier ice, firn and snow derived from two ascending passes of ERS-1, on 27 April and 10 August 1992. In April the surfaces above about 2300 m were covered by dry snow. At lower altitudes on vegetation and rocks/moraines the snow surface was wet. The mean backscattering coefficient of these two classes is influenced by the wet snow cover with very low σ^o . Therefore backscattering from the targets vegetation and rocks is better represented by the values derived from the ERS-1 image of 10 August 1992 with snow free conditions.

Glacier ice shows a strong decrease of σ^o from -5 dB at 15° to about -13 dB at 35° incidence angle, with almost constant σ^o at θ_i higher than 35° . Because the ice was covered by dry in April snow the curves derived from the April and the August image are quite similar. Firn and snow areas reveal similar dependence on θ_i . During melting conditions in August very low σ^o values are observed for both firn and snow. But σ^o of the firn area is slightly lower in April, because the firn contains some thick, quasi-horizontal ice layers.

The incidence angle dependence may be described by different functions. Here a polynomial fit of the form

$$\sigma^o(\theta_i) = a_0 - a_1(30^\circ - \theta_i) + a_2(30^\circ - \theta_i)^2 + a_3(30^\circ - \theta_i)^3 \quad (7.1)$$

was used. The coefficients a_0, a_1, a_2, a_3 are listed for all studied targets for April and August in table 7.4.

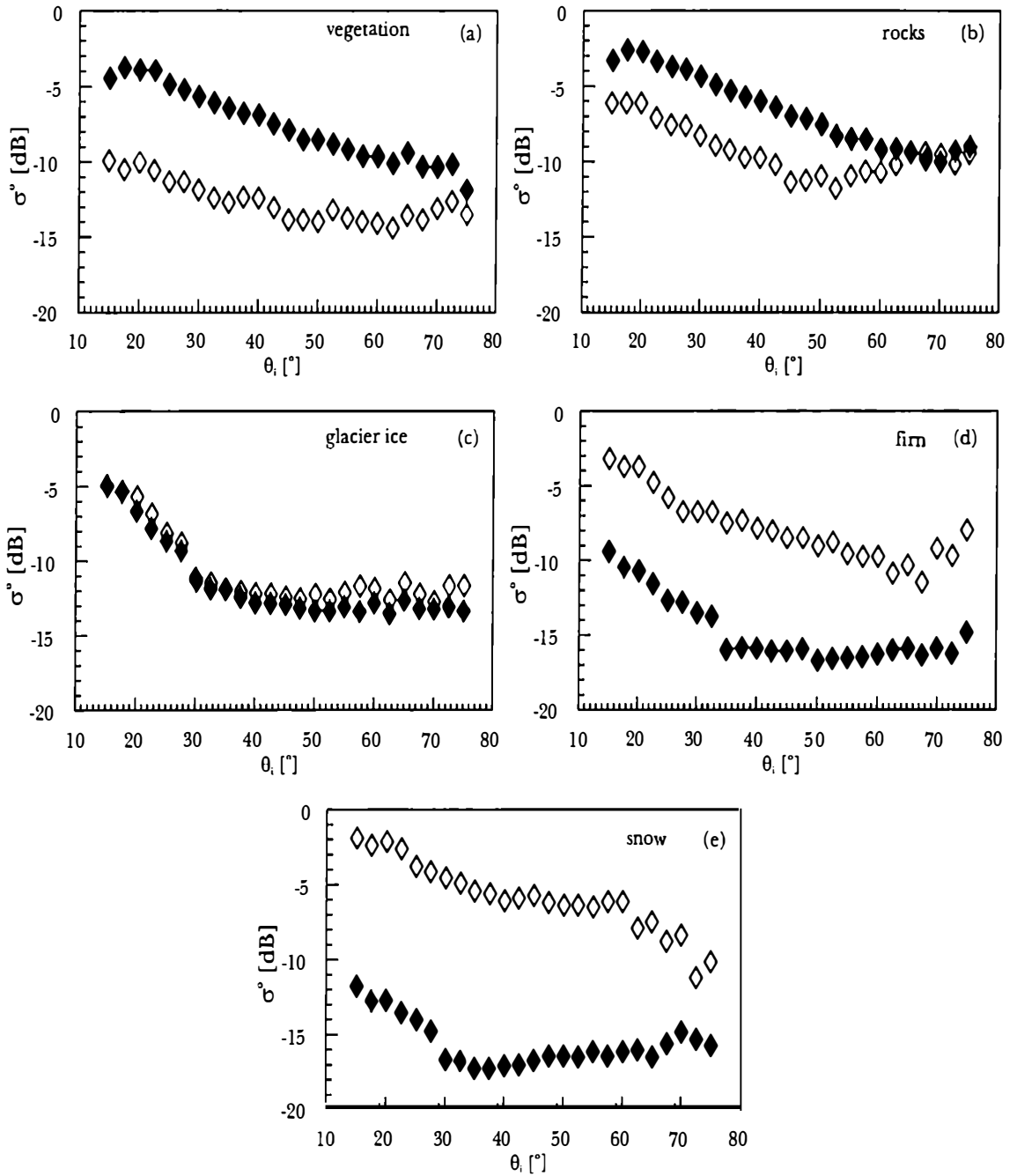


Figure 7.10: Incidence angle dependence of σ^o for different targets based on ascending ERS-1 images acquired on 27 April 1992 (\diamond) and 10 August 1992 (\blacklozenge).

Target	27 April 92			
	a_0	a_1	a_2	a_3
vegetation	$-1.174 \cdot 10^1$	$1.285 \cdot 10^{-1}$	$4.823 \cdot 10^{-4}$	$-4.284 \cdot 10^{-5}$
rocks	$-8.387 \cdot 10^0$	$1.936 \cdot 10^{-1}$	$1.750 \cdot 10^{-3}$	$-7.050 \cdot 10^{-5}$
glacier ice	$-1.047 \cdot 10^1$	$2.887 \cdot 10^{-1}$	$1.347 \cdot 10^{-2}$	$1.873 \cdot 10^{-4}$
névé	$-6.407 \cdot 10^0$	$1.794 \cdot 10^{-1}$	$2.768 \cdot 10^{-3}$	$2.064 \cdot 10^{-5}$
snow	$-4.648 \cdot 10^0$	$1.461 \cdot 10^{-1}$	$5.833 \cdot 10^{-3}$	$1.172 \cdot 10^{-4}$

	10 August 92			
	a_0	a_1	a_2	a_3
vegetation	$-5.537 \cdot 10^0$	$1.641 \cdot 10^{-1}$	$7.709 \cdot 10^{-6}$	$-2.882 \cdot 10^{-5}$
rocks	$-4.432 \cdot 10^0$	$1.624 \cdot 10^{-1}$	$-6.648 \cdot 10^{-4}$	$-3.137 \cdot 10^{-5}$
glacier ice	$-1.068 \cdot 10^1$	$2.917 \cdot 10^{-1}$	$1.067 \cdot 10^{-2}$	$1.218 \cdot 10^{-4}$
névé	$-1.389 \cdot 10^1$	$2.347 \cdot 10^{-1}$	$5.946 \cdot 10^{-3}$	$3.121 \cdot 10^{-5}$
snow	$-1.594 \cdot 10^1$	$1.831 \cdot 10^{-1}$	$8.997 \cdot 10^{-3}$	$1.019 \cdot 10^{-4}$

Table 7.4: Coefficients for polynomial fit of 3rd order, valid for incidence angle range between 18° and 70°.

Date	θ_i [°]	Model input parameters				σ_{IEM}^o [dB]	σ_{ERS-1}^o [dB]
		$k\sigma_h$	kl	ε'	ε''		
1 Jun	17	0.48	14.5	2.95	0.571	-12.6	-14.3
6 Jul	15	0.24	15.7	2.32	0.381	-16.0	-17.3

Table 7.5: Comparison of single scattering IEM model and ERS-1 based backscattering coefficient for a wet snow area on Hintereisferner of descending pass on 1 June and 6 July. The model input parameters ($k\sigma_h$, kl , ε' , ε'') are from field measurements at this site.

7.1.3 Temporal variation of backscattering

To study the temporal change of σ^o several sites were selected, which were imaged in ascending and descending passes of ERS-1. On the glaciers four sites were selected, and one site on rocks / moraines and on high alpine vegetation. For each test site the mean altitude and the mean local incidence angle of the ascending and descending pass is specified. Based on the selected targets changes in backscattering between day and night and variations during the year are discussed. A detailed description of surface conditions during ERS-1 passes is given in section 7.1.1.

Figure 7.11 a and b shows σ^o of glacier ice areas at the termini of HEF and Vernagt Ferner. On Vernagt Ferner σ^o decreases from high values in April, when up to 2 m of winter snow covers the ice, to low values of σ^o of about -18 dB in June and July, when the snow pack was wet. In April surface melting (the area is facing south) during the day pass reduces σ^o by about 5 dB relative to the night pass. Glacier ice was exposed at the surface on 10 August and on 14 September, where the differences of σ^o are caused by surface roughness changes. In August with very rough ice σ^o showed a high value of -7 dB, while in September with smoother ice σ^o was -12 dB. σ^o remains approximately constant from October to March, when dry winter snow with high penetration at C-band covers the glacier ice. On HEF the constant difference of σ^o between day and night of about 2 dB is an effect of different incidence angles of 17° and 29° respectively (see figure 7.10 c). In August some firn patches still covered the glacier ice, so that σ^o at this site reached its highest values in September.

The accumulation and firn areas on the glaciers reveal a pronounced annual variation.

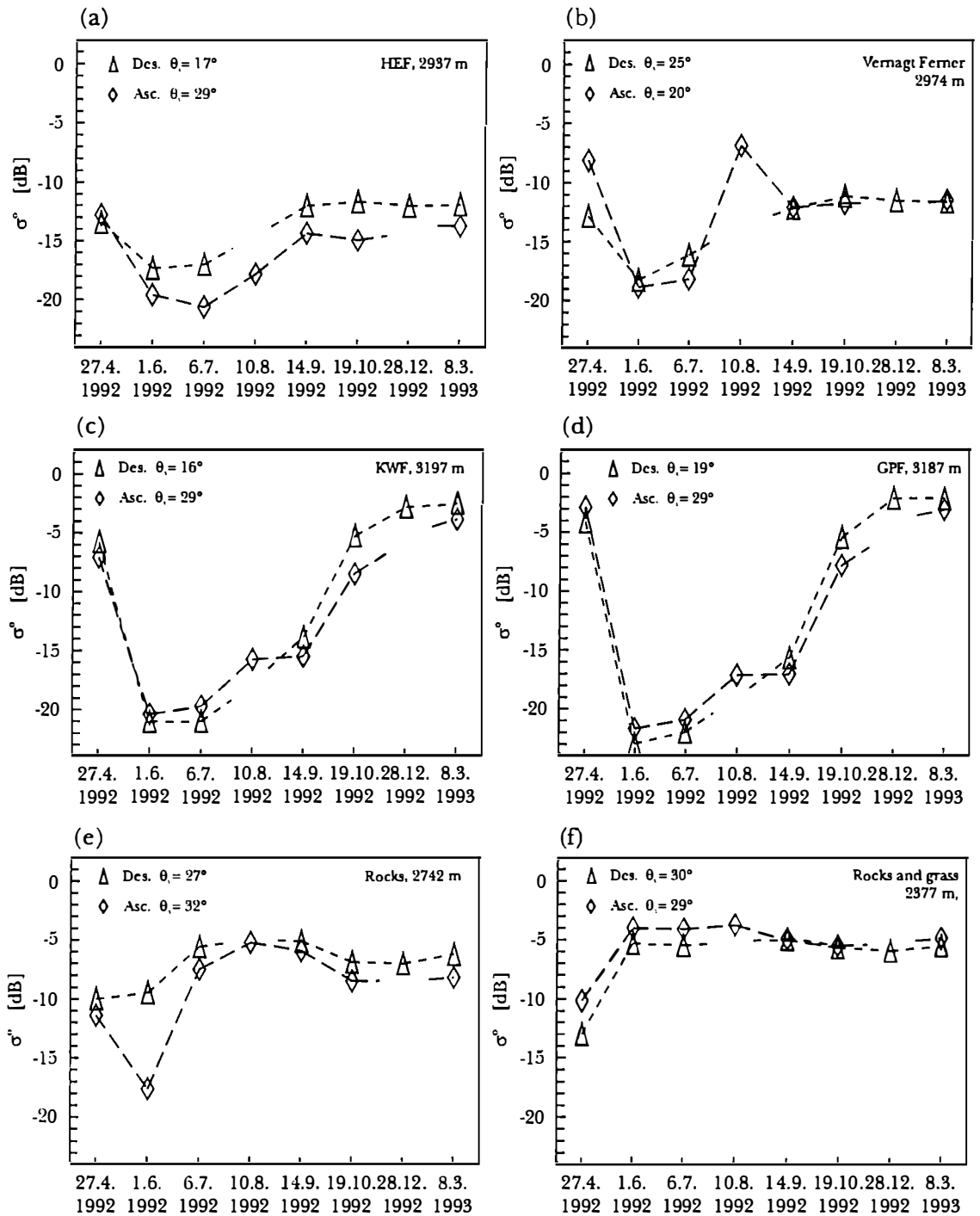


Figure 7.11: Backscattering cross section σ^o of selected areas derived from ERS-1 SAR images of descending (Δ) and ascending (\diamond) passes. θ_i ...mean local incidence angle.

Figure 7.11 c and d shows σ^o of sites in the accumulation areas on KWF and GEF. Between 27 April and 1 June σ^o decreases by about 20 dB. Refrozen firn includes large grains and ice lenses which act as strong scatterers; the dry transparent winter snow has little influence. On 1 June and 6 July, when the winter snow above was wet, mainly the surface and the top layer of the snow pack contribute to the backscattered signal. These conditions can be simulated well by the single scattering surface model IEM (section 6), as is shown in table 7.5. In August and September σ^o increases by about 5 dB relatively to July, an effect of surface roughness and snow structure. In autumn, with increasing depth of refrozen firn, σ^o starts to increase until it reaches the highest values later in winter.

Two ice-free areas (figure 7.11 e and f) were selected. The area in figure 7.11 e shows the lowest σ^o of -17 dB in June with melting snow. After becoming snow free in July σ^o remains constant at about -5 to -8 dB. The second area is a continuous slope at about 2377 m altitude facing to the south. Due to solar illumination melting occurs early in the year, so that in April the snow surface was wet during the day pass showing a σ^o value of -13 dB. During the night σ^o increased to -10 dB which was an effect of refreezing of the snow pack. After becoming snow free σ^o remains constant at a value of -4 to -6 dB similar to figure 7.11 e. Dry winter snow covering the site from October to March has no significant influence on the backscattering.

Figures 7.12 and 7.13 summarize the temporal changes of the backscattering coefficient. To eliminate the influence of the local incidence angle on σ^o all images of ascending and descending passes are normalized by the same image of 19 October 1992 from the corresponding pass. Therefore figure 7.12 and figure 7.13 correspond to the difference of σ^o (in dB) between the actual image and the image of 19 October 1992. The short term variations of σ^o between day and night for different seasons of the year are evident by comparing ascending and descending images of the same date, while the seasonal variation is evident by comparing the images of the same pass at different dates.

Figure 7.14 shows the behaviour of σ^o along a longitudinal profile on HEF for different dates. The profile starts at an altitude of 2500 m, corresponding to the terminus of HEF, and ends in 3100 m. It is several pixels wide and perpendicular to the altitude contour lines. The σ^o values were averaged in 25 m altitude intervals starting at 2500 m. The incidence angle along the profile varies from 26° to 35° (figure 7.14 b).

In April σ^o varied between -16 dB at the glacier terminus to -8 dB at the top of the profile. In June the glacier was covered by wet snow, except the lowest part of the glacier terminus at 2500 m, where σ^o was -13 dB. In July the lower and upper part of the profile differ by 10 dB. The high values of σ^o in the lower part indicate that glacier ice was exposed. The upper part, still covered by wet snow, had σ^o values below -20 dB. The transition zone with alternating patches of snow and glacier ice was situated between 2650 m and 2725 m. In August the transition zone was between 2875 m and 2950 m and the snow above was much rougher than earlier in the summer.

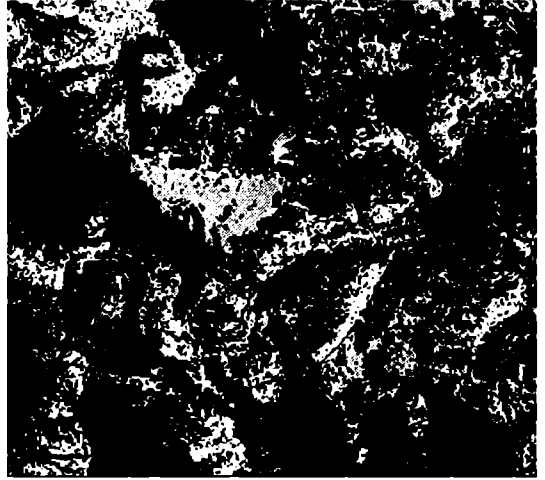
7.1.4 Snow surface roughness experiment

In order to study the effects of roughness on backscattering of snow surfaces, a test field was set up on 6 July on a flat area of KWF. The test field with a size of 100 m in azimuth and 50 m in range direction was made up by ski tracks in the soft snow parallel to the SAR track (figure 7.15). A similar experiment was carried out during the JPL-AIRSAR overflights over the same test site in 1991 [64]. The mean standard deviation of 11 roughness measurements was $\bar{\sigma}_h = 1.6$ cm, the median of the correlation length was $l_{median} = 4.3$ cm. Figure 7.16 a and b shows a roughness profile in the range direction, perpendicular to the ski tracks and its autocorrelation function. In order to learn about

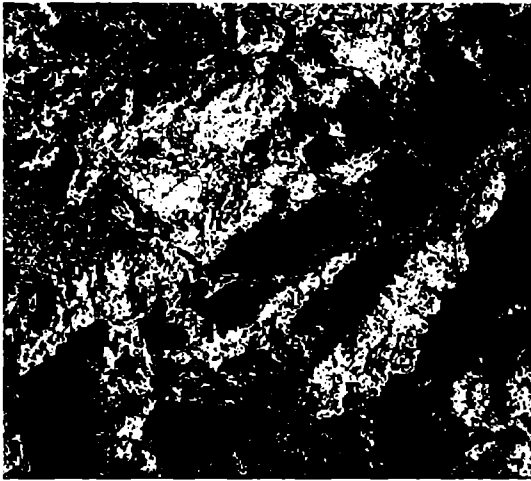
27 April 1992 - Descending Pass - 11:07 MET



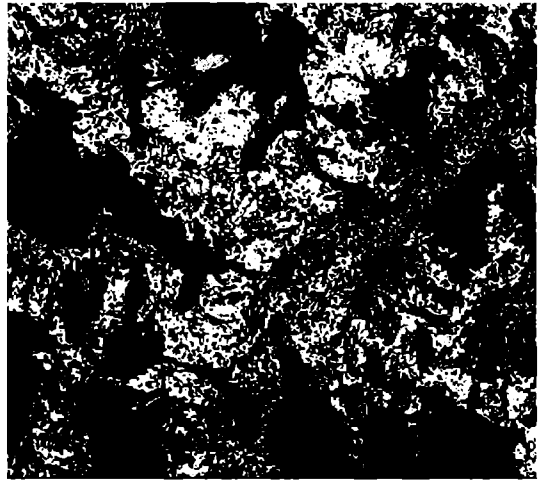
27 April 1992 - Ascending Pass - 22:28 MET



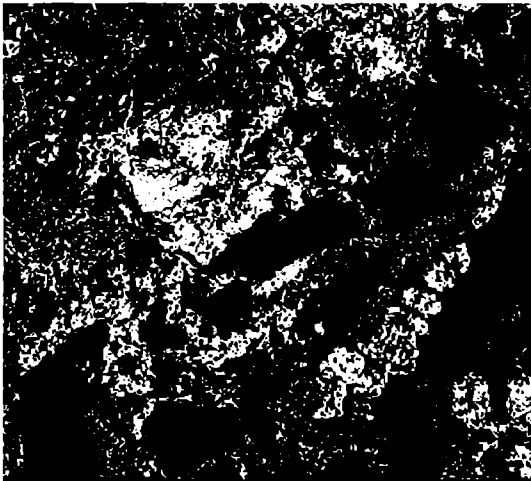
1 June 1992 - Descending Pass - 11:08 MET



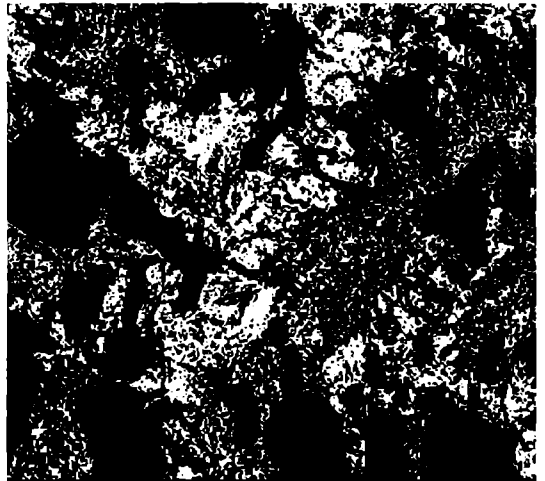
1 June 1992 - Ascending Pass - 22:28 MET



6 July 1992 - Descending Pass - 11:08 MET



6 July 1992 - Ascending Pass - 22:28 MET

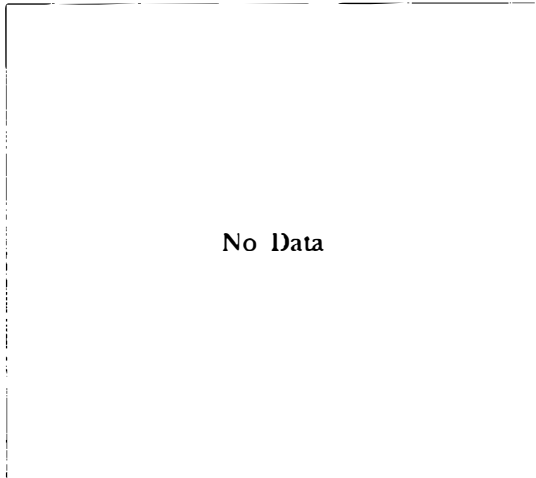


-15 -11 -7.5 -5 -2.5 0 2.5 dB

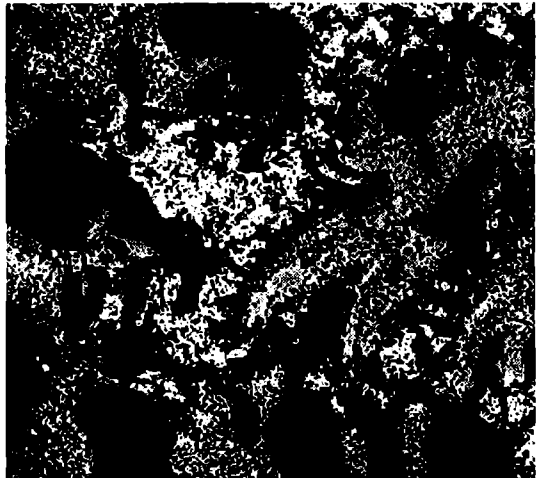


Figure 7.12: Geocoded images of σ^0 -differences in *dB* of the test site Ötztal. Values were derived by forming the ratio of σ^0 of the actual pass with σ^0 of corresponding pass of 19 October 1992 as a reference.

10 Aug 1992 - Descending Pass - 11:07 MET



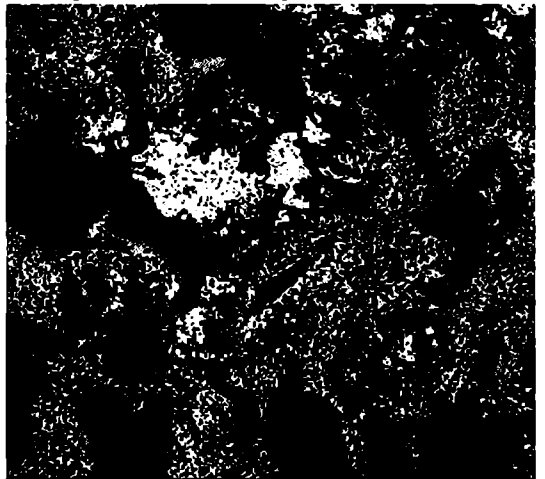
10 Aug 1992 - Ascending Pass - 22:28 MET



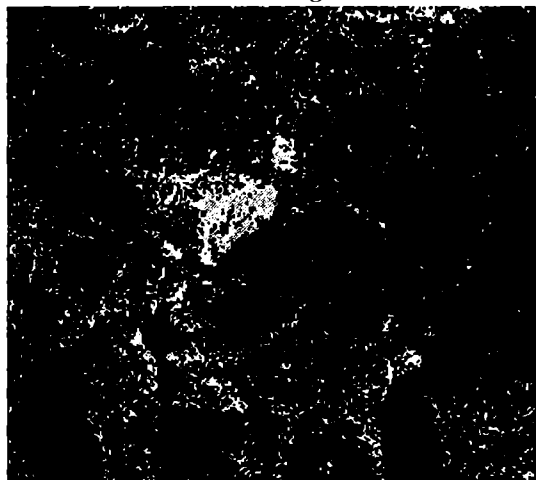
14 Sep 1992 - Descending Pass - 11:08 MET



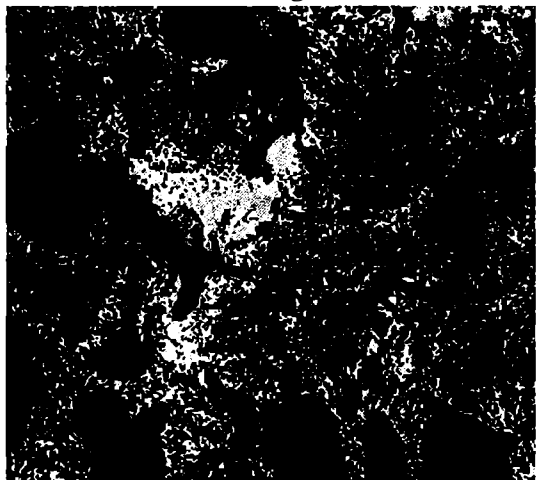
14 Sep 1992 - Ascending Pass - 22:28 MET



8 March 1992 - Descending Pass - 11:08 MET



8 March 1993 - Ascending Pass - 22:28 MET



-15 -11 -7.5 -5 -2.5 0 2.5dB



Figure 7.13: As figure 7.12.

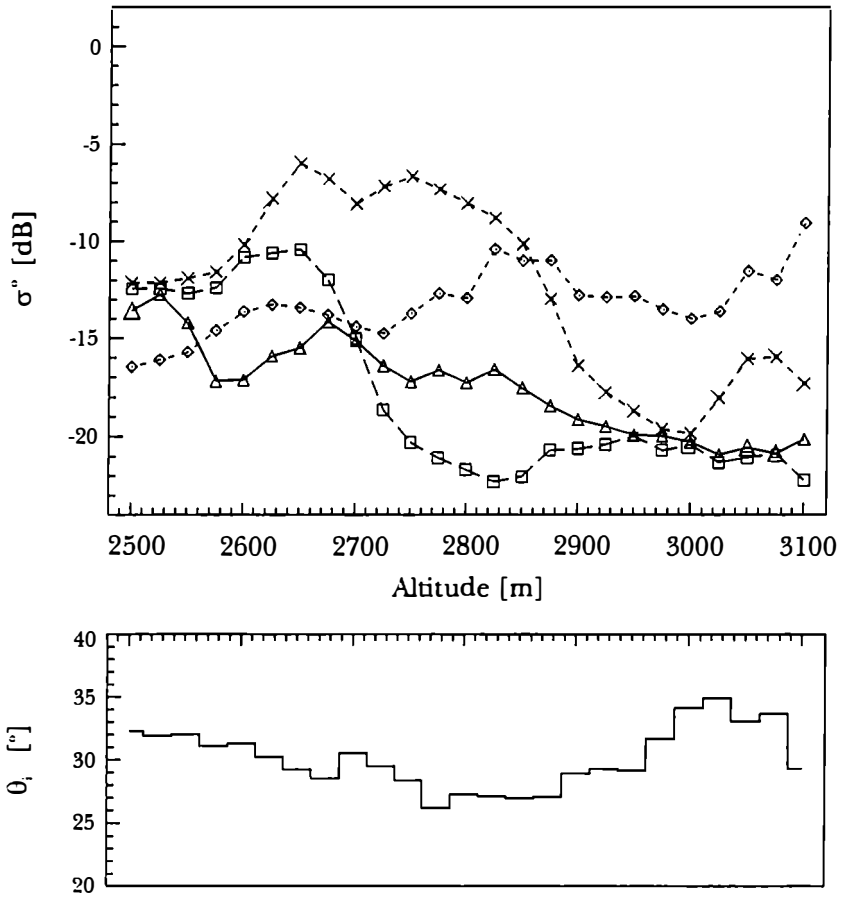


Figure 7.14: Radar cross section σ^o along a longitudinal profile on Hintereisferner from ERS-1 SAR ascending images. 27 April 1992 (\diamond), 1 June 1992 (\triangle), 6 July 1992 (\square), 10 August 1992 (\times).

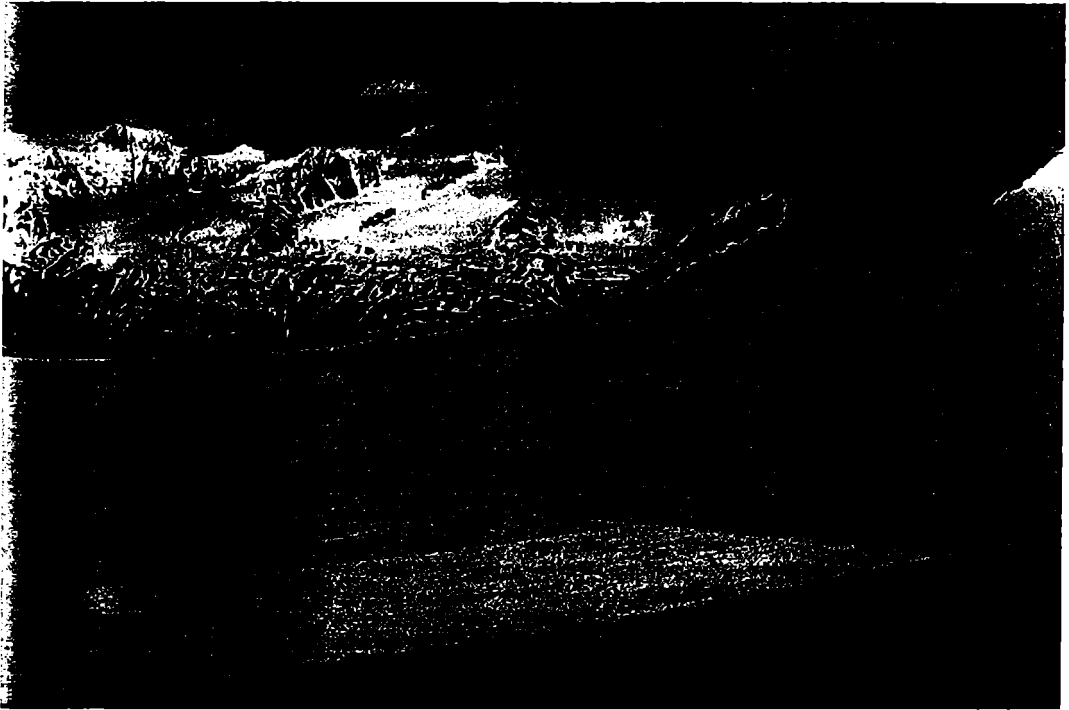


Figure 7.15: Surface roughness test field (50m x 100m) on Kesselwandferner. Ski tracks are parallel to the flight direction of the descending ERS-1 pass, 6 July 1992..

the compression of the snow due to the ski tracks, a horizontal density profile in the depth of 5-13 cm was measured (figure 7.16 c).

The response of the roughness test field can be seen in figure 7.17, a part of the ERS-1 SAR image of the descending pass on 6 July 1992. Three corner reflectors deployed for calibration purposes are labelled K1 to K3, and the roughness test field is marked by an arrow. The artificial roughness has a drastic influence on the backscattering of the snow pack. While the surrounding undisturbed snow surface next to the test field has an average σ^0 of about -19 dB, the roughness test field shows a mean σ^0 -value of -0.5 dB. The σ^0 -value of the roughness test field represents an average of 27 pixels of the original PRI image, which corresponds to about 7 independent looks (section 8.2.3). According to figure 7.16 the test field shows a periodic roughness component. Nevertheless this experiment confirms the strong influence of the roughness of a wet snow surface on the backscattering cross section.

7.2 SRL SIR-C/X-SAR missions in Ötztal

The SRL-1 and SRL-2 data takes of the Ötztal site were acquired during two periods of 5 days duration. This allowed the observation of short term variations of σ^0 . In the following sections the analysis of X-SAR VV-polarized data is discussed. The analysis of polarimetric SIR-C data in C-band and L-band together with single polarization X-SAR data is in progress [71], but will not be considered here.

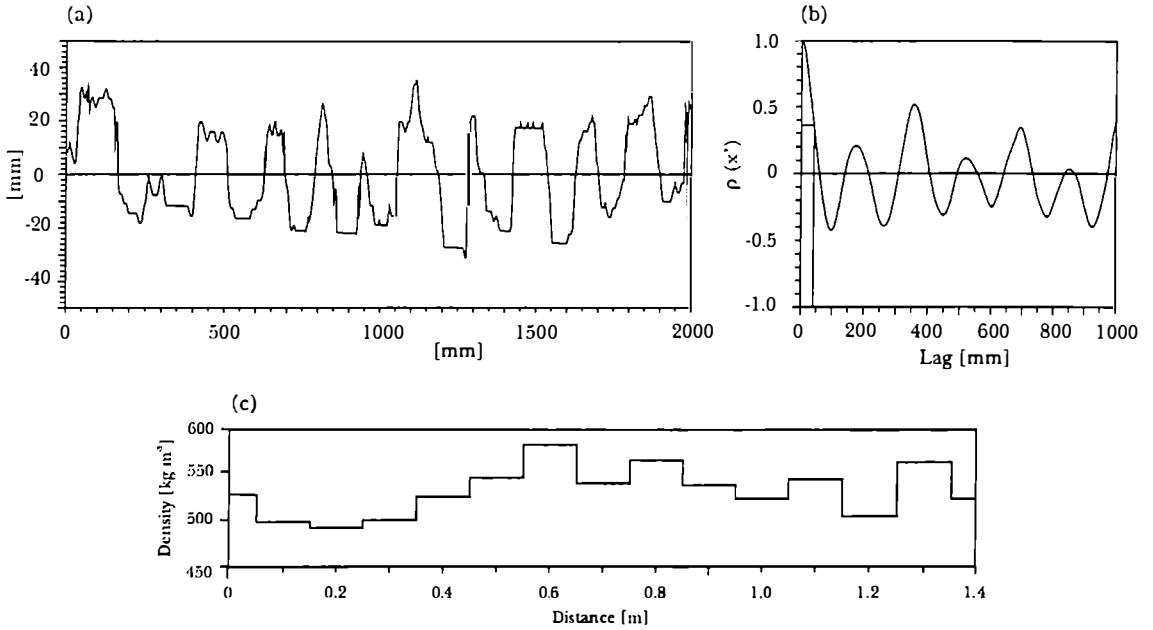


Figure 7.16: Characteristic parameters of the roughness testfield at Kesselwandferner: surface height (a), autocorrelation function (b), horizontal density profile in 10 cm depth (c).

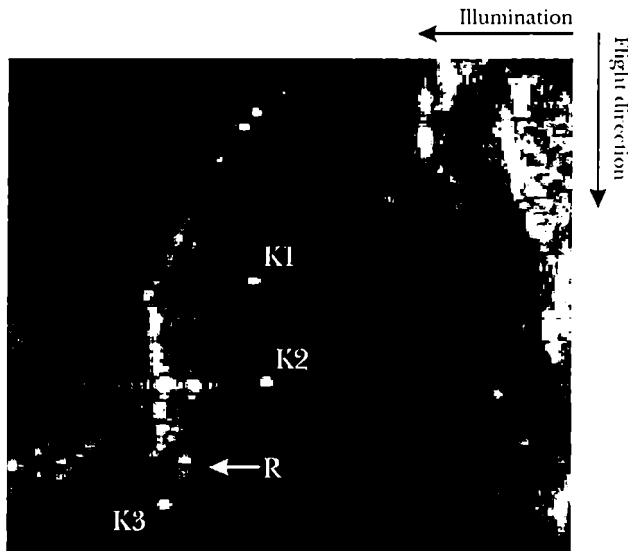


Figure 7.17: ERS-1 PRI image, 6 July 1992, descending orbit of KWF. K1, K2, K3 are corner reflectors, the roughness test field R is marked by the arrow. Illumination is from the right, flight direction from the top to the bottom.

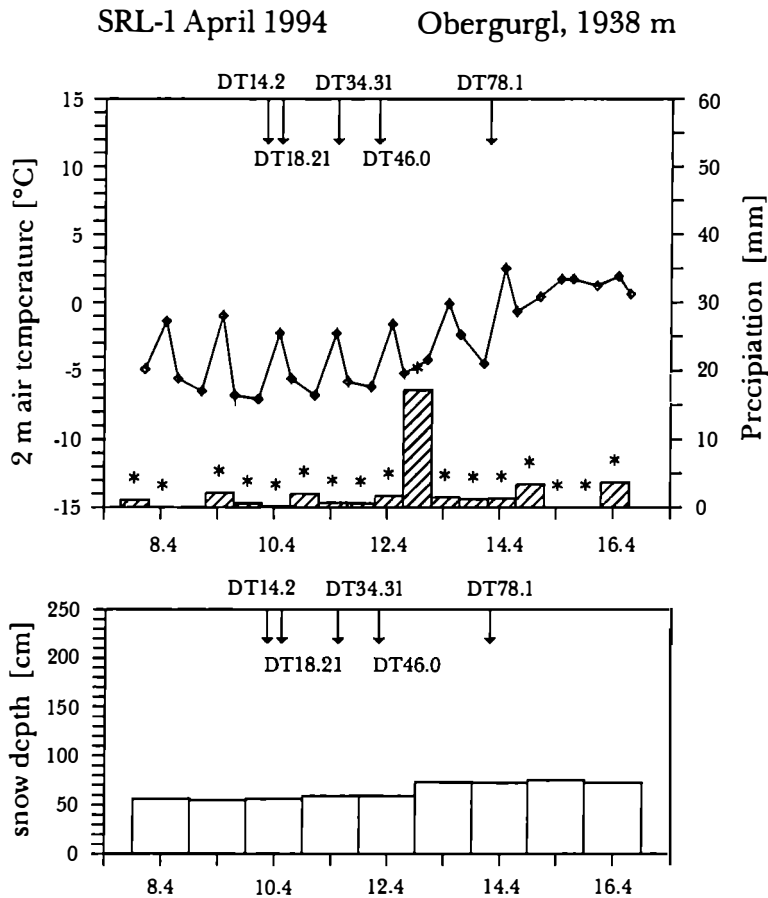


Figure 7.18: Meteorological parameters measured at Obergurgl, Ötztal during the SRL-1 campaign in April 1994: *... precipitation as snow.

7.2.1 Field measurements during SRL-1 and SRL-2

During the SRL overflights in April and October 1994 field measurements were made on HEF and KWF/GEF. The meteorological conditions during SRL-1 and SRL-2 at the station Obergurgl, about 30 km from the glaciers at 1938 m altitude, are shown in figure 7.18. During the SIR-C/X-SAR flight in April typical winter conditions were observed on the glaciers, with air temperatures below -10°C throughout the campaign. The ice and firn areas on the glaciers were covered by 2 m to 3 m of fine grained, dry snow. With a mean density of the snow pack of 326 kgm^{-3} on HEF and 295 kgm^{-3} on KWF, ϵ' at 9.6 GHz was 1.586 and 1.520 respectively, and the power penetration depth was several meters. Due to several snow fall events during the campaign the surface was covered by fresh snow.

Snow conditions on the glaciers during the SRL-2 campaign in October were quite complex. After heavy snowfall in mid September the glaciers were covered with a fresh snow pack. Until the end of September the snow melted and disappeared at altitudes below 3000 m. On 30 September the glacier plateau of KWF / GEF was covered by wet snow. During the SRL-2 campaign the temperature decreased significantly (figure 7.19). At 3000 m the temperature dropped below the freezing point in the evening of 2 October. In the morning of 3 October the top layer of the snow pack was frozen. The old firn below that layer was humid with large grains of up to 3 mm diameter and pronounced ice layers. On 5 October during acquisition of data take 78.1 the temperature was -10°C

SRL-2 October 1994 Obergurgl, 1938 m

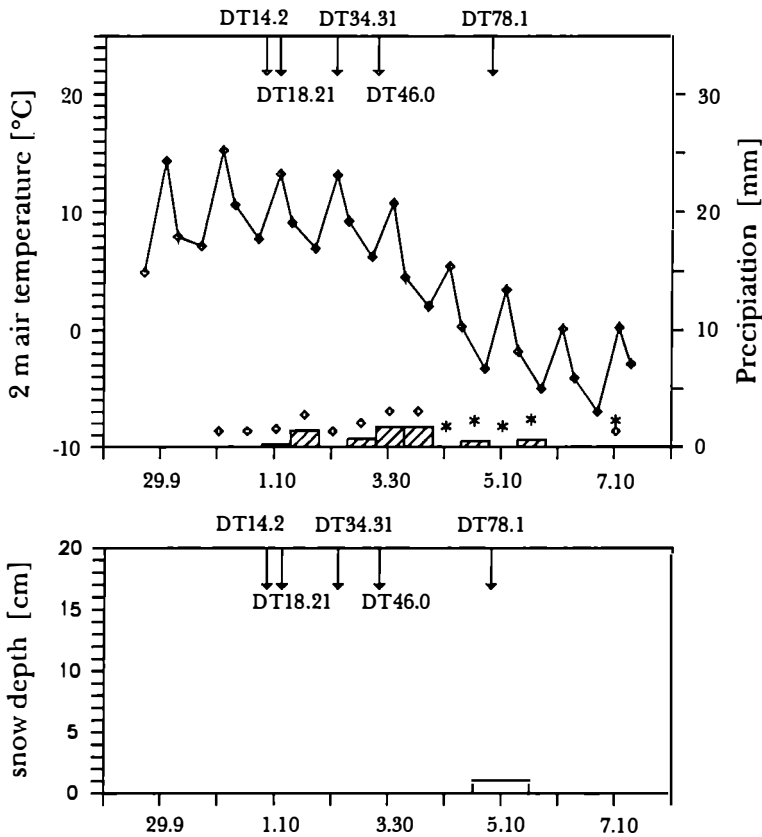


Figure 7.19: Meteorological parameters measured at Obergurgl, Ötztal during the SRL-2 campaign in October 1994: * ... precipitation as snow.◇...precipitation as rain.

at 3200 m at KWF. In table 7.6 and table 7.7 the snow properties measured on HEF and KWF / GEF are summarized, as well as the dielectric properties and the volume absorption coefficient κ_a of the top layer for 9.6 GHz (section 6.1). During the campaign several surface roughness measurements were made using the laser profile meter and a roughness plate. During the first 2 days of the campaign the mean standard deviation of $\sigma_h = 0.68$ cm ($k\sigma_h = 1.36$ for 9.6 GHz) and a median of the correlation length of $l = 10.9$ cm ($kl = 21.92$ for 9.6 GHz) were determined for smooth glacier ice in the upper part of the glacier; the corresponding values for snow and firn were 0.61 cm ($k\sigma_h = 1.22$ for 9.6 GHz) and 9.0 cm ($kl = 18.09$ for 9.6 GHz). According to the Fraunhofer criterion a surface is smooth at X-Band (9.6 GHz, incidence angle 30°), if the relation for the height standard deviation $\sigma_h < 0.13$ cm is valid.

7.2.2 Incidence angle dependence of backscattering in the X-band

The incidence angle dependences of σ^0 were derived for DT 46.10, 12 April 1994, at typical winter conditions when the surfaces were covered by more than 2 m of snow, and from DT 46.0, 3 October 1994, with typical conditions at the end of the ablation period. The shuttle overflight during both missions was in the morning at about 7 h MET (MET=UTC+1h). For the determination of the incidence angle dependence for different targets the same surface masks were used as for the analysis of 1992 ERS-1 data (figure

Site	HEF 2900 m			KWF 3200 m		
Date/Time	10.4.94 15:00 MET			10.4.94 18:00 MET		
d_s [cm]	320			261		
Depth	ρ_s	T_s	GS	ρ_s	T_s	GS
	[kgm^{-3}]	[$^{\circ}C$]	[mm]	[kgm^{-3}]	[$^{\circ}C$]	[mm]
0-20	193	-4.4	0.5	116	-11.5	0.2
21-100	350	-7.1	1.0	320	-13.8	0.5
101- d_s	435	-5.1	1.5	448	-11.7	1.0

Table 7.6: Snow properties measured on HEF and KWF during SRL-1: total snow depth on ice or firn (d_s), mean snow density (ρ_s), mean snow temperature (T_s), mean grain size (GS).

Site		KWF	GEF	KWF	HEF
Date		1.10.94	2.10.94	3.10.94	6.10.94
Time	[MET]	14:00	13:00	14:00	09:15
Altitude	[m]	3220	3270	3280	3200
d_s	[cm]	135	196	231	279
Fresh snow	[cm]	0	0	0	2
ρ_s (0 – 20cm)	[kgm^{-3}]	433	408	435	462
ρ_s (20 – d_s cm)	[kgm^{-3}]	528	532	551	496
GS (0 – 20cm)	[mm]	1-2	1	2	1
GS (20 – d_s cm)	[mm]	2-3	1-4	2-4	—
V_w (5cm)	[%vol]	4	3	1.5	0
ϵ' (5cm)		2.34	2.17	2.05	1.93
ϵ'' (5cm)		0.460	0.345	0.173	$3 \cdot 10^{-4}$
κ_a (5cm)	[m^{-1}]	60.38	47.103	24.23	0.043 *

Table 7.7: Snow properties measured on HEF, KWF and GEF during SRL-2: total snow depth on ice or firn (d_s), mean density (ρ) for two layers, mean snow temperature (T_s), mean grain size (GS) for two layers, snow liquid water content (V_w) at 5 cm depth, real and imaginary part of the dielectric constant and the volume absorption coefficient. *...wet snow below 30 cm .

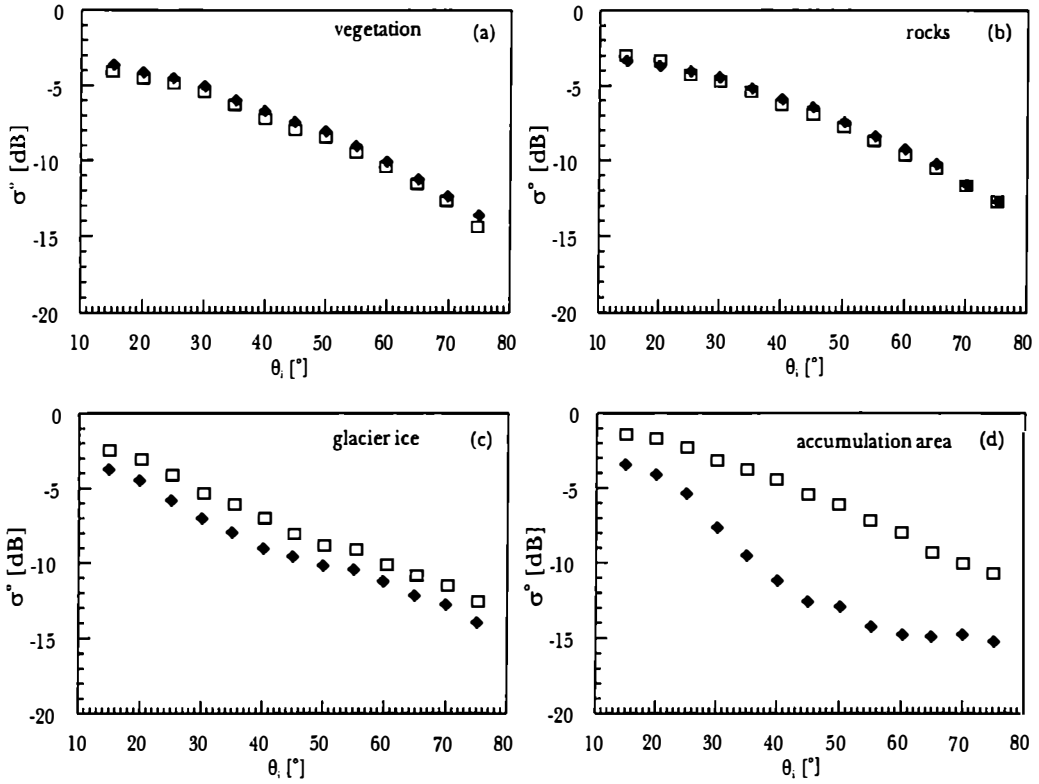


Figure 7.20: Incidence angle dependence of σ^o for different targets derived from SRL-1, data take 46.1, 10 April 1994, 7:34 MET (\square) and SRL-2 data take 14.2, 1 October 1994, 7:43 MET (\blacklozenge).

7.9). The classes vegetation and rocks are represented well by this mask. But the extent of the snow, firn and glacier ice was different than in August 1992, when the Landsat TM image of the masks was acquired. Therefore the firn class was not investigated. The snow (accumulation area) and the glacier ice masks were locally verified with field observation. Figure 7.20 a to d) shows the θ_i -dependence of σ^o for the classes vegetation, rocks, glacier ice and accumulation area. Vegetation and rocks show a pronounced decrease from -3 to -4 dB at $\theta_i = 15^\circ$ to -14 dB to -16 dB at $\theta_i = 80^\circ$. These σ^o values were up to 6 dB higher than those measured by a ground based scatterometer system over a comparatively smooth alpine soil with low grass during SRL-2 campaign [53]. For glacier ice only small differences between April and October were observed. In April the main backscattering occurred at the boundary between glacier ice and the winter snow pack, in October between glacier ice and air. The accumulation area shows a pronounced difference between April and October and a clear dependence on the local incidence angle (figure 7.20 d). The σ^o values decreased from -1 dB to -4 dB at $\theta_i = 15^\circ$ to -11 dB to -15 dB at $\theta_i = 80^\circ$. In April the scattering from the refrozen firn below the winter snow pack contributed significantly to the total backscattering coefficient, which was up to 7 dB higher than in October, when backscattering occurred mainly on the surface and in the top layer of the wet snow pack [48]. The θ_i dependence of σ^o of different surface targets is described by the polynomial fit given in eq. 7.1 with $\theta_{i,ref} = 50^\circ$. The corresponding coefficients are given in table 7.8.

7.2.3 Short term backscatter variations

During the SRL-2 mission in October 1994 the surface properties, especially on the glaciers changed significantly as described in section 7.2.1. To monitor short term variations of σ^o

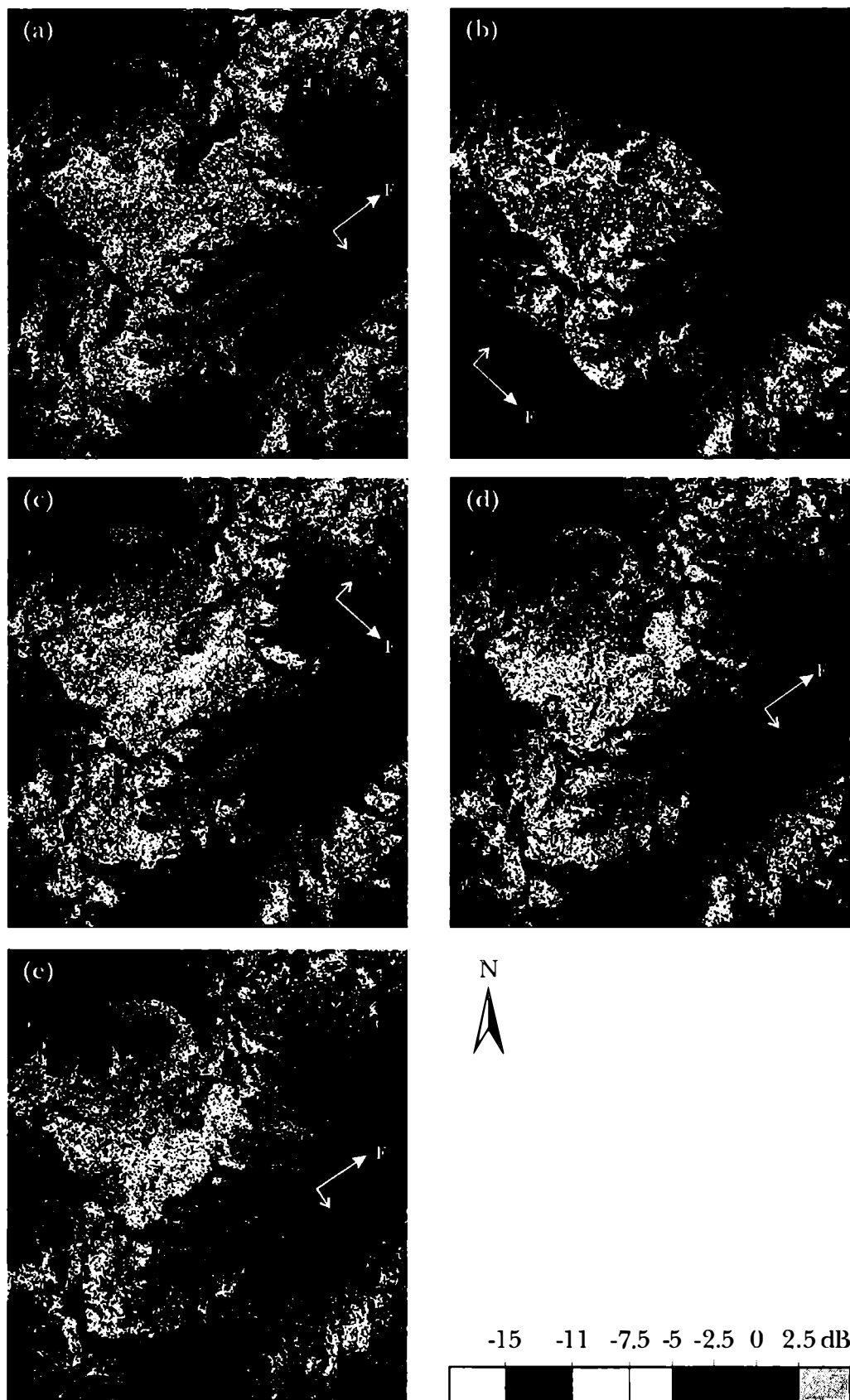


Figure 7.21: Difference of σ° in dB between the corresponding data takes of SRL-1 in April 1994 and SRL-2 in October 1994. Date and time of SRL-2 passes: (a) DT 14.2, 1 October 1994, 7:43 MET, (b) DT 18.21, 1 October 1994, 13:53 MET, (c) DT 34.31, 2 October 1994, 13:32 MET, (d) DT 46.0, 3 October 1994, 7:02 MET, (e) DT 78.1, 5 October 1994, 6:23 MET.

Date	d_f	d_s	V_w	$\rho_{s,10}$	$\rho_{s,40}$	T_s	GS	σ_h	l_{med}
	[cm]	[cm]	[% ^{vol}]	[kgm ⁻³]	[kgm ⁻³]	[°C]	[mm]	[cm]	[cm]
14.09.92	0	sf	—	—	—	—	—	—	—
19.10.92	0	sf	—	—	—	—	—	—	—
28.12.92	3	30	0	250	280	-17.0	0.5-1	0.23	1.9
13.01.93	4	16	1	364	338	-3.9	0.3-2	0.50	7.8
1.02.93	6	25	0	180	250	-6.0	0.5-1.5	0.11	—
17.02.93	—	24	0	228	354	-5.8	0.2-1	0.11	10.6
5.03.93	4	42	0	234	306	-7.0	< 0.2	sm	—
8.03.93	—	80	0	084	246	-7.2	< 0.4	sm	—
9.04.93	—	27	5-7	366	366	0.0	1-2	0.25	17.4
12.04.92	0	psc	—	—	—	—	—	—	—

Table 7.10: Snow properties measured at the test site Leutasch during ERS-1 SAR image acquisitions: depth of frozen ground (d_f), snow depth (d_s , sf...snow free, psc...patchy snow cover), snow liquid water content (V_w), snow density ($\rho_{s,10}$, $\rho_{s,40}$) of layer 0-10 cm and 15-40 cm depth, standard deviation of surface roughness (σ_h , sm...smooth), median of correlation length (l_{med}), snow temperature at 10 cm snow depth (T_s), mean grain size of the top layer of 10 cm thickness (GS).

refreezing of the firn and snow areas proceeded and on 5 October, 6:28 MET at DT 78.1 (figure 7.21 e) typical $\Delta\sigma^o$ values between -10 dB and -2.5 dB are observed. For glacier ice $\Delta\sigma^o$ was significantly higher than for snow and ice areas; typical values were between -5 dB and 0 dB, while in some parts $\Delta\sigma^o$ drops to -7.5 dB.

7.3 Investigations at Leutasch/Innsbruck

7.3.1 Field measurements

Field measurements in the Leutasch-Innsbruck area were made during 9 ERS-1 SAR image acquisitions, between December 1992 and April 1993. During ERS-1 passes a wide range of surface and snow cover conditions were observed on the Leutasch plateau at 1200 m, which include snow free conditions in October, dry snow conditions with up to a maximum snow depth of 0.8 m in February and March, and wet snow with crusts, ice lenses, and a water ice layer above the ground in April. Properties of the snow pack, of the underlying ground and the surface roughness were measured. Table 7.10 gives an overview of typical values of various parameters observed for snow on a cultivated meadow at Leutasch plateau.

In the Inn valley, at 600 m elevation, the surface conditions were more complex showing a higher temporal variation. Table 7.11 summarizes some of the measured parameters. The conditions range from snow free with unfrozen (with different soil moisture contents) or frozen ground to thin wet snow cover of some centimeters. In October the total area was snow free: due to some rain the night before the ground was slightly wet. The fields had been harvested and the meadows had only short grass. In December the top centimeters of the ground were frozen. Between Innsbruck and Zirl the agricultural fields were covered by a thin snow pack, whereas most meadows were snow free. In the upper Inn valley between Zirl and Telfs only some snow patches were found. During the first two weeks in January 1993 the weather was sunny with warm temperatures up to 14°C. On 13 January during the overflight it was raining, and the upper soil layer was wet; in some agricultural fields even small puddles were formed. During this overflight some surface roughness measurements were carried out on relatively smooth fields and meadows near Zirl (figure 7.23). The mean standard deviation of σ_h for these fields was between 0.8 cm



Figure 7.22: Multitemporal repeat pass ERS-1 image of track 437, frame 2655 of 19 October 1992 (red), 9 March 1993 (green), 12 April 1993 (blue). Sites used for signature analysis are marked by F1, F2, M1, M2, C1. At the top of the figure the variation the local incidence angle θ_i along the direction of radar illumination on a flat area is specified.

Date	d_s	V_w	d_f	G	T_g	T_{2m}	R	R_t
	[cm]		[cm]		[°C]	[°C]	[mm]	
14 Sep 92	0	—	0	—	—	16.7	0.1	○
19 Oct 92	0	—	0	—	—	1.7	2.5	○
28 Dec 92	0-4	0	0-10	f	-2.8	-3.4	0	
13 Jan 93	0	0	0	w	0.6	3.8	0.5	○
1 Feb 93	0	0	0-3	f	-0.4	-1.5	0	
17 Feb 93	1-2	wet	0-7	f	-0.8	-0.5	0.1	*
5 Mar 93	10	—	> 1	w	-	-3.4	0.1	*
8 Mar 93	12	wet	> 3	w	-0.6	-0.3	7.6	*
9 Apr 93	0	—	0	w	-	9.2	0.7	○
12 Apr 93	0	—	0	—	-	8.0	2.2	○

Table 7.11: Snow properties in the Inn valley during ERS-1 SAR image acquisitions: snow depth (d_s), snow wetness (V_w), freezing depth of ground (d_f), ground surface condition (G , f...frozen, w...wet) ground temperature at 5 to 10 cm depth (T_g), air temperature at 2 m at time of ERS-1 pass (T_{2m}), precipitation of the last 24 h measured at 7 h (R) fallen as snow (*) or rain (○). All parameters were measured on agricultural fields between Innsbruck and Telfs, except T_{2m} and R , which were recorded at the meteorological station of the University Innsbruck.

	1992			1993						
Date	14.9	19.10	28.12	13.1	1.2	17.2	5.3	8.3	9.4	12.4
MET	11:07	11:07	11:07	11:05	11:07	11:05	22:22	11:08	22:22	11:08
θ_i [°]	21.3	21.3	21.3	25.1	21.3	25.1	20.7	21.3	20.7	21.3

Table 7.12: ERS-1 images used for investigations in Leutasch / Seefeld - Inn valley test area. θ_i is the incidence angle on a horizontal surface in the center of the matched images.

and 1.69 cm (mean 1.17 cm) and the correlation length was between 8.8 cm and 14.3 cm; for meadows σ_h -values between 0.6 cm and 0.8 cm (mean 0.7 cm) and l -values between 1.2 and 1.8 cm were measured. The soil moisture content was 35 % at a meadow in the upper Inn valley near Telfs. On 1 February the top centimeters of the snow free ground were frozen. On 17 February. 5 and 8 March a continuous snow cover was found in the Inn valley near Innsbruck. On 8 March the snow pack was still about 12 cm thick, with a frozen crust at the top and wet snow below. The grain size was 1-2 mm with clusters of grains up to 4 mm diameter. The underlying ground was slightly wet. Due to melting and raining at the end of March the soil near Innsbruck was snow free and wet during the ERS-1 passes in April.

7.3.2 Temporal variations of backscattering

Repeat pass ERS-1 images of phase-C (35 days cycle) of the test site are available from 3 tracks. two descending passes with image acquisition at 11:08 and 11:05 MET and one ascending pass with acquisition at 22:22 MET (table 3.3). The descending passes of track 437 and 165 differ in east-west direction by about 52 km. This causes a difference in local incidence angle on the flat earth surface over the test areas of about 4°. The matching accuracy at the center of the extracted areas of 1500 x 1500 pixel² of corresponding repeat pass scenes is less than 1 pixel. Table 7.12 gives the time of acquisition and θ_i for the center of the matched images for each scene. Because of the unavailability of a DEM the images were calibrated assuming an ellipsoidal earth without any topography, which limits the investigations to flat areas where accurate σ^o -values can be derived.

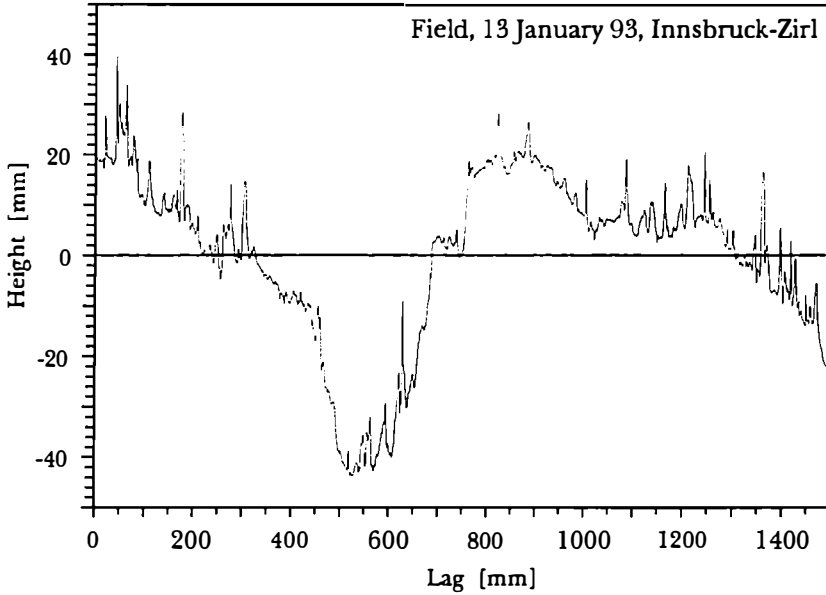


Figure 7.23: Surface roughness profile of an unploughed agricultural field between Innsbruck and Zirl measured by a laser profile meter on 13 January 1993.

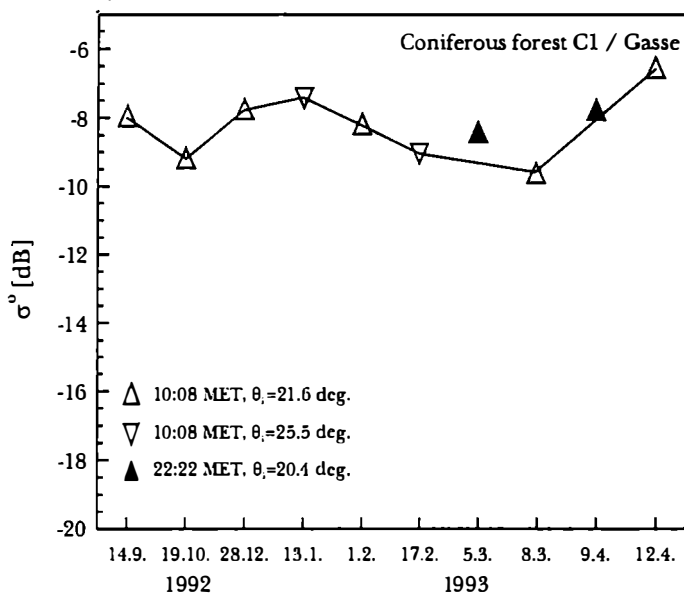


Figure 7.24: Temporal variation of σ^o (C-band, ERS-PRI) of an approximately horizontal area of coniferous forest near Gasse. Leutasch.

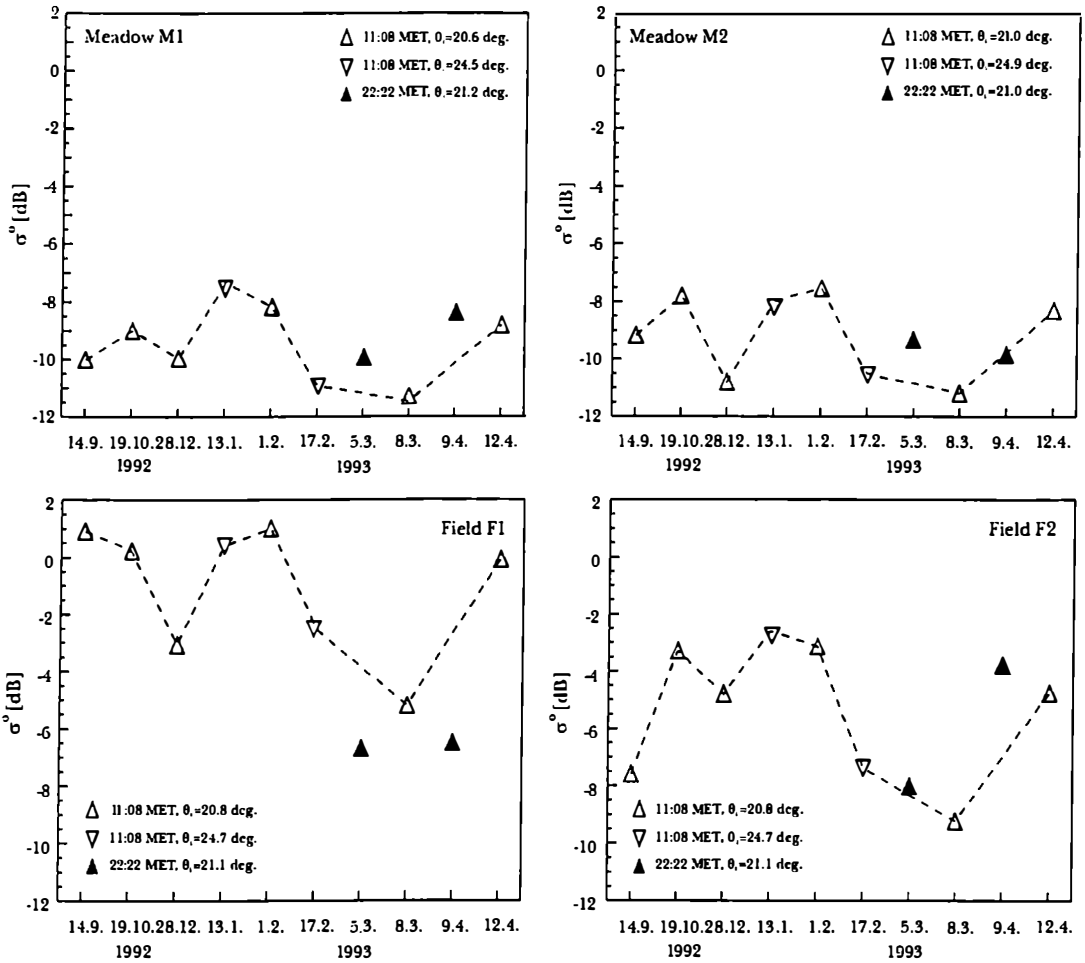


Figure 7.25: Backscattering coefficient σ^0 derived from ERS-1 SAR data for agricultural fields (F1, F2) and cultivated meadows (M1, M2). Different symbols indicate different incidence angles on the target.

Figure 7.22 shows a multi-temporal color composite of ERS-1 images of the area Leutasch / Seefeld and the Inn valley between Innsbruck and Telfs. Changes in radar cross section between 19 October 1992 (red), 9 March 1993 (green) and 12 April 1993 (blue) appear as different colors. The temporal variation of σ^0 can be seen very well in the Inn valley and on the meadows near the village Gasse, Leutasch. The coniferous forest on the slopes in the north and south of the Inn valley shows only minor variations in backscattering of less than 3 dB. Figure 7.24 shows the temporal variation of σ^0 determined for a horizontal area of coniferous forest at Leutasch (target C1 in figure 7.22). In the Inn valley fields and meadows, which show different surface properties (section 7.3.1), are next to each other. They can be easily discriminated in the multi-temporal image based on brightness and color. Different sites were selected for a quantitative analysis. The temporal behaviour of σ^0 of selected sites in the Inn valley is presented in figure 7.25. The locations of the fields F1 and F2 and meadows M1 and M2 are marked in figure 7.22. Agricultural fields (without plants) are in general rougher than cultivated meadows (with only short grass). Some fields were ploughed; if tracks are about normal to the range direction of the SAR images, the backscattering can increase significantly. An example of this effect is field F1, which shows very high σ^0 values (for snow free or dry snow conditions) in the day images.

The temporal variation of σ^0 over bare soil can be due to changes in soil liquid water

f [GHz]	wet ($V_w=38\%$)			frozen ¹ ($V_w = 5\%$)		
	ϵ'	ϵ''	d_p [cm]	ϵ'	ϵ''	d_p [cm]
4.6	21.0	7.4	0.7	3.9	0.5	3.8
7.2	17.8	9.1	0.3	3.7	0.6	2.0

Table 7.13: Dielectric constant and penetration depth for intensity d_p at two frequencies f for frozen and wet bare soil with liquid water content V_w , texture of 37% sand, 45% silt, 18% clay and density of 1.19 gcm^{-3} ; ¹...for $T < 0 \text{ }^\circ\text{C}$ (from Wegmüller, [94]).

content, due to freezing of the top layer and changes in surface roughness as well as due to the coverage by snow. An example of the dielectric constant and penetration depth for bare soil measured by [94] is given in table 7.13. Wegmüller [94] determined a difference of σ° of 3 dB between frozen and unfrozen, wet soil conditions at 7.1 GHz and 20° to 30° incidence angle. Due to the C-band d_p only the properties of the top layer are important for backscattering. This means that a wet layer below the frozen top centimeters has no effect on σ° .

For the test areas in the Inn valley a general decrease of σ° was observed from 19 October, with a unfrozen slightly wet surface, to 28 December, with a frozen ground and a thin snow cover of several centimeters. The drop of σ° was due to freezing of the ground, because the thin dry snow cover had no effect at C-band. With unfrozen soil on 13 January and 1 February σ° was higher by 2 to 3 dB. On 17 February and 8 March σ° had the lowest values, due to the presence of a wet snow cover in the Inn valley (table 7.11). The sites $M1$ and $M2$ show a decrease of σ° of about 3 dB, $F1$ and $F2$ of about 6 dB. The stronger decrease for fields may be due to the reduction of surface roughness by wet snow. During the ascending overflight on 5 March at 22:22 MET the backscattering coefficient of meadows was slightly higher. This may be an effect of refreezing of the wet snow pack, which becomes more transparent and the contribution of backscattering from snow ground boundary increases. The lower σ° on 5 March and 9 April observed for field $F1$ may be due to the change in the angle between the plough-tracks and incident radar beam.

The temporal behaviour of σ° of the site $M3$ near Gasse on the Leutasch/Seefeld plateau is shown in figure 7.26. The highest σ° values were observed for the snow free site, a cultivated meadow with short grass, in October, when the ground was wet. When the site was covered by dry snow in December σ° had about the same value as during dry soil conditions in September. During the winter season with dry or refrozen snow and frozen top layer of the ground σ° shows only small variations (1 and 17 February, 5 and 8 March). On 13 January with slightly wet snow of 1 %^{vol} σ° decreased by about 2 dB. According to theory the increased depth of dry snow on 8 March was not detectable by means of σ° . There is no relation between the water equivalent and σ° , even if only the dry snow cases are considered. The lowest σ° of -18.5 dB was observed in the night overflight on 9 April with very wet snow cover of 5 %^{vol} to 7 %^{vol} liquid water. Based on the measured snow parameters $\epsilon_r = 2.61 - i0.47$, $k\sigma_h = 0.3$, $kl = 1.88$ (table 7.10), the single surface scattering IEM model (with exponential correlation function) predicts a value of $\sigma^\circ(20^\circ) = -15.2 \text{ dB}$, which is 3.2 dB higher than the ERS-1 based σ° . The decrease in backscattering of wet snow of 7 dB appears as a clear signal in multi-temporal SAR images. When the snow cover became patchy, σ° increased on 12 April.

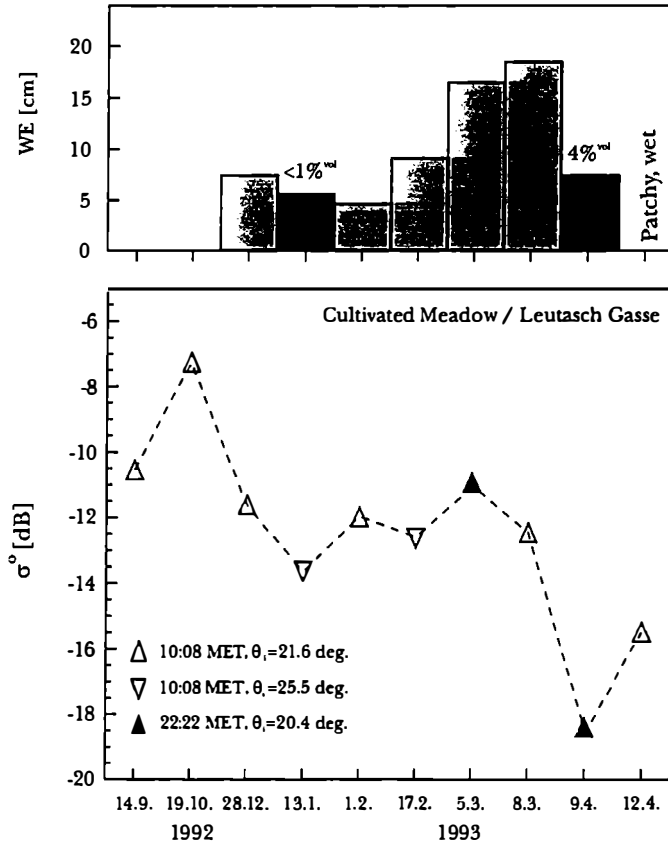


Figure 7.26: Upper figure: water equivalent of the snow pack on a cultivated meadow near Gasse, Leutasch: light grey ... dry snow, dark grey ... wet snow, numbers specify the liquid water content V_w . Lower figure: backscattering coefficient σ^0 derived from ERS-1 SAR data; different symbols indicate different incidence angles of the radar beam.

Chapter 8

SAR image statistics and filtering

In this chapter principles and methods of SAR image analysis are described, which were taken into account for the development of the snow classification procedure. The SAR image statistics and the estimation of statistical parameters from SAR images are presented in section 8.1 and section 8.2, respectively. The detection of changes in backscattering between two SAR images of different dates and the classification of targets by means of these changes is presented in section 8.3. In section 8.4 several filters for speckle reduction are tested on ERS-1 PRI images and their effect on the ratio of two images is investigated.

8.1 Rayleigh clutter model

8.1.1 Statistical properties of the scattered radiation

The Rayleigh clutter model [91] (also called the physical model [54]) can be used to describe the radar backscattering from distributed targets. Although it is not exact in terms of physical scattering mechanisms, it allows an analysis of the imaging process in good agreement with observed phenomena [54]. A short review of this model is useful for further discussions.

When incident waves are scattered by a random distribution of scatterers within a resolution cell (whose size is given by the imaging system) the observed electromagnetic field results from random interference of waves. The phases of backscattered waves from the individual scatterers are independent of the amplitude and are uniformly distributed between $-\pi$ and π . The total electromagnetic field \mathcal{E} is the sum of a large number of randomly phased contributions and is given by [54]

$$\mathcal{E} = \mathcal{E}_r + i\mathcal{E}_i = \sum_{k=1}^N a_k e^{i\psi_k} \quad (8.1)$$

where a_k and ψ_k are the amplitude and phase of the k^{th} scatterer and N is the number of scatterers. It is assumed that a_k is a randomly distributed variable which is uncorrelated for different scatterers. The summation on the right side of eq. 8.1 corresponds to a random walk of \mathcal{E}_r and \mathcal{E}_i in the complex plane. For a large number of scatterers it is expected that \mathcal{E}_r and \mathcal{E}_i are independent identically Gaussian distributed, each with a variance of $\frac{\sigma}{2}$ and zero mean. The statistical properties of the total field \mathcal{E} are then given

by

$$\begin{array}{ll}
 \text{probability density function} & p(|\mathcal{E}|) = \frac{2|\mathcal{E}|}{s} e^{-\frac{|\mathcal{E}|^2}{s}} \\
 \text{mean value} & \widehat{|\mathcal{E}|} = \sqrt{\frac{\pi}{4}} s \\
 \text{standard deviation} & s_{|\mathcal{E}|} = \sqrt{\left(1 - \frac{\pi}{4}\right) s}
 \end{array} \tag{8.2}$$

Eq. 8.2 is known as the Rayleigh distribution. It represents the distribution of the magnitude of the total scattered field at the receiving antenna prior to detection. Further it should be noted, that eq. 8.2 refers to this model including all assumptions made for the backscattering process and should not be confused with the statistical properties of the detected image [91]. All the information about the surface is given by s , which specifies the variance of the backscattered fields \mathcal{E}_r and \mathcal{E}_i .

The above model assumptions lead to a situation which is referred as fully developed speckle [7]. It is observed when many randomly distributed scatterers are within a resolution cell or when the surface is rough relative to the wavelength. This is the case for most natural targets imaged by ERS (C-band) and X-SAR (X-band). However, at P-band or at L-band some natural surfaces may appear smooth so that speckle will not be fully developed. This may be also the case for some man made targets at higher frequencies. Speckle will not be fully developed when a dominating scatterer, e.g. corner reflector, is present in a resolution cell. The field detected from such pixels can be modelled as the sum of contributions from scatterers, which on their own generate fully developed speckle, and a single constant phasor from the corner reflector. The resulting Rician statistics are significantly different from the statistics of natural targets [91] and will not be considered here.

In this work C-band and X-band images of primarily natural targets are analyzed. Therefore throughout the thesis it is assumed that speckle is fully developed and that the physical model is applicable.

8.1.2 Distribution of the detected intensity

At the receiver of the imaging system the amplitude or the intensity of the total backscattered field is detected. ERS-1 and SRL X-SAR use intensity detection, which means that the output voltage of the receiver is proportional to the intensity of the incoming field [16]: this is known as a square law detector [91]. The detected intensity $I = |\mathcal{E}|^2$ can be determined using $pdf(I)dI = pdf(|\mathcal{E}|)d\mathcal{E}$, which results in [7]

$$\begin{array}{ll}
 \text{probability density function} & p(I) = \frac{1}{I} e^{-\frac{I}{s}} \\
 \text{mean value} & \widehat{I} = s \\
 \text{standard deviation} & s_{\widehat{I}} = s \\
 \text{coefficient of variation} & v^2 = 1
 \end{array} \tag{8.3}$$

Eq. 8.3 represents a negative exponential distribution. After detection of the intensity (and multi-looking) the amplitude is often derived for storing images in 16 bit format and to reduce the image contrast. Sometimes the amplitude values are also preferred for analyzing the images instead of intensity values. The amplitude A is related to I by $A = \sqrt{I}$. It can be shown that A has a Rayleigh distribution, equivalent to that given

in eq. 8.2 for the incoming field. Using eq. 8.2 and 8.3 the mean value of the amplitude \widehat{A} and its standard variation s_A can be directly estimated from the mean intensity \widehat{I} by using

$$\begin{aligned} \text{mean value} \quad \widehat{A} &= \sqrt{\frac{\pi}{4}s} = \sqrt{\frac{\pi}{4}\widehat{I}} \simeq 0.886 \sqrt{\widehat{I}} \\ \text{standard deviation} \quad s_A &= \sqrt{\left(1 - \frac{\pi}{4}\right)s} = \sqrt{\left(1 - \frac{\pi}{4}\right)s_{\widehat{I}}} \end{aligned} \quad (8.4)$$

The distributions of the total field prior to detection \mathcal{E} (eq. 8.2), the detected intensity I (eq. 8.3) and the corresponding amplitude (eq. 8.4) depend on the same parameter, the variance s of the incoming field, which carries all the information about the surface. For single SAR images the phase of distributed targets provides no information about the scattering properties [7]. This results directly from the assumption of a uniform distributed phase in the physical model. Further it should be noticed that the exponential distribution is fully defined by its mean value. This has the advantage of low computational costs, because only one parameters is to be derived for characterization of a homogenous target.

8.2 Parameter estimation

A large proportion of image analysis involves estimating parameters within different regions of an image. These parameters supply the basis for local decision making. This is particularly the case for SAR images where the presence of speckle does not allow an image analysis on a pixel by pixel basis. The parameter most commonly required for image analysis is the local mean. For example, the local mean is required for signature analysis, where typical backscattering cross sections of homogeneous targets are determined. A simple estimate of the true mean is the arithmetic average over several samples.

8.2.1 Averaging of samples

For purposes of speckle reduction or for determination of the mean backscattering cross section of homogeneous areas image pixels have to be averaged. The total field characterizing the backscattering from the surface is given by the Rayleigh clutter model. To determine the mean of random samples the maximum likelihood estimator can be used. For statistically independent, Rayleigh distributed amplitude values $\mathcal{E}_1, \mathcal{E}_2, \dots, \mathcal{E}_n$, with unknown mean $\mu_{\mathcal{E}}$ the likelihood F is given by [7]

$$F(\mu_{\mathcal{E}}) = \prod_{i=1}^n \frac{\pi \mathcal{E}_i}{2\mu_{\mathcal{E}}} e^{-\frac{\pi \mathcal{E}_i^2}{4\mu_{\mathcal{E}}}} \quad (8.5)$$

Eq. 8.5 can be solved by calculating its log-likelihood $L(\mu_{\mathcal{E}}) = \ln F(\mu_{\mathcal{E}})$, which has the maximum at the same position as F . Hence the maximum likelihood estimate is found by solving the first derivative of L with respect to $\mu_{\mathcal{E}}$, which is given by

$$\frac{dL}{d\mu_{\mathcal{E}}} = \frac{2n}{\mu_{\mathcal{E}}^3} \left(\frac{\pi \widehat{\mathcal{E}}^2}{4} - \mu_{\mathcal{E}}^2 \right) \quad (8.6)$$

A maximum is reached when $\frac{dL}{d\mu_{\mathcal{E}}} = 0$, which is the case for $\mu_{\mathcal{E}} = \sqrt{\frac{\pi \widehat{\mathcal{E}}^2}{4}}$, where $\widehat{\mathcal{E}}^2$ is the average intensity. Therefore the maximum likelihood estimator is obtained by using the average intensity, rather than the average amplitude. If required the average amplitude is derived from the mean intensity by eq. 8.4.

Therefore in terms of estimating the mean value over homogeneous targets averaging is best carried out on intensity data.

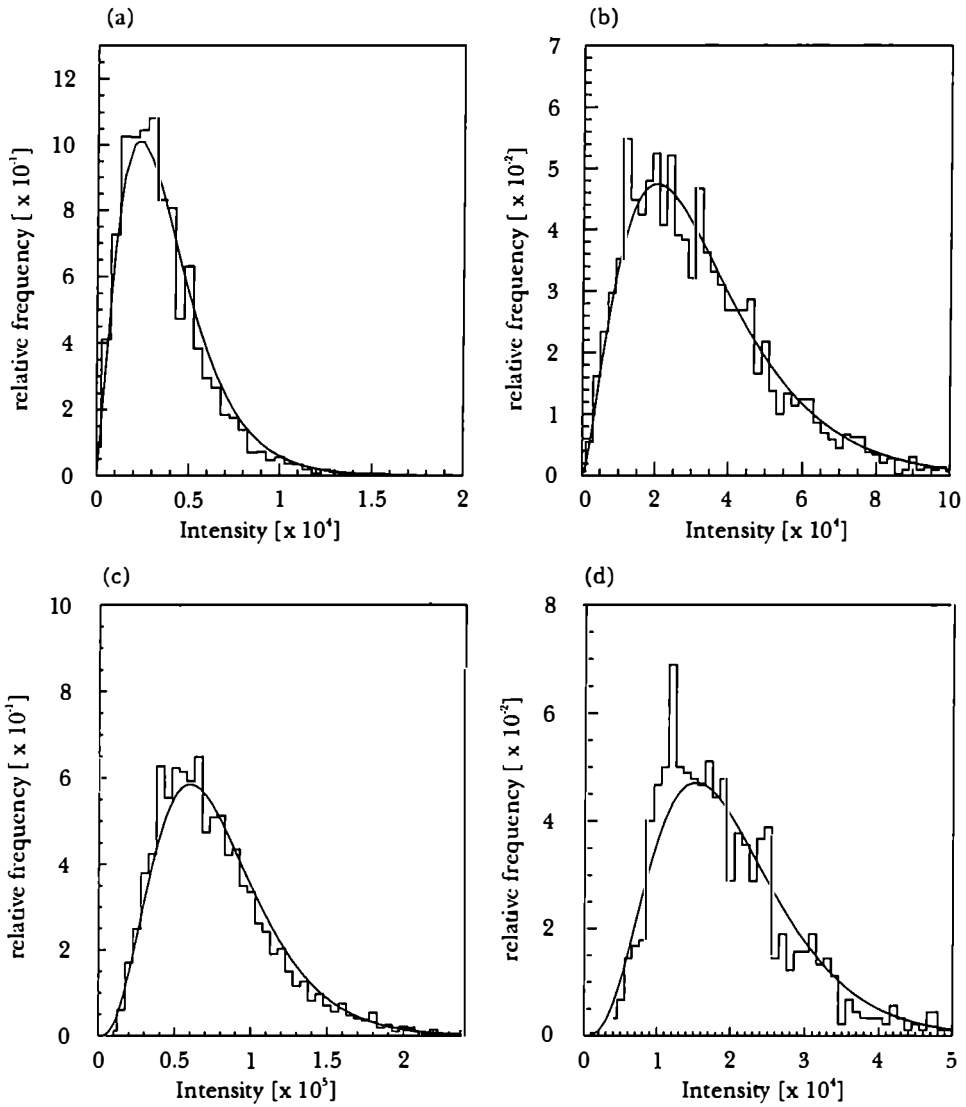


Figure 8.1: Histograms of the intensity and the expected gamma distribution for several sites: (a) snow area on the glacier plateau of Gepatschferner, 1 June 92, ERS-1 PRI ascending pass ($n \approx 3$), (b) rocks and moraines on backslope in the Rofental, 10 August 92, ERS-1 PRI ascending pass ($n \approx 3$): (c) snow area on plateau of Gepatschferner, 12 April 94, X-SAR MGD, DT 46.10 ($n = 4.2$), (d) low vegetation, X-SAR MGD, DT 46.00. ($n = 4.2$).

8.2.2 Effect of multi-looking and averaging on distributions

Both, multi-looking and spatial averaging, have the same effect on the image statistics. Multi-look processing is applied during SAR image generation. In the case of ERS-1 PRI images the azimuth bandwidth of 960 Hz is divided into 3 non-overlapping sub-bands, which are focussed into 3 independent images (looks); the individual looks are then summed incoherently to the final product. Spatial averaging of intensity values is applied after formation of the SAR image and can be applied by the user [7].

In general the distribution of averages of random variables with known distribution is most easily determined by using their characteristic functions Φ [7]. Assuming exponentially distributed intensity values the averaged intensities are gamma distributed with mean μ and order parameter n and can be represented by

$$\begin{aligned}
 \text{probability density function} \quad p_{\hat{I}}(x) &= \frac{x^{n-1} e^{-\frac{x\mu}{n}}}{\Gamma(n) \left(\frac{\mu}{n}\right)^n} \\
 \text{standard deviation} \quad s_{\hat{I}} &= \frac{\mu}{\sqrt{n}} \\
 \text{coefficient of variation} \quad v^2 &= \frac{1}{n}
 \end{aligned} \tag{8.7}$$

where $\Gamma(\cdot)$ is the gamma function. For $n = 1$ eq. 8.7 is equal to the negative exponential distribution given for single look intensity data, while for $n \rightarrow \infty$ the gamma distribution approximates a Gaussian distribution with mean μ and zero variance. Figure 8.1 shows the intensity distribution in ERS-1 PRI and X-SAR MGD images for different surface types. The image derived distributions agree comparatively well with the *pdf* from eq. 8.7, which confirms the model assumptions from section 8.1.1. The effect of averaging over n independent samples (or looks) is that the image contrast v (square root of the coefficient of variation) is reduced by a factor of \sqrt{n} , while the azimuth (or range) resolution is reduced by a factor of n [7].

8.2.3 Statistical sampling effects

This section addresses the derivation of parameters from SAR images (ERS-1 PRI, X-SAR MGD) and how accurately they can be estimated. In general the accuracy of any measurement is limited by the accuracies of the single measurements and by the number of independent samples. So far in section 8.2.1 it was assumed that the samples being averaged are statistically independent. This is in general the case for single look complex data [16]. But ERS-1 PRI and X-SAR MGD images, which are mainly used in this work, include azimuth resampling and slant to ground range projection into a uniform grid on the earth's surface of $12.5 \times 12.5 \text{ m}^2$ spacing [2]. Because one resolution element is larger than the grid spacing adjacent pixels in the final product are more or less correlated in azimuth and range direction. The correlation shows a weak range dependence, while it is independent of the azimuth position. Examples are given in figure 8.2 where the autocorrelation function in range and azimuth direction was derived from a homogeneous target in ERS-1 PRI and X-SAR MGD products. From figure 8.2 it becomes obvious that the correlation of adjacent pixels (in range and azimuth) has to be taken into account in the analysis of SAR images.

One of the most popular parameters in analyzing SAR images is the mean value of the radar cross section of a homogeneous target, which is derived from the mean intensity. For an area with m_r pixels in range and m_a pixels in the azimuth direction the estimated

mean from the intensity, \hat{I} , is given by

$$\hat{I}(x_r, x_a) = \frac{1}{m_r m_a} \sum_{i=0}^{m_r-1} \sum_{j=0}^{m_a-1} I(x_r + i, x_a + j) \quad (8.8)$$

If the intensity samples $I(\cdot)$ are identically distributed with mean μ and standard deviation σ_I , the expected value of \hat{I} is equal to μ , the true mean value of the population. Further it is assumed that the correlation of pixels in azimuth and range direction are independent from each other. Taking the correlation of neighbouring pixels into account the variance of \hat{I} is given by [7]

$$\sigma_{\hat{I}}^2 = \frac{\sigma_I^2}{m_{r_i} m_{a_i}} \quad (8.9)$$

with

$$m_{r_i} m_{a_i} = \frac{m_r m_a}{\sum_{|k_r| < m_r} \sum_{|k_a| < m_a} \left(1 - \frac{|k_r|}{m_r}\right) \left(1 - \frac{|k_a|}{m_a}\right) \rho_a(k_a) \rho_r(k_r)} = \frac{m_r m_a}{S} \quad (8.10)$$

where ρ_a and ρ_r are the normalized autocorrelation functions in azimuth and range respectively; m_r and m_a are the number of image pixels in azimuth and range, m_{r_i} and m_{a_i} correspond to the equivalent number of independent samples. The values k_a and k_r are the displacement in azimuth and range, respectively. The parameter $\sigma_{\hat{I}}^2$ in eq. 8.9 is also referred to as the standard error of the mean and gives an estimation how well the true mean μ is represented by the estimated value \hat{I} . If the pixels of a homogenous target are independent of each other, as it is the case for multi-looking without overlapping sub-bands, the relations $\rho_a = \rho_r = 1$ for $k_r = k_a = 0$, and $\rho_a = \rho_r = 0$ for $k_r \neq 0$, $k_a \neq 0$ are valid. For this case the standard error of mean (eq. 8.9 and eq. 8.10) reduces to the known relation $\sigma_{\hat{I}}^2 = \frac{\sigma_I^2}{m_r m_a}$.

Typical values for ERS-1 PRI images are $\rho_a(1) = 0.5$ and $\rho_r(1) = 0.65$ in near range and $\rho_r(1) = 0.55$ in far range [7]. These values are confirmed by figure 8.2 (a), observed at mid swath of the ERS-1 PRI image of 1 June 1992, ascending pass, of the test site Ötztal. For the data take 46.10, acquired during SRL-1 mission, the X-SAR MGD image shows a similar correlation in range direction but a higher correlation $\rho_a(1)$ in azimuth when compared with typical values for ERS-1 PRI products (figure 8.2 (a) and (b)). For both ERS-1 PRI and X-SAR MGD images the correlation is significant only at lag $k_x = 1$, $x = a, r$, and can be neglected for larger lags, where the magnitude of the correlation in both directions is less than 0.2 indicating independent samples [91]. For estimating the number of independent samples eq. 8.10 can be reduced to

$$m_{r_i} m_{a_i} \simeq \frac{m_r m_a}{1 + 2(\rho_a(1) + \rho_r(1) + \rho_a(1)\rho_r(1))} \quad (8.11)$$

This relation allows a quick estimation of the number of independent samples for a homogeneous area from oversampled images. On the other hand eq. 8.11 enables the estimation of the number of image pixels of a PRI or MGD product necessary to provide a reliable mean value of the radar cross section of a homogeneous target. This means that the estimated mean \hat{I} should be within a fraction f of the true mean value μ , which requires the validity of the condition $\sigma_{\hat{I}} < f\mu$. For n -look intensity data the mean and standard deviation are related by $\mu = \sigma\sqrt{n}$, which leads together with eq. 8.9 and eq. 8.10 to

$$m_r m_a > \frac{S}{f^2 n} \quad (8.12)$$

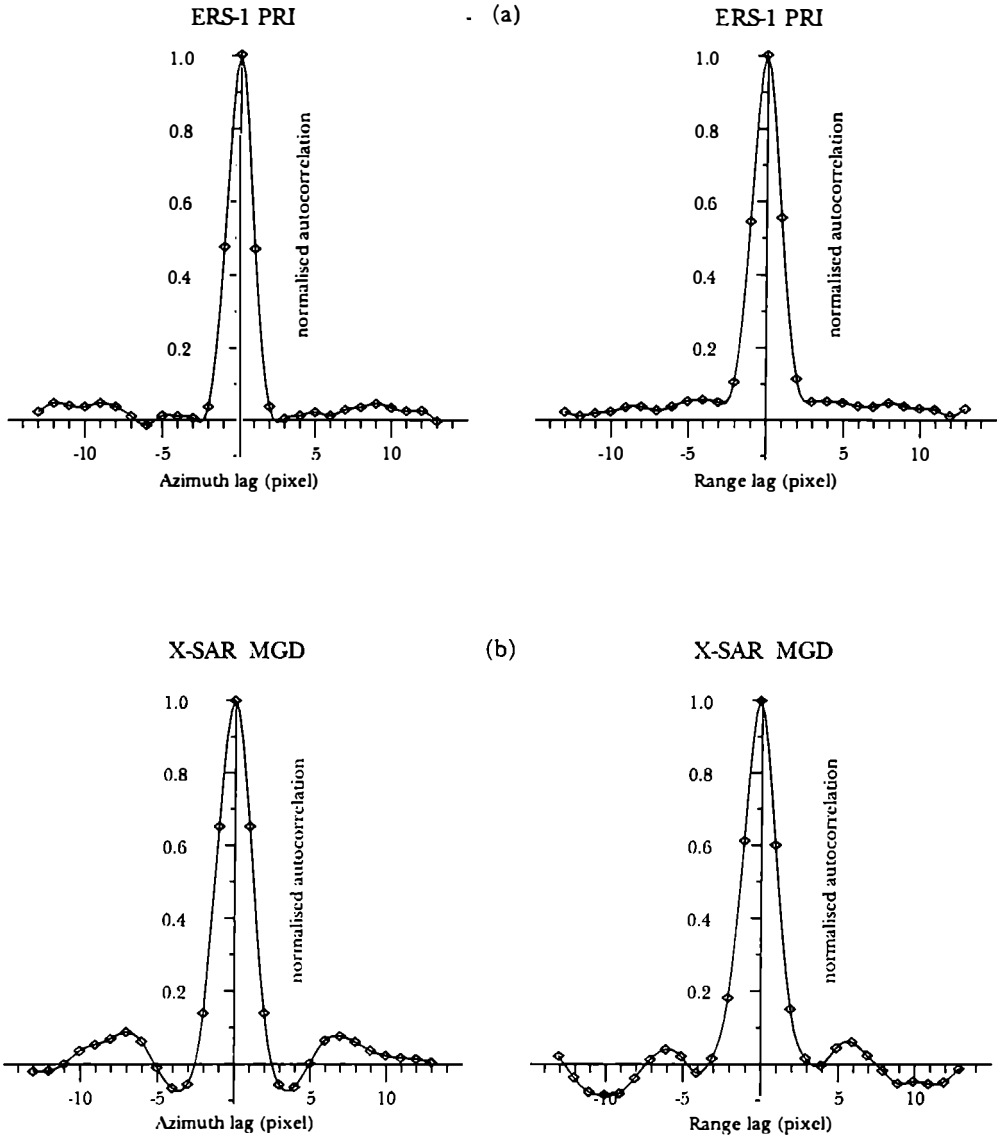


Figure 8.2: Intensity autocorrelation function measured within a homogeneous area on Gepatschferner: (a) ERS-1 PRI image (3 looks in azimuth, 1 look in range) orbit 4597, frame 927, test area in about midswath. (b) SRL-1 X-SAR MGD (3.5 looks in azimuth, 1.2 looks in range) DT 46.10.

For example, to determine σ^o of a homogeneous target from an ERS-1 PRI image with the requirement that the standard error of mean should not exceed 10%, about 34 pixels are required if uncorrelated data ($S = 1$) are assumed; taking the correlation values from figure 8.2 (a) with $\rho_a(1) \simeq 0.48$ and $\rho_r(1) \simeq 0.55$ into account, about 120 pixels are necessary to meet the same requirement, which are nearly 4 times as many pixels as in the uncorrelated case.

8.3 Change detection technique

One of the significant obstacles to analyzing SAR images for detecting changes in backscattering arises from the strong dependence of the image characteristics on the imaging geometry. This may be even worse in mountainous terrain with a large influence of the topography. Spaceborne sensors, like ERS-1, reveal a high stability of orbits. Therefore the look angles of repeat passes to the same target are reproduced within fractions of a degree. The use of two repeat pass images enables an elimination of the influence of the imaging geometry. Thus temporal changes in radar cross section between both images can be explained by changes of the backscattering process on the earth surface.

Orbital repeat pass SAR imaging is often associated with radar interferometry, which is based on phase coherence of two scenes. In terms of the physical scattering model of section 8.1 the speckle of these images will decorrelate if the relative location of the individual scatterers within a resolution cell changes during the period between the image acquisitions. But this temporal decorrelation of speckle is not necessarily accompanied with changes in the backscattering intensity and vice versa [93]. Both changes, the temporal decorrelation of speckle and changes in the mean backscattering, contain independent information about changes on the ground [60].

Although for interferometric analysis of repeat pass images the presence of speckle is crucial, this is not wanted for determination of temporal changes of the mean backscattering of two images. Therefore the following processing is applied:

- accurate coregistration of both images (pixel to subpixel scale)
- application of speckle reduction procedures (multi-looking, spatial averaging, speckle filtering)
- application of change detection procedure

In the following chapters it is assumed that the first two steps are applied. A review about digital change detection techniques applied to remotely sensed data is given in [83], although it concerns mainly optical images. For change detection in SAR images the differencing and ratioing method are usually used [93], [60]. In this section these methods are discussed from the statistical point of view and tested on ERS-1 PRI images. Furthermore the possibilities and limitations for discriminating targets with different change characteristics are analyzed.

In general change detection can be applied to amplitude or to intensity values of image pixels. In this work changes are detected in terms of the physical parameter σ^o which corresponds to the intensity value of an image pixel (see chapter 4).

8.3.1 Difference versus ratio images

The difference and ratio of gamma distributed multi-look SAR images (eq. 8.7) with intensities I_1 and I_2 were investigated for purposes of backscatter change detection by

[60], [93] and for purposes of edge detection by [88]. In ratioing, the changes of one image versus the other is derived by dividing the intensity values, conveniently expressed in dB. In differencing, changes in backscatter are measured by subtracting one image from the other. Because both methods are applied pixel by pixel the statistical properties of the resulting image generated by both methods were analyzed by [60], [93]. It was found that the ratio image should be preferred to the difference image (statistical distributions are given in [88] for the difference image and in section 8.3.2 for the ratio image):

- The difference between two images (image 1 and image 2) depends on the relative change of the mean intensities \hat{I}_1/\hat{I}_2 and on the mean intensities \hat{I}_1 and \hat{I}_2 themselves. Therefore the detection of changes depends on the strength of backscattering of a target; e.g. multiplying both images by the same factor the difference between the mean backscattering of an extended target increases by the same factor. This means, that errors in deriving σ^o (e.g. inaccuracies in the local incidence angle due to errors in the DEM, errors in antenna pattern correction due to wrong look angle on the target) become visible in the difference image. This is especially the case in mountainous terrain, where large differences in the backscattering area per resolution cell result from topography have to be corrected.
- The ratio depends only on the relative change of the mean intensity of one image compared to the other. Because errors in deriving σ^o are exactly reproduced in repeat pass images, they are eliminated during ratioing.
- The ratio method is very sensitive to speckle. Speckle, which is not seen in the original images, becomes visible in the ratio image. This effect can be reduced by increasing the number of independent looks.

8.3.2 Statistics of the ratio image

The multi-look SAR intensities of the images I_1 and I_2 are assumed to be gamma distributed according to eq. 8.7. Further it is assumed that the intensities of homogeneous regions of both images are statistically independent, which is valid for uncorrelated speckle [93]. The *pdf* of the ratio $r = \frac{I_1}{I_2}$ for distributed targets is then given by Touzi *et al.* [88]

$$\begin{aligned}
 \text{probability density function} \quad p_r(r) &= \frac{\Gamma(2n)r^{n-1}\bar{r}^n}{\Gamma(n)^2(r+\bar{r})^{2n}} \\
 \text{mean value} \quad \hat{r} &= \frac{n}{n-1}\bar{r} \\
 \text{standard deviation} \quad s_r &= \frac{n(2n-1)\bar{r}}{(n-1)^2(n-2)}
 \end{aligned} \tag{8.13}$$

where $\bar{r} = \frac{\hat{I}_1}{\hat{I}_2}$ and \hat{I} is the local mean of the image from date 1 and 2 respectively. The parameter \bar{r} represents the change of mean backscattering σ^o of a homogeneous target between two dates and will be also referred as $\Delta\sigma^o$. The theoretical *pdf* of the ratio image predicts rather well the observed distributions, determined from homogeneous targets in repeat pass ERS-1 PRI images, as shown in figure 8.3. The examples are typical for the high alpine targets observed in the test site Ötztal. The range of \bar{r} is from -13 dB for wet snow to more than +2 dB for snow free areas and rough glacier ice.

8.3.3 Discrimination of changes based on the ratio method

A problem for discriminating targets with different mean backscattering changes \bar{r} is the significant influence of speckle on the ratio of two images. This becomes visible from the

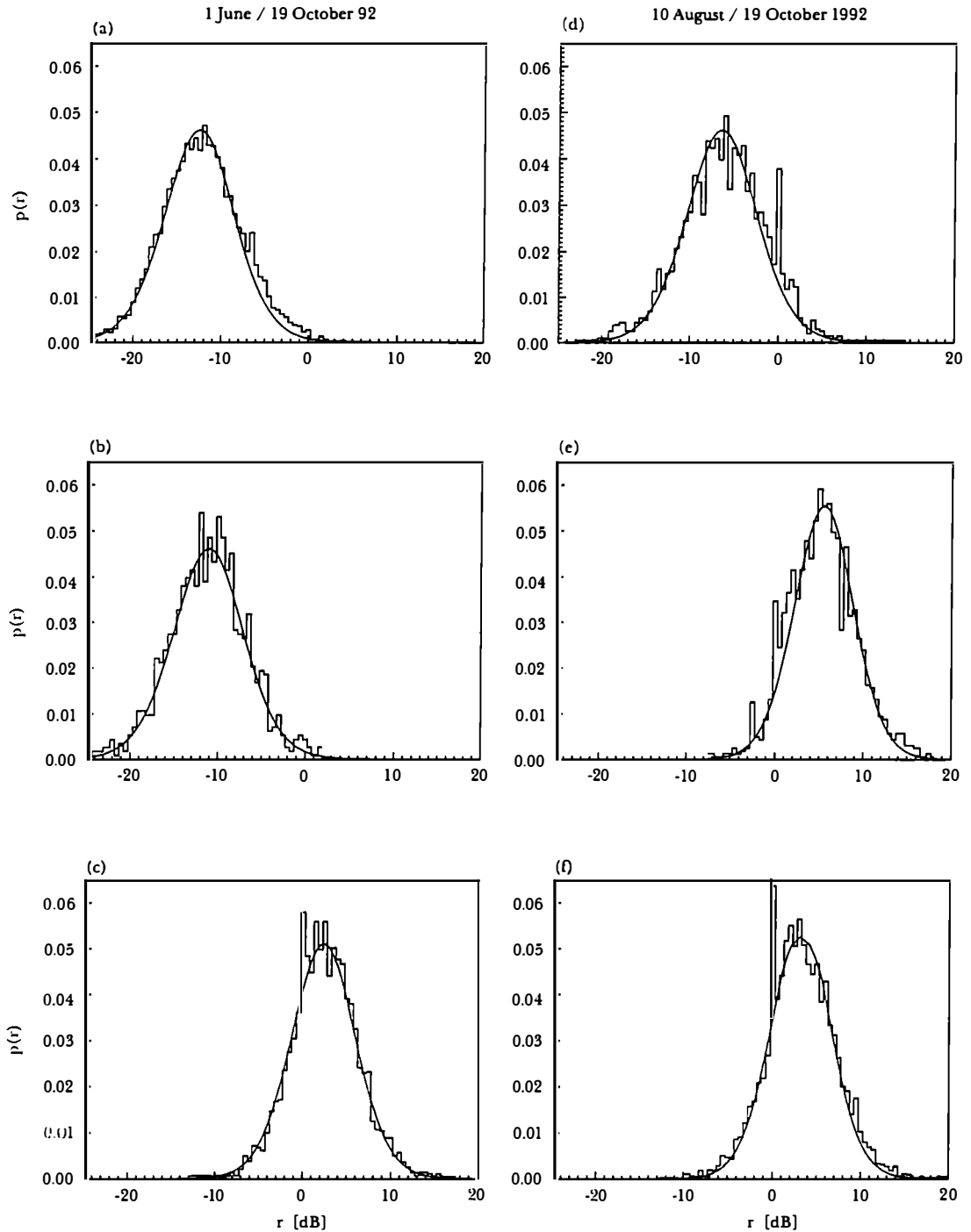


Figure 8.3: Theoretical pdf and histogram of the ratio measured from repeat pass ERS-1 PRI images. ascending pass: 1 June versus 19 October 1992: (a) wet snow in firn area of glacier ($\bar{r} = -13.0$ dB), (b) rocks and vegetation covered by wet snow ($\bar{r} = -11.1$ dB), (c) snow free vegetation ($\bar{r} = 2.3$ dB); 10 August versus 19 October 1992: (d) rough wet snow in glacier firn area ($\bar{r} = -0.4$ dB), (e) very rough glacier ice ($\bar{r} = 5.5$ dB), (f) snow free vegetation and rocks, moraines ($\bar{r} = 3.2$ dB).

wide and overlapping distributions of the ratio values of targets with different \bar{r} as shown in figure 8.3 and figure 8.4. Increasing the number of effective looks before ratioing reduces speckle and the overlap of the distributions of the ratio (figure 8.4), which enables a more accurate classification.

Two targets with different values of \bar{r} are discriminated by assuming a threshold r_o . It is assumed that class A is characterized by a mean ratio of $\bar{r}_A = \left(\frac{\hat{I}_1}{\hat{I}_2}\right)_A$ and class B by $\bar{r}_B = \left(\frac{\hat{I}_1}{\hat{I}_2}\right)_B$ and that a sample belongs to class A if its ratio $r \leq r_o$ and to B if $r > r_o$ for $\bar{r}_B > \bar{r}_A$. Assuming equal a priori probabilities for classes A and B the optimal threshold for discriminating both targets is found by using the conditional probability $p(r_o|\bar{r}_A) = p(r_o|\bar{r}_B)$ leading to [60]

$$r_o = \sqrt{\bar{r}_B \bar{r}_A} \quad (8.14)$$

which is independent of the number of looks. A quantitative measure for the error in classification is the probability of error PE . After determination of the PE for each class A and B the overall PE is separately determined as function of the difference of the mean detected change of class A and B ($\Delta\bar{r} = \bar{r}_B/\bar{r}_A$) and the effective number of looks [60]. The parameter $\Delta\bar{r}$ corresponds to the difference in dB of the mean change \bar{r} of both targets between image 1 and image 2. A plot of the overall PE as a function of $\Delta\bar{r}$ for different numbers of looks is shown in figure 8.5. For discriminating two targets with $\Delta\bar{r} = 3$ dB with a confidence level of more than 90% ($PE < 10\%$) the number of independent looks has to be greater than 32, for detecting changes of 1 dB hundreds of looks are required. For ERS-1 PRI and X-SAR MGD images with about 3 and 4.5 independent looks, respectively, a value of $\Delta\bar{r} = 6$ dB shows a PE of about 20%, while for a 3 dB change PE is larger than 30%. It should be remembered that figure 8.5 is only valid for gamma distributed homogeneous targets and is generally not applicable for heterogeneous targets.

Figure 8.5 enables also the estimation of the number of looks which is required for discriminating targets with given backscattering changes and confidence level. For wet snow detection presented in chapter 10, snow free targets with typical values of $\bar{r}_A \sim -1$ to 1 dB and wet snow areas with $\bar{r}_B \sim -5$ to -7 dB (observed in ERS-1 PRI ratio images of 1 June 92 and 6 July 1992 versus 19 October 1992) should be discriminated. From eq. 8.14 a threshold of $r_o \sim -2$ to -3 dB is determined. For the lower limit with $\Delta\bar{r} \sim 4$ dB about 16 independent looks are required for discrimination with a confidence level of 90%, while for 95% confidence level about 50 looks are needed. Taking the correlation of adjacent ERS-1 PRI pixels in the azimuth and range direction into account (eq. 8.11), spatial averaging over 6×6 ERS PRI pixels (each with a size of 12.5×12.5 m^2) in range and azimuth is required, leading to a final pixel spacing of 75×75 m^2 . For increasing the number of looks without a strong loss of spatial resolution special filtering techniques were developed, which are discussed in the section 8.4.

8.4 Speckle reduction in SAR images

Any image generated by a coherent imaging system, such as SAR, is affected by coherent interference between scatterers. For distributed targets this interference causes the detected intensity to fluctuate from resolution cell to resolution cell. Although often referred to as multiplicative noise, speckle is only a phenomenon of coherent imaging and strictly speaking speckle is not noise [2]. The same imaging configuration leads to the same speckle pattern. Therefore speckle can also be used for detection of changes on the surface properties, based on temporal decorrelation [60]. But on the other hand, for many

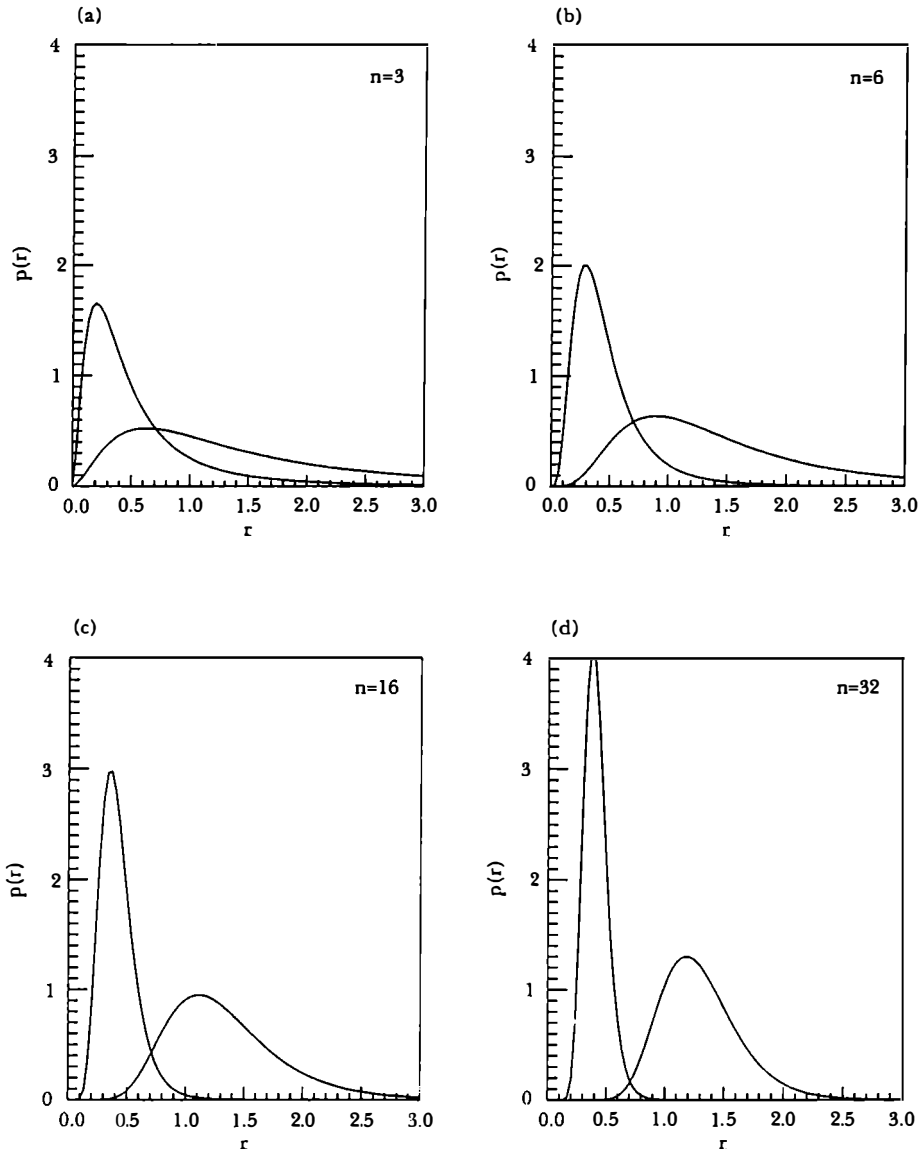


Figure 8.4: Probability density function of the ratio of two intensity images for different mean values $\bar{r} = -4$ dB (solid line) and $\bar{r} = 1$ dB (dashed line) and for different effective number of looks (a) $n = 3$. (b) $n = 6$. (c) $n = 16$. (d) $n = 32$.

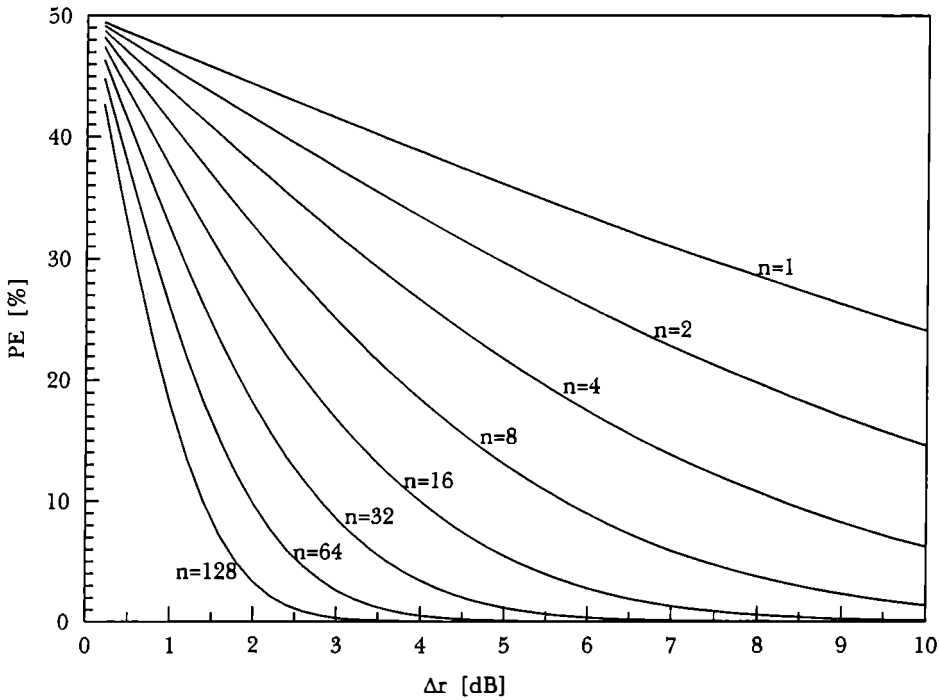


Figure 8.5: Probability of error (in %) of the ratio method for discrimination of targets with difference Δr in mean backscattering change for a number of looks (n) varying between 1 and 128 (after [60])

applications which are based on analysis of the radar cross section of distributed targets, speckle is an unwanted phenomenon because an image cannot be analyzed on a pixel by pixel basis. The analysis of coherently imaged scenes needs to be based on the statistics estimated over regions [7]. Several methods to reduce speckle have been developed.

Methods for speckle reduction can be divided into 3 categories:

- multi-look processing [2]
- spatial averaging (section 8.2.1)
- speckle filtering [43]

In general speckle itself and the achieved speckle reduction can be quantified by the effective number of looks n which is defined as [2]

$$n = \frac{\langle I \rangle^2}{s_I^2} \quad (8.15)$$

where I is the intensity of a pixel in a homogeneous region and s_I^2 is the variance of I .

For statistically uncorrelated samples the first and the second method can be considered as equivalent [82]. The disadvantage is that both reduce speckle by losing spatial resolution. For homogeneous areas spatial averaging is effective and rather simple to apply. Unfortunately most scenes have, in addition to speckle, also high frequency information like texture and edges. Spatial averaging can destroy this information. Therefore special filters have been developed which reduce speckle and preserve other high frequency information. Among these are adaptive filters, which use the local statistics for smoothing

data. These adaptive filters were tested on simulated and real SAR images with different parameters [43]. [82]. In this chapter some of those filters are compared for the use in snow mapping procedures and glacier investigations, described in chapter 10 and 11.

8.4.1 Digital filtering

The requirements for speckle filtering are

- smoothing homogeneous targets while conserving the average backscatter value
- preservation of sharpness and location of edges
- minimal loss of texture
- no creation of artifacts

In this work the Frost, Modified Frost, Gamma MAP and, for comparison, the Median filter are tested with real ERS-1 PRI multi-look images (1 look in range, 3 looks in azimuth). In respect to applications their effect on the ratio of two images is also investigated.

8.4.1.1 Median Filter

The Median filter is a non-speckle specific filter which is often used for smoothing images. The value of the central pixel is replaced by the median of a data window. Generally window sizes of 3x3 to 5x5 pixels are used. Large windows produce a strong smoothing of the data.

8.4.1.2 Frost Filter

The Frost filter is based on the assumption, that the recorded SAR image can be modeled as a convolution between the image model [7] and the SAR impulse response $h(x, t)$.

$$I(x, y) = R(x, y)\zeta(x, y) * h(x, y) \quad (8.16)$$

where $R(x, y)$ describes the backscattering at each point, and $\zeta(x, y)$ represents speckle, which is an independent, unit mean exponentially distributed random variable. In order to estimate $R(x, y)$ the minimum mean square error (MMSE) between the filtered image R and the original stationary image I is calculated. After some simplifications the impulse response meeting the MMSE criterion is given by [43]

$$m(t) = ke^{-AC_I^2(\cdot)|t|} \quad (8.17)$$

with

$$C_I(\cdot) = \frac{\sqrt{s_I^2(\cdot)}}{\mu_I(\cdot)}$$

where t is the absolute distance from the location of the center pixel (x_o, y_o) . Calculations over the predefined moving filter window centered at (x_o, y_o) are denoted as (\cdot) . The parameter k is a normalizing constant, and A controls the clamping of the impulse response function within the filter window. $C_I(\cdot)$ is the coefficient of variation and is derived from a moving window. When $C_I(\cdot)$ is small the filter behaves like a low pass filter, which is the case for homogeneous areas. When $C_I(\cdot)$ is large, i.e. at edges, smoothing is less effective.

8.4.1.3 Modified Frost Filter

This filter, sometimes also referred as Enhanced Frost filter [82], was proposed by Lopes *et al.* [43]. The first step is the testing of the heterogeneity of an area to be filtered, where three classes are distinguished. The first class is given by homogeneous areas where all high frequency information is assumed to be speckle. Box filtering which strongly suppresses high frequency information is applied to such scenes. The second corresponds to heterogeneous areas, where only speckle should be reduced but texture and edges should be preserved. The third class consists of isolated point targets. The classification of these three types is based on the coefficients of variation C_u and C_{\max} . With these assumptions the Frost filter in eq. 8.17 is modified to [43]

$$m(t) = ke^{-A \text{func}[C(\cdot)]|t|} \quad (8.18)$$

with

$$\text{func}[C(\cdot)] = \begin{cases} \mu_I(\cdot) & \text{if } C_I(\cdot) \leq C_u \\ \frac{C_I(\cdot) - C_u}{C_{\max} - C_I(\cdot)} & \text{if } C_u < C_I(\cdot) < C_{\max} \\ I(x_o, y_o) & \text{if } C_{\max} \leq C_I(\cdot) \end{cases}$$

where

$$C_u = \frac{\sqrt{s_u^2}}{\mu_u} \simeq \frac{1}{\sqrt{n}}$$

$$C_{\max} = \sqrt{1 + \frac{2}{n}}$$

C_u is the coefficient of variation of speckle. It can be treated as constant over the total image, because it is a parameter of the imaging system and not dependent on the scene. In comparison with the original Frost filter (section 8.4.1.2) the Modified Frost filter shows similar results for the second class, heterogeneous targets.

8.4.1.4 Gamma MAP filter

In contrast to the Frost and Modified Frost filter the Gamma MAP filter uses the statistical properties of the imaged scene. This means that in the maximum a priori (MAP) approach the knowledge of the *pdf* of the image data is required. It was assumed that the intensity of homogeneous targets is gamma distributed, which is valid for multi-look images [7]. The Gamma MAP filter is given by [82]

$$R(\cdot) = \begin{cases} \mu_I(\cdot) & \text{for } C_I(\cdot) < C_u \\ \frac{(\alpha - n - 1)\mu_I(\cdot) + \sqrt{\mu_I^2(\cdot)(\alpha - n - 1)^2 + 4\alpha n \mu_I(\cdot)}}{2\alpha} & \text{for } C_u \leq C_I(\cdot) \leq C_{\max} \\ I(x_o, y_o) & \text{for } C_{\max} < C_I(\cdot) \end{cases} \quad (8.19)$$

with

$$C_{\max} = \sqrt{2}C_u$$

$$C_u = \frac{1}{\sqrt{n}}$$

$$\alpha = \frac{1 + C_u^2}{C_I^2(\cdot) - C_u^2}$$

where n is the effective number of looks.

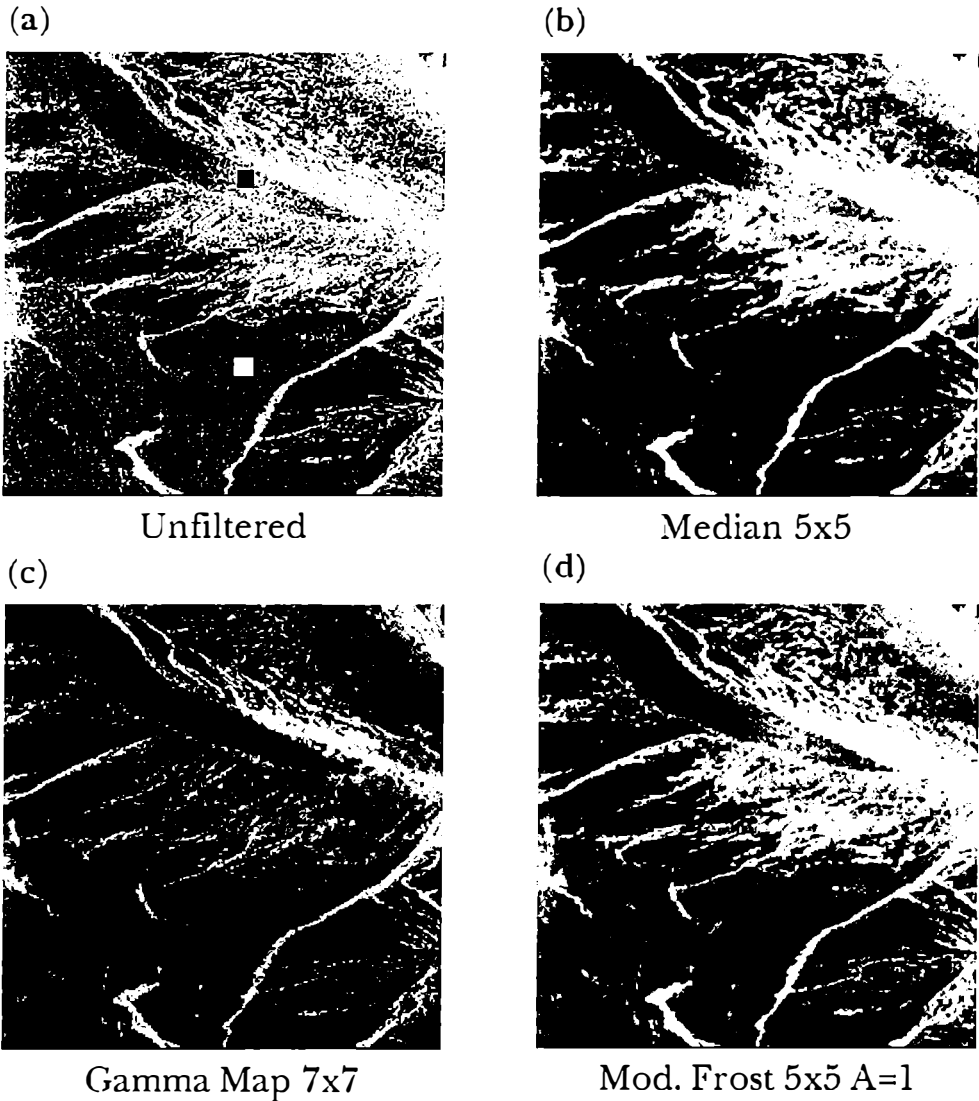


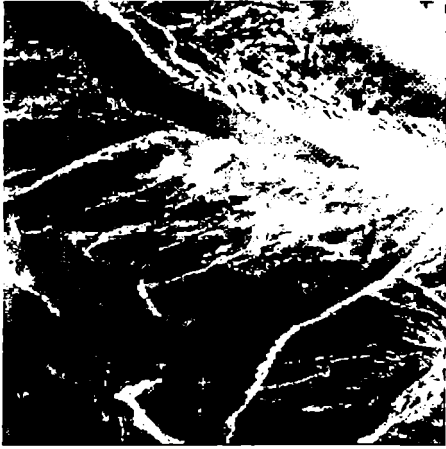
Figure 8.6: ERS-1 PRI image of the area Rofental acquired on 6 July 1992, ascending path. The unfiltered and filtered image are shown. Black and white boxes in (a) correspond to homogeneous areas A (upper) and area B (lower).

8.4.2 Filtering experiments

The selection of a filter and its specific parameters is a kind of trade-off between smoothing of speckle and preserving useful information [82], [43]. It is in general scene dependent and can be estimated by time consuming trial and error. Here the filters described in the last section are tested.

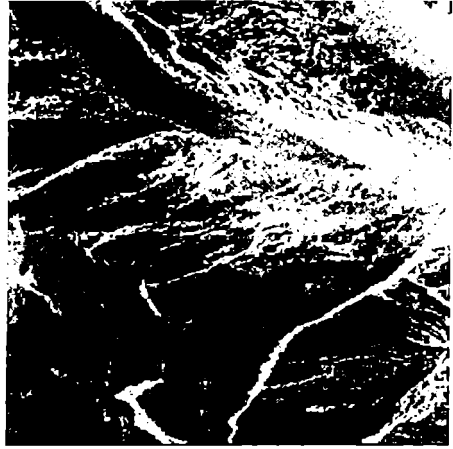
For filter testing an image of $512 \times 512 \text{ pixel}^2$ was extracted from ERS-1 PRI data covering the central part of the test site Ötztal (figure 8.6, figure 8.7). The image contains snow covered areas, glacier ice, rocks, and moraines and is typical for high alpine regions during the melting season. Two homogeneous areas of 144 pixels^2 and 225 pixels^2 , corresponding to the two boxes in figure 8.6 a, are selected to study the modification of statistical parameters by different filters. Target \mathcal{A} is a glacier ice area on the terminus of Hintereisferner with mean σ° of -10 dB , \mathcal{B} is a wet snow area on Kesselwandferner with σ° of -22 dB . Table 8.1 presents a summary of statistical parameters after application of

(e)



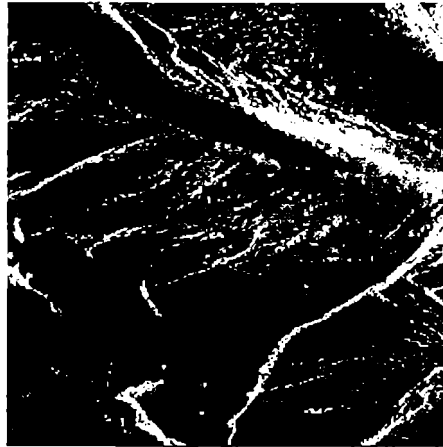
Mod. Frost 9x9 A=1

(f)



Mod. Frost 5x5 A=3

(g)



Mod. Frost 9x9 A=3

Figure 8.7: As figure 8.6.

different filters.

The effective number of looks, the standard deviation and the mean value are calculated for target \mathcal{A} and \mathcal{B} on the basis of the square of PRI pixel values, the calibration constant was not applied. The Frost and modified Frost conserve the mean value within 0.1 dB, the Gamma MAP filter within 0.29 dB. The maximum change to the mean value of the original image is found for the median filter over $5 \times 5 \text{ pixels}^2$ with 0.52 dB for the glacier ice area. The highest values of n_f , indicating strong speckle reduction, are observed for the modified Frost and the Frost filter with filter sizes of $9 \times 9 \text{ pixels}^2$ and low values of damping factor A . Lopes *et al.* [43] showed that a Frost filter with $A=0.1$ suppresses the same amount of high frequency information as simple spatial averaging.

An interesting point is the effect of different filters on ratios. For this purpose a threshold was applied to the final ratio image. The ratio image was formed from the ERS-1 PRI images of 6 July 1992 versus 19 October 1992, after coregistration and separate filtering. The ratio of the unfiltered ERS-1 PRI images shows speckled features all over the image (figure 8.8 a). In figure 8.8 and 8.9 the ratio images after applying different filters on the input images are shown. The corresponding number of pixels below the threshold (shown in grey) for each filter is given in table 8.2. For the Frost, Modified Frost and Gamma MAP between 55% and 58 % of the image are below the threshold, with only small variations for different filter specific parameters. For the Median Filter the number of pixels below the threshold is about 5 % higher. While 3×3 Median filtering shows only little reduction of speckle ($n_f \simeq 7$), a 5×5 Median is more effective ($n_f \simeq 17$), but the edges and point targets become blurred. The Gamma MAP filter shows only a slight dependence on the window size for speckle reduction. By inspection of the ratio image several speckle-like features can be observed (figure 8.8c). The Frost and the modified Frost filter show similar results. Using a damping factor $A = 1$ the speckle is suppressed very well by both filters. A higher factor, e.g. $A = 3$, results in more structure and higher frequency information.

In figure 8.10 small images were extracted showing the boundary between a snow free area and an area covered by wet snow. The intensity difference between the two targets is more than 9 dB. The Frost, modified Frost filter and the Gamma MAP show good edge preservation. Figure 8.11 presents the effect of different filters on point targets. The point target is strongly smoothed by the Median, while the other applied filters preserve at least the maximum.

Area A: Hintereisferner, glacier ice, 12 x 12 pixel ²					
filter	filter size	filter	$\mu_I(\cdot)$	$s_I(\cdot)$	n_f
	[pixel ²]	parameter	[dB]	[dB]	
Unfiltered	—	—	47.81	45.81	2.52
Median	3x3	—	47.56	43.25	7.27
Median	5x5	—	47.29	41.13	17.05
Frost	5x5	A=1	47.84	40.34	31.64
Frost	5x5	A=3	47.84	42.49	11.75
Frost	9x9	A=1	47.78	37.31	124.11
Frost	9x9	A=3	47.85	41.48	18.73
Mod. Frost	5x5	n=3, A=1	47.85	40.03	36.52
Mod. Frost	5x5	n=3, A=3	47.85	40.74	26.40
Mod. Frost	9x9	n=3, A=1	47.74	37.14	131.69
Mod. Frost	9x9	n=3, A=3	47.79	37.24	129.06
G. MAP	7x7	n=3	47.65	38.95	54.72
G. MAP	9x9	n=3	47.54	38.14	76.01

Area B:- Kesselwandferner, wet snow, 15 x 15 pixel ²					
filter	filter size	filter	$\mu_I(\cdot)$	$s_I(\cdot)$	n_f
	[pixel ²]	parameter	[dB]	[dB]	
Unfiltered	—	—	36.58	34.29	2.87
Median	3x3	—	36.37	31.92	7.76
Median	5x5	—	36.31	29.80	20.05
Frost	5x5	A=1	36.59	29.79	22.98
Frost	5x5	A=3	36.57	30.84	14.01
Frost	9x9	A=1	36.61	27.44	68.33
Frost	9x9	A=3	36.63	30.01	21.09
Mod. Frost	5x5	n=3, A=1	36.60	29.54	25.78
Mod. Frost	5x5	n=3, A=3	36.59	29.61	24.84
Mod. Frost	9x9	n=3, A=1	36.60	26.73	94.24
Mod. Frost	9x9	n=3, A=3	36.61	26.79	92.30
G. MAP	7x7	n=3	36.59	28.26	46.41
G. MAP	9x9	n=3	36.56	27.06	79.84

Table 8.1: Statistical parameters derived from homogeneous areas A and B shown in figure 8.6 and figure 8.6 after applying different filters on the intensity image ($n=3$) from 6 July 1992, ascending orbit. All values are square of image pixel values, without applying the calibration constant. Mean value μ_I , standard deviation $s_I(\cdot)$, and effective number of looks of filtered image n_f .

Un-filtered	Median 3x3	Median 5x5	Frost 5x5,A=1	Frost 5x5,A=3	Frost 9x9,A=1	Frost 9x9,A=3
56.20%	63.69%	63.43%	55.88%	56.92%	55.94%	57.65%

M. Frost 5x5,A=1	M. Frost 5x5,A=3	M. Frost 9x9A=1	M. Frost 9x9,A=3	G. MAP 7x7	G. MAP 9x9
56.63%	57.09%	56.86%	57.54%	57.36%	57.48%

Table 8.2: Number of pixels below the threshold (grey area in fig. 8.8 and fig. 8.9) for various filtered input images.

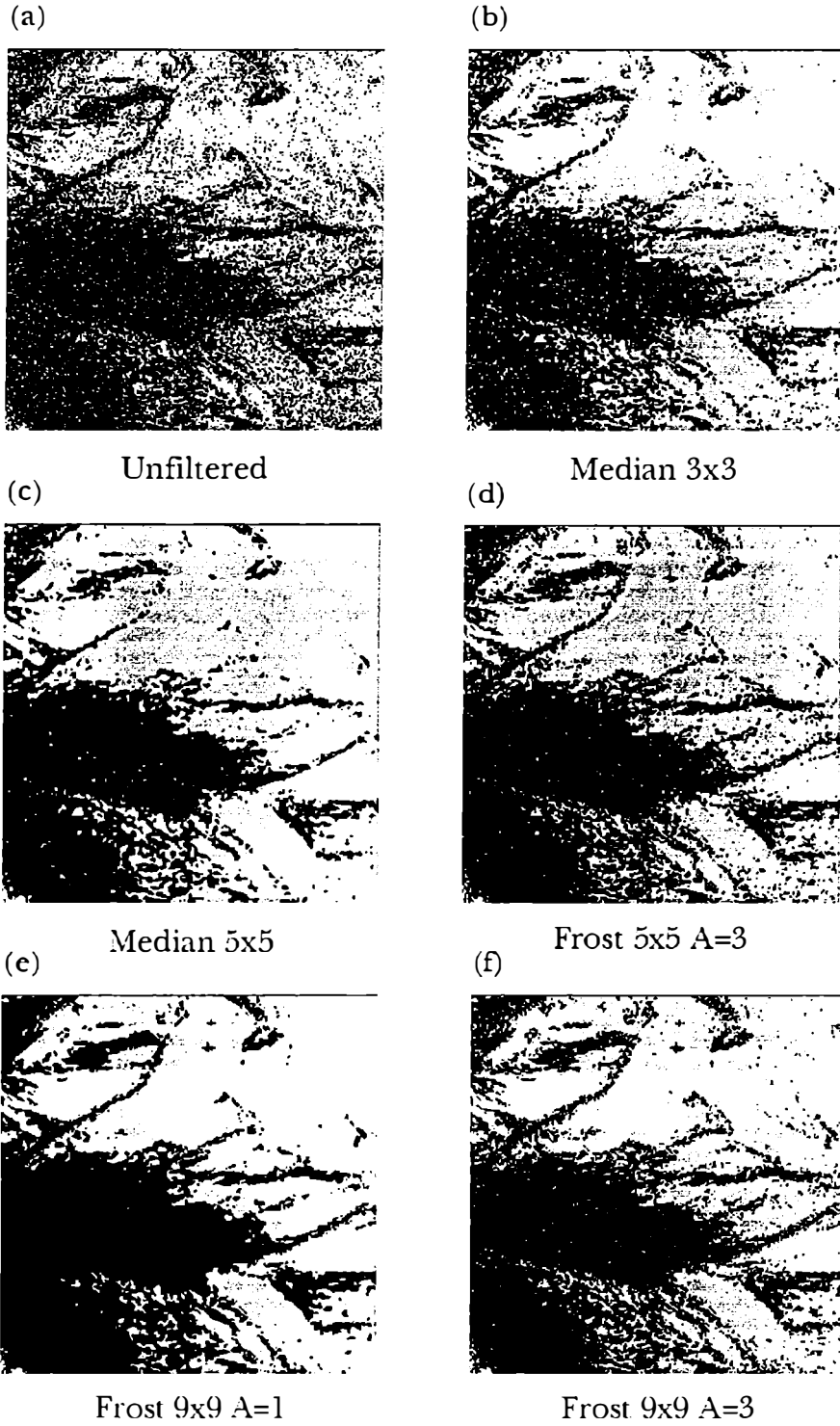


Figure 8.8: Thresholded ratio for filtered input images 6 July 1992 versus 19 October 1992, ERS-1 PRI, ascending pass. A threshold of -3 dB was applied. Grey correspond to areas with ratio lower than the threshold of -3 dB.

(g)



Mod. Frost 5x5 A=3

(h)



Mod. Frost 9x9 A=1

(i)



Mod. Frost 9x9 A=3

(j)



Gamma Map 7x7

Figure 8.9: As figure 8.8, other filters.

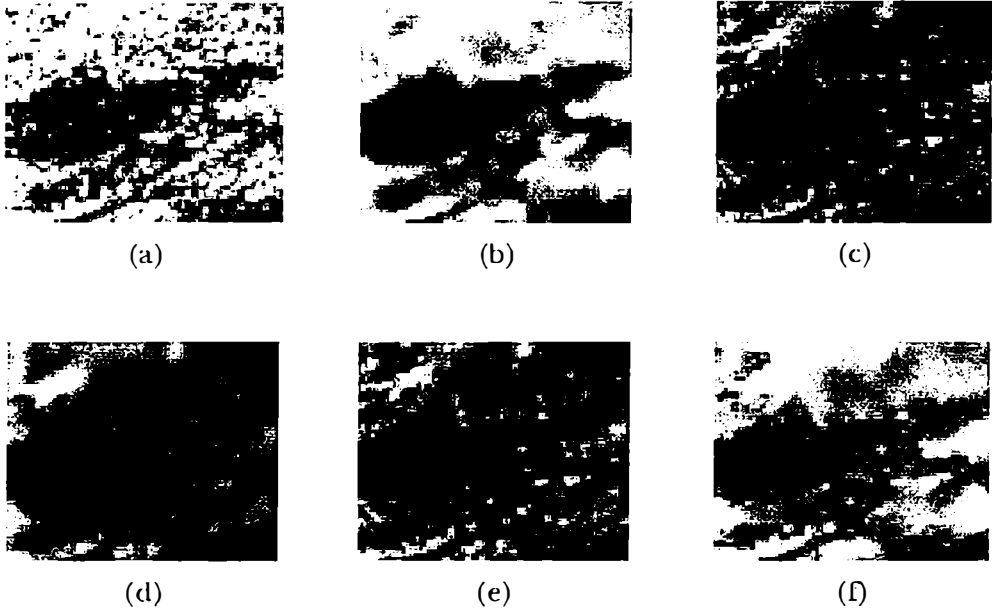


Figure 8.10: Unfiltered image (a) , and 5 filtered images: Median 5×5 (b), Gamma MAP (c), Frost $9 \times 9, A=1$ (d), Frost $9 \times 9, A=3$ (e), Enhanced Frost $9 \times 9, A=1$ (f).

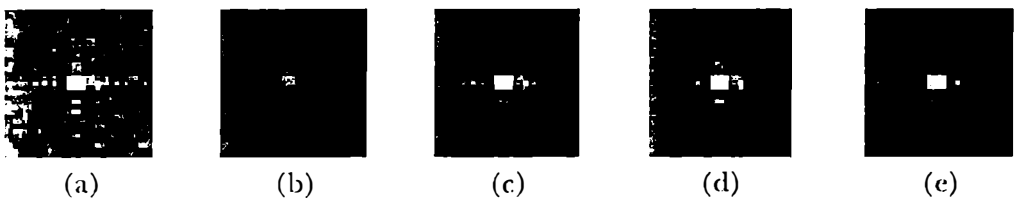


Figure 8.11: Response of corner reflector K1 on Kesselwandferner, 6 July 1992, ascending orbit in the unfiltered image (a) and 5 different filtered images: Median 5×5 (b), Gamma MAP (c), Modified Frost $9 \times 9, A=1$ (d), Frost $9 \times 9, A=1$ (e).

Chapter 9

Classification of snow and glaciers based on Landsat TM

Snow cover and glaciers were analyzed with optical satellite data to produce comparative data sets and to verify the SAR data analysis. In this chapter the techniques for analysis of optical data are described and examples of the analyzed data sets are presented. The investigations included the detection of snow versus other surface types, the identification of clouds, and the compensation of atmospheric and topographic effects. Based on the flowchart in figure 9.1 the single steps for snow mapping are briefly discussed.

9.1 Processing of Landsat TM images

9.1.1 Rectification and auxiliary products

As the first step the TM data are transformed to a cartographic reference system using an imaging model and ground control points. The solar illumination angle at each resolution element of the rectified image and the sun position specified by the solar zenith and azimuth angle, which depend on date and time of the image acquisition, are calculated based on a digital elevation model (DEM) [11].

9.1.2 Calibration of Landsat-5 TM

Different methods were proposed for calibrating Landsat TM data [14], [44]. The data to be calibrated were processed at Earthnet using preflight calibration offset and gain constants A_0 and A_1 [14]. According to this information the spectral radiance L_{TM} [$Wm^{-2}ster^{-1}\mu m^{-1}$] measured by the sensor is given by

$$L_{TM} = \frac{A_0}{b} + \frac{A_1 DN}{b} \quad (9.1)$$

where b [μm] is the full-width half-maximum bandwidth of the TM channel, and DN is the digital number stored on the tape. The prelaunch calibration offset A_0 and gain A_1 for each TM channel and the corresponding mean solar exo-atmospheric irradiance $E_{sun,\lambda}$ [$Wm^{-2}\mu m^{-1}$] are given in table 9.1 [14].

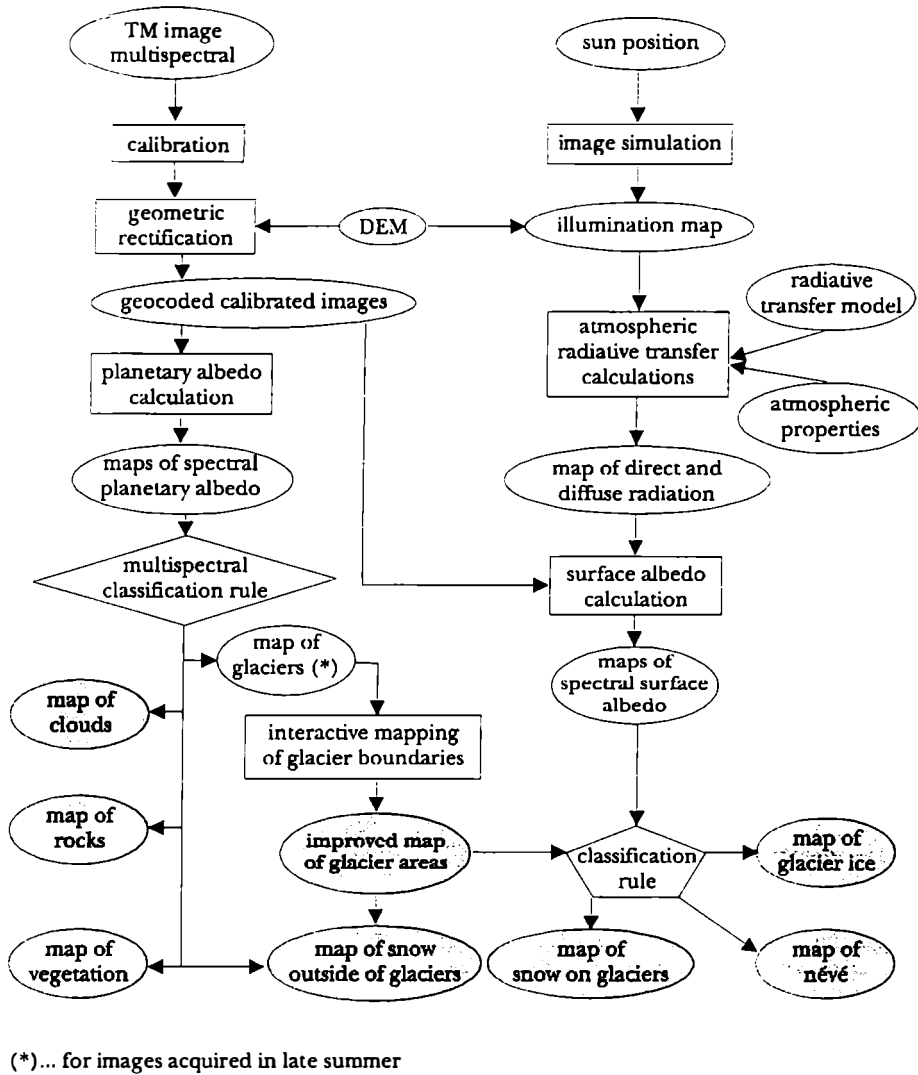


Figure 9.1: Flow chart of snow mapping by means of Landsat-5 TM images.

Channel	λ - Range [μm]	b [μm]	A_0 [$\text{Wm}^{-2}\text{ster}^{-1}$]	A_1 [$\text{Wm}^{-2}\text{ster}^{-1}$]	$E_{sun,\lambda}$ [$\text{Wm}^{-2}\mu\text{m}^{-1}$]
TM - 1	0.45 - 0.52	0.066	-0.06662	0.04197	1957
TM - 2	0.53 - 0.61	0.082	-0.15732	0.10345	1829
TM - 3	0.62 - 0.69	0.067	-0.11269	0.06500	1557
TM - 4	0.78 - 0.90	0.128	-0.23286	0.11705	1047
TM - 5	1.57 - 1.78	0.217	-0.08640	0.02727	219.3
TM - 7	2.10 - 2.35	0.252	-0.05114	0.01692	74.52

Table 9.1: Calibration Constants for Landsat-5 TM images processed at Earthnet. All values are based on full-width half-maximum bandwidth (b); preflight calibration offset (A_0) and gain (A_1), mean solar exo-atmospheric irradiance ($E_{sun,\lambda}$) [14].

9.1.3 Planetary albedo, surface albedo and atmospheric radiative transfer

The planetary albedo r_p is calculated by

$$r_p = \frac{\pi}{E_{sun,\lambda}} \frac{L_{TM}}{\cos \theta_s} d^2 \quad (9.2)$$

where d [AU] is the earth-sun distance in astronomical units, and θ_s [°] is the solar zenith angle.

In mountainous terrain DEMs are widely used to derive the terrain-dependent solar irradiance at the earth surface. Most important is the solar illumination angle θ_v , which is the angle between the normal to a surface element and the incoming direct solar beam. Other terrain parameters such as the sky view angle (the portion of the overlying hemisphere visible to a surface element) and the local horizon are not used here. For classification of different surface types the reflectivity on the earth surface is calculated. The spectral radiance L_λ [$Wm^{-2}ster^{-1}\mu m^{-1}$] in a small wavelength interval $d\lambda$ at the satellite altitude is given by [52]

$$L_\lambda = \frac{r_s e^{(-\tau_\lambda / \cos \theta_v)} E_{g,\lambda}}{\pi} + L_{a,\lambda} + L_{r,\lambda} \quad (9.3)$$

with

$$E_{g,\lambda} = E_{dir,\lambda} \cos \theta_v + E_{dif,\lambda} \quad (9.4)$$

where r_s is the surface albedo, τ_λ is the optical thickness of the atmosphere for the direct beam, θ_v is the sensor viewing angle, $E_{g,\lambda}$ [$Wm^{-2}\mu m^{-1}$] is the spectral global irradiance on a horizontal area at the earth's surface, $E_{dir,\lambda}$ [$Wm^{-2}\mu m^{-1}$] is the spectral solar irradiance of the direct beam on a horizontal area on the earth's surface, $E_{dif,\lambda}$ [$Wm^{-2}\mu m^{-1}$] is the spectral diffuse solar irradiance on a horizontal area on the earth surface (including multiple reflected spectral diffuse irradiance) [33], $L_{a,\lambda}$ [$Wm^{-2}ster^{-1}\mu m^{-1}$] is the atmospheric path radiance originating from the direct solar beam, and $L_{r,\lambda}$ [$Wm^{-2}ster^{-1}\mu m^{-1}$] is the atmospheric path radiance originating from the reflected radiation of adjoining pixels. The quantities τ_λ , $r_{atm,\lambda}$, $E_{dir,\lambda}$, $E_{dif,\lambda}$, $L_{a,\lambda}$, and $L_{r,\lambda}$ can be calculated using the radiative transfer model described in [52]. Figure 9.2 shows the spectral irradiance of the extraterrestrial radiation normal to the incident beam and of the total shortwave and diffuse radiation on a horizontal surface in 2850 m, the average altitude of the test site Ötztal. By integration of eq. 9.3 over the TM-channel bandwidth b , the surface albedo in this channel can be calculated.

The calculations are based on the numerical transfer model with a computer code developed by Neururer [52] for analysis of Landsat TM and NOAA AVHRR data. The model needs several input variables, which describe the actual atmospheric properties:

- total precipitable water (*) of the atmosphere
- total ozone content of the atmosphere
- total aerosol optical thickness (*), and wavelength exponent
- single scattering albedo and scattering phase function of aerosol
- surface pressure.

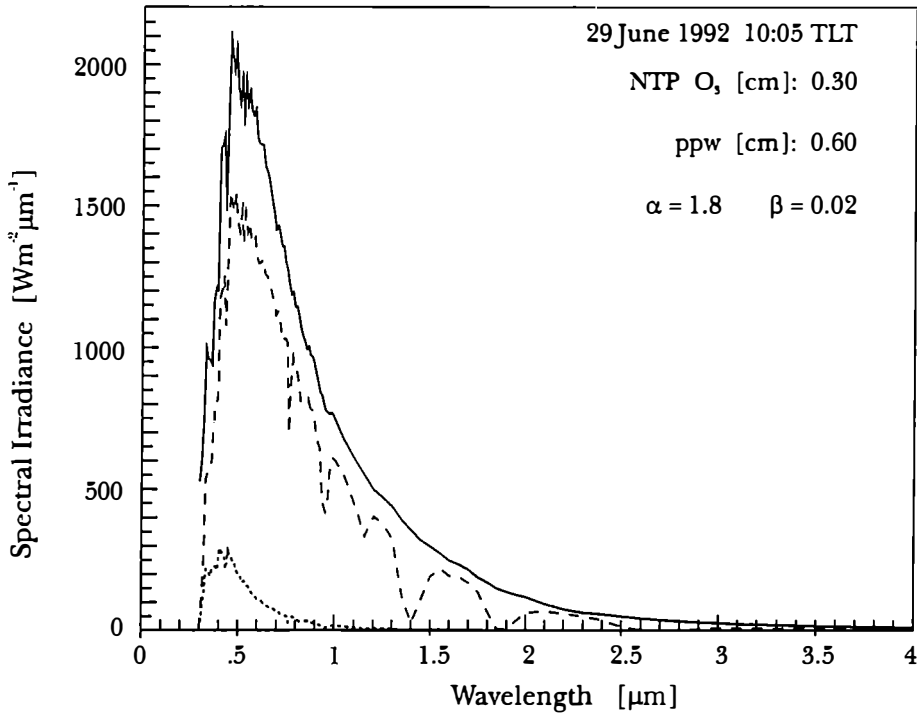


Figure 9.2: Spectral irradiance for extraterrestrial radiation perpendicular to the incident beam and for shortwave and diffuse radiation on a horizontal surface at 2850 m elevation. Calculations are based on the radiative transfer model described in {\protect\cite{Neururur_1991}}. True Local Time (TLT).

The parameters marked by (*) can be modeled as functions of the surface pressure. In general the vertical profiles of these parameters at the time of image acquisition are unknown. Therefore the following approach was applied: the surface pressure of the actual surface element is derived from the altitude, which is available from the DEM, by using the hydrostatic equation. Reasonable values for the other parameters (labelled with (*)) are assumed for two pressure levels, one at the altitude of the mountain peaks and the other at the altitude of the valleys. The altitude dependence of those parameters is then modeled as a linear function of pressure. This procedure provides a set of elevation dependent input parameters, which can be used to solve the radiative transfer model for each pixel.

$L_{r,\lambda}$ and, for a multiple scattering atmosphere, $E_{dif,\lambda}$ are dependent on r_s itself. The calculation of these parameters can be solved by iteration [84], which starts with an estimated value of r_s , and stops if the change of r_s of two consecutive iteration steps is less than 0.001. Generally the iteration converges for 90 % of all pixels after 2 steps, and for 99% of all pixels after 5 steps. For only a few pixels the iteration does not converge after 20 iterations, the maximum number of iterations allowed in the computer code.

Although the calculation of r_s allows a classification of surface types even in rugged terrain, there are still some problems left. Errors of θ_i due to errors in the DEM add to the uncertainty in the radiative transfer calculation, which results mainly from the limited knowledge of the atmospheric conditions. In shadow regions of steep slopes r_s calculated according to eq. 9.3 was too high. The reason is the reflected radiation from surrounding areas to those surface elements, which has not been taken into account here. This effect is well observable when the surrounding area is highly reflective, e.g. snow covered areas in the visible channels. The correction would need high computational power. For the

purpose of surface classification other methods can be applied to reduce these errors.

9.2 Classification rules

Snow classification rules for TM images are based on the parameters r_s and r_p , which we derived above. Typical values of the spectral albedo of different surface types, which are used to choose the classification thresholds, can be found in e.g. [10], [63]. The classification criteria according to [63], [66], [10] applied in the processing chain of figure 9.1, are summarized below:

- For partly cloudy scenes the planetary albedo is used to detect cloud covered pixels. Both targets, clouds and snow show high albedo in the visible bands (TM-1, TM-2, TM-3). For snow the albedo decreases strongly in the near infrared, whereas the albedo of clouds is only slightly reduced [10]. The decision to detect cloud cover is:

$$IF \quad [(r_{p,TM3} + r_{p,TM5}) \geq C_1] \quad \text{and} \quad [r_{p,TM5} \geq C_2] \quad \implies \text{cloud covered} \quad (9.5)$$

where the thresholds C_1 and C_2 are determined empirically. Cloud covered areas are masked and not used in the further analysis.

- After excluding clouds three surface types, vegetation, rocks/moraines and snow/glaciers, were discriminated by the rules

$$\begin{aligned} IF \quad r_{p,TM3}/r_{p,TM5} < C_3 & \implies \text{vegetation} \\ IF \quad C_3 \leq r_{p,TM3}/r_{p,TM5} \leq C_4 & \implies \text{rocks \& moraines} \\ IF \quad C_4 < r_{p,TM3}/r_{p,TM5} & \implies \text{snow \& glaciers} \end{aligned} \quad (9.6)$$

As the reflectivity of glacier ice is clearly lower than the reflectivity of snow, a lower threshold has to be applied for separating the class snow & glacier from vegetation and rocks; $C_4 = 1.5$ was found empirically for the Ötztal site. At the end of the ablation period most of the seasonal snow on unglaciated areas had disappeared. Landsat TM images acquired at that time enable an accurate mapping of the glacier extent. For this study the glaciated area was derived from TM images of 16 August 1992 and 17 September 1992. The use of two images allows the better detection of snow patches outside the glaciers, whereas the glacier area remains stable in both images. The final glacier mask has been used to discriminate between glacier areas and snow outside the glaciers and for signature analysis.

- In addition to the full snow cover class on unglaciated areas an additional class may be introduced for areas near the snow boundary, which show reduced reflectivity in the visible TM bands. This class consists of pixels which are only partly covered by snow. It represents broken snow cover, which can often be observed during melting periods. To discriminate both classes an additional threshold can be introduced [66]. In this study this discrimination was not applied.
- In contrast to most other natural targets snow and ice show generally a strong decrease of r_s from the visible to the near infrared part of the spectrum. The visible to near infrared ratio of r_s uses this spectral behaviour for the detection of snow and ice. An advantage of this classifier is that it is robust against errors in the local illumination angle θ_{LIA} and, at least for two bands spectrally close together, against errors in the calculation of radiative transfer properties. On glaciated areas the ratio technique is not usable because of the similar spectral behaviour of snow,

Date	Altitude	β	α	NTP	P_w
	[m]			[cm]	[cm]
29 June 1992	1800	0.040	1.8	0.3	0.60
	4000	0.015	1.8	0.3	0.25
16 August 1992	1800	0.040	1.8	0.3	0.60
	4000	0.015	1.8	0.3	0.20
17 September 1992	1800	0.040	1.8	0.3	0.50
	4000	0.015	1.8	0.3	0.10

Table 9.2: Altitude dependent parameters specified at two elevations: NTP (normal temperature and pressure) O_3 , β ...aerosol optical thickness, α ...wavelength exponent for aerosol extinction, P_w ... precipitable water [52].

Date	C_1	C_2	C_3	C_4	G_1	G_2
29 June 1992	0.55	0.18	0.5	1.5	0.34	0.59
16 August 1992	n.c.	n.c.	0.5	1.5	0.36	0.59
17 September 1992	n.c.	n.c.	0.5	1.5	0.36	0.59

Table 9.3: Thresholds used for the classification of the available Landsat TM images. No clouds (n.c.).

névé and glacier ice. For glaciated areas snow, firn and glacier ice can be mapped by the decision rules

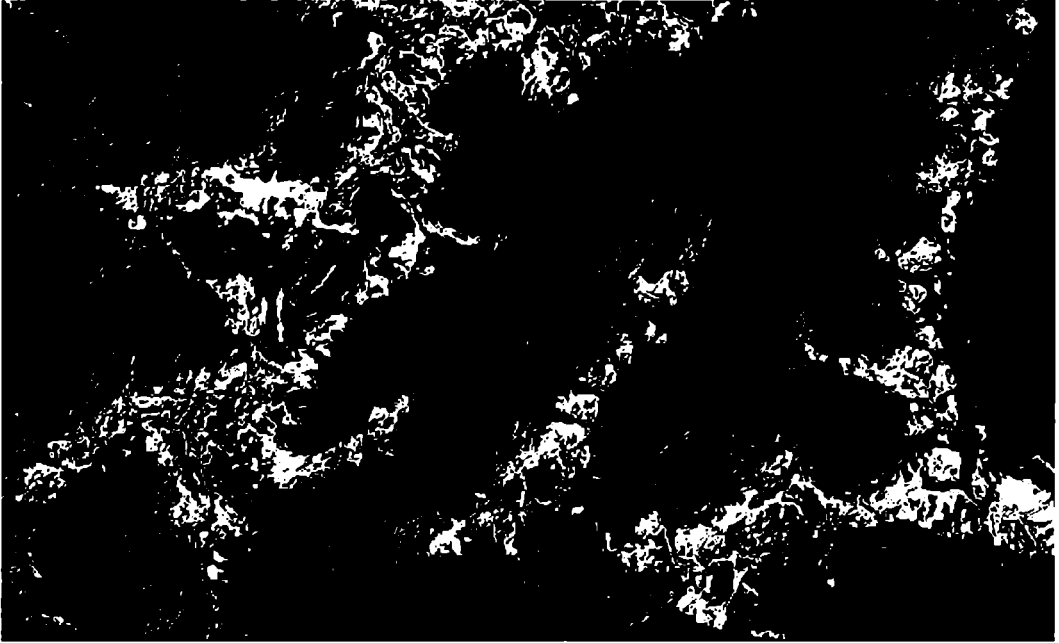
$$\begin{aligned}
 IF \quad r_{s, TM3} < G_1 & \implies \text{glacier ice} \\
 IF \quad G_1 \leq r_{s, TM3} \leq G_2 & \implies \text{firn} \\
 IF \quad G_2 < r_{s, TM3} & \implies \text{snow on glaciers}
 \end{aligned} \tag{9.7}$$

9.3 Analysis of Landsat TM images of Ötztal

In this study 3 Landsat TM images, from 29 June, 16 August and 17 September 1992, with an overflight time at about 9:26 MET were used for comparison with SAR images. All images were rectified into a UTM-32 projection, with 25 E x 25 N and 12.5 E x 12.5 N grid spacing. Figure 9.3 shows the derived surface albedo for TM-band 3 for 16 August 1992 and 17 September 1992. The image specific parameters used for radiative transfer calculation and for classification are specified in table 9.2 and 9.3. In the radiative transfer calculations a constant value for the single scattering albedo of 0.85 and the standard phase function for continental aerosol were used. Figure 9.4 shows the final classification of surface targets.

Over the main parts of the image the effects of different solar irradiance are compensated. Problems arise mainly in shadow zones resulting in too high values for the surface albedo, because the incoming diffuse radiation is increased due to radiation reflected from opposite slopes. Small scale variations may result from errors of the DEM. The surface albedo of the snow free and ice free surfaces was less than 0.2 in both images. In some parts of the glacier termini the albedo increased by more than 0.1 between August and September, which is partly an effect of the lower incidence angle in September resulting in higher reflectance of glacier ice. Another reason may be refreezing of the glacier surface during the night before the TM acquisition, so that the dust and cryconit holes were partly covered by a thin ice layer resulting in higher albedo [78].

16 August 1992



17 September 1992

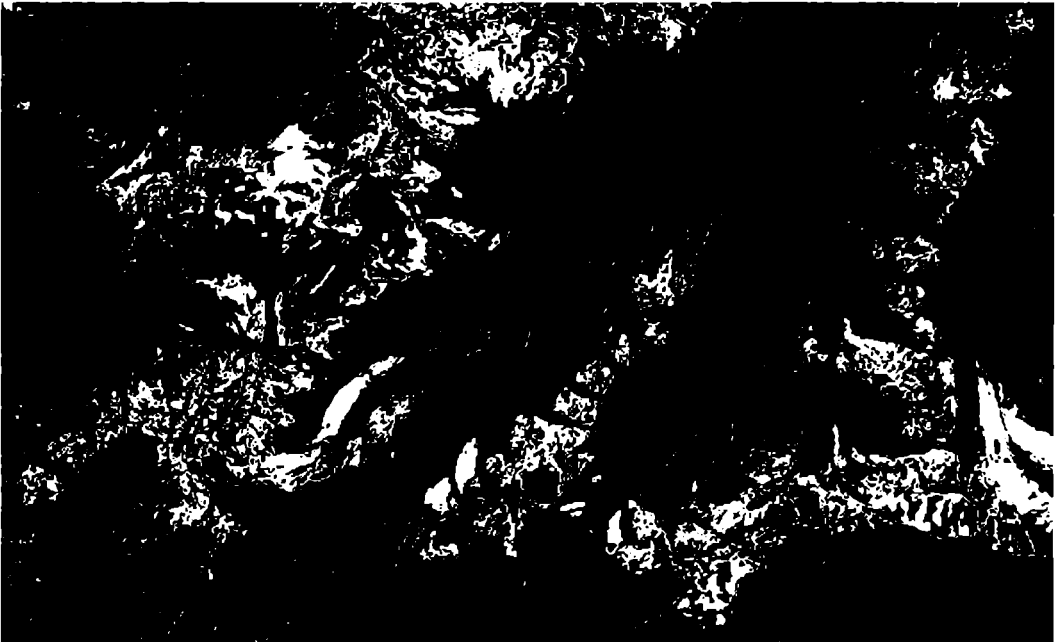
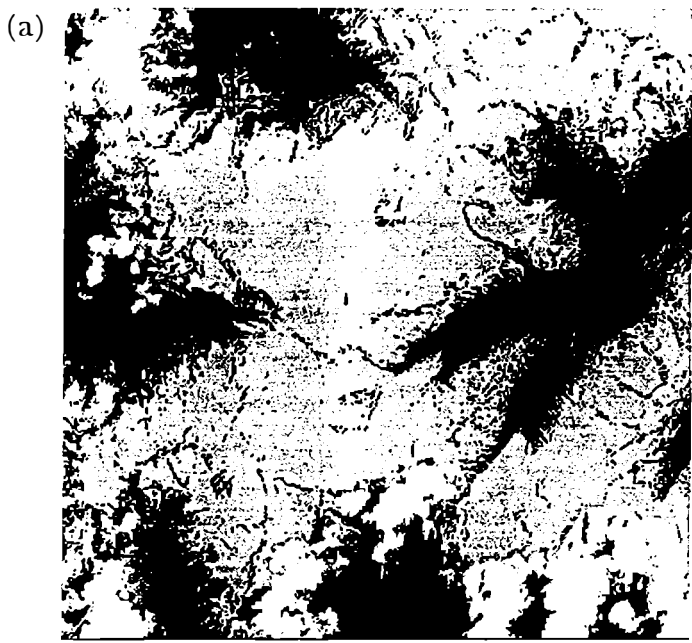


Figure 9.3: Map of spectral surface albedo r_s on 16 August 1992 (top) and 17 September 1992 (bottom) calculated from TM.band 3. The ranges shown for r_s are: $r_s \leq 0.16$ (blue), $0.16 < r_s \leq 0.36$ (green), $0.36 < r_s \leq 0.59$ (yellow), $0.59 < r_s$ (red).



(b)

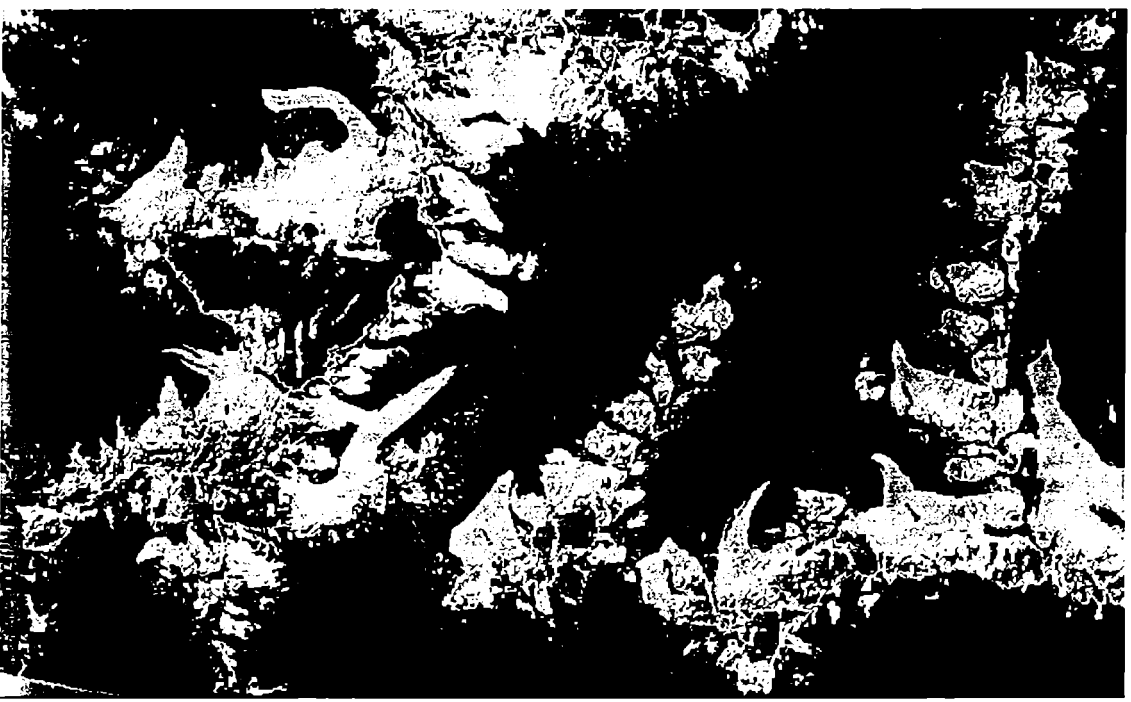


Figure 9.4: Landsat TM classification. (a) 29 June 1992: white...clouds. black...snow free, grey...snow: (b) 16 August 1992: black...rocks/moraines, white...firn, dark, medium, light grey...vegetation. snow, glacier ice.

Chapter 10

Wet snow mapping by means of SAR

10.1 Review of snow mapping procedures

Snow mapping procedures are based on the fact that wet snow efficiently reduces backscattering in C- and X-band. This enables its discrimination from snow free surfaces or dry snow (section 7.1.3). But backscattering depends also on the local incidence angle, which shows large variations, especially in mountainous terrain. Various methods were proposed in the recent years to reduce the influence of different incidence angles for the purpose of snow mapping. Furthermore different preprocessing steps were applied to enhance the classification result.

Rott [61] and Mätzler and Schanda [48] were among the first who showed the capabilities of wet snow detection by SAR. More detailed investigations based on Seasat images and SAR-580 airborne data were reported by Rott *et al.* [65], [67] (section 10.1.1.1). Images of the full polarimetric NASA/JPL AIRSAR, taken in 1989 and 1991 over the test site Ötztal, were used for further testing of the procedure and enabled new approaches for snow mapping using polarimetric parameters [62], [80], [81] (section 10.1.2).

After the launch of ERS-1 in 1991 a lot of images acquired over the whole year became available and further development of snow mapping procedures started. The stable orbit of ERS-1 with accurate repeat pass images enabled a new approach for snow mapping based on multitemporal analysis, which was first proposed by Rott and Nagler [68], [69], [70]. The procedure was tested in the test site Ötztal with a sequence of images covering a whole cycle from snow melt in spring to winter conditions. The usefulness for water runoff prediction was demonstrated by Rott and Nagler [78] using the ERS-1 based snow maps as input for the hydrological snowmelt runoff model (SRM). Haefner *et al.* [29] proposed a simpler procedure for snow detection using crossing orbits from a single date (section 10.1.1.2). They report problems for detecting snow in their test site near Davos, Switzerland. Their classification procedure [29] uses a similar correction for the incidence angle dependence of σ° to that used by Shi and Dozier [80] and Shi *et al.* [81] (section 10.1.1.2). Guneriussen *et al.* [28] confirmed the capabilities of ERS-1 Fast Delivery (FD) products for wet snow mapping by investigations in the region of Kvikne, southern Norway. Kelley [36] investigated the detection of wet snow in Scotland by ERS-1. After geometric correction of the SAR image he applied a threshold of -13.5 dB to separate wet snow from other targets.

First approaches for inferring snow wetness from polarimetric AIRSAR and SIR-C/X-SAR data were proposed by Shi [79]. Bernier and Fortin [3], [4] indicated the possibility

to indirectly detect dry snow and estimate the water equivalent using ERS-1 C-band data under specific conditions, which may not be applicable to other sites (section 7.3.2. figure 7.26).

10.1.1 Snow mapping procedures using single SAR images

10.1.1.1 Snow mapping procedure of Rott *et al.* (1985)

Rott *et al.* [65] showed qualitatively the capabilities of snow mapping using SAR images of different test sites and from different SAR instruments (Seasat SAR, SIR-A, and the airborne SAR-580). Based on these investigations Rott *et al.* [67] proposed a procedure for snow mapping by SAR in alpine regions. The procedure was tested using an airborne SAR-580 X-band image of the Niederjoch basin, Ötztal, Austria acquired on 7 July 1981. The flow chart of the processing steps is shown in figure 10.1. Based on the local incidence angle map a reference image is simulated by assuming a theoretical or empirical backscatter function. Rott *et al.* [67] used a backscatter function of the type

$$\sigma^{\circ}(\theta_i) = a \exp\left(-\frac{\theta_i}{\phi}\right) + c\sqrt{\cos\theta_i} \quad (10.1)$$

where σ° is the radar cross section per m^2 , θ_i is the local incidence angle of the radar beam. and the parameters a , c and ϕ are dependent on the surface type; in this case study the function $\sigma^{\circ}(\theta_i)$ for moraine and rock surfaces with $a = 0.35$, $c = 0.55$, $\phi = 10^{\circ}$ was applied [65] (see also figure 10.2). Preprocessing steps of the real SAR image include calibration, geocoding, and lowpass filtering.

Because of the high dynamic range of SAR data, the real and the simulated power images were scaled by the fourth root. In order to enhance the difference between the real and the simulated image two relations were tested: subtraction of the simulated from the real image and the ratio of the real versus the simulated image. Thresholding the difference image generates a digital map of snow covered areas. Rott *et al.* [67] found better results for snow mapping using the difference image based on $\sqrt[4]{\sigma^{\circ}}$ than using the ratio image. In regions of radar shadow and layover areas, where no information can be derived, the snow covered area was estimated by taking the altitude distribution of the snow cover into account. When compared with the snow extent derived from oblique aerial photographs taken during the SAR survey the difference in snow coverage was less than 1% for the Niedertal near Vent.

This procedure was again tested by Rott *et al.* [64] with data from the NASA/JPL AIRSAR acquired over the Ötztal on 18 August 1989. A Landsat TM image from 24 August 1989 enabled the validation of the SAR classification product. The AIRSAR operated in polarimetric mode at P-band (440 MHz), L-band (1.25 GHz), and C-band (5.3 GHz). The C-band HH image was selected for snow mapping. The backscattering function for snow free rock and moraines was again used to generate the simulated image. Based on the ratio of the amplitude images mapping of 3 surface classes (snow, glacier ice, and snow- and ice free areas) was possible within a local incidence angle range of 15° to 80° . For the separation of the 3 classes the following conditions were used [63]:

$$\begin{array}{lll} \text{for} & A_{hh}/A_{sim} \leq 1.8 & \implies \text{snow- and ice free} \\ \text{for} & 1.8 < A_{hh}/A_{sim} < 3.5 & \implies \text{glacier ice} \\ \text{for} & 3.5 \leq A_{hh}/A_{sim} & \implies \text{snow} \end{array} \quad (10.2)$$

A_{hh} is the amplitude of the real C-band HH image after subtraction of the system noise, A_{sim} is the amplitude of the simulated image. In comparison with the multispectral

classification based on TM data, the best agreement was found for ice- and snow free areas. Ice areas were partly mis-classified as rock (very rough ice surface) or snow (smooth ice surface). The areal extent of snow surfaces on the glaciers was underestimated in the SAR classification compared with the classification result of the TM data [63].

10.1.1.2 Snow mapping procedures of Haefner *et al.* (1993) and Shi and Dozier (1993)

Haefner *et al.* [29], Shi and Dozier [80] and Shi *et al.* [81] proposed a similar procedure for snow mapping in mountainous regions using single polarized SAR data. Haefner *et al.* used ERS-1 precision images (PRI) of crossing passes, while Shi *et al.* and Shi and Dozier used a modified method using polarimetric NASA/JPL AIRSAR data. In contrast to [67] and [64], a simple cosine function was used for reducing the incidence angle dependence of σ^o . The following normalization function was used by these authors

$$\sigma_n^o = \frac{\sigma^o(\theta_i)}{f(\theta_i)}$$

with

$$f(\theta_i) = \cos^n(\theta_i) \begin{cases} n=1 & \text{for C-band VV ,ERS-1, Haefner[29]} \\ n=1.8 & \text{for C-band VV ,AIRSAR, Shi [80]} \\ n=1.5 & \text{for L-band HH ,AIRSAR, Shi [80]} \\ n=2.2 & \text{for C-band VV ,AIRSAR, Shi et al. [81]} \\ n=1.9 & \text{for C-band HV ,AIRSAR, Shi et al. [81]} \end{cases} \quad (10.3)$$

The normalization functions used for snow mapping are compared in figure 10.2. The procedure of Haefner *et al.* [29] includes lowpass filtering, geocoding, image simulation and the optimal resolution approach for combining images of crossing orbits. The snow classification was performed by thresholding the normalized radar cross section σ_n^o . The comparison with ground measurements and with a snow map based on a classification of Landsat TM channel-4 data of the same period showed some remarkable differences. Based on this analysis Haefner *et al.* [29] came up with three conclusions, which show the limitations of this procedure:

- no correct classifications are possible on foreshortening regions near layover due to the poor local resolution
- snow classification is only possible in open and wide areas
- some snow free areas are miss-classified as snow covered, which may be caused by wet soil.

Shi and Dozier [80] and Shi *et al.* [81] classified wet snow, glacier ice and rocks by means of single-pass NASA/JPL AIRSAR data of the test site Ötztal, acquired on 18 August 1989 and 25 June 1991. They analyzed images of different frequency and different polarization. L-band (1.25 GHz) at HH polarization and C-band (5.3 GHz) at VV, HV and HH polarization. The normalized σ_n^o given in [80], [81] are specified in eq. 10.3. The classification based only on σ_n^o at C-band VV gave an overall agreement of 66%, when compared with the Landsat TM classification. Additionally a texture parameter $s_t = s_i/\mu_i$, where s_i is the local standard deviation and μ_i is the local mean value of σ^o , was calculated over a 9×9 moving window. Including textural information the classification agreement improved to 74.5% [80]. Among all investigated polarizations, C-band HV revealed the best discrimination. Re-analyzing the data of 1989 AIRSAR survey a different value of the normalization exponent n was determined (eq. 10.3). This indicates the

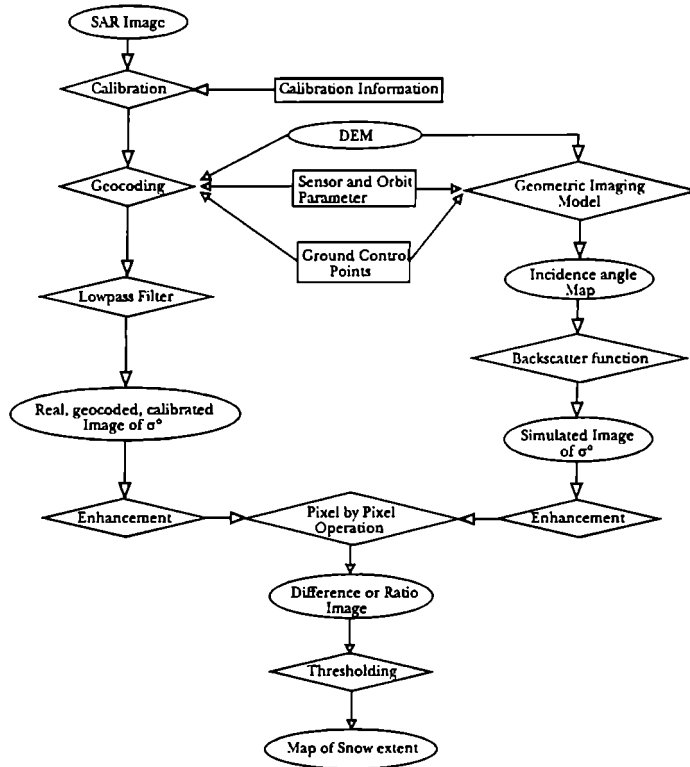


Figure 10.1: Flow chart for generating snow mask using one single SAR image (Rott *et al.* [65]).

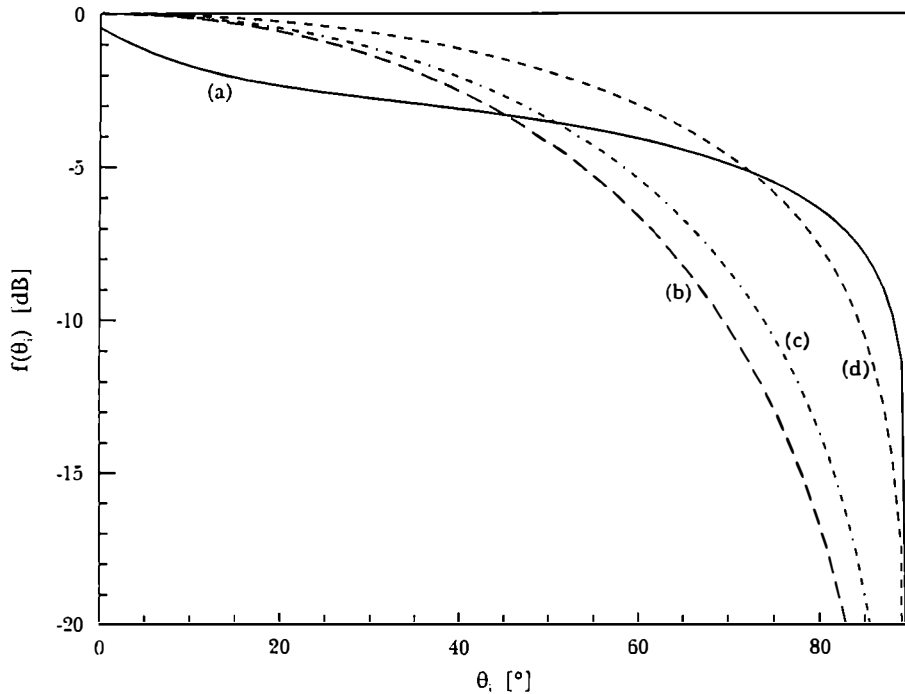


Figure 10.2: Comparison of normalization functions in dB: (a) $\sigma^0(\theta_i)$ (Rott *et al.*, [67]), (b) $\cos(\theta_i)^{2.2}$ (Shi *et al.*, [81]), (c) $\cos(\theta_i)^{1.8}$ (Shi and Dozier, [80]), (d) $\cos(\theta_i)$ (Haefner *et al.*, [29]).

strong dependence on the more or less empirically determined normalization strength, and reduces the applicability to other regions, where information for selecting the exponent n is unavailable.

The basic idea of the procedures of snow mapping by a single SAR images described in section 10.1.1.1 and 10.1.1.2 is to reduce the topographic effects by normalizing σ^o using an empirical or theoretical backscatter function. The main error sources are inaccuracies/errors in the derivation of the incidence angle due to errors in the DEM and, eventually, uncertainties in the knowledge of the flight path, as well as the limited knowledge of the backscatter functions and the local variations of the dielectric and geometric surface properties within the image.

10.1.2 Snow classification using polarimetric parameters

Analysis of polarimetric responses at different frequencies shows the high potential for discriminating various high alpine surface types such as snow, glacier ice, and moraines [62], [64]. But up to now no procedure which uses all the polarimetric information for mapping of surface types has become available.

A first simple approach to use polarimetric information for snow mapping was reported by Rott [64]. The method is an extension of the procedure for classifying snow with a single SAR image, which was presented above [67]. This procedure was tested with a NASA/JPL AIRSAR image of the site Ötztal from 18 August 1989. Rott [63] combined the results of the single channel classification, described in eq. 10.2, with the condition

$$P_{HV}/P_{VV} < m \implies \text{snow covered} \quad (10.4)$$

where $m = 0.04$ was used. P_{HV}/P_{VV} describes the depolarization of the incident wave, where P_{HV} and P_{VV} are the power of the cross-polarized and co-polarized channel in C-band after subtraction of the system noise. Using the same SAR data Shi *et al.* [81] tested three polarimetric parameters: the degree of polarization for VV polarization, the depolarization factor $\sigma_{hv}^o/\sigma_{vv}^o$, and the normalized cross product of VV polarization. In agreement with [63] the depolarization factor provided the best discrimination of the classes snow, glacier ice and ice free.

10.2 Snow mapping based on repeat-pass SAR images

In this section a new procedure for mapping wet snow in mountainous regions is presented [68], [69]. The procedure was developed using ERS-1 AMI SAR images, ascending and descending orbits, in PRI format from the test site Ötztal, Austria, from April 1992 to March 1993. The test site is described in section 3.1, comparative field measurements in chapter 7.1.1.

As discussed in chapter 6, a dry snow cover is highly transparent at C band. Therefore it is hardly possible to discriminate snow free areas and areas covered by dry winter snow. In this study SAR images acquired at such surface conditions are called reference images. With wet snow conditions backscattering is significantly lower (section 7.1.3). SAR images acquired under wet snow conditions are called wet snow images or, in this chapter, just snow images. The change in backscattering between snow and reference images enables wet snow detection.

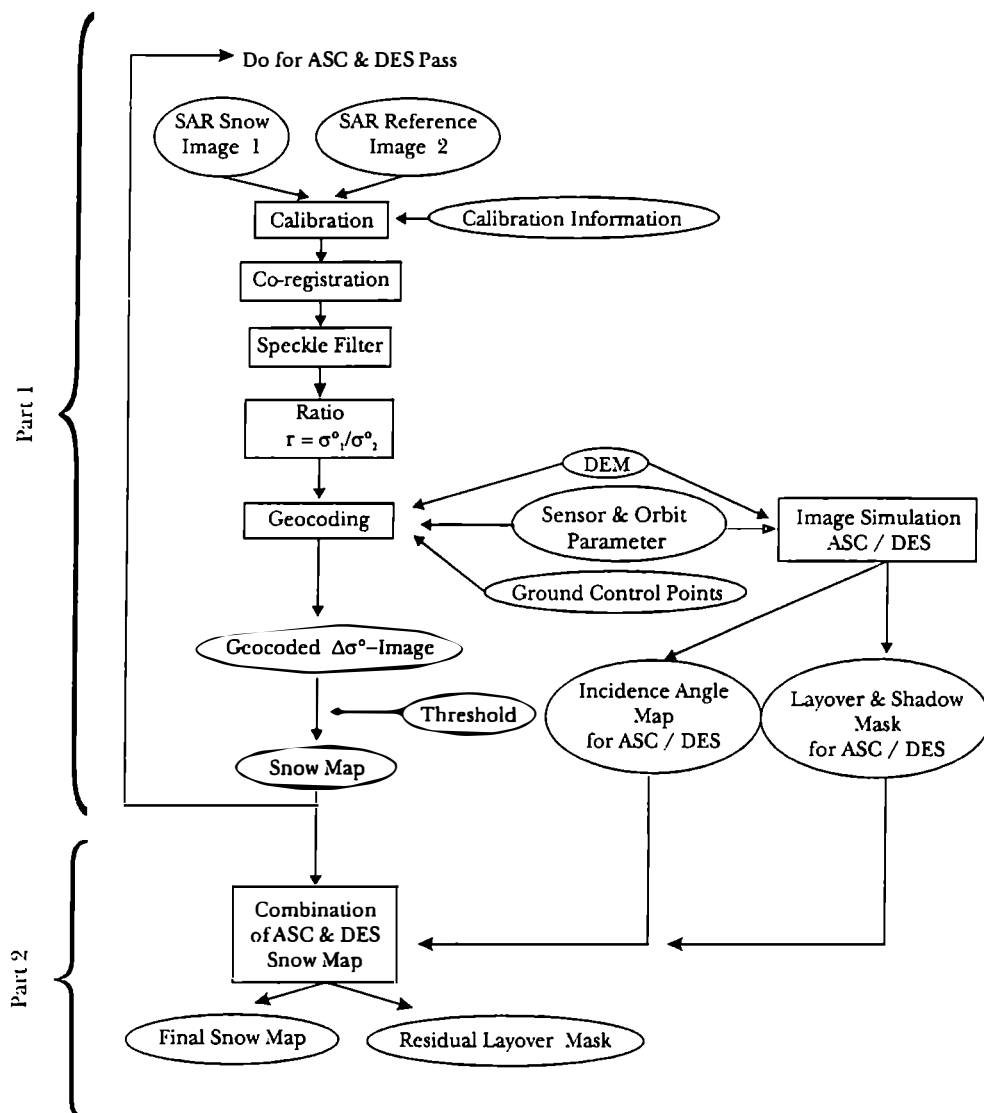


Figure 10.3: Wet snow mapping procedure based on multitemporal repeat pass images of crossing orbits.

10.2.1 Discussion of the wet snow mapping procedure

The wet snow mapping procedure consists of two main parts. The first part includes the preprocessing of each SAR image (calibration, coregistration, speckle filtering), the application of the change detection technique, geocoding and the classification rule for calculating the snow map. This part is carried out separately for ascending and descending pass. In the second part ascending and descending passes are merged to reduce the loss of information due to layover and shadow. Figure 10.3 shows a flow chart of the processing steps.

10.2.1.1 Required input data

The following input data are required:

- SAR snow and reference images of crossing orbits (ascending and descending pass)

- high precision digital elevation model (DEM)
- sensor and orbit parameters of each SAR image
- ground control points
- calibration information

The selection of the reference image is a crucial point in the snow mapping procedure. Potential reference images available for this study were acquired on 19 October 1992 and 8 March 1993. The October image was chosen as the reference image, because of better contrast in the lower parts of the valleys, where melting of snow occurred during the March surveys. The sensor and orbit parameters are extracted from the SAR CEOS header information and includes position and velocity vectors, heading angle of the sensor, and incidence angle of the SAR to a reference point. The parameter requirements depend on the geocoding and SAR image simulation software. Figure 10.4 shows the sections of the ascending and descending PRI images of 6 July 1992 covering the test site Ötztal.

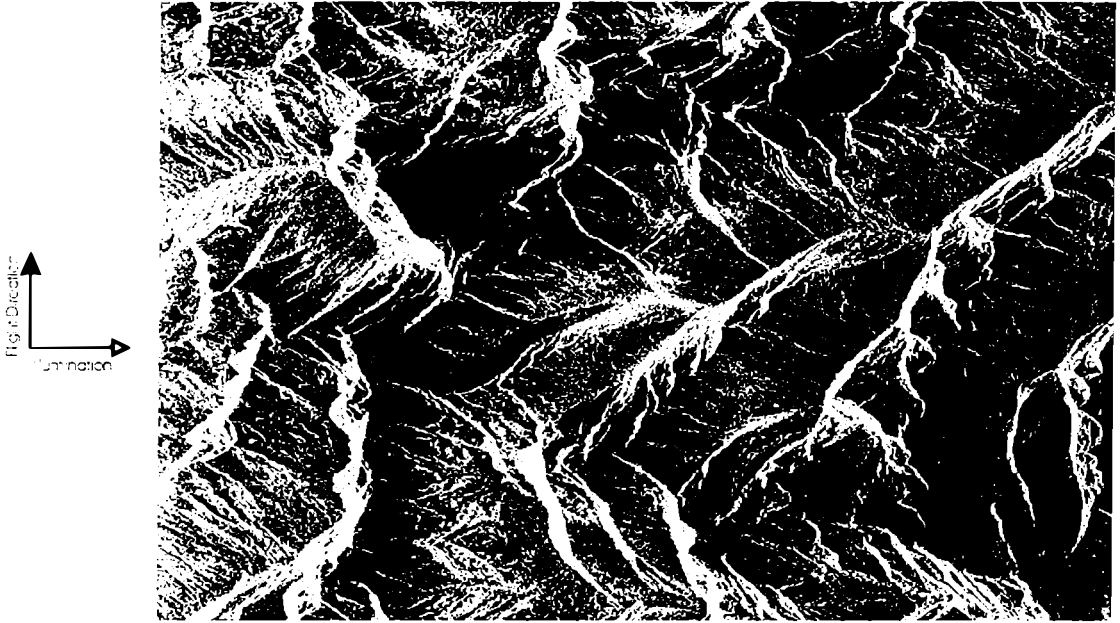
10.2.1.2 Co-registration, calibration, and lowpass filtering of repeat-pass images

In order to detect changes on the earth surface the σ^0 -ratio of the wet snow versus the reference image is calculated for both passes, which requires an accurate coregistration of the images. During the first multidisciplinary phase (phase-C) ERS-1 followed accurate repeat orbits with a 35-day cycle. For repeat passes the incidence angle of the radar signal on the observed areas was repeated within fractions of a degree. Geometric and radiometric distortions introduced by the topography are generally well reproduced. In mountainous regions with steep foreslopes, large areas with drastic transitions in backscatter may be covered in just one pixel. Registration of repeat pass images is straightforward, and usually a translational shift of the PRI scenes is sufficient for this task.

The misregistration of the snow images in respect to the reference image was determined by cross-correlation of image chips extracted from the original PRI amplitude data (pixel spacing $12.5 \times 12.5 \text{ m}^2$) with window sizes between $51 \times 51 \text{ pixels}^2$ and $301 \times 301 \text{ pixels}^2$. For mountainous regions stable features, such as bright layover and foreshortening regions, which preserve their shape in repeat pass images, can be found. At first both images are roughly matched with an accuracy of about 1 to 2 pixel. Then the cross-correlation matrix in azimuth and range direction was calculated for each position of the image chip. After cubic interpolation of the cross-correlation matrix by a factor of 10, the subpixel shift of the snow versus the reference image was determined. Table 10.1 shows examples of the matching quality for ERS-1 PRI scenes of the test site Ötztal. For most of the images used here the misregistration is less than 12.5 m in azimuth and range. Only for the descending image on 6 July 92 (table 10.1) the matching shows a trend in the range direction. If resampling is necessary the statistical distribution of the original should be preserved [8].

Due to the multiplicative nature of the algorithm absolute calibration is in principle not necessary for change detection. But when time sequences of images are analyzed calibration differences of the individual images may become visible in the temporal sequence, which may lead to misinterpretation. In the case of ERS it is proposed to correct the snow and reference image for scene specific corrections, such as replica power variations or the ADC-loss. Processor specific corrections are only necessary if the images have been processed by different PAFs or processor versions; these corrections include antenna power gain, range spreading loss, and calibration constant $K_{\sigma^0}(\theta_{ref})$. Terrain specific

Ascending



Descending

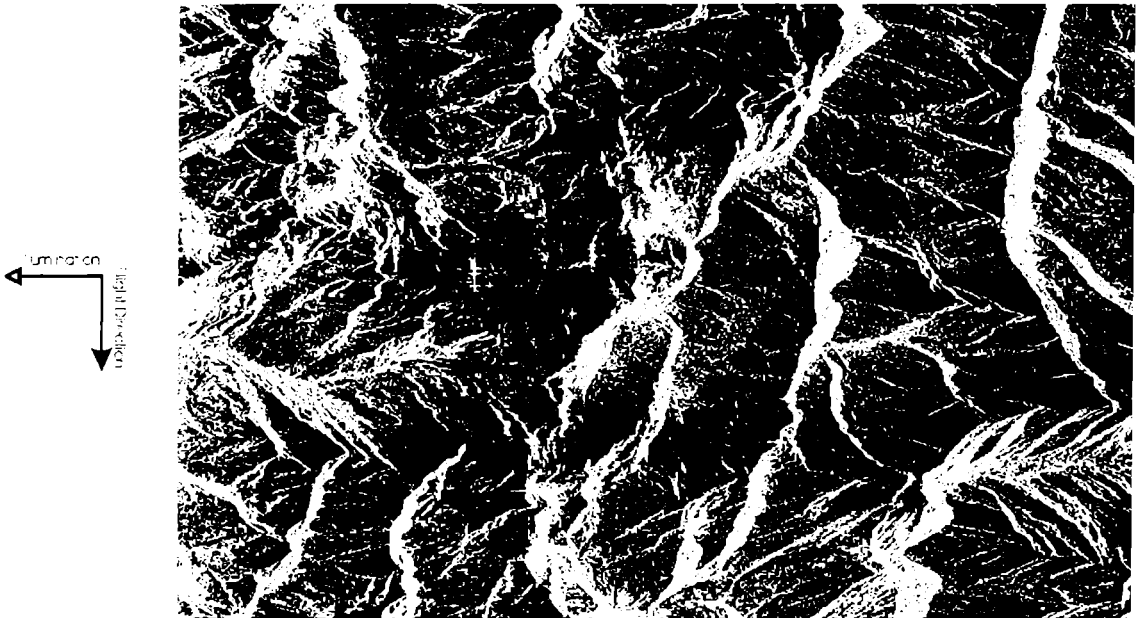


Figure 10.4: ERS-1 PRI images of ascending (top) and descending (bottom) orbit of 6 July 1992 covering the test site Ötztal.

	Ascending pass			Descending pass		
Rng	Azimuth position			Azimuth position		
	early time	center	late time	early time	center	late time
near	(0.3,0.2)	(0.2,0.1)	(0.4,0.1)	(-2.6, 0.8)	(-2.6, 1.0)	(-2.7, 0.9)
	(0.3,0.2)	(0.5,0.2)	(0.3,0.2)	(-1.5, 0.6)	(-1.4, 0.6)	(-1.7, 0.6)
mid	(0.5,0.3)	(0.4,0.1)	(0.5,0.1)	(-0.5, 0.6)	(-0.2, 0.7)	(-0.6, 0.5)
	(0.5,0.2)	(0.5,0.2)	—	(0.5, 0.4)	(0.9, 0.4)	(0.9, 0.6)
	(0.6,0.2)	(0.5,0.1)	(0.6,0.1)	(1.9, 0.5)	(1.8, 0.4)	(2.2, 0.5)
far				(2.5, 0.5)	(2.6, 0.4)	(2.6, 0.3)

Table 10.1: Matching accuracy after linear shift of original PRI data covering the Ötztal test site (size: 2700 pixel in range, 1500 pixel in azimuth) of 6 July 1992 and 19 October 1992, ascending and descending pass. Image chip size: 201 x 201 *pixel*², cross-correlation of image chips higher than 0.6. Matching vector: (range-shift, azimuth-shift) in units of PRI pixel spacing.

corrections need not to be applied, because they are canceled by forming the ratio of the snow to reference image (chapter 4).

To increase the effective number of looks the PRI images were block averaged by 2×2 pixels² and then speckle filtered. The effect of several speckle filters on the ratio image, calculated in the next step, is discussed in section 8.4. According to this analysis a Frost filter of 5×5 pixel² and a damping factor $A = 2$ was applied. The ratio images for the descending and ascending orbit are calculated on a pixel by pixel basis. The ratio for the (i, j) pixel is given by

$$r_{pass} = 10 \log_{10} \left(\frac{\sigma_{ws,pass}^{\circ}}{\sigma_{ref,pass}^{\circ}} \right) \quad (10.5)$$

The indices ws , ref , and $pass$ specify the wet snow image, the reference image, and the ascending or descending pass respectively.

Geocoding of the images is not necessary for the snow detection process itself, but it is a crucial point for the combination of information from crossing orbits (chapter 5).

10.2.1.3 Classification rule for snow covered areas

In this step the preprocessed, geocoded snow and reference image of the same orbit as well as the corresponding incidence angle map, layover and shadow masks are involved. The classification rule is applied pixel by pixel based on the decisions

$$\begin{array}{lll}
 \theta_{i,\min} < \theta_i(i, j) < \theta_{i,\max} & \text{— no —} & L_{pass}(i, j) = \text{yes} \\
 \downarrow & & \\
 \text{Layover or Shadow} & \text{— yes —} & L_{pass}(i, j) = \text{yes} \\
 \downarrow & & \\
 r_{pass}(i, j) < TVAL & \text{— no —} & I_{pass}(i, j) = \text{snowfree} \\
 \downarrow & & \\
 I_{pass}(i, j) = \text{snow covered} & & \\
 L_{pass}(i, j) = \text{no} & &
 \end{array} \quad (10.6)$$

The determination of the value of the threshold for snow detection, $TVAL$, will be discussed later in section 10.2.2. The first decision excludes all pixels with very steep and with grazing incidence angles. For this study values of $\theta_{i,\min} = 17^\circ$ and $\theta_{i,\max} = 78^\circ$ were selected empirically. Layover and shadow zones are excluded by the second decision. The third decision identifies the snow areas using the temporal change of σ° . It classifies a pixel as snow covered or snow free. The results of this procedure are images (for ascending and

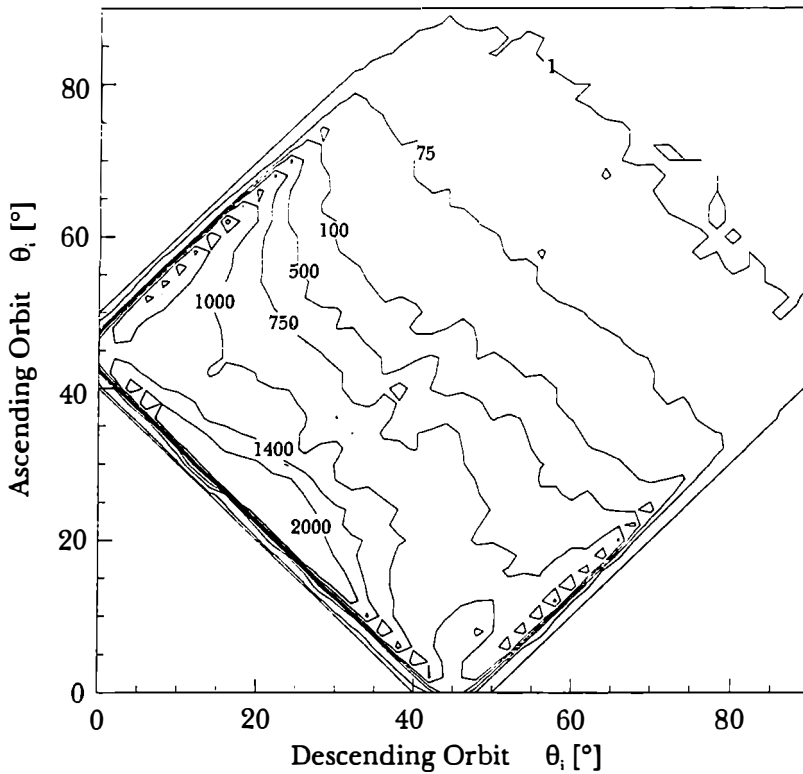


Figure 10.5: Two dimensional histogram of local incidence angle θ_i for pixels in test site Ötztal as seen in ascending and descending pass of ERS-1 (layover regions are not taken into account).

descending pass) containing the information I_{pass} (snow cover map) and a binary mask of areas L_{pass} (residual layover, shadow, and excluded incidence angles).

10.2.1.4 Combination of snow maps of ascending and descending orbits

Due to crossing of ascending and descending orbits the same surface elements are seen at different local incidence angles. For investigations of the Ötztal test site the ascending orbit is more suitable in the region of Hintereisferner, because the layover obscures large parts of this area in the descending image. On the other hand for the lower part of Gepatschferner the descending image is more suitable. For combining images of crossing orbits the pixel is taken from that scene with the higher incidence angle. Figure 10.5 shows a two dimensional histogram of the number of pixels as a function of their incidence angle in the ascending and descending ERS-1 images (layover regions are excluded). The total number of pixels is 633196. E.g. 32% of the pixels with $10^\circ \leq \theta_i < 12^\circ$ in the ascending pass are seen at incidence angles between 36° and 40° in the descending pass, respectively.

For the combination of ascending and descending passes layover, shadow and improper incidence angles must be taken into account. The combination rule, applied pixel by pixel,

is defined as

$$\begin{aligned}
 \text{for } L_{asc} = \text{yes} \text{ and } L_{des} = \text{yes} &\Rightarrow L_{final} = \text{yes} \\
 \text{for } L_{asc} = \text{yes} \text{ and } L_{des} = \text{no} &\Rightarrow I_{final} = I_{des} \\
 \text{for } L_{asc} = \text{no} \text{ and } L_{des} = \text{yes} &\Rightarrow I_{final} = I_{asc} \\
 \text{for } L_{asc} = \text{no} \text{ and } L_{des} = \text{no} &\Rightarrow \\
 \Rightarrow \begin{cases} \theta_{i,asc} > \theta_{i,des} &\Rightarrow I_{final} = I_{asc} \\ \theta_{i,asc} < \theta_{i,des} &\Rightarrow I_{final} = I_{des} \\ \theta_{i,asc} = \theta_{i,des} &\Rightarrow I_{final} = \min(I_{asc}, I_{des}) \end{cases}
 \end{aligned} \tag{10.7}$$

where L_{final} is the remaining area of layover and shadow zones. and I_{final} contains the merged information. In the Ötztal test site the loss of information due to incidence angle effects is reduced from 35.7 % and 40.5 % in ascending and descending images to 7.7 % in the combined image.

Some problems for snow detection may result from different conditions during the day and the night pass (see section 7); e.g. when due to solar illumination the top layer of the surface melts during the day and refreezes in the evening. The resulting daily variation of r (figure 7.12 a and b) may influence the classified snow area depending on the pass from which a pixel is selected.

10.2.2 Temporal dynamics of snow extent by means of SAR

In this section the wet snow mapping procedure based on repeat pass SAR images is applied to a sequence of ERS-1 images, acquired between April 1992 and October 1992. The ERS-1 image acquired in October was selected as the reference image, whereas the images acquired on 27 April, 1 June, 6 July, 10 August and 17 September are used for snow classification. Depending on the surface conditions three types of snow images are distinguished, which will be presented here.

10.2.2.1 Estimation of the threshold TVAL

For estimation of the threshold TVAL the frequency distribution of r for snow free and snow covered areas was determined. For discriminating two targets by SAR the image statistics have to be taken into account. It depends on the number of looks and on the difference in r between both targets (section 8.3). Figure 10.6 shows the distribution of r (1 June 1992 versus 19 October 1992) and r (6 July 1992 versus 19 October 1992) for snow covered and snow free areas, which were classified based on the Landsat TM image of 29 June 1992. Due to the dynamics of snow melt the TM based snow extent on 29 June was smaller than the actual snow extent on 1 June and larger than the actual snow extent on 6 July. This explains the enhanced overlap of the two classes in figure 10.6. The modes of the histograms of snow covered and snow free areas are observed at about -7 dB and at about +2 dB, respectively. Assuming that the modes of r for each class are not affected by the differences in snow extent of the SAR and TM images, a threshold of -3 dB was determined (section 8.3) to separate the two classes. Examples of the effect of different thresholds on the SAR based snow extent are shown in section 10.2.3.

10.2.2.2 Late winter conditions

In late winter the top snow layer may melt in the valleys during the day, while the snow pack is still dry on the high glacier plateaus. Such conditions were observed during the field campaign in April 1992 (chapter 7.1.1). Figure 10.7 shows the ERS-1 based snow cover map from 27 April 1992. Because the snow on the high glacier plateaus was dry

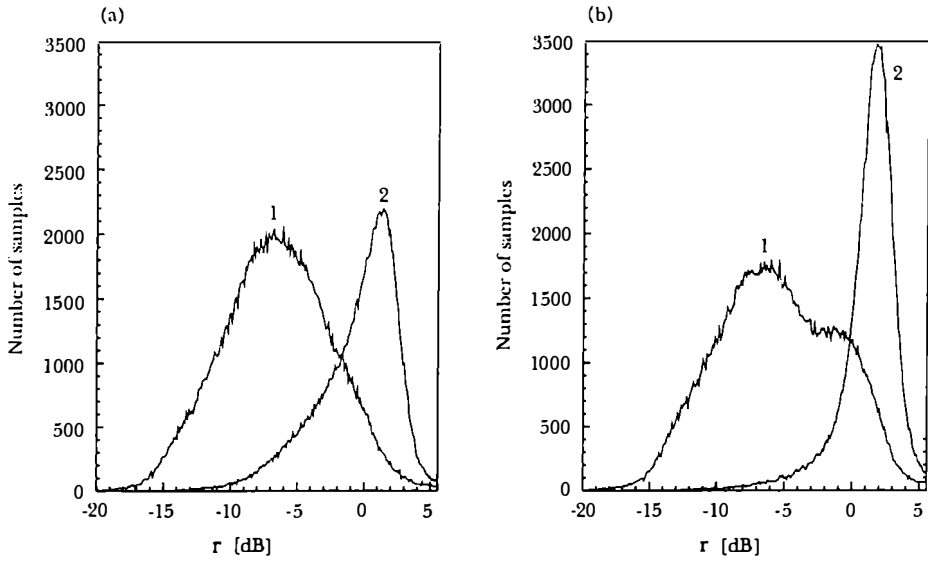


Figure 10.6: Frequency distribution of the ratio r derived from ERS-1 images (2×2 pixel averaged and then Frost filtered with $A=2$, 5×5 pixel² window size) of (a) 1 June 1992 and (b) 6 July 1992 for areas covered by snow (curve 1) and for snow free areas (curve 2) on 29 June 1992, as derived from a Landsat TM image.

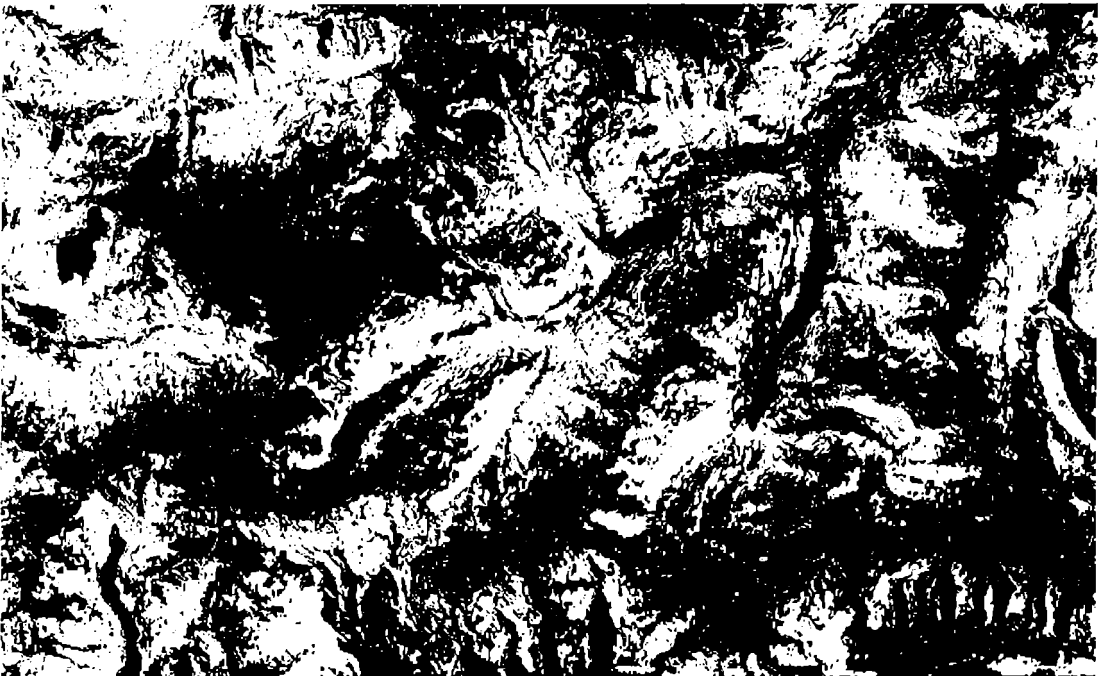


Figure 10.7: Wet snow cover based on ERS-1 SAR images from 27 April 1992 (snow image) and 19 October 1992 (reference image). Threshold: -3 dB: wet snow cover (white), dry snow or snow free (grey), remaining layover (black).

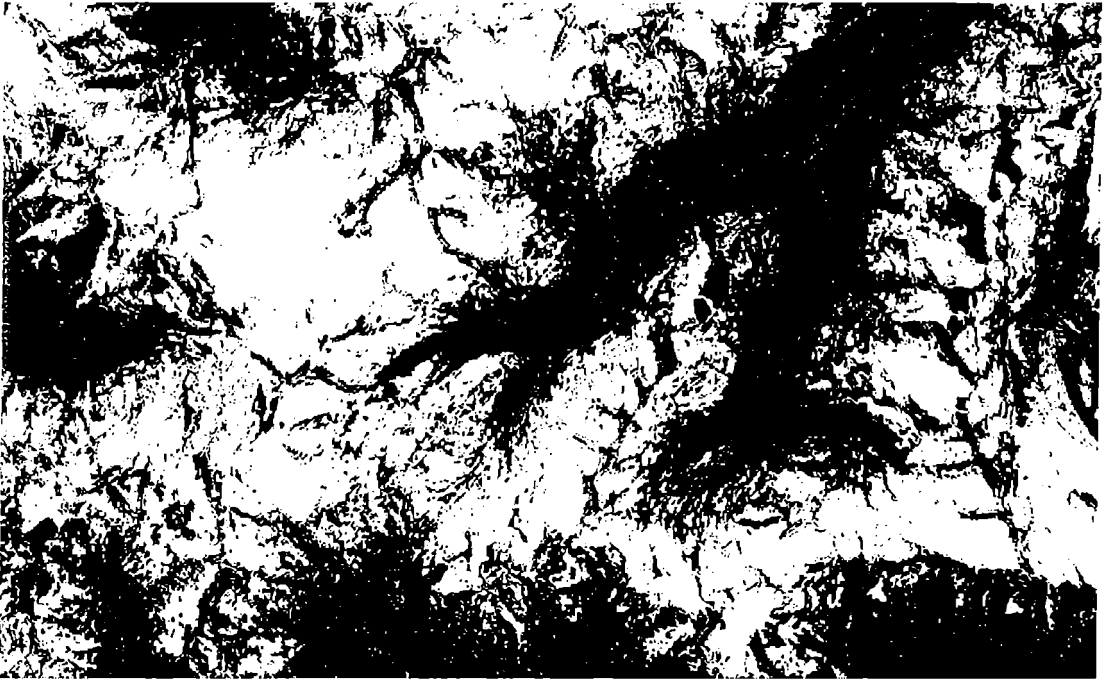


Figure 10.8: Wet snow cover based on ERS-1 SAR images from 1 June 1992 (snow image) and 19 October 1992 (reference image). Threshold: -3 dB. Wet snow cover (white), dry snow or snow free (grey), remaining layover (black).

they are classified as snow free. Wet snow is detected only in lower valleys and on slopes facing to the sun.

10.2.2.3 Spring conditions

In general May to July is the main melting period in high alpine regions and the most interesting for observing the seasonal snow cover. The snow pack at all altitudes becomes wet, at lower elevations the snow cover is patchy and the snow line retreats. Depending on the weather the snow extent may decrease significantly within a few days. On the high glacier plateaus the winter snow surface melts during the day and refreezes during the night forming a surface crust. For these conditions SAR is a good tool for monitoring snow cover changes. Figures 10.8 and 10.9 show the SAR detected snow extent on 1 June and 6 July 1992. The retreat of the snow line can be clearly detected (see section 10.2.3).

10.2.2.4 Summer conditions

At the end of the main melting period most of the snow cover on unglaciated areas had disappeared, and only some patches of snow may be found. Three surface types (snow, firn, and glacier ice) can be identified on the glaciers. Such conditions were observed during ERS-1 SAR surveys on 10 August 1992 and 14 September 1992. The classes vegetation, rocks/moraines and glacier ice can barely be discriminated by means of ERS-1 only. Wet snow areas can be very well identified in the ice-free areas, but on glaciers this is more difficult. It is obvious from the signature analysis in chapter 7 that snow and firn on glaciers can barely be discriminated. This is confirmed by the analysis of the frequency distribution of the ratio r derived from the ratio image 10 August versus 19 October 1992 with snow and firn masks based on the Landsat TM classification of 16 August 1992 (figure

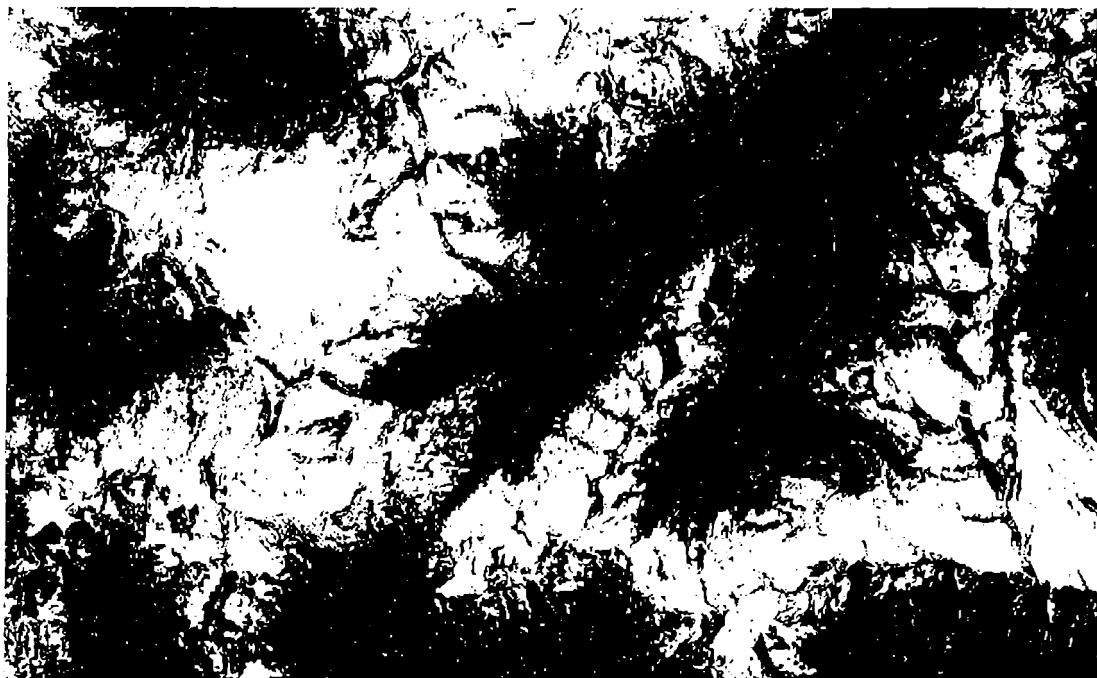


Figure 10.9: Wet snow cover based on ERS-1 SAR images from 6 July 1992 (snow image) and 19 October 1992 (reference image). Threshold: -3 dB. Wet snow cover (white), dry snow, snow free or glacier ice (grey), remaining layover (black).

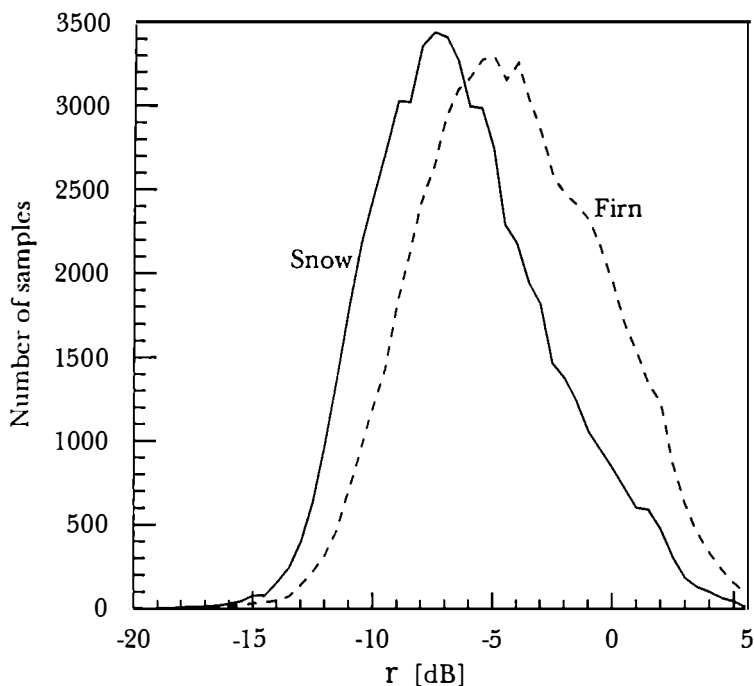


Figure 10.10: Distribution of the ratio r of backscattering coefficient of 10 August 1992 versus backscattering coefficient of 19 October 1992 for snow and firn areas, as derived from Landsat TM of 16 August 1992.

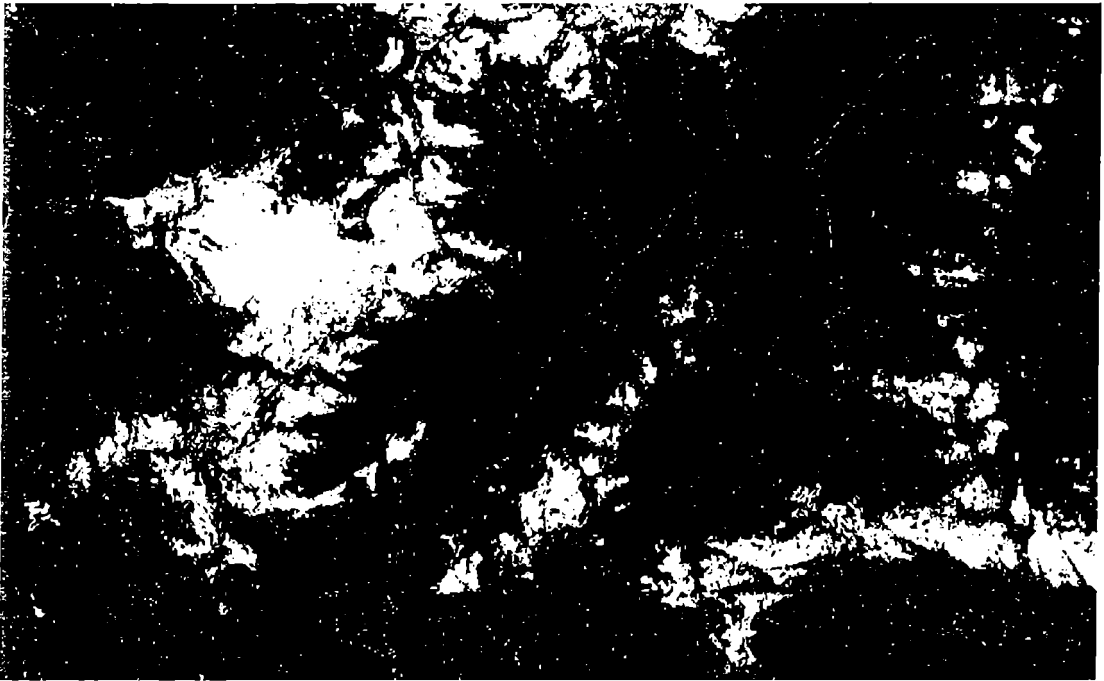


Figure 10.11: Wet snow cover from ERS-1 SAR images of 14 September 1992 (snow image) and 19 October 1992 (reference image). Threshold: -3 dB. Wet snow cover (white), snow free and glacier ice (grey), remaining layover (black).

10.10).

The reason is that snow, accumulated in the recent winter, has similar scattering properties in the microwave region as firn, which is snow from previous years, whereas the optical albedo is different. The modes of the frequency distribution of the ratio r of snow and firn are only 2 dB apart ($\Delta\bar{r} = r_{firn} - r_{snow} = 2$ dB). From section 8.3 this would require more than 64 effective looks to discriminate firn from snow with a probability of error lower than 10%. For snow mapping purposes snow and firn are treated as one class. Misclassification of this class snow/firn as glacier ice is observed when the snow/firn surface is very rough and consequently backscattering is high. Figure 10.11 shows the SAR based snow extent on 14 September 1992.

10.2.3 Comparison of SAR based and TM based snow maps

The comparison with TM based snow extent enables the quantitative estimation of the quality of SAR based snow maps. Because of the high temporal dynamic of snow extent (especially during the main melting season) SAR and optical images should be acquired at the same time. In this section SAR based snow maps are compared with Landsat TM images from 29 June 1992 and 16 August 1992, acquired 6 days before and after the SAR surveys.

10.2.3.1 ERS-1 SAR images of 1 June and 6 July versus TM image of 29 June

Because SAR and TM data are acquired at different dates (ERS-1: 1 June 1992 and 6 July 1992, TM: 29 June 1992) a pixel by pixel verification is not appropriate to estimate the quality of the SAR based snow maps. But the sequence of the three images in combination

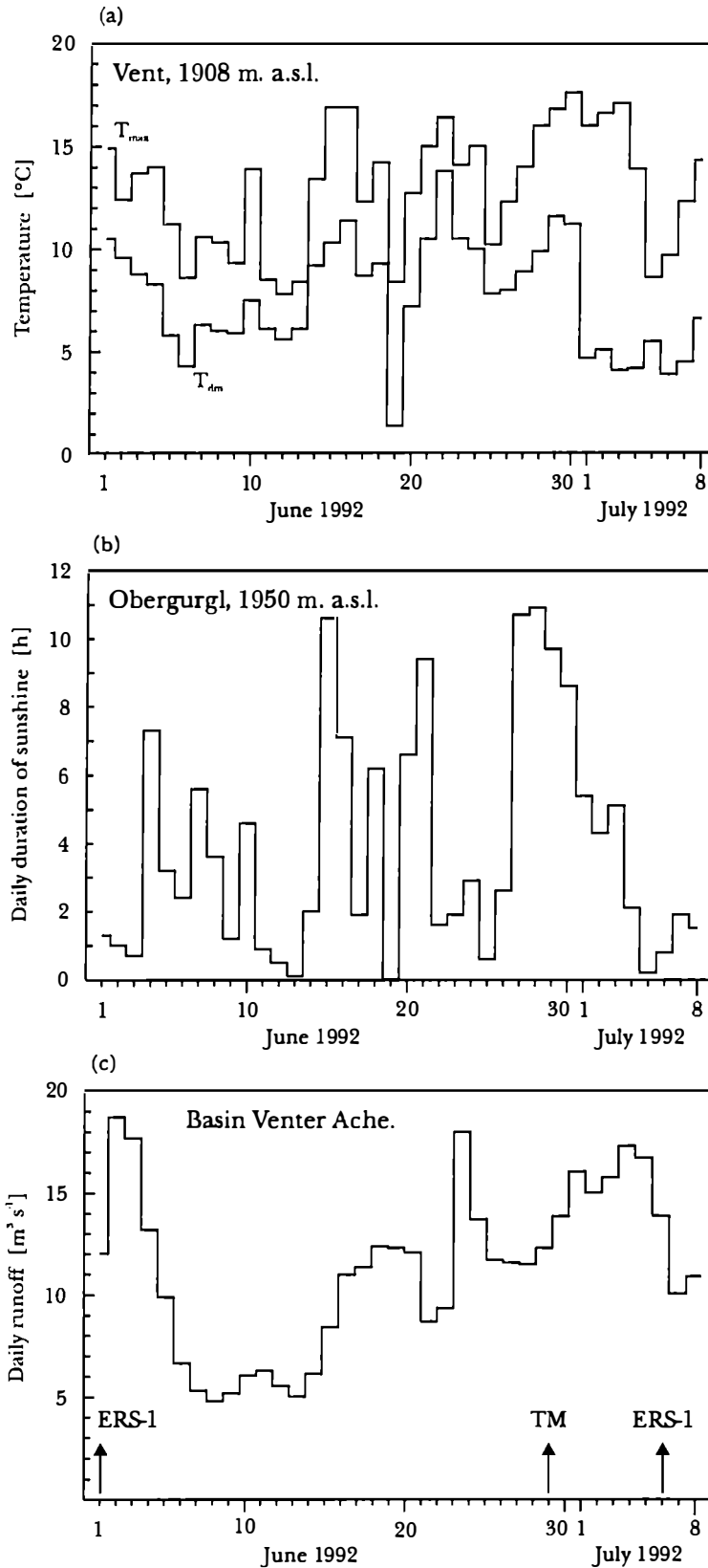


Figure 10.12: Maximum 2 m air temperature (T_{max}) and daily mean 2 m air temperature (T_{dm}) in Vent, daily duration of sunshine in Obergurgl and mean daily runoff of the basin Venter Ache. Dates of ERS-1 and Landsat TM image acquisition are marked by arrows. (sources: Inst. f. Meteorologie und Geophysik, Univ. Innsbruck, Hydrolog. Jahrbuch 1992)

with records of meteorological parameters reveals the temporal change of snow extent. On the other hand this analysis demonstrates the synergistic use of SAR and optical images for snow monitoring.

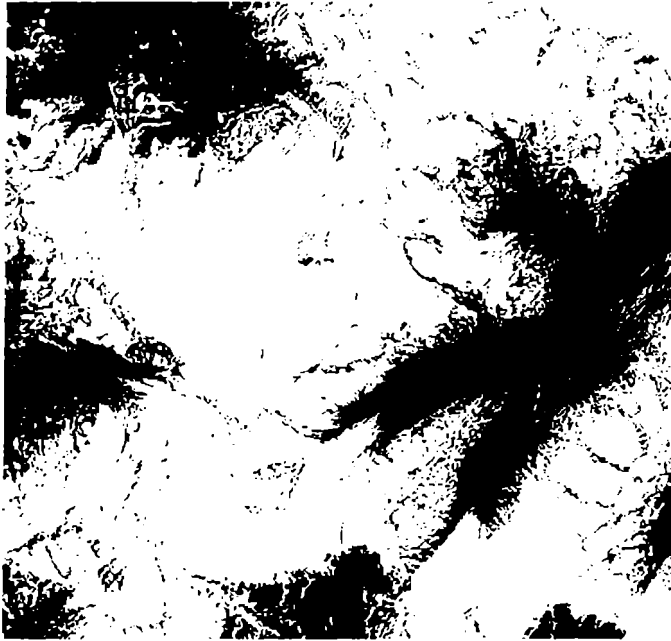


Figure 10.13: Classification based on Landsat TM 29 June 1992 ; snow covered (white), snowfree (grey), clouds (black).

Meteorological and hydrological parameters, such as daily duration of sunshine, maximum and mean daily temperature¹ and runoff measured at climatological and hydrological stations within the test site are strongly related to snow melt. Warm temperatures, long duration of sunshine and high runoff values indicate significant melting in the middle of June and in end of June/early July (figure 10.12). At Venter maximum temperatures of about 18°C and daily mean temperatures up to 14°C were observed. Temperatures at the synoptic station Zugspitze (2960 m a.s.l.), situated in the north of the test site, reached 7.5°C . The runoff measurements of the basin Venter Ache, which covers a large part of the test site, are related to the amount of melted snow. They show the highest values in the period 29 June to 5 July.

Figure 10.13 shows the snow extent based on the Landsat-5 TM image of 29 June 1992; figure 10.14 and 10.15 show the ERS-1 SAR based snow extent from 1 June and 6 July with thresholds of -2 dB and -3 dB. In general the SAR classification is more noisy, especially in those regions with low $\Delta\bar{\tau}$ (section 8.3). For example assuming 8 effective looks and a value of $\Delta\bar{\tau} \simeq -10 \text{ dB}$ the probability of error PE is about 3% (figure 8.5; only valid for gamma distributed homogeneous targets). But $\Delta\bar{\tau}$ may be smaller locally.

In spite of the different dates the confusion matrix of the ERS-1 and TM snow maps provides some hints on the classification accuracy (table 10.2) [59]. For comparison between the Landsat TM snow classification of 29 June 1992 and the ERS-1 snow map of 6 July 1992 it can be assumed that the snow free area in the Landsat TM classification was also snow free during the ERS-1 SAR overflight. The agreement for the snow free areas of the two dates is 95% with a threshold of -3 dB.

¹ Here the daily mean air temperature was calculated according to $T_{dm} = (\sum_1^3 T_{xxh}) / 3$, where T_{xxh} are the 2 m air temperatures measured at 7h, 14h and 21h.

(a) ERS-1 SAR 1 June 1992 TVAL = -2 dB



(b) ERS-1 SAR 1 June 1992 TVAL = -3 dB

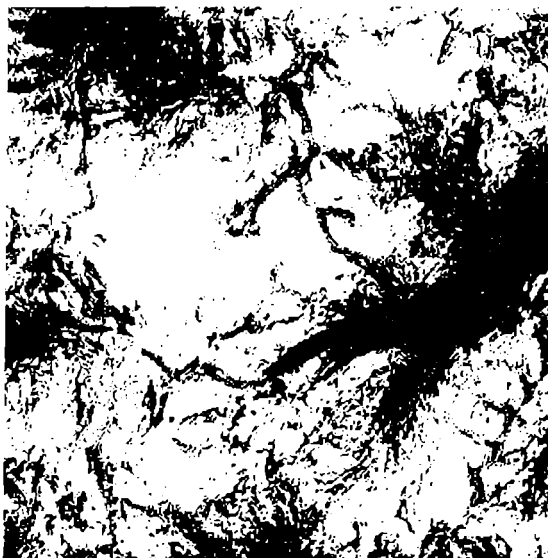


Figure 10.14: Classification based on ERS-1 SAR images of 1 June 1992 for thresholds of -2 dB (a) and -3 dB (b): snow covered (white), snow free (grey), layover and foreshortening (black).

(a) ERS-1 SAR 6 July 1992 TVAL = -2 dB



(b) ERS-1 SAR 6 July 1992 TVAL = -3 dB



Figure 10.15: Classification based on ERS-1 SAR 6 July 1992 for thresholds of -2 dB (a) and -3 dB (b): snow covered (white), snow free (grey), layover and foreshortening (black).

TM	TVAL=-2 dB				TVAL=-3 dB			
	SAR 1Jun92		SAR 6Jul92		SAR 1Jun92		SAR 6Jul92	
	SC	SF	SC	SF	SC	SF	SC	SF
SC	86.3	13.7	75.7	24.3	80.6	19.4	69.7	30.3
SF	26.9	73.1	7.0	93.0	19.6	80.4	4.7	95.3
Overall: 81.4%		Overall: 82.2%		Overall: 80.5%		Overall: 79.2%		

Table 10.2: Confusion Matrix in % of TM Classification of 29 June 1992 and ERS-1 SAR classifications of 1 June and 6 July 1992 (ratio threshold -2 dB, -3 dB). The temporal difference between SAR and TM has to be kept in mind. SC...Snow Covered including firn, SF...Snow Free including glacier ice, rocks, moraines and low vegetation. Layover, shadow regions and cloud covered areas are excluded. Total number of samples: 407343.

About 70% (TVAL=-3dB) or 76% (TVAL=-2dB) of the snow covered area from TM is also classified as snow by ERS-1 SAR on 6 July 1992. Even by taking into account the decrease of the snow extent between TM and ERS-1 image acquisitions the SAR seems to result in lower snow area, as evident from the comparison of the TM snow map of 29 June and the SAR snow map of 1 June. The overall agreement (weighted by the number of pixels of each class [59]) is about 80%.

For applications in hydrology the snow covered area is of main interest. Figure 10.16 shows the snow coverage as a function of the altitude derived from Landsat TM (curve 2) and ERS-1 SAR images (curve 1 and 3). The altitude distribution of the snow coverage gives further information about the snow melt. The decrease of snow extent in the lower parts of the basin can be well documented by the synergy of SAR and TM. Above 3000 m, where glaciated areas prevail, the TM snow extent is slightly larger than the SAR based snow coverage. The SAR analyses of 1 June and 6 July show only minor differences of the snow covered area at high altitudes, which agrees well with field observations. In summary, SAR tends to underestimate the snow extent in regions with high percentage of snow cover. Because of the high albedo and because of the saturation of visible bands TM tends to overestimate in areas with patchy snow cover.

10.2.3.2 ERS-1 SAR of 10 August versus Landsat TM 16 August 1992

The Landsat TM image was acquired 6 days after the ERS-1 SAR acquisition. Because the temporal change in snow extent is much smaller than in spring, the time difference is less important. Therefore this image pair enables better pixel by pixel comparison between optical and SAR derived snow maps than the June/July images. Figure 10.17 and figure 10.18 show the snow extent based on Landsat TM, acquired on 16 August 1992, and based on ERS-1 SAR data from 10 August 1992, for a threshold of -3 dB. Because the image acquisition of the descending pass of ERS-1 failed, 35% of the area is excluded due to layover and foreshortening. On glaciers snow (accumulation area) and firn represent a class in the SAR analysis. 82% of the snow/firn class in the TM classification is also detected by SAR (table 10.3). The overall agreement of both classifications is more than 90 %. For comparison a lower threshold of -4 dB was applied, which has the effect that the snow area by SAR is reduced, and the fraction of misclassified snow free pixels increases.

10.2.4 Temporal consistency of SAR based snow maps

During the melting period the temporal consistency of snow maps can be assessed. It can be assumed that areas (pixels) which are snow free at a certain date should still be snow

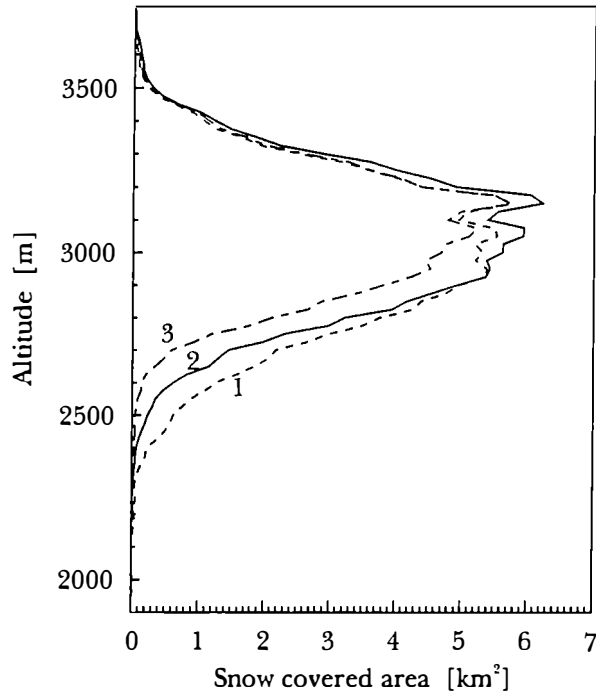


Figure 10.16: Snow covered area sampled for altitude zones of 25 m. ERS-1 SAR 1 June 1992 (curve 1), Landsat TM 29 June 1992 (curve 2), ERS-1 SAR 6 July 1992 (curve 3).

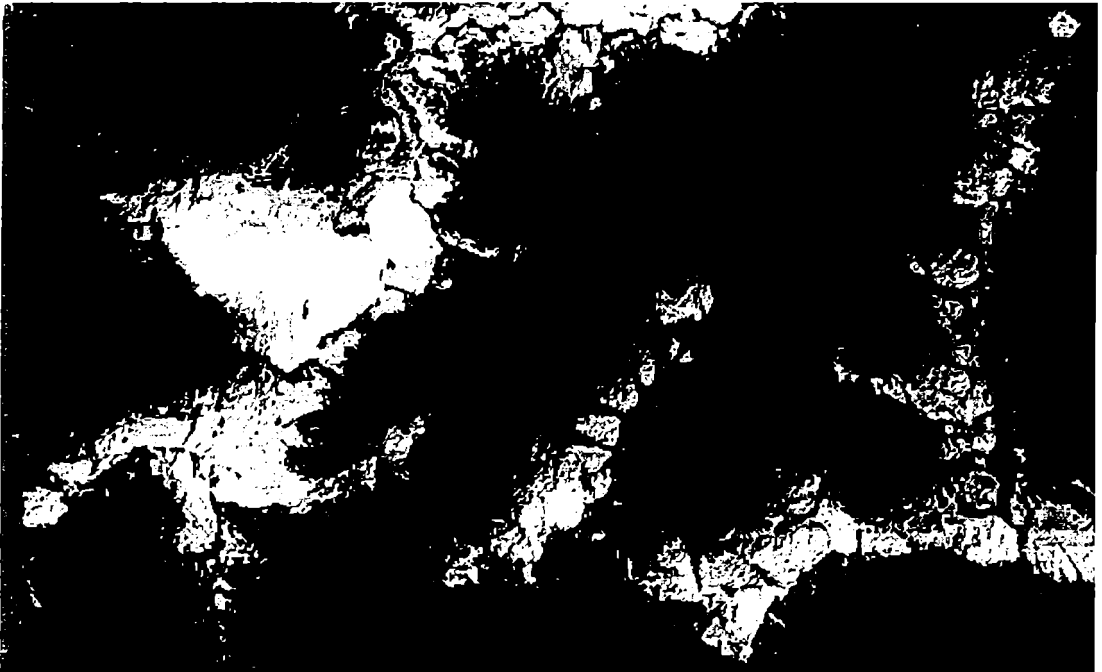


Figure 10.17: Classification based on Landsat- TM, 16 August 1992: snow free (grey), snow (white), firn (light grey), glacier ice (black).

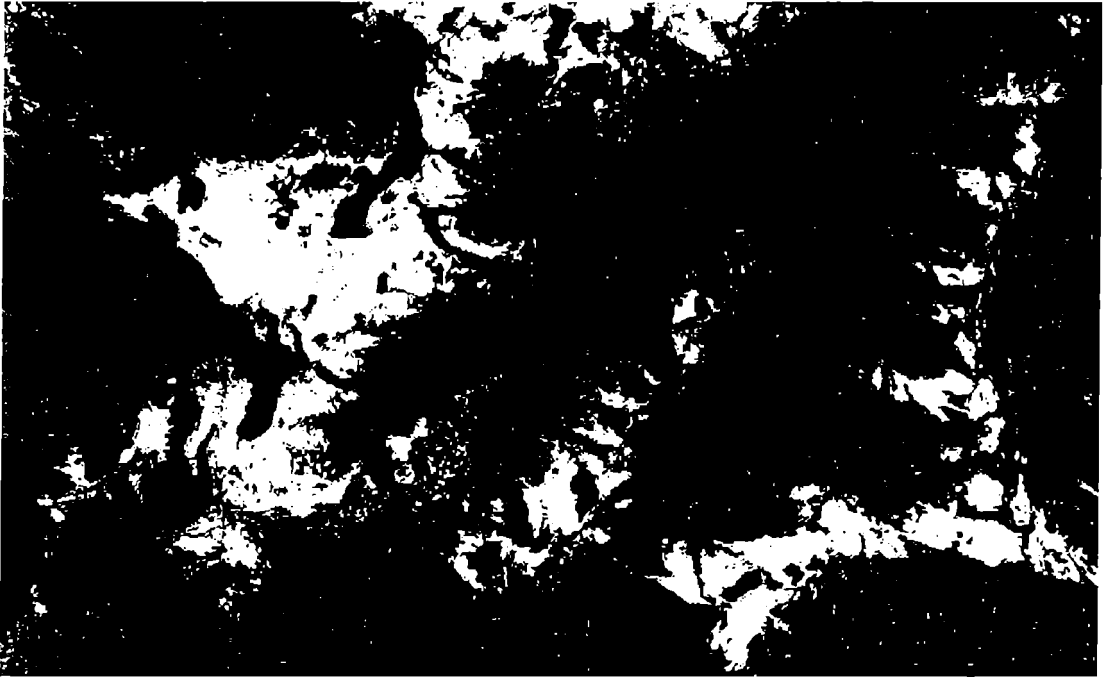


Figure 10.18: Classification based on ERS-1 SAR image, 10 August 1992: snow free and glacier ice (grey), snow and firn (white), layover and shadow (black).

TM	TVAL=-3 dB		TVAL=-4 dB	
	SAR 10Aug92		SAR 10Aug92	
	SC	SF	SC	SF
SC	81.6	18.4	73.7	26.3
SF	6.5	93.5	4.3	95.7
	Overall: 90.7%		Overall: 90.6%	

Table 10.3: Confusion Matrix in % of TM Classification of 16 August 1992 and ERS-1 SAR classification of 10 August 1992 (threshold -3 dB left, -4 dB right). SC...Snow Cover including firn, SF...Snow Free including glacier ice, rocks, moraines and low vegetation. Layover, shadow regions are excluded. Total number of samples: 407343.

TVAL=-3 dB	SC _{1jun92}	SC _{6jul92}	SC _{14sep92}
SC _{1jun92}	—	—	—
SC _{6jul92}	3.2 %	—	—
SC _{14sep92}	1.0 %	0.9 %	—

Table 10.4: Percentage of pixels classified as snow covered, which belong to the snow free class on an earlier date (based on ERS-1 snow classification with TVAL=-3dB).

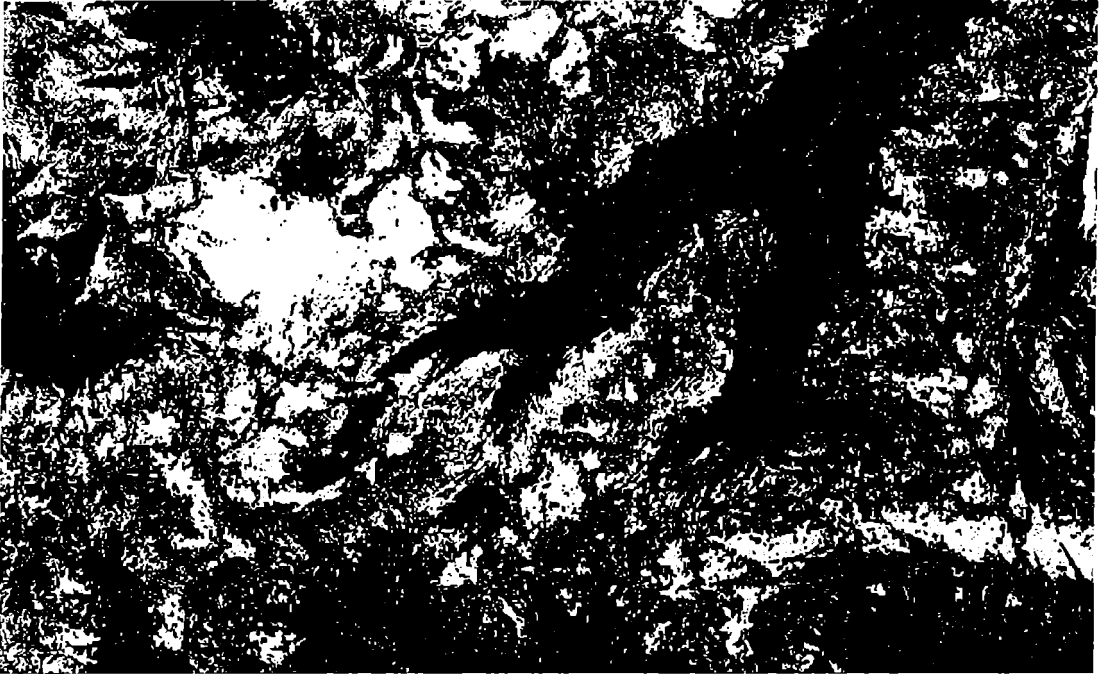


Figure 10.19: Snow cover retreat from 1 June to 6 July (white), 6 July to 14 September (medium grey), snow extent on 14 September (light grey); snow free at all dates (dark grey), layover (black).

free later in the season. This concept is in general valid during the main melting season, but it cannot be applied in the case of fresh snow fall. Table 10.4 shows the percentage of pixels classified as snow covered, which belong to the snow free class at an earlier date. About 3.2 % of snow free pixels in June are classified as snow in the July classification. This may have two reasons: the first is SAR image statistics (section 8.3), the second one is inaccuracy in geocoding and co-registration. The change in snow extent between two dates can also be directly determined by using the date with the lower snow extent than the reference image. Figure 10.19 shows the snow extent and the change in snow cover between 1 June 1992, 6 July 1992, and 14 September 1992.

10.2.5 Snow extent of the basin Venter Ache based on SAR

To demonstrate the applicability of the SAR wet snow maps for snow melt runoff modelling, the snow extent for the basin Venter Ache in the period April to September 1992 was determined [78]. Figure 10.20 shows a geocoded Landsat image from 16 August 1992 with the boundaries of the basin. The drainage basin covers an area of 164.7 km². According to the Landsat TM based classification from 17 September 1992 the area includes 38% glaciers. In table 10.5 the results of the snow cover analysis from the SAR data are listed. The basin is divided into glaciers and icefree areas for different elevation zones, the

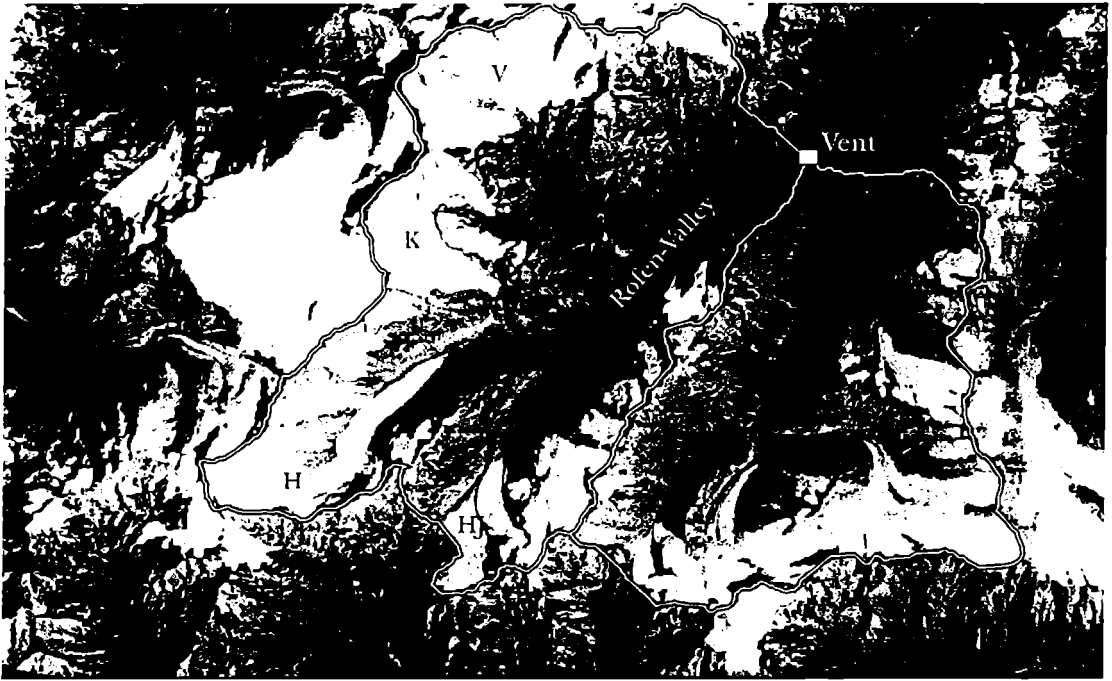


Figure 10.20: Basin of Venter Ache, with sub-basin of Rofenache (only left part).

snow extent and residual layover and foreshortening is given in per cent of the area of each elevation zone. For August only the image of the ascending orbit was available. Therefore the percentage of layover is much higher than for the other dates. In April the snow cover was dry in the higher parts of the basin. For this reason the snow extent based on SAR images is too small.

Elevation [m]	SF	A [km ²]	27 Apr [%]	1 Jun [%]	6 Jul [%]	14 Sep [%]	L _r [%]	10 Aug [%]	L _{asc} [%]
1800-2499	U	21.03	54	0	0	1	15	0	36
2500-2799	U	29.98	73	16	1	0	1	0	30
2800-2999	U	26.48	64 ^D	62	18	0	2	3	30
3000-3199	U	16.44	46 ^D	65	49	1	7	12	42
2500-2799	G	3.83	30 ^D	67	38	4	>1	2	7
2800-2999	G	11.90	26 ^D	95	91	18	>1	23	12
3000-3199	G	27.49	21 ^D	97	96	67	2	79	15
3200-3772	U&G	28.24	19 ^D	86	88	60	14	83	34

Table 10.5: Snow extent for basin Venter Ache, 1992, derived from ERS-1 SAR images for unglaciated (U) and glaciated (G) areas and different elevation zones of area A. SF specifies the surface type. L_r denotes the residual layover and foreshortening, L_{asc} denotes the layover and foreshortening for the ascending pass: ^D stand for predominantly dry snow conditions.

Chapter 11

SAR as a tool for glacier investigations

11.1 Introduction

Mass balance studies are concerned with changes in the mass of a glacier and the distribution of these changes in space and time. Climatic fluctuations cause variations in the amount of snow deposited on a glacier and in the amount of snow and ice lost by melting. These processes of mass change influence significantly the temporal advance or retreat of glaciers.

In several countries glaciers supply much of the water for hydroelectric power plants or irrigation. Glaciers act as natural reservoirs storing water as snow during winter and releasing it during warm summers, when water from other sources gets short. Mass balance studies determine the amount of water stored/released on glaciers and the expected variations from year to year [55].

11.1.1 Definitions

The gains and losses in the glacier's budget are represented by accumulation and ablation. Accumulation includes all processes adding mass to the glaciers, while ablation includes all losses. Accumulation and ablation areas are divided by the equilibrium line. Mass balance measurements at selected points are usually expressed as equivalent mass of water or as equivalent volume of water. The net balance b_n [kgm^{-2}] for a time period t_1 to t_2 at any point is given by the algebraic sum of accumulation b_c and ablation b_a [55]

$$b_n [kgm^{-2}] = b_a + b_c = \int_{t_1}^{t_2} (\dot{b}_c + \dot{b}_a) dt \quad (11.1)$$

where \dot{b}_c and \dot{b}_a are the accumulation and ablation rates given in kgm^{-2} per time unit. A mass balance year y can be defined as the period between two successive minima of glacier thickness, which corresponds in general to the end of the ablation period. Its length is about 365 days and can vary from year to year. In the Alps for practical purposes the mass balance year is usually specified as the period between $t_1 = 1$ October and $t_2 = 30$ September of the following year.

Mass balance measurements at many representative points distributed over the glacier can be integrated over the total glacier area S to determine the net balance of the total

glacier B_n :

$$B_n[kg] = \int_S b_n dS = \int_{S_c} b_c dS + \int_{S_a} b_a dS \quad (11.2)$$

At the end of a mass balance year the glacier area can be divided into areas of net accumulation S_c with $b_n > 0$ and areas of net ablation S_a with $b_n < 0$. The total glacier area is $S = S_c + S_a$. The average specific net mass balance \bar{b}_n is the most useful parameter for summarizing the change of a glacier during the year [55]. It is defined as

$$\bar{b}_n[kgm^{-2}y^{-1}] = \frac{B_n}{S} \quad (11.3a)$$

The parameter \bar{b}_n enables the comparison between glaciers of different size.

In order to determine B_n , the net mass balance at several representative points in the ablation and accumulation area is measured at the end of the balance year and integrated over S . Within the ablation area b_a is measured by means of ablation stakes; in the accumulation area b_c is derived from snow pits. This method requires significant man power, which is the reason why this kind of mass balance studies (also called direct glaciological method [32]) is carried out only on a few glaciers world wide [66]. Often the total mass balance is estimated manually from point measurements of the mass budget and from oblique pictures. The subjectivity of this method was investigated by Kaser *et al.* [35], when four experienced glaciologists analyzed independently from each other the same data set of the Weissbrunnferner, Ortler-Cevedale, Italy. The determined mass balances were within a range of $83 kgm^{-2}y^{-1}$, which corresponds to 14 % of the mean value.

11.1.2 Mass balance studies on Ötztal glaciers

A long record of mass budgets exists for a few glaciers in Ötztal, where investigations based on the direct glaciological method were carried out since 1952/53 on Hintereisferner and Kesselwandferner and since 1964/65 on Vernagtferner. Point measurements of b_n in the accumulation and ablation area together with oblique photographs are the basis for deriving the pattern of accumulation and ablation, and the parameters \bar{b}_n , S_c/S and the mean altitude of the equilibrium line ELA [66]. As shown in figure 11.1 a clear relation exists between these parameters. But these relations are characteristic for each glacier and may vary even for adjacent glaciers in the same mountain group [38]. Different glacier topography and different dynamic response times in respect to climatic changes may be reasons for these variations. To study the mass balance estimation from satellite images, \bar{b}_n and ELA are modeled as a function of S_c/S . Based on the least square method using singular value decomposition a polynomial was fitted to the data (figure 11.1), which has the form

$$Y = a_0 + a_1 (S_c/S) + a_2 (S_c/S)^2 + a_3 (S_c/S)^3 \quad (11.4)$$

where S_c/S is given in ‰ and Y stands for \bar{b}_n in $kgm^{-2}y^{-1}$ or ELA in m , respectively. For Hintereisferner, Kesselwandferner and Vernagtferner the corresponding coefficients a_i , $i = 0, 3$, are given in table 11.1.

Under certain conditions spaceborne and airborne remote sensing methods offer the possibility to estimate the mass balance of glaciers. This was demonstrated by Rott and Markl [66] using Landsat TM images over the Ötztaler Alps. From the satellite images S_c and S were determined at the end of the mass balance year, from which \bar{b}_n can be derived. For glaciers without any previous information about the mass balance, \bar{b}_n can only be roughly estimated. The use of optical images requires cloudless conditions at the end of the ablation period, which are not available every year. In the following section the

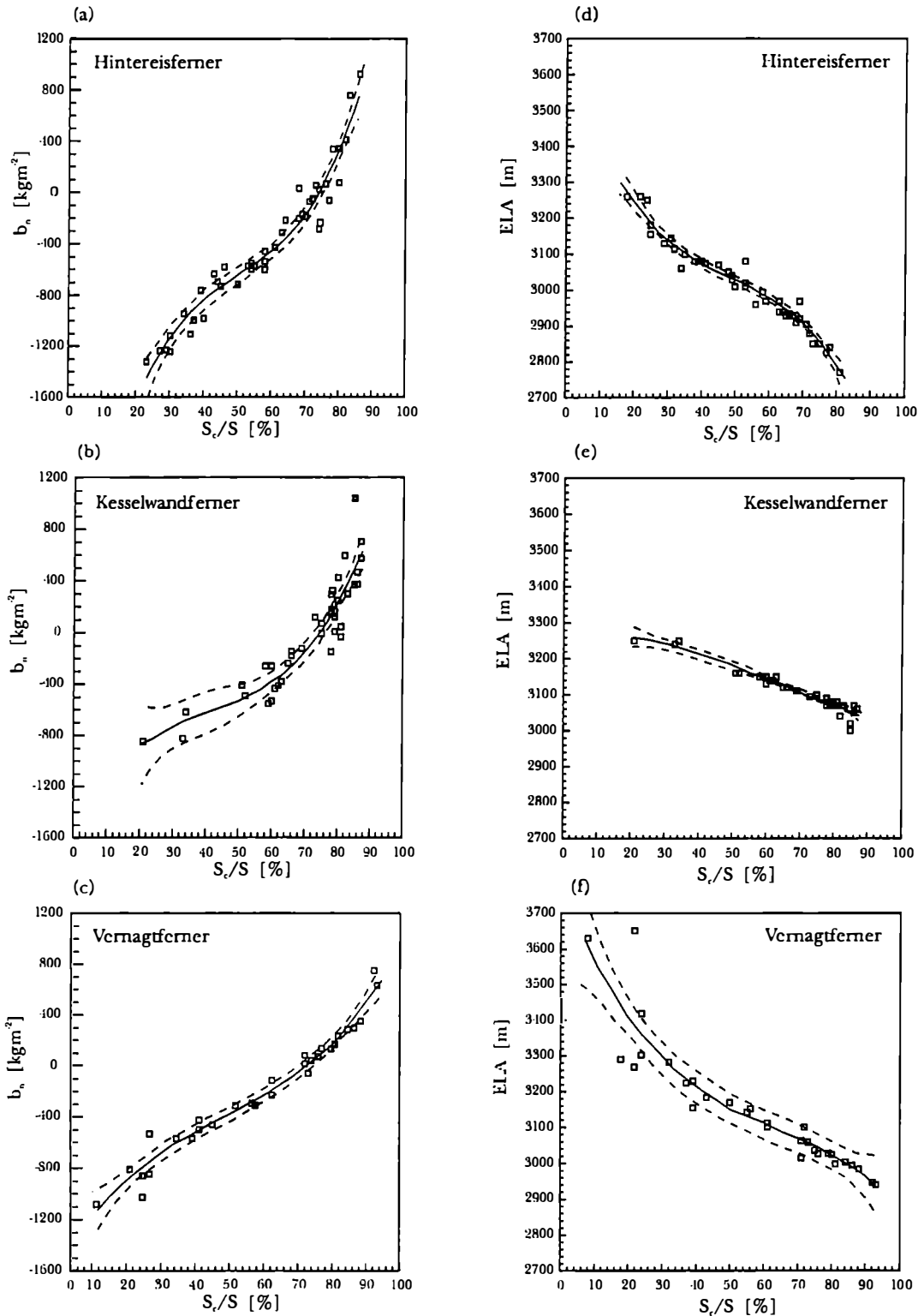


Figure 11.1: Relation of \bar{b}_n with S_c/S and ELA for Hintereisferner (a, d) and Kesselwandferner (b,e), data records from 1952/53 to 1994/95 and Vernagtferner (c, f), data record 1964/65 to 1993/94. Lines corresponds to polynomial fit of 3rd order, dashed lines indicate confidence limits of 95%.

Hintereisferner						
		a_0	a_1	a_2	a_3	R^2
\bar{b}_n	$\left[\frac{kg}{m^2y}\right]$	$-3.058 \cdot 10^3$	$1.265 \cdot 10^2$	$-2.420 \cdot 10^0$	$1.783 \cdot 10^{-2}$	0.95
ELA	$[m]$	$3.685 \cdot 10^3$	$-3.127 \cdot 10^1$	$5.476 \cdot 10^{-1}$	$-3.710 \cdot 10^{-3}$	0.96
Vernagtferner						
		a_0	a_1	a_2	a_3	R^2
\bar{b}_n	$\left[\frac{kg}{m^2y}\right]$	$1.402 \cdot 10^3$	$-3.772 \cdot 10^1$	$-5.253 \cdot 10^{-1}$	$3.812 \cdot 10^{-3}$	0.97
ELA	$[m]$	$3.780 \cdot 10^3$	$-2.404 \cdot 10^1$	$3.105 \cdot 10^{-1}$	$-1.610 \cdot 10^{-3}$	0.87
Kesselwandferner						
		a_0	a_1	a_2	a_3	R^2
\bar{b}_n	$\left[\frac{kg}{m^2y}\right]$	$-1.581 \cdot 10^3$	$5.140 \cdot 10^2$	$-1.022 \cdot 10^0$	$8.277 \cdot 10^3$	0.86
ELA	$[m]$	$3.278 \cdot 10^3$	$1.892 \cdot 10^{-1}$	$-5.635 \cdot 10^2$	$2.690 \cdot 10^4$	0.93

Table 11.1: Coefficients for polynomial function of eq. 11.4 3rd order to describe the relation of \bar{b}_n in $kgm^{-2}y^{-1}$ with S_s/S and equilibrium line (ELA). R^2 is the coefficient of determination. The polynomial fits are based on mass balance data records of Hintereisferner and Kesselwandferner from 1952/53 to 1994/95, Institut für Meteorologie und Geophysik, Univ. Innsbruck, and of Vernagtferner from 1964/65 to 1993/94, Bayerische Akademie der Wissenschaften, München.

wet snow mapping procedure (section 10) is extended to estimate the areal ratio and the mass budget of alpine glaciers based on SAR images.

11.2 Procedure for mass balance estimation based on SAR

The derivation of glaciological parameters from SAR data is based on the estimation of the areal ratio of the accumulation area S_c to the total glacier area S . The determination of S_c is mainly based on the snow mapping procedure described in section 10. The estimation of other glaciological parameters (such as the net specific mass balance and the altitude of the equilibrium line) requires additional knowledge. Figure 11.2 shows the extension of the snow mapping flowchart (figure 10.3) for glaciological applications.

For glacier applications the total glacier area is required. In SAR images glacier ice, bare soil and vegetation are difficult to discriminate in terms of σ^0 (section 7.2.3). Misclassifications occur often for rough ice surfaces, in particular crevassed zones, which show about the same σ^0 as ice free areas [80]. By inspection of SAR images trained experts may identify glacier boundaries in the SAR images due to texture and characteristic shape [73].

On the other hand, glacier boundaries can be well derived from optical images based on the clear difference in surface albedo between glaciers and ice free areas (chapter 9). In the Alps the annual variation of the glacier termini are only of the order of a few meters to a few tens of meters [66]. Therefore the glacier boundaries derived from optical images, which were acquired during the summer of a given year or even from the previous years, represent quite well the total glacier area $S = S_c + S_a$ for a period of a few years.

If the SAR image of a glacier includes layover and shadow regions S_c/S can be approximated by

$$\frac{S_c}{S} \simeq \frac{S_{c,sar}}{S - S_{ts}} \quad (11.5)$$

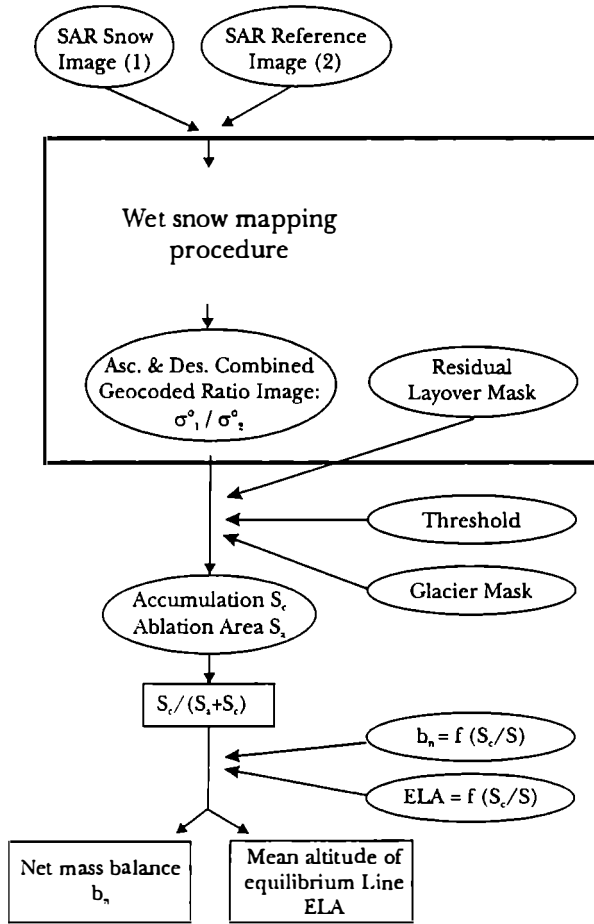


Figure 11.2: Flow chart for estimation of mass balance by means of multitemporal SAR.

TM	SAR		TM	SAR	
	snow	ice		snow	ice
snow	20203	16731	snow	54.7 %	45.3 %
ice	11860	57706	ice	17.0 %	83.0 %
Overall agreement: 73.1 %					

Table 11.2: Confusion matrix of Landsat TM channel 3 classification, 17 September 1992, and ERS-1 SAR data analysis, 14 September 1992, for snow and ice areas given in number of pixels (left) and in per cent (right).

where S_{ls} is the area of radar layover and shadow on the glacier, and $S_{c,sar}$ is the accumulation area determined by means of SAR over the area $S - S_{ls}$.

From the glaciological point of view the following definitions of snow and firn are used:

- snow: located above the equilibrium line and belongs to the accumulation area. It is mainly accumulated in the previous winter season.
- firn: located below the equilibrium line. Snow accumulated before the previous 1 October; firn and glacier ice belong to the ablation area.

The signature analysis in section 7.1.2 and 7.1.3 showed that snow and firn can barely be discriminated by single frequency C- and X-band SAR. Regarding this problem two approaches are possible. One possibility is to assume that the equilibrium line corresponds to the snow line at the end of the mass balance year. This may lead to significant errors, if the previous mass balance was more positive. The second approach is to reduce the threshold in the wet snow mapping procedure by 1 dB to 2 dB (figure 10.10) to exclude at least some parts of the firn areas, which is shown in table 10.3.

11.3 Examples for SAR based glacier investigations

11.3.1 Glacier mass balance estimation using C-band SAR

The procedure for glacier investigations, presented in section 11.2, was tested on several glaciers in the Ötztal covering 66.6 km² in area. As snow and reference images ERS-1 SAR data of crossing orbits acquired on 14 September 1992 and 19 October 1992 are used. The quality of the SAR based accumulation(snow) area estimation was determined by comparison with the ablation pattern and the ratio S_c/S from other sources. Figure 11.3 presents the classification results from Landsat TM of 17 September 1992 and ERS-1 SAR of 14 September 1992, both in UTM-32 projection with 25 x 25 m² grid spacing. The co-registration error is on the average less than 2 pixels, but varies locally. According to [66] snow is present in the TM image if the surface albedo in band 3 is higher than 0.6. The confusion matrix of the pixel by pixel comparison of Landsat TM and SAR based classification is presented in table 11.2. For the ice class both sources correspond well. Misclassifications of crevassed zones at the lower glacier termini as snow by SAR are obvious and can be manually corrected. The main differences between the Landsat TM and SAR classification are observed in the snow class. This may be due to several reasons:

- TM measures the surface reflectance of solar radiation [10], whereas microwave radiation penetrates into the snowpack and is sensitive also to subsurface properties. Because of snow fall in mid September 1992. some areas of the glacier ice were

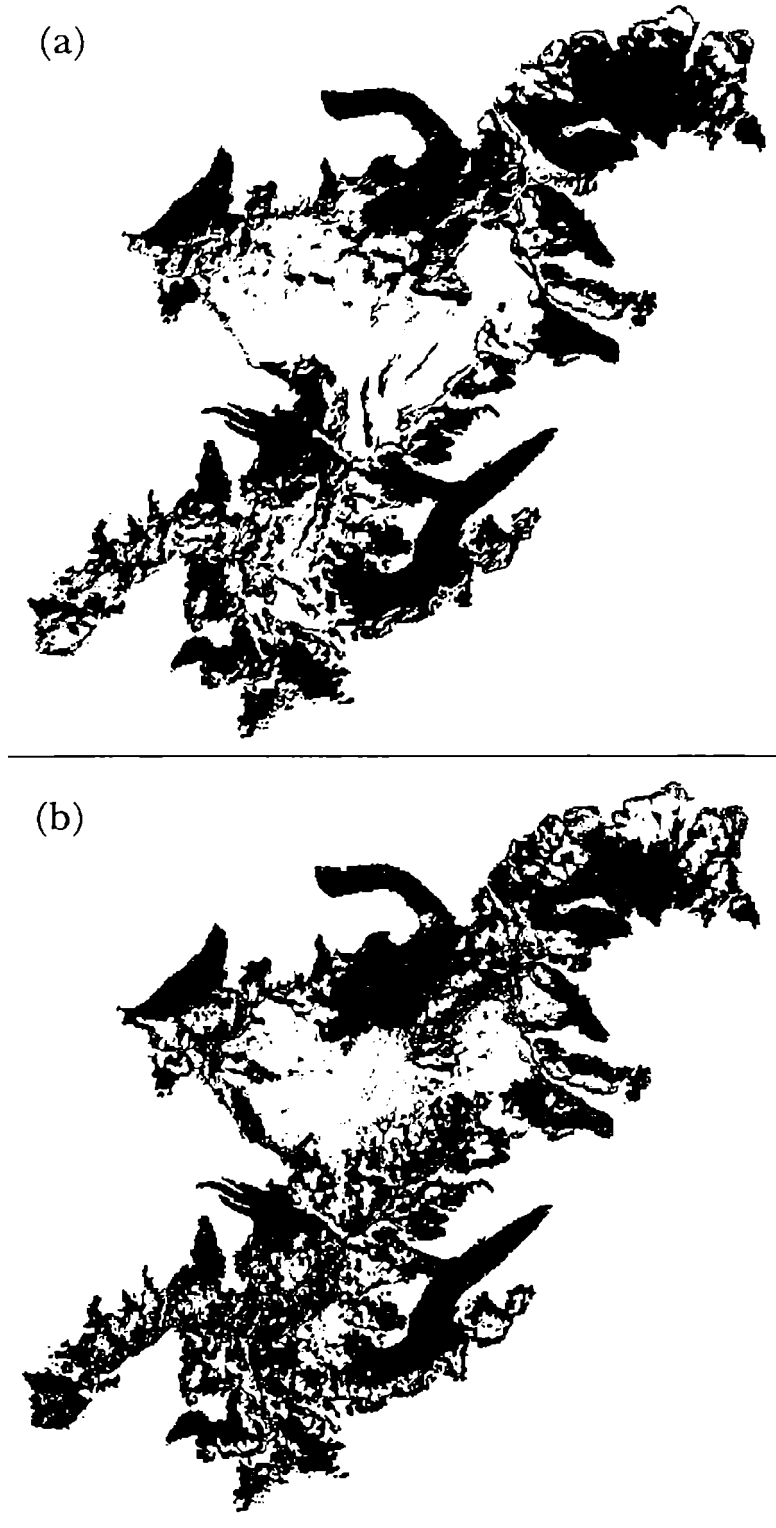


Figure 11.3: Landsat TM snow classification (surface albedo of TM channel 3 ≥ 0.6) from 17 September 1992 (a), and ERS-1 SAR wet snow classification ($TVAL = -5dB$) of 14 September 1992 (b). Glacier ice (black), wet snow (white), layover and shadow areas with $\theta_i < 17^\circ$ or $\theta_i > 78^\circ$ (dark grey), ice free area (light grey).

Hintereisferner				
Source	S_{ls}	S_c/S	b_n	ELA
	$[km^{-2}]$		$[kgm^{-2}y^{-1}]$	$[m]$
Field	—	0.24	-1119	3155
LS-TM	—	0.21	-1305	3236
ERS-1	0.19	0.26	-1094	3177

Vernagtferner				
Source	S_{ls}	S_c/S	b_n	ELA
	$[km^{-2}]$		$[kgm^{-2}y^{-1}]$	$[m]$
Field	—	0.22	-858	3270
LS-TM	—	0.15	-941	3483
ERS-1	0.19	0.31	-806	3259

Kesselwandferner				
Source	S_{ls}	S_c/S	b_n	ELA
	$[km^{-2}]$		$[kgm^{-2}y^{-1}]$	$[m]$
Field	—	0.51	-413	3160
LS-TM	—	0.58	-355	3151
ERS-1	0.34	0.60	-316	3144

Table 11.3: Mass balance parameters from the year 1 October 1991 to 30 September 1992 derived from analysis of field observations and measurements, and estimated from Landsat TM band 3 (17 September 1992) and from ERS-1 SAR (14 September 1992). Area of layover and shadow on the glacier was excluded from the ERS-1 analysis (S_{ls}).

masked by a thin fresh snow cover during the Landsat TM acquisition on 17 September 1992. These zones are classified as snow in the TM image, but as ice in the ERS-1 analysis.

- In the microwave region it is hardly possible to discriminate between firn and snow (section 7.1.2), whereas the surface albedo in TM band 3 enables the identification of snow and firn; though the discrimination is not good if the firn is clean. By using a lower classification threshold firn areas can be partly excluded.

Due to these restrictions the overall agreement between TM and ERS-1 analysis is not more than 73.1% on a pixel by pixel basis.

For the glaciers Hintereisferner, Kesselwandferner and Vernagtferner the glaciological parameters based on Landsat TM, ERS-1 SAR and field observations are compared in table 11.3. The areal ratios S_c/S of the three sources are within a variation bandwidth of 0.16. For \bar{b}_n and ELA estimated from the satellite derived S_c/S the differences from field observations are reasonably small considering the uncertainties in figure 11.1 and eq. 11.4. For all glaciers of figure 11.3 the areal ratio derived from TM analysis was $S_c/S = 0.35$ and $S_c/S = 0.30$ from the ERS-1 SAR data.

11.3.2 Glacier mass balance studies by means of X-SAR

The procedure for mass balance estimation by means of SAR was applied on the glaciers Hintereisferner, Kesselwandferner and Vernagtferner using X-SAR data of the SRL-1/2 missions in 1994. The analysis is based on X-SAR images of DT 46.10 and DT 78.00 of SRL-2. DT 46.10 and DT 78.10 of SRL-1 are used as reference images in the procedure

of figure 11.2. The images of SRL-2 were acquired on 3 and 5 October 1994 close to the end of the mass balance year. The images are available as GTC (geocoded terrain corrected) products provided by D-PAF. Local incidence angle maps, layover and shadow masks (GIM products) for each data take are available. The glacier mask, derived from the Landsat TM image of 17 September 1992, was manually updated to the glacier extent from autumn 1994 using oblique photographs. Only minor corrections were necessary. Because no Landsat TM image was available in September 1994, the SAR based accumulation-ablation pattern is qualitatively compared with the analysis based on field observations. The parameters S_c/S , \bar{b}_n and ELA enable a quantitative comparison.

Figure 11.4 shows the map of accumulation and ablation areas of Hintereisferner and Vernagtferner for different thresholds applied to DT 46 and DT 78. Kesselwandferner shows about the same trend as these glaciers (figure 11.7). The comparison of figure 11.4 with figure 11.5 shows in general a similar ablation pattern of field and spaceborne surveys, but the fine structure is different.

For DT 46 the thresholds of -6 dB and -7 dB were applied (figure 11.4 a, b, c, d), for DT 78 -5 dB and -6 dB (figure 11.4 e, f, g, h). The reason for the different thresholds is changes of the surface properties due to temperature decrease between the two overflights (section 7.2.3). The main differences between the different thresholds are only in the small scale. Choosing the lower thresholds misclassifications are observed at local incidence angles lower than 15° and larger than 70° . In general, the SAR based analysis shows a pronounced patchy structure, but this structure seems to be more realistic than the manual analysis as known from oblique photographs. For Hintereisferner and Kesselwandferner the agreement with field observations (figure 11.5) is good for a threshold of -7 dB for DT 46, while for Vernagtferner the threshold of -6 dB looks more reasonable. For DT 78 the threshold of -5 dB shows a good agreement with field measurements for both glaciers. These examples indicate the necessity to adjust the threshold to the snow characteristics during the acquisition of the snow image. The sensitivity of S_c/S as function of $\Delta\sigma^\circ$ for Hintereisferner and Vernagtferner is shown in figure 11.6. A change of the threshold of about 1 dB (in the range of -7 dB to -5 dB) results in a change of S_c/S between +0.07 to +0.09.

Table 11.4 summarizes the parameters for Hintereisferner and Vernagtferner derived from the analysis of X-SAR DT 46 and DT 78. The values of S_c/S derived by SAR are in good agreement with the field observations, with values of $S_c/S = 0.31$ for Hintereisferner and $S_c/S = 0.22$ for Vernagtferner. For Kesselwandferner field measurements report $S_c/S = 0.33$, which is smaller than the derived areal ratio based on SAR. For DT 46 with a threshold of -6 dB the deviation from the field measurements is less than 0.07, for DT 78 and a threshold of -5 dB it is less than 0.04. Based on eq. 11.4 and on the corresponding coefficients of table 11.1 the specific net balance \bar{b}_n and the altitude of the equilibrium line ELA are derived (table 11.4). The uncertainties in the derivation of \bar{b}_n for a given S_c/S by eq. 11.4 plays a role. To demonstrate this problem an example is given: using $S_c/S = 0.31$ (0.22) for Hintereisferner (Vernagtferner) based on field observations eq. 11.4 predicts $\bar{b}_n = -933$ (-786) $kgm^{-2}y^{-1}$, while \bar{b}_n determined by the direct glaciological method was $\bar{b}_n = -1107$ (-1029) $kgm^{-2}y^{-1}$. The resulting residual is -174 (-243) $kgm^{-2}y^{-1}$, which shows that this year deviates significantly from the mean relation between S_c/S and \bar{b}_n . On the other hand eq. 11.4 predicts a value of $\bar{b}_n = -1024$ (-1018) $kgm^{-2}y^{-1}$ for the SAR based areal ratio with $TVAL = -7$ dB (table 11.4). In this case the SAR based \bar{b}_n is closer to \bar{b}_n from the direct glaciological method than the predicted \bar{b}_n of field observed areal ratios. The mean altitude of the equilibrium line from SAR differs only by 12 m from the field data for Hintereisferner.

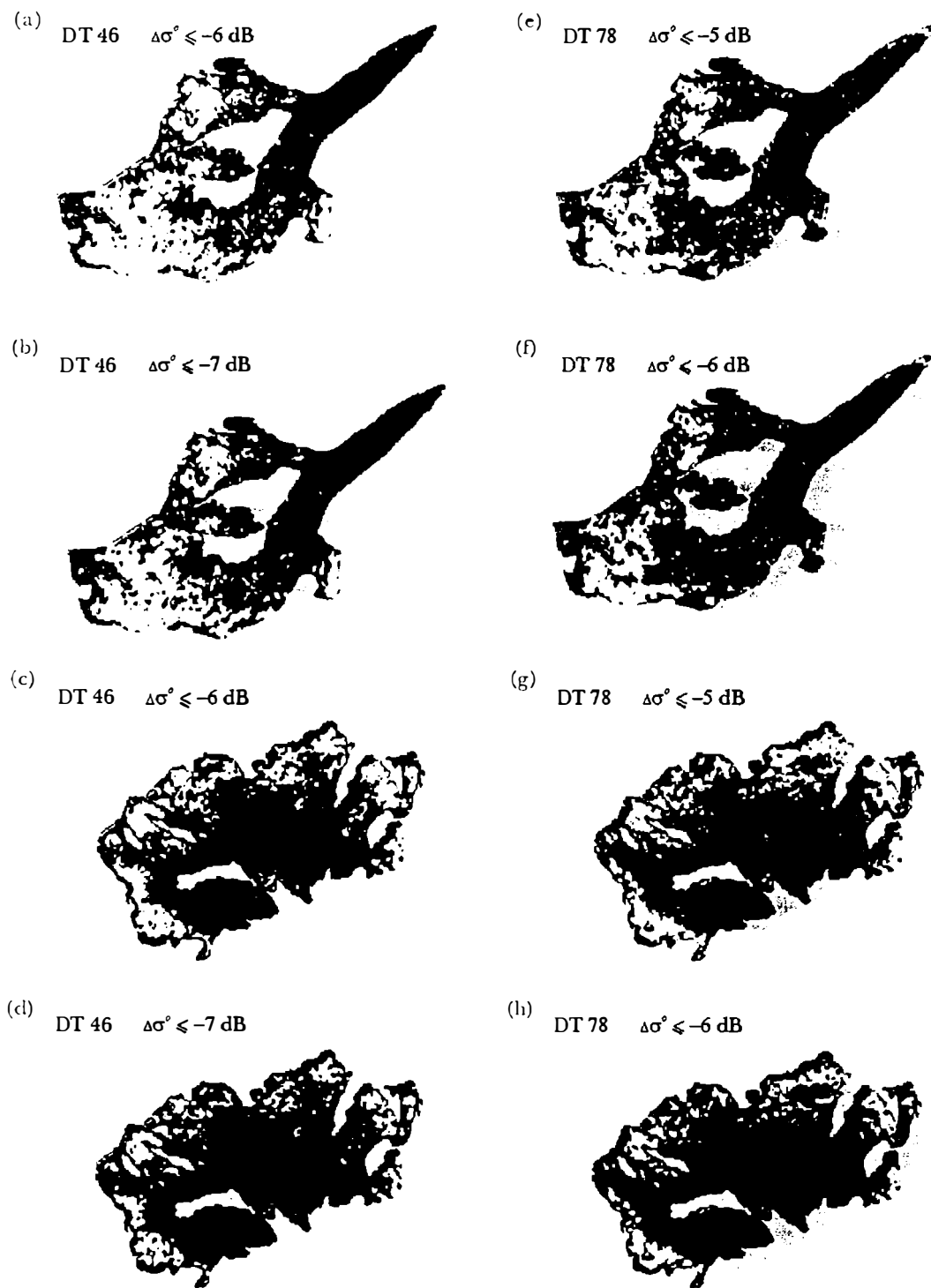


Figure 11.4: Accumulation areas (white) derived from XSAR images DT 46 (3 October 1994) and DT 78 (5 October 1994) for Hintereisferner (a, b, e, f) and Vernagtferner (c, d, g, h) derived by means of change detection (reference images from SRL-1), with different thresholds. Glacier ice (black), layover and shadow (dark grey).

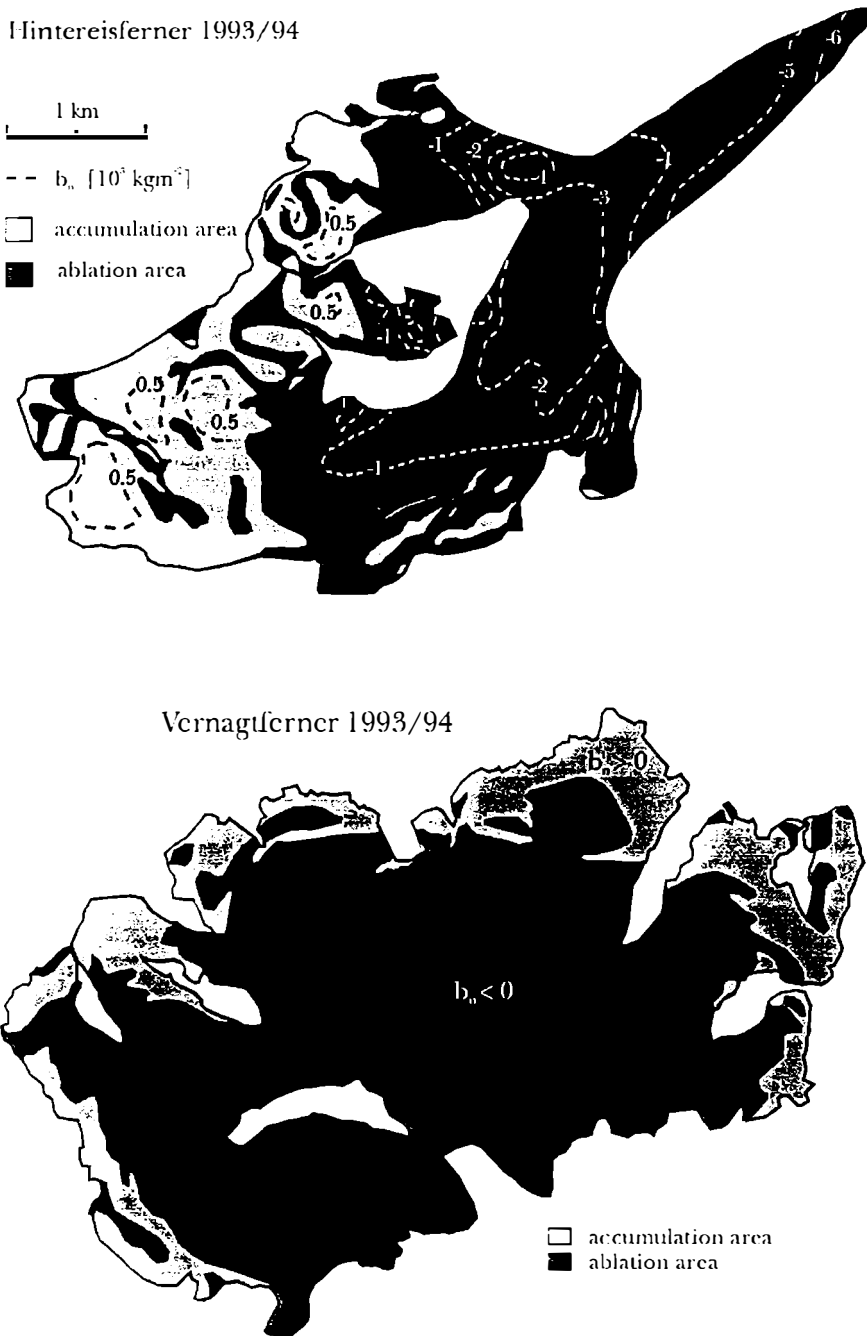


Figure 11.5: Accumulation (light grey) and ablation (dark grey) pattern of Hintereisferner (top) and Vernagtferner (bottom) from field observations. For Hintereisferner contour lines of the specific net balance are shown. (Sources: Institut für Meteorologie und Geophysik, Univ. Innsbruck, and Bayerische Akademie der Wissenschaften. Kommission für Glaziologie).

Hintereisferner								
DT	TVAL	$\frac{S_{ls}}{S}$	$\frac{S_c}{S}$	$\Delta \frac{S_c}{S}$	\bar{b}_n	$\Delta(\bar{b}_n)$	ELA	$\Delta(\text{ELA})$
	[dB]	[%]			$[\frac{kg}{m^2y}]$	$[\frac{kg}{m^2y}]$	[m]	[m]
46	-6	2.1	0.37	0.06	-791	316	3090	-55
46	-7	2.1	0.28	-0.02	-1024	83	3157	12
78	-5	8.3	0.25	-0.06	-1131	-24	3187	42
78	-6	8.3	0.18	-0.13	-1462	-355	3278	142

Vernagtferner								
DT	TVAL	$\frac{S_{ls}}{S}$	$\frac{S_c}{S}$	$\Delta \frac{S_c}{S}$	\bar{b}_n	$\Delta(\bar{b}_n)$	ELA	$\Delta(\text{ELA})$
	[dB]	[%]			$[\frac{kg}{m^2y}]$	$[\frac{kg}{m^2y}]$	[m]	[m]
46	-6	1.6	0.20	-0.02	-827	201	3411	—
46	-7	1.6	0.12	-0.10	-1018	10	3533	—
78	-5	4.7	0.18	-0.04	-870	158	3438	—
78	-6	4.7	0.11	-0.11	-1045	-17	3551	—

Kesselwandferner								
DT	TVAL	$\frac{S_{ls}}{S}$	$\frac{S_c}{S}$	$\Delta \frac{S_c}{S}$	\bar{b}_n	$\Delta(\bar{b}_n)$	ELA	$\Delta(\text{ELA})$
	[dB]	[%]			$[\frac{kg}{m^2y}]$	$[\frac{kg}{m^2y}]$	[m]	[m]
46	-6	0.99	0.52	0.19	-453	373	3173	-67
46	-7	0.99	0.41	0.08	-587	239	3209	-31
78	-5	5.4	0.48	0.15	-507	319	3187	-53
78	-6	5.4	0.37	0.04	-631	195	3221	-19

Table 11.4: Mass balance parameters derived from analysis of X-SAR images of DT 46 and DT 78 for Hintereisferner, Kesselwandferner and Vernagtferner: threshold applied to ratio image (TVAL), area of layover and shadow on the glacier excluded from the analysis (S_{ls}), S_c/S , \bar{b}_n , ELA are based on XSAR analysis, $\Delta(\cdot)$ specifies the difference between SAR derived parameters and those based on field observations.

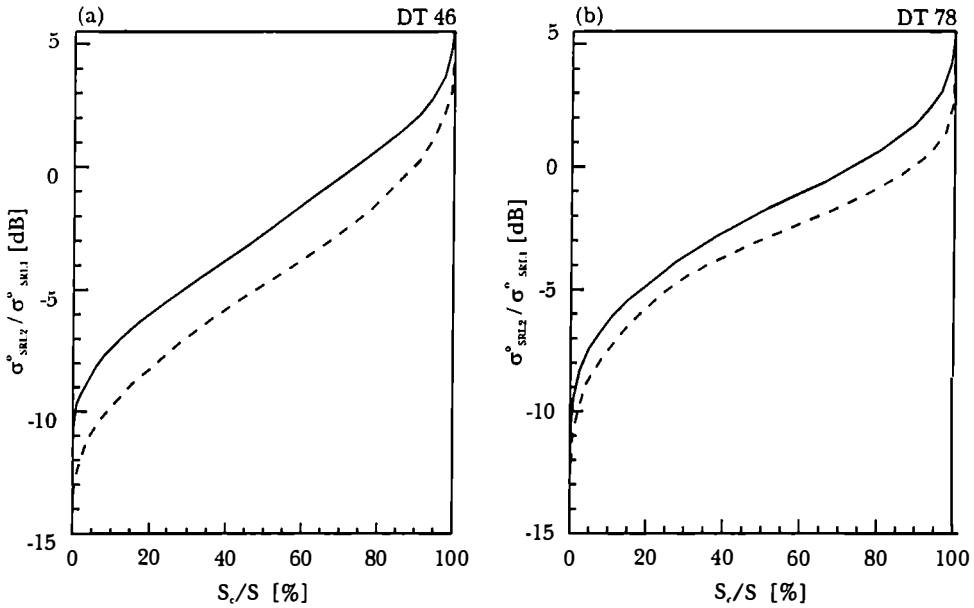


Figure 11.6: Areal ratio S_c/S in % as a function of the change of $\Delta\sigma^o$ between the snow and reference image for Vernagtferner (full line) and Hintereisferner (dashed line) for DT 46 (a) and DT(78).

11.3.3 Regional trend of glacier behaviour derived from SAR images

As shown in the last section it is possible to estimate the specific net balance from the ratio of the accumulation area to the total glacier area, derived by means of SAR, if the relation between these parameters is known. Although the investigated glaciers Hintereisferner, Kesselwandferner and Vernagtferner are located within some kilometers they revealed significant differences in the specific net balance. In this section an approach is made to estimate the behaviour of the other glaciers in this region and to learn about the representativeness of the mass balance studies.

The analysis is based on the X-SAR images of DT 46 of SRL-1 and SRL-2. As no optical imagery from 1994 was available, the glacier extent was derived from the Landsat TM image of 17 September 1992. This may result in some minor inaccuracies for the total glacier area and for the final determination of S_c/S . Because of the missing link between the specific net balance and S_c/S , \bar{b}_n was not be estimated.

Figure 11.7 shows a sketch map of the investigated area. The investigated area is limited by the extent of the available DEM. 16 glaciers of different size and orientation are analyzed with respect to S_c/S . For this purpose they were separated into four groups (figure 11.7). The derived parameters for each group and for all glaciers are listed in table 11.5. Figure 11.8 shows the SAR based accumulation-ablation pattern.

The ratio S_c/S for the different groups varies significantly. This is due to various effects, mainly differences in the topography and in the accumulation [38]. The highest value $S_c/S \simeq 0.34$ is observed for Gepatschferner and Kesselwandferner (group 3), where large parts of the glaciers are situated on a high plateau. The analysis indicates significant losses for the whole investigated area ($S_c/S = 0.27$), because for equilibrium mass budget the ratio is $S_c/S \simeq 0 - 7$ in the Ötztaler Alps. Although SAR data cannot provide estimations of the specific net balance without supporting data, they provide information about the variability between individual glaciers and between glacier regions.

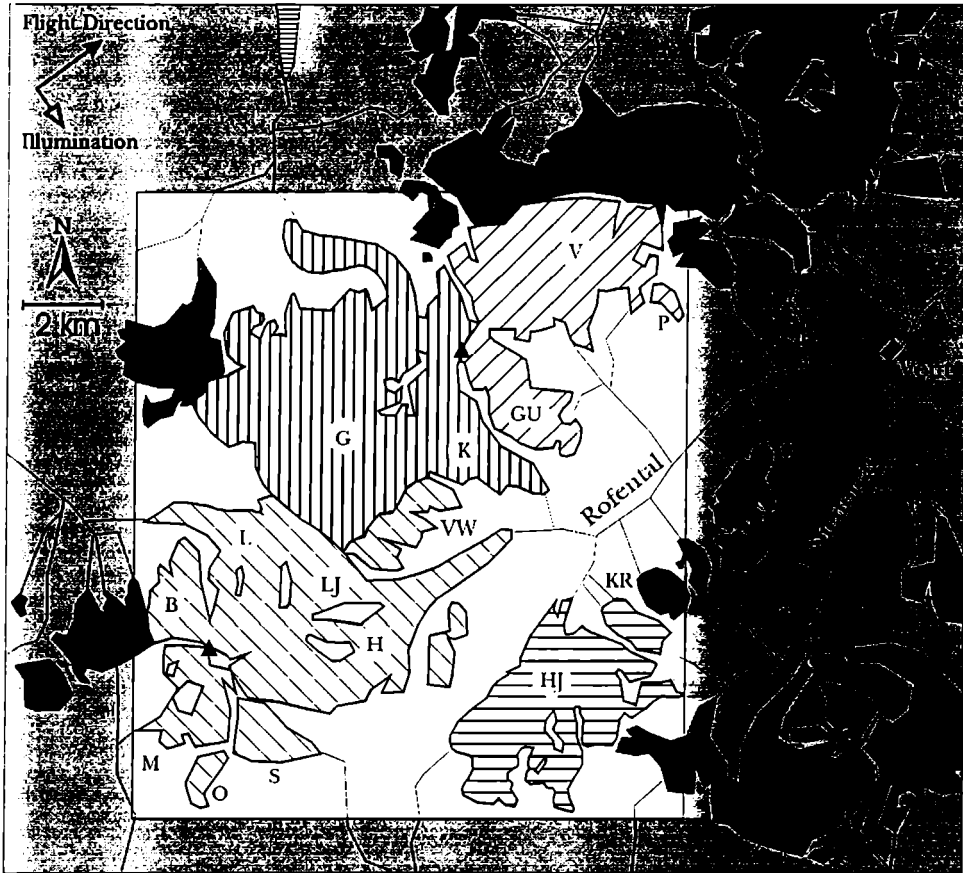


Figure 11.7: Sketch map of the test site Ötztal, the investigated area is shown in white. Four groups of glaciers are indicated by different hatching: Group 1: Hochjochferner (HJ), Kreuzferner (KR, partly). Group 2: Hintereisferner (H), Langtauferer-Ferner (L), Langtaufererjoch-Ferner (LJ), Bärenbart-Ferner (B), Matscher-Ferner (M), Oberrettes-Ferner (O), Steinschlag-Ferner (S), Vernaglwandferner (VW). Group 3: Gepatschferner (G), Kesselwandferner (K). Group 4: Guslarferner (GU), Vernagterferner (V), Platteiferner (P).

	No.	S	$S - S_{Is}$	S_c	$S_c / (S - S_{Is})$
		$[km^2]$	$[km^2]$	$[km^2]$	
Group 1	3	9.0	8.8	2.6	0.30
Group 2	8	21.8	20.9	5.6	0.27
Group 3	2	26.7	25.9	8.8	0.34
Group 4	3	12.1	11.9	1.6	0.13
All	16	69.6	67.6	18.5	0.27

Table 11.5: Parameters of the four groups of glaciers based on X-SAR data of DT 46 of SRL-2 (reference image: DT 46 SRL-1) and TVAL=-7dB. S is derived from Landsat TM classification from 17 September 1992.



Figure 11.8: Extent of firn areas (white) and ablation areas (black) on glaciers in Ötztal, derived from X-SAR data from 3 October 1994. Layover and shadow areas are shown in medium grey, ice free areas in light grey.

Chapter 12

Summary and conclusions

Available data set and calibration of SAR images

Basic principles of SAR imaging and technical characteristics of the SAR systems of ERS-1 and X-SAR are described in chapter 2. The available data set for this work is summarized in chapter 3. It includes 21 SAR scenes of the European Remote Sensing Satellite ERS-1 from 1992/93 and 10 X-SAR scenes of the Shuttle Imaging Radar-C / X-SAR from April and October 1994, acquired over the high alpine region Ötztal and the region near Innsbruck. Furthermore, 3 Landsat TM images of 1992 of the test site Ötztal and extensive field measurements during the SAR overflights (chapter 7) are available for comparison with the SAR analysis.

The ESA calibration strategy for ERS-1 SAR and the extraction of backscattering coefficients from ERS-1 PRI and X-SAR MGD products are presented in chapter 4. The calibration constant and the necessary correction factors are specified for the different Processing and Archiving Facilities (PAFs) and for different processor versions, including the update of the antenna pattern gain. A method is described to derive the calibration constant K_{σ^0} from external calibration targets. Using this method K_{σ^0} was derived from corner reflectors deployed on the Ötztal glaciers Hintereisferner and Kesselwandferner/Gepatschferner during the ERS-1 surveys in 1992. These calibration constants tend to be slightly lower than corresponding calibration factor of ESA. One reason for this may be the missing power loss correction for ADC saturation. Another reason may be minor deviations of the true cross section of the corner reflectors from the theoretical value. For accurate calibration the variation of the replica power had to be corrected. Optionally, the normalized mean average chirp energy density per sample was used, which resulted in a slightly different correction factor. The maximum difference between the two corrections was 0.22 dB, but in most cases it was less than 0.1 dB. For 21 analyzed PRI scenes of 1992/93 the replica power correction was between -0.05 dB and -0.79 dB.

Geocoding of SAR images

A procedure developed by B. Guindon and M. Adair [26] was applied for terrain-corrected geocoding of ascending and descending ERS-1 PRI images of the test site Ötztal (Chapter 5). The principles for generating the layover and shadow mask, which are required for snow mapping, are described. After co-registration the stack of repeat pass images can be geocoded within a few minutes on a SPARC-20 by using the same geocoding parameters. For this study ERS-1 SAR PRI images of the test site Ötztal were geocoded using the DEM with 12.5 and 25 m grid resolution in UTM-32 projection. The standard way

to determine the geometric accuracy of geocoded images is to identify Ground Control Points (GCP) in both the geocoded image and the reference map, which can be analyzed by statistical methods [56]. The mean absolute error of the geocoded ascending and descending ERS-1 PRI images of the test site Ötztal, using geodetically surveyed corner reflectors as references, was between 15 m and 40 m, with an overall quality parameter Q between 2 and 6 (0 best, 9 worst quality). After combining the geocoded images of the ascending and descending ERS-1 passes on 6 July and 14 September 1992 the corner reflectors were on the average relatively displaced by 23 m and 50 m. Significant errors in geocoding result from inaccuracies of the DEM. This is especially problematic for glacier areas, because the DEM is based on maps which are about 20 years old. Typical local differences between the true height of the glacier surface and the DEM range from several meters to more than 10 meters.

Field measurements and signature analysis of alpine targets

Principles of microwave interaction with snow and ice are discussed in chapter 6. Using a simple one-layer model the contributions of the scattering at the air-snow boundary, the volume scattering within the snow layer, and the scattering at the snow-ground boundary are calculated for dry and slightly wet snow. Using the exponential correlation function and field measurements of the snow parameters the IEM surface backscattering model can predict quite well the observed ERS-1 backscattering coefficients for wet snow; differences between model and observations are about 2 dB.

An extensive description of the field observations at the two test sites, the high alpine test site Ötztal (with accumulation (snow), firn and ice area on glaciers, low alpine vegetation, rocks/moraines) and the test site Innsbruck/Leutasch (cultivated meadows, agricultural fields, and forests), is given in chapter 7. The measured target properties are used for interpretation and modelling of the backscattering signatures. For the main targets the incidence angle dependence, the seasonal changes, and the short term variations of backscattering were determined. The signature analysis showed that:

- σ^0 , derived from ERS-1 data, for glacier ice, firn and accumulation areas decreases significantly at incidence angles lower than about 30° , and remains almost constant between 30° and 60° . For areas with high alpine vegetation, which show usually a quite rough surface, and for rocks σ^0 decreased approximately linearly in dB with increasing incidence angle.
- Accumulation and firn areas on the glaciers show the largest temporal changes of σ^0 , with seasonal variations up to 22 dB in C-band and X-band. Due to melt/freeze conditions σ^0 may change up to 10 dB within several hours and days. Particularly at X-band backscattering is very sensitive to changes in the snow morphology resulting from changing weather conditions.
- For areas covered by high alpine vegetation and for rocks seasonal changes of σ^0 are of the order of several dB. The lowest values were observed when they are covered by wet snow and the signal contribution from the ground - snow interface is negligible. Backscattering from alpine vegetation and rocks is in general not very sensitive to changing meteorological conditions as long as the surfaces are free of snow.
- The decrease of backscattering due to the presence of liquid water enables the detection of wet snow based on multitemporal SAR data. This agrees with ground based scatterometer measurements.

- The roughness experiment on a glacier plateau during the ERS-1 survey on 6 July 1992 revealed a strong influence of the surface roughness on backscattering from wet snow. For the roughness test field with regular roughness pattern σ^o was about 18 dB higher than for the adjacent undisturbed snow areas.
- For cultivated meadows with dry snow and frozen soil the C-band VV-polarized σ^o differed by about 2 dB to 3 dB compared to the snow free cases. In general dry snow could not be discriminated from frozen soil and dry soil without snow, and not from high Alpine surfaces without snow.
- For bare agricultural fields the temporal change of σ^o during the winter season was more pronounced than for cultivated meadows. Reasons are temporal changes of surface roughness and variations of the liquid water content and/or freezing state.
- The multitemporal analysis of coniferous forests in ERS-1 images revealed variations of σ^o of up to 4 dB during the winter period October 1992 to April 1993 partly related to snow wetness conditions below the trees.

Speckle filtering and segmentation

The SAR image statistics is discussed in chapter 8 using the Rayleigh clutter model. Under these model assumptions the intensity of homogeneous targets in multi-look images is gamma distributed (with order parameter n , where n is the number of looks). This distribution is compared with ERS-1 PRI (3-looks) and X-SAR MGD (4-looks) data. It is shown that for the estimation of parameters the correlation of neighbouring pixels in the range and azimuth direction with a correlation coefficient of 0.45 to 0.65 for ERS PRI and X-SAR MGD data, respectively. For detection of changes in backscattering between two images the ratio method has been selected, because of its independence on the strength of backscattering and on calibration errors. It is shown that the target discrimination by means of segmentation based on the backscattering ratio of two images is a function of the backscatter differences and of the number of looks. To learn about the possibilities for the suppression of speckle, three adaptive filters (Frost, modified Frost, Gamma MAP) and the Median Filter with different filter specific parameters and filter sizes were studied. The effect of different filters on the mean value and on the reduction on speckle the effective number of looks for two homogeneous glacier areas, one with high and one with low backscattering, are investigated. Furthermore, the conservation of edges and point targets was tested using ERS-1 PRI data. The effects on the backscattering ratio after filtering the input images was shown. The Frost and the Modified Frost filter showed similar results. The Gamma MAP behaved slightly different, but showed still some noisy features in the ratio image. As best choice for snow mapping the Frost Filter with a filter size of 5×5 pixel² and a damping factor of 2 was selected.

Snow mapping by means of SAR

The state of the art of snow mapping by means of single polarized SAR images is reviewed in chapter 10. A new procedure for mapping wet snow has been developed using repeat pass images of crossing orbits and a segmentation technique based on the temporal backscattering ratio. On the snow image (acquired at the actual date) and the corresponding reference image (acquired during dry snow or snow free conditions) several pre-processing steps are applied including calibration, accurate coregistration to subpixel

scale, and speckle filtering. Most ERS-1 repeat pass images could be matched to sub-pixel scale by simple linear transformation. Only in one case a misregistration trend of up to 5 pixels over the test site was observed requiring resampling. The ratio between the snow and reference image is formed in SAR geometry with known image statistics. The ratio image is then geocoded, and thresholded to form the wet snow map. Based on signature analysis and on comparison with oblique pictures taken during the field surveys a threshold of the ratio of -3 dB was determined for snow / no snow segmentation. Image simulation is used to derive a local incidence angle map and layover and shadow masks. Wet snow maps, which are generated for ascending and descending passes separately, are merged to reduce the loss of information due to layover and shadow. For the Ötztal test site the layover and shadow region is reduced from 36% and 41% in the ascending and descending image, respectively, to 8% in the combined image. The new snow procedure works well for spring and summer conditions with wet snow cover, but it fails for dry snow, because σ^0 is similar to snow free areas.

For verification, the SAR based snow maps were compared with oblique pictures taken during the SAR image acquisition and with classifications based on Landsat TM data, which, however, were not acquired at the exact dates of the ERS-1 passes. The classification procedure for Landsat TM is discussed in Chapter 9. In spite of the temporal difference of the image acquisitions, the pixel by pixel comparison of the Landsat TM classification of 29 June 1992 with the ERS-1 SAR snow maps of 1 June 1992 and 6 July 1992 shows an overall correspondence of about 80%. The decrease of snow extent at lower elevations was well documented by the synergy of SAR and TM. SAR tends to underestimate the snow extent slightly in regions with high percentage of snow. Because of high albedo and saturation in the visible channels Landsat TM tends to overestimate the snow extent in regions with patchy snow cover, which were not treated as a separate class in the TM classification. During the summer season with less temporal change of the snow extent the overall agreement was about 90% between the Landsat TM classification of 16 August 1992 and the ERS-1 SAR snow map of 10 August 1992. For a better comparison of both sources optical and SAR data acquired on the same day are required. For demonstrating the use of the wet snow classification procedure, the snow extent for the alpine drainage basin Venterache was determined on a 35 day cycle between April and September 1992. The temporal dynamics of snow melt could be monitored very well.

Glacier investigations by means of SAR

For application in glaciology the wet snow classification algorithm was applied only for glaciated areas to estimate the accumulation area and to map the ablation pattern. The investigations were based on ERS-1 SAR data acquired in summer and autumn 1992 and X-SAR data acquired during October 1994. The following problems for classification on the glaciers by means of C-Band VV data were observed:

- snow (accumulated the recent winter) and firn (old snow from previous years) cannot be discriminated by ERS-1 data
- snow and firn together can be well discriminated against rough glacier ice, vegetation, and rocks
- glacier ice cannot be discriminated against snow free vegetation and rocks by means of σ^0 , but glacier boundaries can be delineated manually due to the characteristic shape and texture.

In the Alps and other regions with slowly changing glacier areas it is recommended to derive the total glacier area from optical images, acquired in the same year or even some years earlier. The main problem for the determination of the accumulation area was the similarity of the C-band VV backscattering coefficient of snow (accumulation area) and firn (part of the ablation area). In the analyzed examples the area covered by firn was only small. By reducing the threshold of the backscattering ratio to -5 dB for ERS-1 data a significant part of the firn areas was assigned to the ice surfaces. But, as shown by X-band data, the contrast between the accumulation and ablation area changed significantly with melting and freezing of the surface. In X-band a change of the backscattering of more than 8 dB was found in the accumulation area of the Ötztal glaciers within 3 days due to the change from melting to frozen snow, while on glacier ice the change was about 3 dB.

The net specific mass balances and the mean altitudes of the equilibrium line were estimated from the SAR derived ratios of the accumulation area to total glacier area using established relationships between the areal ratio and the mass balance. Good agreement was found for the mass balance estimated from SAR derived accumulation to total glacier area in comparison with field observations for the glaciers Hintereisferner, Kesselwandferner, and Vernagtferner. With this method the glacier behaviour of 16 glaciers in the Rofental and its surroundings, separated in 4 groups, was analyzed by means of SAR data. The ratio of accumulation to total glacier area varied between 0.13 and 0.34 for the 4 glacier groups, indicating clearly negative mass balance throughout the region for the period 1 October 1993 to 30 September 1994.

Future work

The wet snow mapping algorithm developed in this thesis shows good capabilities for monitoring of the wet snow extent in mountainous terrain, as the data from the Ötztal have shown. Further tests in other regions are recommendable to learn about the general applicability and accuracy. According to the present knowledge some refinements, as for example new filtering techniques, may lead to minor improvements. Due to the launch of several SAR sensors such as Radarsat, ERS-2 and ENVISAT (planned for launch in 1998) the continuity of SAR data is guaranteed, with short repeat observations (of about 3 days in mid-latitudes) over the next decade. With these data the operational potential of snow monitoring by means of SAR should be exploited. As promising application the SAR based snow extent can be used as input parameter for hydrological distributed area models for runoff modelling and forecasting.

Dry snow detection by means of SAR is still a point of discussion. Possibilities for dry snow mapping have been reported for a site in the Canadian prairies [5]. But signature studies of ERS-1 data over alpine terrain and meadows, carried out in this work, showed that dry snow cannot be separated from snow free frozen ground.

Regarding the applications in glaciology major problems for discriminating snow from the current year versus firn from previous years by means of multitemporal single polarized C-band or X-band SAR have been identified. Current studies show that these two classes may be distinguished by using polarimetric parameters at several frequencies [71]. However, polarimetric SARs are presently operating on aircrafts and have been operating only during short term space missions. The presented method for mapping the accumulation and ablation area as basis for mass balance estimation provides only accurate results when the area covered by firn is much smaller than the accumulation area. This is the case if the mass balance in the previous years was similar or more negative than in the current year. Furthermore, SAR interferometry is becoming increasingly important for

glacier investigations, but this technique was beyond the objectives of this thesis.

Appendix A

ERS-1 PRI image quality assessment based on corner reflectors

The impulse response or point spread function of a SAR system is defined as the response to a point target with dimensions much smaller than the spatial resolution, i.e. the radar reflectivity of a target has the form of a Dirac delta function [19]. The form of the IRF depends on the degree of coherence in both the scene and the SAR system [19]. Lack of coherence, which modifies the form of the IRF, can be caused by uncompensated motion of the platform, by moving surfaces such as the ocean surface, and by phase errors due to interaction with the ionosphere. This means that the shape of the IRF may vary from scene to scene and depends also on the location in the scene. Trihedral corner reflectors can be considered as completely coherent and can so be used in checking the form of the IRF. The most common image quality parameters measured from SAR images are derived from the impulse response function (IRF) and describe the shape of the IRF [19]. For all field campaigns during ERS-1 overflights (except on 27 April 1992) trihedral corner reflectors between 1.25 m and 1.8 m in size were deployed on the firm areas of Kesselwandferner/Gepatschferner and Hintereisferner. In the following sections the derived quality parameters for each ERS-1 image are presented. For each available image two tables are shown. The first one gives information about the point targets in the image (in our case trihedral corner reflectors), the second one shows the corresponding image quality parameters.

In the table describing the point targets the following parameters are summarized:

- Abbreviation for corner reflector identification (Kx , Hx , where x is a identification number)
- Abbreviation of the glacier name, where the targets are deployed: Hintereisferner (HEF), Kesselwandferner (KWF).
- Size in meters corresponding to the side length of corner reflectors (which is the shorter side of the trihedral reflectors).
- Exact geographic location of the targets is given in three columns, where E and N are the position in local Gauss-Krüger coordinates (Transverse Mercator) and Alt is the altitude above mean sea level.
- Position of the point target in the PRI file referring to the pixel number in ground range (PX_r) and azimuth (PX_a).

- The incidence angle θ_i on a horizontal plane at the same location as the point target.

The second table presents the image quality parameters. The exact definition of the parameters is given in [17]. The IRF for each point target was obtained by extracting a subarea of 32 x 32 pixels centered on the peak of the main lobe from the original PRI image. This area was then interpolated by a factor of 8 in both directions. The interpolation was carried out on the amplitude data in two dimensions by Fast Fourier Transformation (FFT), zero padding and Inverse Fast Fourier Transformation (IFFT). The mean background power was then subtracted from the data. A method for estimating the mean reflected power by the background is described in section A. The following parameters were derived from the IRF:

- Peak intensity of uninterpolated PI_{uint} and interpolated data PI_{int} .
- Spatial resolution in azimuth r_a and ground range r_g (referred to mid swath).
- Peak to side lobe ratio (PSLR), four values derived for each side of the point target. Near Range PSLR $PSLR_{nr}$ and far range PSLR $PSLR_{fr}$ for the side lobes located before and after the peak in the range direction respectively; $PSLR_{a1}$ and $PSLR_{a2}$ for the side lobes located before and after the peak in the azimuth direction respectively.
- Integrated side lobe ratio in ground range $ISLR_r$, and azimuth direction $ISLR_a$, and 2-dimensional ISLR $ISLR_{2D}$.
- Background to signal ratio BSR .

In addition to the derivation of image quality parameters, 1- and 2-dimensional plots of the impulse response function were created. All image quality parameters were derived from the interpolated data of the subarea. except for calculating the peak energy, where interpolated and uninterpolated data were used. Data of some images could not be used, since snow had accumulated in the trihedral corner reflectors due to snow drift and precipitation and thus their response was significantly attenuated. In the following sections the image quality parameters are summarized for each ERS-1 survey at Ötztal; special notes are given on the condition of the CR at the time of the overflights.

Estimation of the background power

The background area is defined as that part of the extracted subarea which is outside the main lobe and side lobe areas (figure A.1). It can be divided into four background regions. For each region the average of the backscattered power is calculated. Those two regions with the lowest mean power are then averaged again to get the final average power backscattered by the background. The other two subareas, which show higher power values, are not taken into account in this averaging. With this method bright targets in the background area near the corner reflectors are excluded and they will not influence the average backscattered background power.

ERS-1 SAR PRI images of 1 June 1992

One corner reflector of size 1.8 m was deployed in the test field. This corner reflector was set up on a mean slope of ca 15 degrees towards the South-East (table A.1). Due to

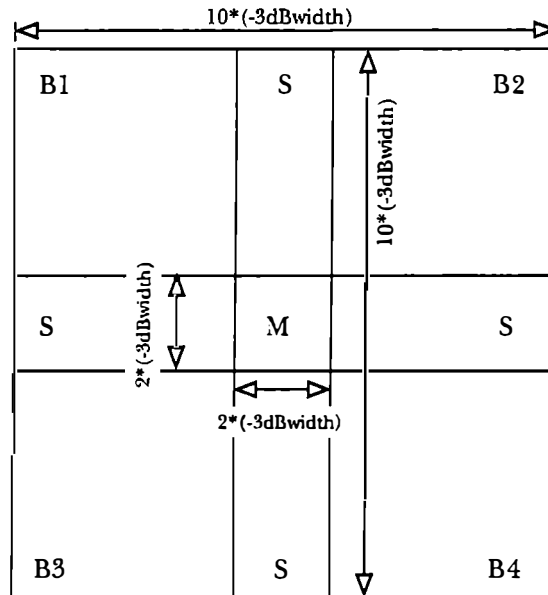


Figure A.1: Definition of parameters for deriving image quality parameters.

	Glacier	Size	E	N	Alt	PX _r	PX _a	θ_i
H0	HEF	1.8 m	32511	5184406	3200 m	6032	6015	24.80°

Table A.1: Description of trihedral Corner Reflector.

foreshortening and layover effects this point target cannot be seen in the SAR image of the descending orbit. Therefore image quality parameters reported in table A.2 are only derived from the ascending pass.

ERS-1 SAR PRI images of 6 July 1992

For the overflights on 6 July 1992 corner reflectors of different sizes were deployed on Kesselwandferner (KWF) and Hintereisferner (HEF). The corner reflectors were set up on nearly horizontal or low sloping locations on the glacier, so that they can be seen in both day and night images and were orientated parallel to the flight direction. The deviation in azimuth and elevation angle from the direction with the maximum response was also measured with an accuracy of ± 1 degree for each reflector. Description and analysis for CR during ERS-1 survey in July are given in table A.3, table A.4, table A.5 and table A.6.

The day image shows a low background to signal peak ratio below -25.71 dB, except for a value of -18.12 dB near the reflector H1. Due to the high backscattering of the

	BSR	r_g	r_a	ISLR _r	ISLR _a	ISLR _{2D}
H0	-31.74 dB	24.89 m	23.16 m	-16.38 dB	-17.83 dB	-13.85 dB

	PSLR _{nr}	PSLR _{fr}	PSLR _{a1}	PSLR _{a2}	PI _{uint}	PI _{int}
H0	-20.69 dB	-21.69 dB	-22.41 dB	-19.97 dB	70.57 dB	71.67 dB

Table A.2: Image quality parameters of 1 June 92. Orbit 4597, Frame 927, night overflight, ascending orbit.

	Glacier	Size	E	N	Alt	PX _r	PX _a	θ_i
K1	KWF	1.50 m	34436	5190071	3249 m	3494	6949	22.50°
K2	KWF	1.80 m	34248	5189616	3209 m	3490	6980	22.50°
K3	KWF	1.80 m	33982	5189354	3215 m	3521	7018	22.53°
H1	HEF	1.25 m	—	—	—	3633	7495	22.63°
H2	HEF	1.80 m	—	—	—	3619	7484	22.61°

Table A.3: Description of trihedral Corner Reflectors. 6 July 92, day overflight, descending orbit.

background at H1 the integrated side lobe ratio (ISLR) and the peak side lobe ratio (PSLR) could not be evaluated for this target. In the night image the BSR is between -30.75 dB and -35.63 dB for all reflectors. The mean ground range and azimuth resolutions at mid swath are 27.53 m and 21.25 m for the day image and 25.75 m and 21.04 m for the night image. Due to the very low background almost 5 side lobes of the point target response can be observed. Figure A.2 and figure A.3 show a 2-dimensional plot and 1-dimensional cuts in range and azimuth direction through the peak of the IRF of the target K2 in the night image.

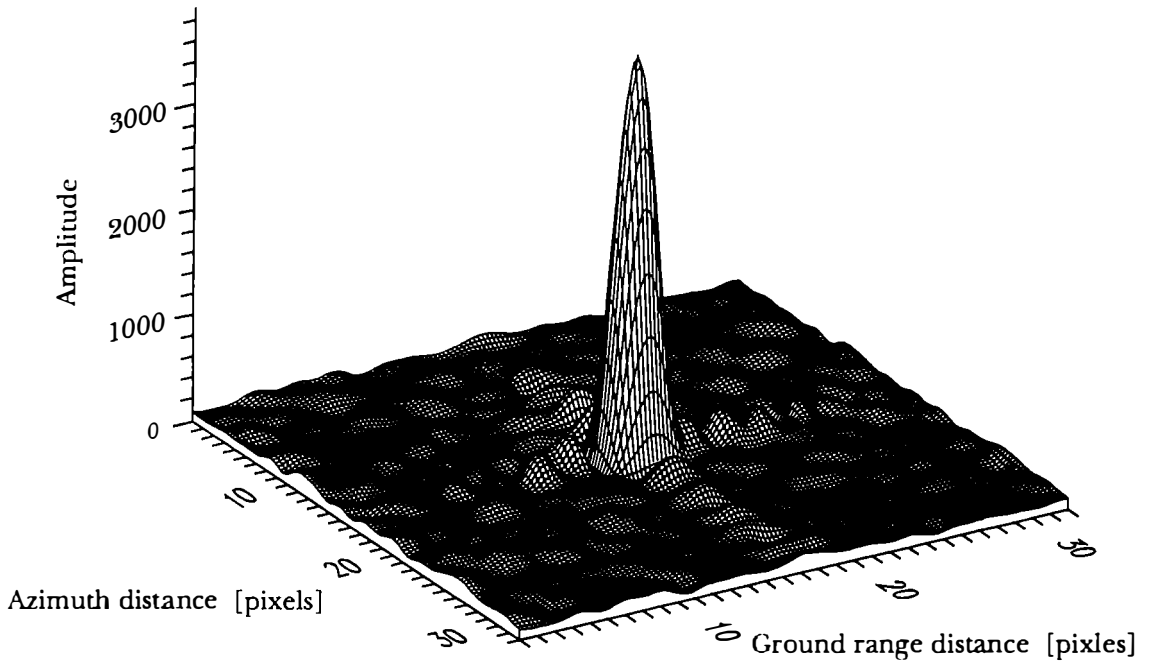


Figure A.2: Impulse response function of trihedral corner reflector K2, ERS-1 PRI image, 6 July 1992. ascending pass.

ERS-1 SAR PRI image of 10 August 1992

Due to technical problems no image was acquired during the day and only the night image is available. Table A.7, table A.8 document the characteristics for the August image. Due to snow fall before and during the night overflight, wet snow had accumulated in the trihedrals, which is the reason that PI is lower than in the July images. Nevertheless, the mean ground range resolution at mid swath (25.32 m) and mean azimuth resolution (21.91 m) are similar to the corresponding values derived from the July images.

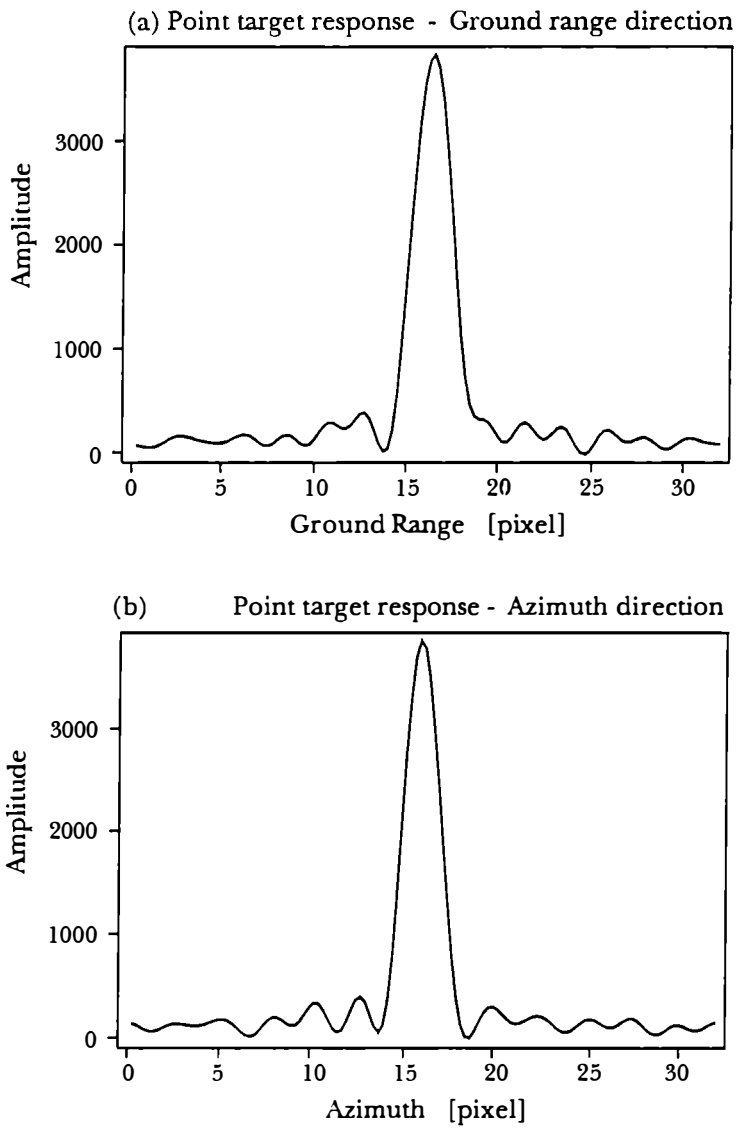


Figure A.3: Azimuth and range cut through the peak of the impulse response of trihedral corner reflector K2. ERS-1 PRI image, 6 July 1992, ascending pass.

	Glacier	Size	E	N	Alt	PX _r	PX _a	θ_i
K1	KWF	1.50 m	34436	5190071	3249 m	6197	6452	24.95°
K2	KWF	1.80 m	34248	5189616	3209 m	6200	6419	24.95°
K3	KWF	1.80 m	33982	5189354	3215 m	6152	6398	24.91°
H1	HEF	1.25 m	—	—	—	5908	5996	24.70°
H2	HEF	1.80 m	—	—	—	5947	5995	24.73°

Table A.4: Description of trihedral Corner Reflectors. 6 July 92, night overflight, ascending orbit.

	BSR	r_g	r_a	ISLR _r	ISLR _a	ISLR _{2D}
K1	-27.96 dB	26.98 m	20.55 m	-15.95 dB	-15.03 dB	-12.97 dB
K2	-30.26 dB	28.16 m	21.73 m	-15.31 dB	-16.14 dB	-11.80 dB
K3	-29.98 dB	27.83 m	21.82 m	-15.84 dB	-16.49 dB	-12.34 dB
H1	-18.12 dB	27.35 m	20.96 m	—	—	—
H2	-25.71 dB	27.33 m	21.18 m	-16.89 dB	-14.48 dB	-11.38 dB

	PSLR _{nr}	PSLR _{fr}	PSLR _{a1}	PSLR _{a2}	PI _{uint}	PI _{int}
K1	-20.14 dB	-21.16 dB	-21.45 dB	-26.00 dB	67.52 dB	68.44 dB
K2	-19.12 dB	-23.85 dB	-23.69 dB	-21.12 dB	69.94 dB	70.49 dB
K3	-23.69 dB	-22.81 dB	-21.55 dB	-20.16 dB	21.92 dB	70.59 dB
H1	—	—	—	—	65.31 dB	65.40 dB
H2	-19.55 dB	-18.37 dB	-17.54 dB	-21.44 dB	70.04 dB	70.62 dB

Table A.5: Image quality parameters of 6 July 92, Orbit 5091, Frame 2655, day overflight, descending orbit.

	BSR	r_g	r_a	ISLR _r	ISLR _a	ISLR _{2D}
K1	-30.75 dB	25.69 m	21.31 m	-17.13 dB	-17.55 dB	-14.66 dB
K2	-33.32 dB	26.33 m	22.22 m	-16.84 dB	-17.80 dB	-14.28 dB
K3	-33.70 dB	26.01 m	20.38 m	-17.03 dB	-15.17 dB	-12.72 dB
H1	-30.37 dB	25.55 m	20.19 m	-15.51 dB	-14.79 dB	-11.90 dB
H2	-35.63 dB	25.17 m	21.12 m	-16.35 dB	-15.26 dB	-12.68 dB

	PSLR _{nr}	PSLR _{fr}	PSLR _{a1}	PSLR _{a2}	PI _{uint}	PI _{int}
K1	-23.68 dB	-21.44 dB	-21.04 dB	-20.06 dB	67.59 dB	68.50 dB
K2	-20.31 dB	-22.90 dB	-20.14 dB	-22.74 dB	71.39 dB	71.69 dB
K3	-21.38 dB	-23.18 dB	-20.85 dB	-23.04 dB	70.88 dB	71.96 dB
H1	-21.35 dB	-23.44 dB	-22.69 dB	-22.41 dB	64.20 dB	66.55 dB
H2	-20.74 dB	-21.51 dB	-21.93 dB	-23.17 dB	70.56 dB	71.86 dB

Table A.6: Image quality parameters of 6 July 92, Orbit 5098, Frame 927, night overflight, ascending orbit.

	Glacier	Size	E	N	Alt	PX _r	PX _a	θ_i
K1	KWF	1.50 m	34612	5190461	3294 m	6181	6462	24.94°
K2	KWF	1.80 m	34437	5190071	3249 m	6168	6436	24.93°
K3	KWF	1.80 m	34494	5189734	3214 m	6172	6407	24.93°
K4	KWF	1.80 m	34071	5189419	3222 m	6156	6390	24.92°
H1	HEF	1.25 m	31768	5183659	3045 m	5876	5979	24.68°
H2	HEF	1.80 m	32228	5183762	2966 m	5929	5979	24.72°

Table A.7: Description of trihedral Corner Reflectors. 10 August 92, night overflight, ascending orbit.

	BSR	r_g	r_a	ISLR _r	ISLR _a	ISLR _{2D}
K1	-11.71 dB	26.08 m	22.81 m	-4.96 dB	-12.19 dB	-1.24 dB
K2	-17.43 dB	27.16 m	22.64 m	—	—	—
K3	-21.61 dB	26.14 m	21.77 m	-15.05 dB	-13.12 dB	-11.14 dB
K4	-14.02 dB	22.93 m	20.39 m	—	—	—
H1	-17.49 dB	23.39 m	21.98 m	-3.82 dB	-14.99 dB	-0.67 dB
H2	-27.46 dB	26.24 m	21.84 m	-16.92 dB	-15.89 dB	-13.59 dB

	PSLR _{nr}	PSLR _{fr}	PSLR _{a1}	PSLR _{a2}	PI _{uint}	PI _{int}
K1	-9.17 dB	-11.22 dB	-11.52 dB	-9.49 dB	56.52 dB	56.61 dB
K2	—	—	—	—	60.14 dB	60.77 dB
K3	-17.70 dB	-19.41 dB	-17.07 dB	-15.50 dB	62.75 dB	63.22 dB
K4	—	—	—	—	53.77 dB	55.17 dB
H1	-10.89 dB	-9.76 dB	-11.92 dB	-17.21 dB	56.01 dB	57.74 dB
H2	-21.85 dB	-19.97 dB	-22.56 dB	-20.77 dB	64.09 dB	64.70 dB

Table A.8: Image quality parameters of 10 August 92, Orbit 5599, Frame 927, night overflight, ascending orbit.

	Glacier	Size	E	N	Alt	PX _r	PX _a	θ_i
K1	KWF	1.50 m	34543	5190428	3282 m	3344	6963	22.39°
K2	KWF	1.80 m	34433	5190092	3248 m	3355	6991	22.40°
K3	KWF	1.80 m	34561	5189757	3209 m	3344	7015	22.39°
K4	KWF	1.80 m	34151	5189364	3219 m	3367	7048	22.41°
H1	HEF	1.25 m	31730	5183627	3048 m	—	—	—
H2	HEF	1.80 m	32235	5183749	2964 m	3475	7524	22.51°

Table A.9: Description of trihedral Corner Reflectors. 14 September 92, day overflight, descending orbit.

ERS-1 SAR PRI images of 14 September 1992

Six corner reflectors were deployed parallel to the ascending and descending overflight on the 14 September 1992 in the firn areas of Kesselwandferner/Gepatschferner and Hintereisferner (table A.9, table A.10). Image quality parameters are given in table A.11 and table A.12. The PI is on the average of 70.60 dB for reflectors of 1.8 m size and 68.76 dB for the reflector of 1.5 m size. The mean ground range resolution at mid swath is 26.23 m and the mean azimuth resolution is 21.87 m. Reflector H1 does not show up in the day image.

Due to a light snow fall before and during the night overflight with air temperatures slightly below 0°C, a small amount of dry snow had accumulated in the reflectors. The effect of snow in the reflectors becomes obvious in a comparison of the PI in the day and

	Glacier	Size	E	N	Alt	PX _r	PX _a	θ_i
K1	KWF	1.50 m	34436	5190071	3249 m	3494	6949	22.50°
K2	KWF	1.80 m	34248	5189616	3209 m	3490	6980	22.50°
K3	KWF	1.80 m	33982	5189354	3215 m	3521	7018	22.53°
H1	HEF	1.25 m	—	—	—	3633	7495	22.63°
H2	HEF	1.80 m	—	—	—	3619	7484	22.61°

Table A.10: Description of trihedral Corner Reflectors. 14 September 92, night overflight, descending orbit.

	BSR	r_g	r_a	ISLR_r	ISLR_a	ISLR_{2D}
K1	-25.44 dB	26.78 m	22.36 m	-15.87 dB	-15.46 dB	-13.38 dB
K2	-27.59 dB	26.16 m	23.13 m	-16.64 dB	-16.59 dB	-13.85 dB
K3	-26.88 dB	26.38 m	19.93 m	-16.54 dB	-14.10 dB	-12.17 dB
K4	-22.76 dB	26.00 m	22.59 m	-19.83 dB	-20.63 dB	-19.06 dB
H1	—	—	—	—	—	—
H2	-22.92 dB	25.76 m	21.34 m	-14.24 dB	-13.55 dB	-9.05 dB

	PSLR_{nr}	PSLR_{fr}	PSLR_{a1}	PSLR_{a2}	PI_{uint}	PI_{int}
K1	-22.49 dB	-20.64 dB	-17.90 dB	-20.30 dB	68.26 dB	68.76 dB
K2	-19.46 dB	-22.15 dB	-20.78 dB	-19.59 dB	70.93 dB	71.16 dB
K3	-20.41 dB	-20.81 dB	-18.70 dB	-20.94 dB	69.41 dB	70.73 dB
K4	-21.30 dB	-20.92 dB	-21.49 dB	-21.38 dB	69.84 dB	70.22 dB
H1	—	—	—	—	—	—
H2	-16.74 dB	-17.60 dB	-18.90 dB	-16.20 dB	69.50 dB	70.21 dB

Table A.11: Image quality parameters of 14 September 92, Orbit 6093, Frame 2655, day overflight, descending orbit.

night image. The reflectors K1, K3 and K4 show a peak intensity PI_{int} in the night image which is between 3.7 and 2.5 dB lower than in the day image. K2, which was nearly snowfree on the next day, shows the highest peak intensity PI of 71.25 dB. The corner reflector H2 at Hintereisferner cannot be seen in the night image, as it was displaced by strong winds.

ERS-1 SAR PRI images of 19 October 1992

During the ascending and descending ERS-1 overflights on 19 October 1992 two corner reflectors of 1.25 m and 1.8 m size were deployed at the Hintereisferner (table A.13). No point targets were set up on the glacier plateau of Kesselwandferner/Gepatschferner. In the day image the corner reflectors H1 and H2 cannot be detected very well and are not taken into account. The evaluated mean ground range and azimuth resolution derived at mid swath for the night image are 25.71 m and 22.79 m. The image quality parameters are shown in table A.14.

	BSR	r_g	r_a	ISLR_r	ISLR_a	ISLR_{2D}
K1	-25.26 dB	26.01 m	21.06 m	-15.27 dB	-14.49 dB	-10.63 dB
K2	-31.69 dB	26.20 m	21.44 m	-18.16 dB	-16.70 dB	-14.34 dB
K3	-28.09 dB	26.69 m	20.88 m	-16.88 dB	-14.64 dB	-12.39 dB
K4	-24.21 dB	27.09 m	21.64 m	-15.94 dB	-17.87 dB	-12.78 dB
H1	-25.62 dB	25.27 m	21.90 m	-12.89 dB	-15.46 dB	-8.44 dB
H2	—	—	—	—	—	—

	PSLR_{nr}	PSLR_{fr}	PSLR_{a1}	PSLR_{a2}	PI_{uint}	PI_{int}
K1	-19.32 dB	-17.44 dB	-19.40 dB	-21.35 dB	65.43 dB	66.29 dB
K2	-20.85 dB	-22.80 dB	-20.89 dB	-20.32 dB	70.66 dB	71.25 dB
K3	-20.20 dB	-20.58 dB	-22.81 dB	-19.24 dB	67.12 dB	67.69 dB
K4	-20.54 dB	-19.48 dB	-19.66 dB	-22.66 dB	66.14 dB	66.51 dB
H1	-18.79 dB	-18.42 dB	-18.71 dB	-20.34 dB	64.56 dB	65.49 dB
H2	—	—	—	—	—	—

Table A.12: Image quality parameters of 14 September 92, Orbit 6100, Frame 927. night overflight, ascending orbit.

	Glacier	Size	E	N	Alt	PX_r	PX_a	θ_i
H1	HEF	1.25 m	—	—	—	5809	5953	-24.61°
H2	HEF	1.80 m	—	—	—	5867	5953	-24.66°

Table A.13: Description of trihedral Corner Reflectors. 19 October 92, night overflight, ascending orbit.

	BSR	r_g	r_a	ISLR_r	ISLR_a	ISLR_{2D}
H1	-17.17 dB	25.80 m	22.67 m	—	—	—
H2	-26.33 dB	25.62 m	22.90 m	-16.04 dB	-18.12 dB	-13.26 dB

	PSLR_{nr}	PSLR_{fr}	PSLR_{a1}	PSLR_{a2}	PI_{uint}	PI_{int}
H1	—	—	—	—	61.31 dB	61.39 dB
H2	-18.13 dB	-18.70 dB	-19.51 dB	-19.90 dB	69.05 dB	69.22 dB

Table A.1-4: Image quality parameters of 14 September 92, Orbit 6100, Frame 927. night overflight, ascending orbit.

Bibliography

- [1] BAMLER, R., BREIT, H., STEINBRECHER, U., AND JUST, D. Algorithms for X-SAR processing. In *Proc. IGARSS'93* (Tokyo, Japan 1993), pp. 1589–1592.
- [2] BAMLER, R., AND SCHÄTTLER, B. SAR data acquisition and image formation. In *SAR Geocoding: Data and Systems*, G. Schreier, Ed. Wichmann Verlag GmbH, Karlsruhe, 1993, ch. 3, pp. 53–102.
- [3] BERNIER, M., AND FORTIN, J. Evaluation of the potential of C- and X-band SAR data to monitor dry and wet snow snow cover. In *Proc. Of IGARSS'91, Espoo* (3-6 June 1991), pp. 2315–2318.
- [4] BERNIER, M., FORTIN, J., AND GAUTHIER, Y. The potential of RADARSAT data to estimate the snow water equivalent based on results from ERS-1. In *Proc. IGARSS'95* (10-14 July 1995, Firenze, Italy 1995), pp. 1496–1498.
- [5] BERNIER, M., AND FORTIN, P. Potential of ERS-1 SAR data for snow cover monitoring. In *Proc. Of IGARSS'92, Houston, Texas* (26-29 May 1992), pp. 1664–1666.
- [6] BORN, M., AND WOLF, E. *Principles of Optics*, 6th ed. Pergamon Press, 1991.
- [7] CAVES, R. *Automatic Matching of Features in Synthetic Aperture Radar Data to Digital Map Data*. PhD thesis, University of Sheffield, 1993.
- [8] CURLANDER, C., AND MCDONOUGH, R. *Synthetic Apertur Radar: Systems and Signal Processing*. Wiley series in Remote Sensing. Wiley Inc., 1991.
- [9] DENOTH, A. Snow dielectric measurements. *Adv. Space Res.* 9, 1 (1989), 233–243.
- [10] DOZIER, J. Spectral signatures of alpine snow cover from Landsat Thematic Mapper. *Remote Sens. Environ.* 28 (1989), 9–22.
- [11] DOZIER, J., AND FREW, J. Rapid calculations of terrain parameters for radiation modeling from digital elevation data. *IEEE Trans. Geosci. Remote Sensing* 28, 5 (1990), 963–969.
- [12] EINEDER, M., AND BAMLER. Noise calibration of ERS-1 SAR products. In *SAR Calibration Workshop* (20-24 September 1993), CEOS Cal/Val working group, SAR Calibration Subgroup, pp. 237–245.
- [13] ELACHI, C. *Spaceborne radar remote sensing: applications and techniques*. IEEE Press, 1987.
- [14] EPEMA, G. Determination of planetary reflectance for Landsat-5 Thematic Mapper Tapes Processed by Earthnet (Italy). *ESA Journal* 14 (1990), 101–108.

- [15] ESA. The data book of ERS-1. ESA BR - 75 Issue 1, ESA Earthnet, 1991.
- [16] ESA. ESA ERS-1 Product Specification. ESA SP 1149 Issue 3.0. ESA, 1 June 1992.
- [17] ESA EARTHNET ERS-1. Technical note on the ECISAR test image. ER-TN-EPO-GP-1901 ISSUE 1, Rev. 0, ESA Earthnet, 1990.
- [18] FAHNESTOCK, M., AND BINDSCHADLER, R. Description of a program for SAR investigations of the Greenland ice sheet and an example of margin change detection using SAR. *Ann. Glaciol.* 17 (1993), 332-336.
- [19] FREEMAN, A. SAR Calibration: An Overview. *IEEE Trans. Geosci. Remote Sensing* 30, 6 (1992), 1107-1121.
- [20] FUNG, A. *Microwave Scattering and Emission Models and their Applications*. Artech House Inc., 1994.
- [21] FUNG, A., AND CHEN, M. Modelling of microwave emission and scattering from snow and soil. *Adv. Space Res.* 9, 1 (1989), 297-306.
- [22] FUNG, A., AND CHENG, K. Dependence of the surface backscattering coefficients on roughness, frequency and polarisation states. *Int. J. Remote Sensing* 13, 9 (1992), 1663-1680.
- [23] FUNG, A., LI, Z., AND CHEN, K. Backscattering from a randomly rough dielectric surface. *IEEE Trans. Geosci. Remote Sensing* 30, 2 (March 1992), 356-369.
- [24] GEUDTNER, D. Die interferometrische Verarbeitung von SAR Daten. Forschungsbericht 95-28, Deutsche Forschungsanstalt für Luft- und Raumfahrt e.V., 1995.
- [25] GRAY, A., VACHON, P., LIVINGSTONE, C., AND LUKOWSKI, T. Synthetic Aperture Radar calibration using reference reflectors. *IEEE Trans. Geosci. Remote Sensing* 28, 3 (1990), 374-383.
- [26] GUINDON, B., AND ADAIR, M. Analytic formulation of spaceborne SAR image geocoding and value-added product generation procedures using digital elevation data. *Canadian Journal of Remote Sensing* 18, 1 (1992), 2-11.
- [27] GUINDON, B., AND MARUYAMA, H. Automated matching of real and simulated SAR imagery as a tool for ground control point acquisition. *Canadian Journal of Remote Sensing* 12 (1986), 149-258.
- [28] GUNERIUSSEN, T., JOHNSEN, H., AND SAND, K. DEM corrected ERS-1 SAR data for snow monitoring. *Int. J. Remote Sensing* 17, 1 (January 1996), 181-195.
- [29] HAEFNER, H., HOLECZ, F., MEIER, E., NÜESCH, D., AND PIESBERGEN, J. Capabilities and limitations of ERS-1 SAR data for snowcover determination in mountainous regions. In *Proc. Of 2nd ERS-1 Symposium. Hamburg* (11-14 Oct. 1993), ESA, pp. 971-976.
- [30] HALLIKAINEN, M., ULABY, F., DOBSON, M., EL-RAYES, M., AND WU, L. Microwave dielectric behaviour of wet soil - Part 1: Empirical models and experimental observations. *IEEE Trans. Geosci. Remote Sensing* 23, 1 (January 1985), 25-34.
- [31] HOFER, R., AND MÄTZLER, C. Investigations of snow parameters by radiometry in the 3 to 60 mm region. *J. Geophys. Res.* 85(C1) (1980), 453-459.

- [32] HOINKES, H. Methoden und Möglichkeiten von Massenhaushaltsstudien auf Gletschern. *Zeitschr. f. Gletscherk. u. Glazialgeol.* 6, 1-2 (1970), 37-90.
- [33] IQBAL, M. *An Introduction to Solar Radiation*. Academic Press, 1983.
- [34] JIN, Y.-Q. *Electromagnetic scattering modelling for quantitative remote sensing*. World Scientific Publishing, 1993.
- [35] KASER, G., MUNARI, M., NOGGLER, B., OBERSCHMIED, C., AND VALENTINI, P. Ricerche sul bilancio di massa del Ghiacciaio di Fontana Bianca (Weissbrunnferner) nel gruppo Ortleres - Cevedale. *Geogr. Fis. Dinam. Quat.* 18, 2 (1995). in press.
- [36] KELLY, R. Snow monitoring in UK using active microwave data. In *Progress in Environmental Remote Sensing Research and Applications, Proc. of the 15th EARSeL Symposium, 4-6 September 1995, Basel, Switzerland*, (1996), E. Parlow, Ed., EARSeL, A.A. Balkema/Rotterdam/Brookfield, pp. 253-259.
- [37] KOVACS, A., GOW, A., AND MOREY, R. A reassessment of the in-situ dielectric constant of polar firn. CRREL Report 93-26, December 1993.
- [38] KUHN, M., MARKL, G., KASER, G., NICKUS, U., OBLEITNER, F., AND SCHNEIDER, H. Fluctuations of climate and mass balance: different responses of two adjacent glaciers. *Zeitschr. f. Gletscherk. u. Glazialgeol.* 21 (1985), 409-416.
- [39] LAUR, H. Derivation of backscattering coefficient σ^0 in ERS1.SAR.PRI products. Technical Note Issue 1, Rev.0, ESA/ESRIN, October 1992.
- [40] LAUR, H. ERS-1 SAR products: Quality and calibration. In *Proc. Of the EARSeL Workshop* (Eger, Hungary, 7 September 1992), pp. 18-23.
- [41] LAUR, H., BALLY, P., MEADOWS, P., SANCHEZ, J., SCHAETTLER, B., AND LOPINTO, E. Derivation of backscattering coefficient σ^0 in ESA ERS SAR PRI products. Tech. Rep. Issue 2, Rev. 2 ES-TN-RS-PM-HL09, ESA/ESRIN, 28 June 1996.
- [42] LAUR, H., MEADOWS, P., SANCHEZ, J., AND DWYER, E. ERS-1 SAR Radiometric Calibration. In *SAR Calibration Workshop* (ESTEC, Noordwijk, NL, 20-24 Sept. 1993 1993), CEOS Calibration/Validation Working Group, pp. 257-281.
- [43] LOPES, A., TOUZI, R., AND NEZRY, E. Adaptive speckle filters and scene heterogeneity. *IEEE Geosci. Remote Sensing* 28, 6 (1990), 992-1000.
- [44] MARKHAM, B., AND BARKER, J. Landsat MSS and TM post calibration dynamic ranges, exoatmospheric reflectances and at-satellite temperatures. *EOSAT Landsat Tech. Notes*, 1 (1986), 2-8.
- [45] MÄTZLER, C. Applications of the interaction of microwaves with the natural snow cover. *Remote Sensing Rev.* 2 (1987), 259-387.
- [46] MÄTZLER, C. Microwave properties of ice and snow. B.Schmitt, C. de Bergh, and M. Festou, Eds.. *Proc. International Symp. Solar System Ices* in press.
- [47] MÄTZLER, C. Microwave permittivity of dry snow. *IEEE Trans. Geosci. Remote Sensing* 34, 2 (March 1996), 573-581.
- [48] MÄTZLER, C., AND SCHANDA, E. Snow mapping with active microwave sensors. *Int. J. Remote Sensing* 5, 2 (1984), 409-422.

- [49] MÄTZLER, C., WEISE, T., STROZZI, T., FLORICIOIU, D., AND ROTT, H. Microwave snowpack studies made in the Austrian Alps during SIR-C/X-SAR Experiment. Tech. Rep. 96-3, Institute of Applied Physics, Sidlerstr. 5, CH-3012 Bern, February 1996.
- [50] MEIER, E., FREI, U., AND NÜESCH, D. Precise terrain corrected geocoded images. In *SAR Geocoding: Data and Systems*, G. Schreier, Ed. Wichmann Verlag, Karlsruhe, BRD, 1993, ch. 7, pp. 173–185.
- [51] NAGLER, T. Verfahren der Analyse der Schneebedeckung aus Messungen des Special Sensor Microwave\Imager (SSM\I). Master's thesis, Science Faculty, Univ. of Innsbruck, 1991.
- [52] NEURURER, A. Oberflächentemperaturen und Albedo aus NOAA-AVHRR daten in Westgrönland. Master's thesis, Science Faculty, Univ. of Innsbruck, 1991.
- [53] ÖHRENER, C. Funktionsanalyse des Mikrowellen-Radio-Scatterometers RSM und Signatur-Messungen über alpiner Grasheide. Master's thesis, Institut f. Meteorologie und Geophysik, Univ. Innsbruck, Institut f. Nachrichtentechnik und Hochfrequenztechnik, TU Wien, May 1995.
- [54] OLIVER, C. Information from SAR images. *J. Phys. D: Appl. Phys.* 24 (1991), 1493–1514.
- [55] PATERSON, W. *The Physics of Glaciers*, 3rd ed. Pergamon/Elsevier Science Ltd., 1994.
- [56] RAGGAM, J., STROBL, D., AND HUMMELBRUNNER, W. Product quality enhancement and quality evaluation. In *SAR Geocoding: Data and Systems*, G. Schreier, Ed. Wichmann Verlag, Karlsruhe, 1993, ch. 8, pp. 187–206.
- [57] RANGO, A. An international perspective on large scale snow studies. *Hydrological Sciences Journal* 30 (1985), 225–238.
- [58] REBER, B., MÄTZLER, C., AND SCHANDA, E. Microwave signatures of snow crusts: Modelling and measurements. *Int. J. Remote Sensing* 8, 11 (1987), 1649–1665.
- [59] RICHARDS, J. *Remote sensing digital image analysis: an introduction*. Springer Verlag, 1986.
- [60] RIGNOT, E., AND VAN ZYL, J. Change detection techniques for ERS-1 SAR data. *IEEE Trans. Geosc. Remote Sensing* 31, 4 (1993), 896–906.
- [61] ROTT, H. The analysis of backscattering properties from SAR data of mountain regions. *IEEE J. Oceanic Eng. OE-9*, 5 (Dec. 1984), 347–355.
- [62] ROTT, H. Multi-parameter SAR experiments on snow and glacier application. In *Proc. Of 11th EARSeL Symposium* (3-5 July 1991), EARSeL, pp. 79–91.
- [63] ROTT, H. Thematic studies in alpine areas by means of polarimetric SAR and optical imagery. *Adv. Space Res* 14, 3 (1994), 217–226.
- [64] ROTT, H., DAVIS, R., AND DOZIER, J. Polarimetric and multifrequency SAR signatures of wet snow. In *Proc. Of IGARSS'92* (26-29 May 1992), pp. 1658–1660.

- [65] ROTT, H., DOMIK, G., MÄTZLER, C., MILLER, H., AND LENHART, K. Study on use and characteristics of SAR for land snow and ice application. Contract Report 5441/83/D/IM(SC), ESA, 1985.
- [66] ROTT, H., AND MARKL, G. Improved snow and glacier monitoring by the Landsat Thematic Mapper. In *Proc. Of Earthnet Pilot Project on Landsat Thematic Mapper Application, Frascati, Italy, Dec. 1987*, ESA SP-1102 (1989), ESA, pp. 3-12.
- [67] ROTT, H., MÄTZLER, C., STROBL, D., BRUZZI, S., AND LENHART, K. Study on SAR land applications for snow and glacier monitoring. Contract Report 6618/85/F/FL(SC), ESA, 1988.
- [68] ROTT, H., AND NAGLER, T. Snow and glacier investigations by ERS-1 SAR - First results. In *Proc. Of the First ERS-1 Symposium, ESA SP-359* (4-6 Nov. 1992), ESA, pp. 577-582.
- [69] ROTT, H., AND NAGLER, T. Capabilities of ERS-1 SAR for snow and glacier monitoring in alpine areas. In *Proc. Of 2nd ERS-1 Symposium, Hamburg* (11-14 Oct. 1993), ESA, pp. 965-970.
- [70] ROTT, H., AND NAGLER, T. Monitoring temporal dynamics of snowmelt with ERS-1 SAR. In *Proc. Of IGARSS'95* (10-14 July, Firenze, Italy 1995), pp. 1747-1749.
- [71] ROTT, H., NAGLER, T., AND FLORICIOIU, D. Snow and glacier parameters derived from single channel and multi-parameter SAR. In *Proc. of International Symposium on Retrieval of Bio- and Geophysical Parameters from SAR data for Land Applications* (10-13 Oct. 1995, Toulouse, France 1995).
- [72] ROTT, H., SKVARCA, P., AND NAGLER, T. Rapid collapse of northern Larsen Ice Shelf. Antarctica. *Science* 271, 5250 (9 February 1996), 788-792.
- [73] ROTT, H., AND STROBL, D. Synergism of SAR and Landsat TM imagery for thematic investigations in complex terrain. *Adv. Space Res.* 12, 7 (1992), 425-431.
- [74] ROTT, H., AND STURM, K. Microwave signature measurements of antarctic and alpine snow. In *Proc. 11th EARSeL Symposium* (3-5 July, Graz, Austria 1991), pp. 140-151.
- [75] ROTT, H., STURM, K., AND MILLER, H. Active and passive microwave signatures of Antarctic firn by means of field measurements and satellite data. *Ann. Glaciol.* 17 (1993), 337-343.
- [76] RUCK, G., BARRICK, D., STUART, W., AND KRIECHBAUM, C. *Radar Cross Section Handbook*, vol. 1. Plenum, New York, 1970.
- [77] SCHREIER, G. Geometrical properties of SAR images. In *SAR Geocoding: Data and Systems*, G. Schreier, Ed. Wichmann Verlag, Karlsruhe, BRD, 1993, ch. 4, pp. 104-134.
- [78] SEPHTON, A., PARTINGTON, K., MEADOWS, P., ROTT, H., NAGLER, T., WHITELAW, A., HOWES, S., AND BAMBER, J. Simultaneous implementation of a Synthetic Aperture Radar and a High Resolution optical imager (Phase B). Tech. rep., ESA/ESTEC, August 1995.

- [79] SHI, J. *Radar polarimetry modeling and observations of snow-covered terrain*. PhD thesis, University of California, St. Barbara, December 1991.
- [80] SHI, J., AND DOZIER, J. Measurements of snow- and glacier-covered areas with single-polarization. *Ann. Glaciol.* 17 (1993), 72-76.
- [81] SHI, J., DOZIER, J., AND ROTT, H. Snow mapping in alpine regions with Synthetic Aperture Radar. *IEEE Trans. Geosci. Remote Sensing* 32, 1 (January 1994), 152-158.
- [82] SHI, Z., AND FUNG, K. A comparison of digital speckle filters. *Proc. of IGARRS'94, Pasadena* (1994).
- [83] SINGH, A. Digital change detection techniques using remotely-sensed data. *Int. J. Remote Sensing* 10, 6 (1989), 989-1003.
- [84] SINGH, S., AND CRACKNELL, A. The estimation of atmospheric effects for SPOT using AVHRR channel-1 data. *Int. J. Remote Sensing* 7, 3 (1986), 361-377.
- [85] STILES, W., AND ULABY, F. Dielectric properties of snow. In *Proc. of Workshop of the Properties of Snow, Snowbird, Utah, 8-10 April 1981* (1982), CRREL Special Report 82/18, pp. 91-103.
- [86] STROZZI, T., AND MÄTZLER, C. In-situ backscattering measurements of snowcover with coherent scatterometers at 5.3 and 35 ghz. In *Proc. Of IGARSS'95, 10-14 July 1995, Florence, Italy* (1995), pp. 1502-1504.
- [87] TIURI, M., SIHVOLA, A., E.G.NYFORS, AND HALLIKAINEN, M. The complex dielectric constant of snow at microwave frequencies. *IEEE J. Oceanic Engin.* 9, 5 (December 1984), 377-382.
- [88] TOUZI, R., LOPES, A., AND BOUSQUET, P. A statistical and geometrical edge detector for SAR images. *IEEE Trans. Geosci. Remote Sensing* 25, 6 (November 1988), 764-773.
- [89] TSANG, L., DING, K., AND WEN, B. Polarimetric signatures of random discrete scatterers based on vector radiative transfer theorie. In *Progress in Electromagnetic Research. Polarimetric Remote Sensing* (1990), J.A.Kong, Ed., *Progress in Electromagnetic Research, Polarimetric Remote Sensing*, Elsevier, Vol. 3, pp. 75-142.
- [90] TSANG, L., KONG, J., AND SHIN, R. *Theory of microwave remote sensing*. Wiley Series in Remote Sensing. Wiley & Sons, Inc., 1985.
- [91] ULABY, F., AND DOBSON, M. *Handbook of radar statistics for terrain*. Artech House Inc.. 1989.
- [92] ULABY, F., MOORE, R., AND FUNG, A. *Microwave Remote Sensing: Radar Remote Sensing and Surface Scattering and Emission Theory*, Vol. 2 of *Remote Sensing*. Addison-Wesley Publ. Comp. Inc.. 1982.
- [93] VILLASENOR, J., FATLAND, D., AND HINZMAN, L. Change detection on Alaska's north slope using repeat pass ERS-1 SAR images. *IEEE Trans. Geosci. Remote Sensing* 31, 1 (January 1993), 227-236.
- [94] WEGÜMLER, U. The effect of freezing and thawing on the microwave signatures of bare soil. *Remote Sens. Environ.* 33 (1990), 123-135.

- [95] WEN, B., TSANG, L., AND WINEBRENNER, D. Dense medium radiative transfer theory: Comparison with experiment and application to microwave remote sensing and polarimetry. *IEEE Trans. Geosc. Remote Sensing* 28, 1 (January 1990), 46–59.
- [96] WEST, R., TSANG, L., AND WINEBRENNER, D. Dense medium radiative transfer theory for two scattering layers with Rayleigh distribution of particle size. *IEEE Trans. Geosc. Remote Sensing* 31, 2 (March 1993), 426–437.
- [97] WEST, R., WINEBRENNER, D., TSANG, L., AND ROTT, H. Microwave emission from density-stratified antarctic firn at 6 cm wavelength. *J. Glaciol.* 42, 140 (1996), 63–76.
- [98] WOODE, A., DESNOS, Y., AND JACKSON, H. The development and first results from the ESTEC ERS-1 active radar calibration unit. *IEEE Trans. Geosci. Remote Sensing* 30, 6 (1992), 1122–1130.
- [99] ZINK, M., AND BAMLER, R. X-SAR radiometric calibration and data quality. *IEEE Trans. Geosci. Remote Sensing* 33, 4 (July 1995), 840–847.
- [100] ZYL, J. V., CHAPMAN, B., DUBOIS, P., AND SHI, J. The effect of topography on SAR calibration. *IEEE Trans. Geosci. Remote Sensing* 31, 5 (September 1993), 1036–1043.

Curriculum Vitae

Thomas Nagler

Born on 19 April 1965 in Innsbruck

Current Position Research scientist (*Vertragsassistent*) at the Institut für Meteorologie und Geophysik, Universität Innsbruck

Education

- 1971 to 1975 Volksschule Angergasse, Innsbruck.
- 1975 to 1980 Akademisches Gymnasium, Angerzellgasse , Innsbruck.
- 1980 to 1983 Bundesoberstufenrealgymnasium mit ergänz. Unterricht aus Biologie und Umweltkunde sowie Physik und Chemie, Fallmerayerstr., Innsbruck.
- 3 Jun 1983 School leaving exam (*Matura*) at the Bundesoberstufenrealgymnasium, Fallmerayerstr., Innsbruck.
- 1 Oct 1983 to
31 Mar 1984 Military service.
- 6 Mar 1984 Enrollment at the Universität Innsbruck, Studienrichtung Erdwissenschaften.
- 3 Oct 1984 Beginning of the study of Meteorology and Geophysics at the Universität Innsbruck.
- 18 Nov 1991 Final examination, Title of the Diploma Thesis: *Verfahren zur Analyse der Schneebedeckung aus Messungen des Special Sensor Microwave/Imager (SSM/I)*.
- 30 Nov 1991 Graduation to *Magister rerum naturarum* at the Universität Innsbruck.
- since 1 Dec 1991 Research scientist (*Vertragsassistent*) at the Institut für Meteorologie und Geophysik, Universität Innsbruck.

Scientific Experience

- Jul to Sep 1987 Work contract: Analysis of passive microwave data of Antarctica, Institut für Meteorologie und Geophysik, Universität Innsbruck.
- Jul to Sep 1988 Work contract: Alpinwetterdienst des Alpenvereins at the Wetterdienststelle Innsbruck, ZA für Meteorologie, Austria.
- from WS 1990/91
to WS 1993/94 Teaching assistant for *Digitale Bilddatenverarbeitung* and for *Grundlagen der Fernerkundung* at the Institut für Meteorologie und Geophysik, Universität Innsbruck.
- 1990 to 1991 Several work contracts on the topic: Airborne Synthetic Aperture Radar (SAR) experiments in the test site Ötztal und investigations on calibration of polarimetric SAR data.
- 23 Jul 1991 to
1 Aug 1991 Participation at the summer school in Alpbach: *Global Environment: Processes and monitoring from space*.
- 1996 Member of the Organizing Committee of the PIERS'96 Symposium. Innsbruck 1996.

Research visits and scientific expeditions

- May to Jun 1992 Research of mapping of seasonal snow cover and determination of snow heights from data of spaceborne passive microwave sensors at the Cooperative Institute on Research in Environmental Sciences (CIRES), Boulder, CO.
- Apr 1992 to
Mar 1993 Several field campaigns at the test site Ötztal and Innsbruck/Leutasch during ERS-1 passes.
- May/June 1993 Research about SAR data analysis at the Department of Applied and Computational Mathematics, University of Sheffield.
- Apr / Okt 1994 Field campagne in the test site Ötztal during SIR-C/ X-SAR passes.
- Feb/Mar 1994,
Nov/Dec 1995 Field expedition for ERS-1 und SIR-C/X-SAR experiments to the Southern Patagonia Icefield.
- Oct to Dec 1994 Glaciological field work for ERS on the Larsen Iceshelf, Antarctica.
- Aug 1995 Fieldcampaign at the test site Ötztal during ERS-1 / ERS-2 Tandem Mission.

Member of international working groups

- since 1990 Special Sensor Microwave/Imager (SSM/I) Products Working Team of NASA.